Realisation of an atomic quantum Hall system in four dimensions

Jean-Baptiste Bouhiron

PSL
UNIVERSITÉ PARIS

THÈSE DE DOCTORAT
DE L'UNIVERSITÉ PSL

Préparée à l'École Normale Supérieure

Realisation of an atomic quantum Hall system in four dimensions

Soutenue par
Jean-Baptiste Bouhiron
Le 11 Décembre 2023

École doctorale n°564
Physique en Île-de-France

Spécialité
Physique quantique

Composition du jury :

Hannah PRICE University of Birmingham	*Rapporteuse*
Thomas BOURDEL Institut d'optique	*Rapporteur*
Frédéric CHEVY École Normale Supérieure	*Président*
Sylvain NASCIMBÈNE École Normale Supérieure	*Directeur de thèse*

ENS | PSL

Laboratoire Kastler Brossel
Physique quantique et applications

COLLÈGE DE FRANCE
1530

Abstract

This thesis presents experimental realisations of topological systems obtained with dysprosium atoms. Our protocols consist in encoding synthetic dimensions in dysprosium's large spin, $J = 8$, and in coupling these synthetic dimensions to momentum via Raman transitions.

We first emulate quantum Hall systems in two dimensions (one synthetic and one spatial), on a planar geometry and on a cylindrical geometry. In the latter, we were able to implement for the first time Laughlin's topological charge pump, which is intimately linked to the Hall conductance quantisation. Afterwards, we present the main result of this thesis : the realisation a 4D quantum Hall system, by combining two spatial dimensions and two synthetic ones. We compare our findings with the predictions of an effective model, which describes our system as a direct sum of a pair of 2D Landau levels. We unveil typical features of the 4D quantum Hall effect, including the anisotropic edge modes, the non-linear electromagnetic response and the quantisation of the second Chern number.

Finally, we return to the 2D geometry, and investigate the entanglement Hamiltonian of a single-particle quantum Hall system. An approximation of the entanglement Hamiltonian is experimentally realised by following the Bisognano-Wichmann theorem. We present a roadmap for extending this protocol to interacting topological systems.

Résumé

Cette thèse présente des réalisations expérimentales de systèmes topologiques, obtenues avec des atomes de dysprosium. Nos protocoles consistent à encoder deux dimensions synthétiques dans le grand spin du dysprosium, $J = 8$, et à les coupler à la quantité de mouvement des atomes via des transitions Raman.

Tout d'abord, nous simulons des systèmes de Hall quantiques en deux dimensions, sur une géométrie plane et sur une géométrie cylindrique. Dans cette dernière, nous avons pu mettre en œuvre pour la première fois la pompe topologique de Laughlin, qui est intimement liée à la quantification de la conductance de Hall. Nous présentons ensuite le résultat principal de cette thèse : la réalisation d'un système de Hall quantique en 4D, en combinant deux dimensions spatiales et deux dimensions synthétiques. Nous comparons nos résultats avec les prédictions d'un modèle effectif, décrivant notre système comme une somme directe d'une paire de niveaux de Landau en 2D. Nous révélons des caractéristiques typiques de l'effet de Hall quantique en 4D, notamment les états de bord anisotropes, la réponse électromagnétique non linéaire et la quantification du second nombre de Chern.

Enfin, nous revenons à une géométrie bidimensionnelle et étudions l'hamiltonien d'intrication d'un système de Hall quantique à une particule. Une approximation de l'hamiltonien d'intrication est réalisée expérimentalement en s'appuyant sur le théorème de Bisognano-Wichmann. Nous présentons une feuille de route pour étendre ce protocole à des systèmes topologiques avec interactions.

Remerciements

Je dédie les premières lignes de ce manuscrit à toutes les personnes qui m'ont accompagnées durant la thèse, et sans qui je n'aurai pas pu mener à bien ce doctorat. C'était un honneur et un plaisir d'avoir réalisé cette aventure avec vous !

Ces remerciements s'adressent tout d'abord à mes directeurs de thèse, Sylvain Nascimbène et Raphael Lopes. Raphael a beaucoup travaillé avec nous pendant le début de ma thèse, puis est allé construire sa propre expérience. Malgré cela, Raphael est resté très disponible pour nous aider lorsque nous avions des soucis au labo (laser bleu !) ainsi que pour discuter régulièrement de l'avancée des projets. De son côté, Sylvain était mon directeur de thèse « à plein temps ». Derrière sa modestie se cache un brillant scientifique, toujours plein de bonnes idées pour proposer de nouveaux projets ou pour nous débloquer lorsqu'une expérience ne fonctionnait pas. Sylvain est resté extrêmement disponible pour ses doctorants durant toute la thèse, prenant toujours le temps de répondre à nos questions, et souvent avec une incroyable justesse. Je vous remercie tous les deux pour votre disponibilité et pour m'avoir accueilli dans l'équipe, j'ai beaucoup apprécié ces quelques années.

Lors de mon arrivée en 2020, j'ai eu la chance de rejoindre une équipe extrêmement chaleureuse et bienveillante. Je remercie tous les anciens membres de l'équipe, avec qui je n'ai pas travaillé, pour avoir construit l'expérience. Je remercie Alexandre, Tanish et Aurélien de m'avoir accueilli et de m'avoir tout appris de l'expérience. Je remercie en particulier Aurélien, avec qui j'ai travaillé presque durant toute ma thèse et qui m'a beaucoup impressionné par son efficacité dans le travail au quotidien. Puis, Quentin et Qi nous ont rejoint. Nous avons réussi à mener à bien des projets techniquement difficiles, merci à vous pour votre patience pour la réalisation de nos expériences et pour les prises de données, toujours dans une ambiance conviviale. Plus récemment, nous avons eu la chance d'accueillir Nehal, à qui c'était un plaisir de faire découvrir notre manip. L'expérience dysprosium est entre de bonnes mains, bon courage pour la suite !

Plus généralement, je remercie les autres chercheurs permanents de notre étage : Fabrice Gerbier, Alexei Ourjoumtsev et Jérôme Beugnon pour diverses discussions durant la thèse nous permettant de nous débloquer ou d'approfondir nos idées. Je remercie Jean Dalibard, titulaire de la chaire Atome et rayonnement au Collège De France, où notre groupe est situé. Les cours dispensés par Jean étaient extrêmement riches, profonds, et surtout merveilleusement bien construits. Je remercie aussi Carmen Toderasc, très réactive et très gentille et qui permet le bon fonctionnement du groupe au quotidien.

La thèse ce n'est pas uniquement le labo, mais aussi tous les moments informels le midi ou après le boulot. A ce titre, je remercie bien sûr les doctorants de l'équipe dysprosium, mais aussi celles et ceux des expériences Yb, Rb3, Rb4, Dy-K : Remi, Brice, Chloé, Guillaume

Chauveau, Franco, Guillaume Trouffier, Sarah, Maxime, Alexandre. Un remerciement particulier pour les Rb avec qui j'ai passé pas mal de moments durant ma thèse, et notamment avec qui j'ai partagé des *fruitful discussions*. Je vous remercie tout d'abord pour les sorties « en EF » (que l'on commençait avec Guillaume C. à 7h45 du matin en plein hiver au début de notre thèse... quelle folie !). Je vous remercie aussi pour toutes les pauses déjeuner (de tupper, où au libanais). Je vous remercie enfin pour les parties de pool, même si nous n'avons pas réussi à percer malheureusement (quoique, Quentin, dit « le code », a un potentiel !), mais c'était un plaisir de jouer avec vous. Je souhaiterai remercier en particulier Guillaume Chauveau qui a rejoint le groupe en même temps que moi et avec qui j'ai partagé toute ma thèse. Merci pour tes conseils avisés sur la course, pour le trail de la Galinette, pour ton accompagnement lors du marathon de Paris (que ce soit à l'entraînement ou le jour J), pour le soutien régulier durant la thèse. Bon courage pour la dernière ligne droite !

Je remercie le jury : Frédéric Chevy, Thomas Bourdel, H.M Price pour le temps qu'ils ont consacré à la lecture du manuscrit et pour avoir assisté à ma soutenance. C'était un honneur de vous avoir dans mon jury.

Un grand merci à mes ami(e)s qui m'entourent depuis longtemps, et je l'espère pour encore de longues années. J'étais très content d'avoir pu partager cette journée importante qu'est la soutenance de thèse en votre compagnie.

Mes principaux remerciements vont à ma famille, mes parents pour leur soutien infaillible durant la thèse, et à Marjorie. Merci à toi de m'avoir merveilleusement bien accompagné pendant ces années de doctorats (et merci beaucoup pour ton talent artistique qui m'a été précieux pour la réalisation de divers schémas de ce manuscrit, notamment pour « le tite atome » !).

Contents

Introduction

In 1980, Klaus von Klitzing et al made the unexpected discovery of the quantum Hall effect [1]. By studying the motion of a quasi two-dimensional gas of electrons in a MOSFET transistor at low temperature, they were able to detect the quantisation of the Hall conductance. This discovery had both practical and fundamental applications. The quantum Hall effect is used as a standard to measure resistances by defining the ohm based on fundamental constants [2, 3]. Moreover, it led to the emergence of the TKKN theory two years later, introduced by Thouless, Kohmoto, Nightingale and den Nijs in their seminal paper [4]. In it, they proposed an interpretation of the Hall conductance quantisation based on topology.

Topology in physical systems

Topology is a branch of mathematics studying the properties of objects that are conserved under continuous deformations. Its application to quantum physics started in the 1970s, where topological arguments were used in gauge theories, for instance to understand the Aharonov-Bohm effect or to study magnetic monopoles [5, 6]. With the discovery of the quantum Hall effect, topology has played an increasingly important role in condensed matter physics. Following the work of TKKN and S.Pancharatnam [7], Michael Berry popularised the concepts of Berry phase and Berry curvature [8, 9], that are now commonly used in the field. By integrating the Berry curvature over the Brillouin zone of a system, one can compute the topological invariant of this system and characterise its topological properties. In short, a topological property is *robust* to disorder or to a deformation. The primary observation of von Klitzing is an example of topological property.

Initially, topological properties were believed to arise only in two-dimensional electronic systems submited to high magnetic fields. In 1988, Haldane made the first change to this paradigm [10] , by showing that the key ingredient to obtain the quantum Hall effect is not the presence of a magnetic field, but the breaking of time-reversal symmetry. More recently, Kane and Mele generalised the concept of topology to the case of time-reversal invariant systems in [11, 12], via the discovery of the quantum spin Hall effect in two dimensions, which have been since then realised [13–16]. This also led to the notion of 'topological insulator' [17, 18].

The creation of the topological classification in the late 2000s [19–21] generalised the study of topological systems. This classification predicts, as a function of the symmetries of the system and its dimensionality, the presence of a non-trivial topology. This classification not only considers quantum Hall systems or topological insulators, but it also includes topological superconductors [22]. To summarise, the study of topological properties went from the 2D quantum Hall effect to a much richer family of physical systems, of various dimensions and symmetries.

Some of these topological systems are expected to exhibit exciting properties, particularly when considering higher dimensions. The generalisation of the quantum Hall effect to 4D [23] and 6D [24, 25] or the generalisation of 3D topological Weyl semimetals [26] to 5D [27] predict exotic physical phenomena. As an example, the 4D quantum Hall effect is quantised by a new topological invariant, the second Chern number, quantifying the non-linear response to an electromagnetic perturbation.

Extending the classification to interacting systems also leads to new physical phenomena. For instance, 2D fractional quantum Hall states [28–30] could host non-Abelian anyon excitations [31–33], whose statistics are not bosonic nor fermionic. These anyons could have important applications in quantum computing [34].

Most of the topological systems remain to be explored, and other fields of physics have joined the effort of solid-state systems to study these exotic new phases of matter. Photonics is one of them [35–37]. This field has enabled the observation of numerous new topological phases, with for example observations of Floquet topological insulators [38–40] or 4D quantum physics [41]. A more recent branch, topological electronic circuits, has permitted the measurement of the first topological insulator in class AI and in four dimensions [42]. Ultracold atomic gases represent another field that can contribute to the exploration of topological quantum matter [43–46].

Cold atom experiments

Cold atom experiments study dilute ultracold gases of neutral atoms, with a high degree of control achieved through electromagnetic fields. This field of research has been highly productive over the last thirty years and has observed many theoretical predictions of new phases of matter. Bose-Einstein condensation was observed in 1995 [47, 48] and the degeneracy of a Fermi gas was reached in 1999 [49]. More recently, there has been an effort to simulate topological phases of matter.

These experiments offer various methods for emulating topological condensed matter systems. The most common one involves the use of optical lattices, which naturally mimic the physics of electrons in a crystalline potential. As we sill see later on, topological properties generally require external gauge fields and spin-orbit coupling to arise [43]. The cold atoms community has thus developed several tool to engineer these gauge fields on neutral atoms, going beyond the standard static optical lattices.

A significant advantage of cold atom experiments lies in the ability to finely tune the interactions between atoms, for instance through Feshbach resonances. It is thus an interesting platform to realise many-body topological phases of matter, such as fractional quantum Hall states. A recent example of this was achieved using two atoms on a 4×4 lattice [30], and could be use to probe non-abelian anyonic excitations if the system's size was extended. Another key advantage of these experiments is the capability to probe the topological nature of the simulated model, which is often a challenging task due to the lack of local order parameter to identify it. For instance, edge modes can be observed through the ability to load atoms directly into the edge states and via atomic in-situ imaging [50], revealing the topology through the bulk-edge correspondence [51]. The topological invariant of the model (for instance, the Chern number in a quantum Hall system) can be obtained by measuring the center of mass response to a perturbation [52], enabling the characterisation of the topology.

Artificial gauge fields

Many topological effects are a consequence of spin-orbit coupling and external gauge fields [43]. This is the case for the topological Bloch bands arising in quantum Hall systems.

However, cold atom experiments involve neutral atoms, that do not experience the Lorentzi force responsible for the quantum Hall effect. Instead, we use artificial gauge fields that analogously mimic the effects of magnetic fields on electrons. In this manner, Hamiltonian of the form

$$H = \frac{[\boldsymbol{p} - \boldsymbol{A}(\boldsymbol{r})]^2}{2M}, \tag{1}$$

can be emulated on neutral atoms, where the artificial gauge field $\boldsymbol{A}(\boldsymbol{r})$ can be made Abelian or non-Abelian [53, 54].

These artificial gauge fields can be engineered in various ways in cold atom experiments. The first one is through rotations of an atomic gas, where the Coriolis force replaces the Lorentz force [55]. A second and fruitful possibility is the use optical lattices as mentioned previously. By implementing laser-induced tunelling between the different lattices site [56, 57], or by Floquet engineering [58], artifical gauge fields can be produced, leading to the simulation of various topological phases of matter. For instance, [59] reported the exploration of 4D quantum Hall physics via time modulation of an optical superlattice. The Haldane model [58], or the Hofstadter Hamiltonian [52] were realised in modulated optical lattices. A third approach, which is employed in our laboratory, consists in treating the atom's spin as a synthetic dimension. By using Raman processes, we can couple the atomic spin to its momentum, thereby generating spin-orbit coupling.

Synthetic dimensions

The use of synthetic dimensions has several advantages. First, it permits the emulation of higher-dimensional systems [60]. For example, a one-dimensional lattice could be mapped onto a two-dimensional system by taking into account the internal degree of freedom of the atoms. Secondly, synthetic dimensions permit the engineering of both a bulk and sharp boundaries, thereby allowing the observation of the edge states that occur at the boundaries of a topological system. Additionally, they allow the implementation of radial artificial gauge fields [61–63], something that is difficult to implement in solid-state systems. It is worth noting that synthetic dimensions are not restricted to cold atom experiments and are extensively used in other plateforms, such as photonics [36, 64, 65].

However, this method of engineering artificial gauge field comes with a drawback : it requires implementing rather strong light shifts, which often result in a significant heating due to off-resonant photon scattering when used with alkali atoms, the most common species in cold atom experiments. This issue can be overcome by manipulating lanthanides atoms, whose electronic structures lead to a more favorable interaction between light and matter.

Lanthanides

Lanthanides are a family of chemical elements whose atomic numbers range between 57 to 71. Despite being more challenging to manipulate and to cool than most alkali elements, this family of atomic species has been gaining increasing interest.

The peculiar electronic structure of lanthanides (meaning, their open f shell) leads to a rich landscape of electronic transitions, and for some of them, to a large spin in the ground state. For instance, erbium and dysprosium have respectively a spin $J = 6$ and $J = 8$ in their ground state, resulting in a strong magnetic moment and therefore strong dipolar interactions. To illustrate, the dipolar interaction between two dysprosium atoms is about 100 times higher than the one between two rubidium atoms [66]. These dipolar interactions are the primary reason for the growing popularity of lanthanide experiments. Indeed, these long-range interactions can give rise to new states of matter, such as quantum droplets that

were observed recently [67, 68]. Another striking example is the roton-maxon spectrum and its supersolid character, that have been experimentally studied [69–72].

An alternative area of research using lanthanides atoms (and more particularly dysprosium atoms) consists in considering their macroscopic spin J as $2J$ fictitious qubits. This can be used to study nonclassical states made of these virtual qubits, and have potential applications in metrology [73–75].

In our group, we are recently interested in the quantum simulation of topological systems by considering dysprosium's spin as synthetic dimensions. We leverage dysprosium's large spin $J = 8$ to have both a bulk and sharp edges. Moreover, our protocols require the use of strong light shifts, which would result in significant heating if implemented with alkali atoms, as mentioned earlier. Dysprosium is well-suited to overcome this issue because its transitions arrangement, consisting of many isolated narrow transitions, permits to avoid off-resonant scattering. Secondly, the shape of the light-matter interactions for dysprosium (and more generally for lanthanides) benefits from the non-vanishing tensorial polarisability, and we can engineer first and second-order light shifts. We also note that combining the light-matter interaction with dipolar-dipolar interactions could lead to the realisation of more intriguing topological phases of matter [66].

In this thesis, we focus on the simulation of topological quantum Hall systems using an ultracold gas of dysprosium atoms. An artificial gauge field is generated by using Raman process and by considering dysprosium's spin as synthetic dimensions. This manuscript is organised as follows:

Chapter 1 is dedicated to the presentation of our experimental apparatus and of dysprosium properties. We detail the interaction between light and dysprosium and see that the light polarisation is the key ingredient to describe it. We present a few techniques to measure the light polarisation and the magnetic field strength using dysprosium atoms.

Chapter 2 introduces our protocol to emulate quantum Hall systems using the example of the 2D quantum Hall ribbon, already realised previously in our group. In short, by coupling dysprosium's spin to its momentum via Raman transitions, we can emulate artificial gauge fields in a space-synthetic system.

Chapter 3 centers on the encoding of two synthetic dimensions within dysprosium's large spin. We theoretically demonstrate the emergence of these two dimensions, one of them being cyclic. We then use this cyclic synthetic dimension to engineer a quantum Hall cylinder in which we implement Laughlin's topological charge pump.

Chapter 4 provides a theoretical exploration of 4D quantum Hall systems. We first introduce the topological classification and expose a few typical properties of topological higher-dimensional systems. We then delve into a synthetic 4D quantum Hall system, made of the two synthetic dimensions studied in chapter 3 and two spatial ones.

Chapter 5 presents the main result of this thesis, namely the experimental realisation of a 4D quantum Hall system. We first reveal the system's topology by measuring anisotropic chiral edge modes at the boundaries. We then characterise the bulk topology by measuring a second Chern marker equal to unity. Finally, we explore the peculiar nature of cyclotron orbits in 4D, as well as the non-linear electromagnetic response.

Chapter 6 focuses on the notion of entanglement spectrum. We follow Bisognano-Wichmann prescription to realise an approximation of the entanglement Hamiltonian of a 2D non-interacting quantum Hall system. We measure its spectrum and unveil a chiral dispersion relation, identifying the topology of our system via the bulk-edge correspondence. Finally, we offer a proposal to extend our protocol to interacting systems.

During my thesis, I contributed to four different projects, three of them being discussed in this manuscript, with a strong emphasis on the realisation of a 4D quantum Hall system. I had also the opportunity to work on the notion of pairwise entanglement, that I don't detail here. In short, we considered dysprosium's large spin J as $2J$ fictitious qubits and studied the entanglement between these virtual qubits. This study led to a publication [76] that we provide in Appendix A. It is extensively described in thesis [77, 78].

1 An ultracold dysprosium experiment

This chapter is dedicated to the study of dysprosium properties and to the presentation of our experiment. We start by describing a few general properties of dysprosium. We study the contact and dipolar interactions between two atoms, and see that they can be neglected on the timescales of our experiments. We then focus on the interaction of dysprosium with light. Thanks to its rich electronic structure, dysprosium has many transitions. The arrangement of these transitions is quite favorable. In particular, it permits to work in the vicinity of a given narrow transition without suffering too much from scattering. In this regime, we show that the light-matter interaction can be greatly simplified, and that first and second-order spin-dependent operators can be engineered on a dysprosium atom with light.

Following this theoretical study, we briefly describe the dysprosium machine at Collège de France. We then move on to the beams preparation and calibration. Since the polarisation of light has a strong influence on the light shift properties, we attach great importance to

the polarisation calibration of each laser beam. Subsequently, we focus on the magnetic field control, from the ability to perform magnetic field rotations to the measurement of the magnetic field norm.

Finally, we propose an experimental upgrade that would permit us in the future to have a more robust Bose-Einstein condensate. This would be the first step towards the exploration of many-body topological phases in our experiment.

1.1 Dysprosium properties

Dysprosium is a rare-earth element located at the 6^{th} line and 12^{th} column of the periodic table. Its atomic number is 66. It is mainly found in four isotopes, see Fig. 1.1, ^{1}64Dy isotope being the most abundant [79]. At room temperature and atmospheric pressure, it's a grey and ductile metal. At the moment, dysprosium has only few applications. It is used for data storage (thanks to its high magnetic susceptibility), being incorporated in the surface coatings of some hard drives. Dysprosium is also used in dosimeters, where its luminescence, once exposed to ionising radiation, provides a measurement of the radiation level.

Dysprosium has one of the largest magnetic moment among the periodic table, which makes it of peculiar interest for fundamental physics, for instance to study long-range interactions. Moreover, as we will see in this manuscript, its huge spin $J = 8$ (for bosonic dysprosium) is a useful tool to emulate condensed matter systems.

a

Isotope	^{161}Dy	^{162}Dy	^{163}Dy	^{164}Dy
Abundance	18.9%	25.5%	24.9%	28.3%
Nuclear spin	$I = 5/2$	$I = 0$	$I = 5/2$	$I = 0$

b

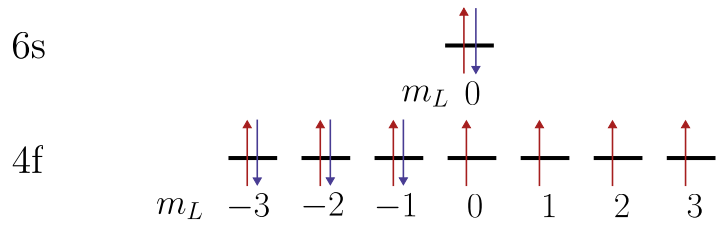

Figure 1.1: Isotopes of dysprosium and electronic configuration. **a**: Four most abundant isotopes of dysprosium in nature. All the results presented in this thesis involve the ^{162}Dy isotope. Data from [79]. **b** : Electronic configuration of dysprosium in its ground state.

1.1.1 Electronic structure

The electronic structure of dysprosium can be written as :

$$[\text{Xe}]4f^{10}6s^2 \tag{1.1}$$

Even though the $6s$ shell of dysprosium is filled, the $4f$ shell lacks 4 electrons, which leads to an orbital momentum $L = 6$ and an electronic spin $S = 2$, see Fig. 1.1b. Thus, the total angular momentum is $J = L + S = 8$. The bosonic isotopes of dysprosium have no nuclear spin, $I = 0$, and hence no hyperfine structure. The ground state of a bosonic dysprosium is made of 17 degenerate Zeeman sublevels : $|J = 8, m = -8\rangle, ..., |J = 8, m = 8\rangle$.

The four unpaired valence electrons of dysprosium lead to a high number of electronic levels, thus a high number of electronic transitions. We show some of these transitions in

Fig. 1.2. During this thesis, we essentially manipulated the atomic internal and external degrees of freedom using the optical transitions at 421 nm and the 626 nm between the electronic ground state and two excited states. Both are associated with the promotion of an electron of the 6s shell to a 6p orbital.

a

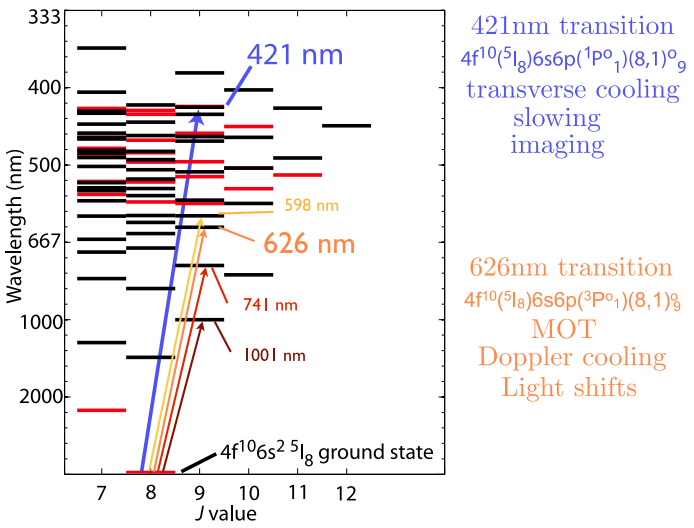

b

λ	$\Gamma/(2\pi)$	T_D	I_{sat}
421 nm	31.9 MHz	765 μK	55.8 mW.cm^{-2}
626 nm	135 kHz	3.2 μK	72 µW.cm^{-2}

Figure 1.2: Electronic transitions of dysprosium. Figure adapted from [80]. **a** : Electronic transitions of dysprosium. Red states (resp. black states) correspond to states of even (resp. odd) parity. We depict a few transitions of dysprosium. The ones used in our experiment are the blue transition at 421 nm and the so-called 'orange transition' at 626 nm. **b** : Properties of the 421 nm and the 626 nm transitions : linewidth, Doppler temperature and saturation intensity.

1.1.2 Interactions between dysprosium atoms

Contact interactions

The contact interactions between two dysprosium atoms depend on the total spin J_{tot} of the two atoms. For s-wave interactions, the exchange symmetry [81] imposes that the collision is vanishing if the total spin is an odd number. For ^{162}Dy, one should consider 9 collision channels, with $J_{\text{tot}} = 0, 2, ..., 16$. The interaction potential between two atoms can be written as [82] :

$$V = \delta(\boldsymbol{r}) \sum_{\text{even } J_{\text{tot}}} g_{J_{\text{tot}}} P_{J_{\text{tot}}}, \tag{1.2}$$

where $\boldsymbol{r}$ is the intra-particle distance, $P_{J_{\text{tot}}}$ is the projector on the subspace of total spin J_{tot} and $g_{J_{\text{tot}}}$ is an interaction parameter. Nine interactions parameters, i.e nine scattering lengths $a_{J_{\text{tot}}} = M g_{J_{\text{tot}}}/(4\pi\hbar^2)$, are thus necessary to fully describe dysprosium interactions. Indeed, if two interacting atoms in $|-8\rangle$ or in $|+8\rangle$ only involve a_{16}, interactions between other m states involve many channels, hence many scattering lengths.

The high complexity of dysprosium electronic structure makes the theoretical calculation of these scattering lengths challenging [83, 84]. We thus rely on experiments to get

information on these scattering lengths. For the ^{162}Dy and ^{162}Dy, measurements using self-bound dipolar droplets were realised, leading to a value $a_{16} = 140(7)a_0$ for ^{162}Dy [72] and $a_{16} = 69(4)a_0$ for ^{164}Dy [68]. For now, we only know the scattering length a_{16} for the channel $J_{\text{tot}} = 16$ among the 9 scattering lengths that fully describe the contact s-wave interactions.

Dipolar interactions

With its high magnetic moment, dysprosium has the strongest dipolar interactions in its ground state among neutral atoms. Stronger dipolar interactions can still be obtained for molecules or Rydberg atoms. We briefly describe dipolar interactions in this paragraph, more details can be found in [66].
The dipolar-interaction potential between two dysprosium atoms separated by a vector $\boldsymbol{r} = (x, y, z)$ has the following form :

$$V_{\text{dd}} = \frac{\mu_0 g_J^2 \mu_B^2}{4\pi r^3} \left(\frac{r^2 \boldsymbol{J_1} \cdot \boldsymbol{J_2} - 3(\boldsymbol{J_1} \cdot \boldsymbol{r})(\boldsymbol{J_2} \cdot \boldsymbol{r})}{r^2} \right), \tag{1.3}$$

where $\boldsymbol{J} = (J_x, J_y, J_z)$ is the angular momentum operator, g_J the Landé factor, μ_B the Bohr magneton and μ_0 the vacuum permeability. The index 1 and 2 refer to two different particles. Eq. (1.3) can be rewritten [66, 85, 86] :

$$\begin{aligned} V_{\text{dd}} = \frac{\mu_0 g_J^2 \mu_B^2}{4\pi r^3} [& J_{1z} J_{2z} + \frac{1}{2}(J_{1+} J_{2-} + J_{2+} J_{1-}) \\ & - \frac{3}{4}[(2\tilde{z} J_{1z} + \tilde{r}_- J_{1+} + \tilde{r}_+ J_{2-})(2\tilde{z} J_{2z} + \tilde{r}_- J_{2+} + \tilde{r}_+ J_{1-})]], \end{aligned} \tag{1.4}$$

where $\tilde{r}_\pm = \dfrac{x \pm iy}{r}$ and $\tilde{z} = \dfrac{z}{r}$. Three different physical process can be extracted from this interaction, as demonstrated in [66] :

(i) First, the terms proportional to $J_{1z} J_{2z}$ conserve the spin of each atom.

(ii) Secondly, the terms proportional to $J_{1+} J_{2-} + J_{1-} J_{2+}$ don't conserve the spin of each atom, but conserve the magnetisation of the pair. Providing there is no quadratic Zeeman shift, the magnetic energy is also conserved.

(iii) Finally, the terms proportional to $J_{1z} J_{2-}$ and to $J_{1-} J_{2-}$ (as well as their Hermitian conjugates) result in a modification of the total magnetisation.

In the presence of a magnetic field, contribution (iii) leads to a conversion of Zeeman energy into kinetic energy. This is the so-called 'dipolar relaxation' and is a source of heating. The rates of dipolar relaxation are, for bosons, an increasing function of the magnetic field. Working at high magnetic fields with bosonic dysprosium in any state other than $|-8\rangle$[1] is thus challenging, especially at high density. We show in Fig. 1.3 an example of dipolar relaxation in our experiment.

[1] the state $|J = 8, m = -8\rangle$ doesn't undergo dipolar relaxation since $J_- |J = 8, m = -8\rangle = 0$.

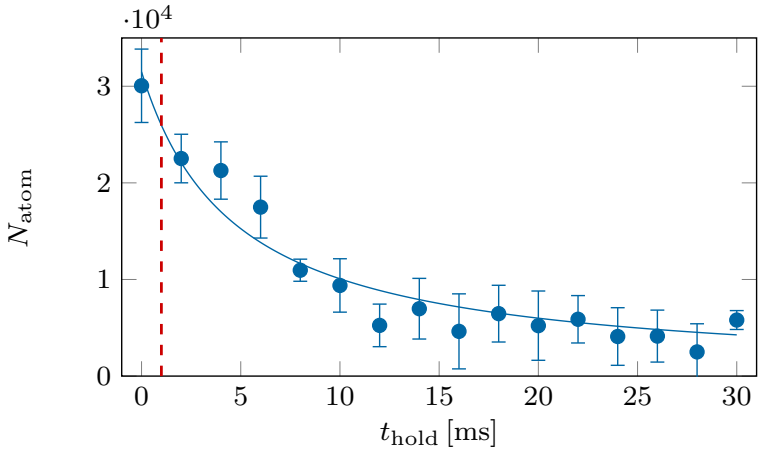

Figure 1.3: Dipolar relaxation at a $1G$ magnetic field. Atoms are initially prepared in a coherent state of average magnetisation $\langle J_z \rangle \simeq 0$. They are held in the dipole traps for various durations. Solid line is a two-body loss fit. The red dashed line indicates the usual maximum duration of our experiments $t_{\text{max}} \simeq 1\,\text{ms}$. Note that the decay occuring here is not only due to the dipolar relaxation involving two spin states $m = 0$. Indeed, overtime, the contact interactions redistribute the spin populations. Hence, many different dipolar relaxation channels can occur in parallel. The decay displayed here results from the combination of all these different channels.

Competition between contact and dipolar interactions

The strength of contact interactions and dipolar interactions can be characterised by (respectively) the scattering length a and the magnetic length :

$$a_{\text{dd}} = \frac{\mu_0 \mu^2 M}{12\pi\hbar^2}, \tag{1.5}$$

where M is the atomic mass, and μ is the dipolar moment of the species under study. The ratio between the scattering length and the magnetic length, $\epsilon_{\text{dd}} \equiv a_{dd}/a$, quantifies the dipolar character of an atomic species.

We show in Fig. 1.4 a comparison of the magnetic length and the scattering length of ^{87}Rb, ^{162}Dy and ^{164}Dy. As one can see, this ratio is way higher for bosonic dysprosium than for rubidium. Moreover, we also see that it is higher for ^{164}Dy than for ^{162}Dy (due to its smaller scattering length). The isotope ^{164}Dy is thus more interesting to probe dipolar-related physics, such as supersolidity [69, 71, 87, 88]. However, our group uses ^{162}Dy to implement artificial gauge field in its synthetic dimension, because its large scattering length favors evaporative cooling.

	^{87}Rb	^{162}Dy	^{164}Dy
a	$a_{11} = 100.9a_0$	$a_{16} = 140(7)a_0$	$a_{16} = 69(4)a_0$
a_{dd}	$0.7a_0$	$129a_0$	$131a_0$
ϵ_{dd}	0.007	0.92(5)	1.89(11)

Figure 1.4: Contact and dipolar interactions for dysprosium and rubidium. Scattering length for ^{87}Rb is taken from [89].

The results presented in this thesis are performed with a (cold) thermal cloud of dysprosium atoms. The experiments are performed at relatively short timescales (below the ms level), so if not mentioned, interactions will be neglected in the rest of the thesis. In the next section, we focus on the interaction between a dysprosium atom and a photon.

1.2 Light-matter interaction

In this section, we first introduce the polarisability for a simple quantum system, and then move on to the case of dysprosium atom.

1.2.1 Toy model

We suppose that an electric field $\boldsymbol{E} = \frac{E}{2}\mathrm{e}^{-i\omega t}\boldsymbol{\epsilon} + \text{c.c}$, where $\boldsymbol{\epsilon}$ is the polarisation, is applied on an atom. The coupling between light and matter is written as :

$$H = -\boldsymbol{d}\cdot\boldsymbol{E} \tag{1.6}$$

where $\boldsymbol{d}$ is the dipole operator. We suppose that the electric field is not resonant with any transition. In this case, the interaction between light and matter can be considered by a virtual absorption of a photon followed by a virtual emission. To treat this problem, we use the dressed state formalism where we consider the system $\{\text{atom} + \text{photon}\}$ as a whole. The interaction between light and matter leads to a shift of eigenenergy that can be computed using second-order perturbation theory. The energy shift of the ground state is given by :

$$dV = \frac{|\boldsymbol{E}|^2}{4}\sum_{e\neq g}\frac{|\langle g|\,\boldsymbol{d}\cdot\boldsymbol{\epsilon}\,|e\rangle|^2}{E_e - E_g - \hbar\omega} + \frac{|\langle g|\,\boldsymbol{d}\cdot\boldsymbol{\epsilon}\,|e\rangle|^2}{E_e - E_g + \hbar\omega} \tag{1.7}$$

For our model to describe the finite lifetime of the excited state, we write the energy of the excited state with a non-vanishing imaginary part : $E_e = \hbar\omega_e + i\frac{\hbar\Gamma_e}{2}$ where Γ_e is the width of the excited state. The energy of the ground state is given by $E_g = \hbar\omega_g$. In the end, we are left with :

$$dV = \frac{|\boldsymbol{E}|^2}{4}\sum_{e\neq g}\frac{|\langle g|\,\boldsymbol{d}\cdot\boldsymbol{\epsilon}\,|e\rangle|^2}{\hbar(\omega_{eg} - \omega) + i\hbar\Gamma_e/2} + \frac{|\langle g|\,\boldsymbol{d}\cdot\boldsymbol{\epsilon}\,|e\rangle|^2}{\hbar(\omega_{eg} + \omega) + i\hbar\Gamma_e/2}, \tag{1.8}$$

where $\omega_{eg} \equiv \omega_e - \omega_g$. The second term of Eq. (1.8) is often neglected using the rotating wave approximation (RWA)[90], leading to the simpler expression :

$$dV = \frac{|\boldsymbol{E}|^2}{4}\sum_{e\neq g}\frac{|\langle g|\,\boldsymbol{d}\cdot\boldsymbol{\epsilon}\,|e\rangle|^2}{\hbar(\omega_{eg} - \omega) + i\hbar\Gamma_e/2} \tag{1.9}$$

This equation can be written in a much more compact form $dV = -\alpha(\omega)|\boldsymbol{E}|^2$, which defines the frequency-dependent atomic polarisability $\alpha(w)$ of the ground state. The energy shift $dV = U - i\frac{\hbar\Gamma_{\text{scat}}}{2}$ and the polarisability has both a real and an imaginary part, each of them describing different physical processes.

Real part

The real part is related to the (real) energy shift of the atomic levels, and is often referred to as the light shift. It describes a conservative potential :

$$U(\boldsymbol{r}) = -Re\left[\alpha(\omega)\right]|\boldsymbol{E}(\boldsymbol{r})|^2. \tag{1.10}$$

Within RWA and introducing the detuning $\Delta_{eg} = \omega_{eg} - \omega$, it can be expressed as :

$$U(\boldsymbol{r}) = \frac{|\boldsymbol{E}(\boldsymbol{r})|^2}{4\hbar} \sum_{e \neq g} \frac{|\langle g| \boldsymbol{d} \cdot \boldsymbol{\epsilon} |e\rangle|^2 \Delta_{eg}}{\Delta_{eg}^2 + \Gamma_e^2/4} \tag{1.11}$$

The sign of this potential thus depends on the sign of the detuning : a red-detuned (resp. blue-detuned) laser will lead to an attractive (resp. repulsive) potential. The spatial dependance of the potential is given by the light intensity profile. This opens plenty of possibilities to trap the atoms, from the optical dipole traps creating an harmonic confinement to optical lattices, where the atoms are trapped in the interference patterns whose typical size is set by the laser wavelength.

Imaginary part

The imaginary part of the energy shift describes the scattering :

$$\Gamma_{\text{scat}}(\boldsymbol{r}) = -\frac{2}{\hbar} \text{Im}\left[\alpha(\omega)\right] |\boldsymbol{E}(\boldsymbol{r})|^2 \tag{1.12}$$

Similarly, it can be expressed as :

$$\hbar\Gamma_{\text{scat}}(\boldsymbol{r}) = \frac{|\boldsymbol{E}(\boldsymbol{r})|^2}{4\hbar} \sum_{e \neq g} \frac{|\langle g| \boldsymbol{d} \cdot \boldsymbol{\epsilon} |e\rangle|^2 \Gamma_e}{\Delta_{eg}^2 + \Gamma_e^2/4} \tag{1.13}$$

This term accounts for the absorption/spontaneous emission cycles, due to the finite lifetime of the excited states. To limit the scattering, the ratio Γ_e/Δ_{eg} needs to be reduced, which means working further away from resonances or using narrower transitions.
In practice, as seen on Eq. (1.11) and Eq. (1.13), the real part scales in $1/\Delta_{eg}$ whereas the imaginary part scales in $1/\Delta_{eg}^2$. We can thus neglect the scattering compared to the light shift, when we are working with an off-resonant beam.

To summarise, we have seen with this simple model how a detuned light can be used to shape attractive or repulsive potential on the atoms, via the real part of the atomic polarisability. We now move on to the more complicated case of dysprosium atoms.

1.2.2 Off-resonant light-matter interaction for Dyprosium

The above model doesn't take into account the internal structure of the ground state. The formalism of light-matter interaction for real atoms is well established [90], and we summarise here the principal results for the case of dysprosium atoms. More details can be found in [91, 92]. The off-resonnant light-matter potential for a dysprosium atom in a given J state can be separated into three contributions :

$$V = V_{\text{scalar},J} + V_{\text{vectorial},J} + V_{\text{tensorial},J}, \tag{1.14}$$

where :

$$\begin{aligned} V_{\text{scalar},J} &= \alpha_{\text{scalar},J}(\omega)|\boldsymbol{\epsilon}|^2 \mathbb{1} \\ V_{\text{vectorial},J} &= -i\alpha_{\text{vectorial},J}(\omega)\left(\boldsymbol{\epsilon}^* \times \boldsymbol{\epsilon}\right) \cdot \frac{\boldsymbol{J}}{2J} \\ V_{\text{tensorial},J} &= \alpha_{\text{tensorial},J}(\omega) \frac{3\left[(\boldsymbol{\epsilon}^* \cdot \boldsymbol{J})(\boldsymbol{\epsilon} \cdot \boldsymbol{J}) + (\boldsymbol{\epsilon} \cdot \boldsymbol{J})(\boldsymbol{\epsilon}^* \cdot \boldsymbol{J})\right] - 2\boldsymbol{J}^2}{2J(2J-1)} \end{aligned} \tag{1.15}$$

While the vectorial and tensorial components depend on the spin, the scalar does not. The prefactors $\alpha_{\text{scalar}}, \alpha_{\text{vectorial}}, \alpha_{\text{tensorial}}$ are respectively called the scalar, vectorial and tensorial polarisability. They carry the dependence on the light intensity.

They can be expressed as :

$$\begin{aligned}
\alpha_{\text{scalar},J} &= \sqrt{\frac{1}{3(2J+1)}} \sum_{J'} (-1)^{J'+J} \begin{Bmatrix} 1 & 0 & 1 \\ J & J' & J \end{Bmatrix} V_{J,J'}, \\
\alpha_{\text{vectorial},J} &= -\sqrt{\frac{6J}{(J+1)(2J+1)}} \sum_{J'} (-1)^{J'+J+1} \begin{Bmatrix} 1 & 1 & 1 \\ J & J' & J \end{Bmatrix} V_{J,J'}, \\
\alpha_{\text{tensorial},J} &= -\sqrt{\frac{10J(2J-1)}{3(J+1)(2J+1)(2J+3)}} \sum_{J'} (-1)^{J'+J+2} \begin{Bmatrix} 1 & 2 & 1 \\ J & J' & J \end{Bmatrix} V_{J,J'},
\end{aligned} \tag{1.16}$$

where the sum spans all the possible transitions and where the curly braces represent the Wigner-6j symbols. The prefactor $V_{J,J'}$ contains the dependency on the transition and on the light via $V_{J,J'} = \dfrac{3\pi c^2}{2\omega_{J,J'}} \dfrac{\Gamma_{J,J'}}{\Delta_{J,J'}} I$. First, $\Gamma_{J,J'}$ refers to the transition linewidth and $\hbar\omega_{J,J'}$ is the transition energy. On the other hand, $\Delta_{J,J'}$ is the detuning between the light frequency and the resonance, and I is the light intensity.

As we see, the off-resonant interaction between light and a dysprosium atom is quite complicated. Interestingly, at first sight, all the transitions are involved to describe the interaction between an atom and a photon at frequency ω. Fortunately, Eq. (1.14) can be greatly simplified by considering two different regimes. This simplification is permitted by the peculiar distribution of dysprosium transitions.

Dysprosium transition structure

As seen in the beginning of this chapter, the complex electronic structure of dysprosium leads to many different transitions. These transitions follow a typical pattern. At high energy (near-UV wavelengths), dysprosium exhibits three broad and nearby transitions : 405 nm, 419 nm, 421 nm. On the other hand, in the visible and IR domains, dysprosium has only narrow transitions, which are all well separated. We propose in Fig. 1.5 a schematic of dysprosium's transition landscape. This structure leads to two different regimes that we detail below.

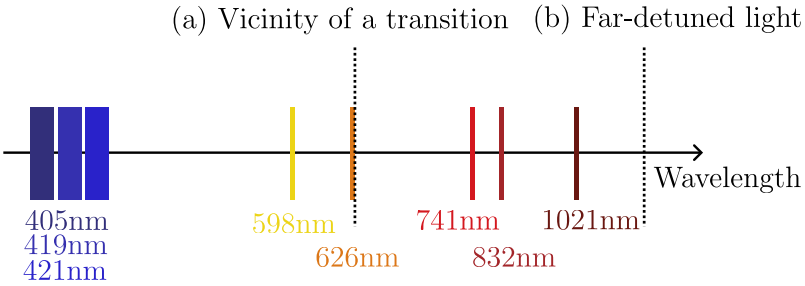

Figure 1.5: Schematic of dysprosium transitions. Only a few of them are depicted. There is a triplet of broad transitions in the near-UV regime. On the other hand, there are several narrow transitions in the visible and IR domains. Regime (a) : We are in the vicinity of a transition, here the 626 nm transition. Regime (b) : We are far-detuned from any transition.

Far-detuned light

For a far-detuned light, the main contribution of the interaction comes from the triplet of broad transition in the near-UV regime. Indeed, these transitions have a much bigger

linewidth, and the ratio Γ/Δ, proportional to the interacting potential, is much more favorable for any transition of the blue triplet than for any narrow transitions. For example, assuming a 1070 nm light, we have :

$$\begin{aligned} \frac{\Gamma_{626}}{|\Delta_{626}|} &\simeq 6.8 \times 10^{-10} \\ \frac{\Gamma_{421}}{|\Delta_{421}|} &\simeq 7.4 \times 10^{-8} \end{aligned} \tag{1.17}$$

In this configuration, the majority of the interaction is due to the scalar contribution of the near-UV triplet. Indeed, the contribution to the vectorial and tensorial polarisabilities[1] of the three blue transitions nearly cancels out when the light is far-detuned from this UV-triplet [91, 92]. This regime is used to trap atoms in the optical dipole traps.

Vicinity of a narrow transition

In the vicinity of a narrow transition, the scalar 'background' contribution due to the near-UV triplet can be neglected in front of the contribution of the transition under study. In such case, the scalar, vectorial and tensorial contributions of the polarisability are of the same order of magnitude. We can hence engineer spin-dependent light shifts. The light-matter interaction Eq. (1.14) can be greatly simplified in this regime. We are left with [91]:

$$V = U\left[\alpha_0 \mathbb{1} - i\alpha_1 \left(\boldsymbol{\epsilon}^* \times \boldsymbol{\epsilon}\right) \cdot \frac{\boldsymbol{J}}{2J} + \alpha_2 \frac{3\left[\left(\boldsymbol{\epsilon}^* \cdot \boldsymbol{J}\right)\left(\boldsymbol{\epsilon} \cdot \boldsymbol{J}\right) + \left(\boldsymbol{\epsilon} \cdot \boldsymbol{J}\right)\left(\boldsymbol{\epsilon}^* \cdot \boldsymbol{J}\right)\right] - 2\boldsymbol{J}^2}{2J(2J-1)}\right], \tag{1.18}$$

where the coefficients $\alpha_0, \alpha_1, \alpha_2$ are frequency-independent, their value being only given by the excited state involved in the transition. The interaction is described by three terms : the scalar light shift, the vectorial light shift and the tensorial light shift.

We provide the values of these coefficients in Fig. 1.6. The prefactor U is often referred to as the light shift for Clebsch-Gordan coefficients equal to unity. It contains the dependency on the light power and detuning, and is given by :

$$U = \frac{3\pi c^2}{2\omega_0}\frac{\Gamma}{\Delta} I, \tag{1.19}$$

where I is the light intensity, Γ the transition linewidth, Δ the detuning between the resonance and the light frequency, and ω_0 is the resonance frequency.

	$J' = J-1$	$J' = J$	$J' = J+1$
α_0	$\frac{(2J-1)}{3(2J+1)} \simeq 0.29$	$\frac{1}{3}$	$\frac{(2J+3)}{3(2J+1)} \simeq 0.37$
α_1	$-\frac{(2J-1)}{(2J+1)} \simeq -0.88$	$-\frac{1}{(J+1)} \simeq -0.11$	$\frac{J(2J+3)}{(J+1)(2J+1)} \simeq 0.99$
α_2	$-\frac{2J-1}{3(2J+1)} \simeq -0.29$	$\frac{(2J-1)}{3(J+1)} \simeq 0.56$	$-\frac{J(2J-1)}{3(J+1)(2J+1)} \simeq -0.26$

Figure 1.6: $\alpha_0, \alpha_1, \alpha_2$ coefficients. We encircle in orange the column corresponding to the 626 nm transition, that is the transition we use to engineer spin-dependent light shifts in this thesis.

[1] defined in Eq. (1.16)

Most of the results of this thesis were obtained in this regime, by working in the vicinity of the 626 nm transition. In the following, we present two examples of spin-dependent light shifts that will be encoutered during this manuscript, obtained by working in the vicinity of a narrow and well-isolated transition.

Example : linear polarisation

We assume that the quantisation axis is the z axis. We assume that the light is propagating along the y axis and that its polarisation is perfectly linear, making an angle θ with the quantisation axis. The polarisation vector can thus be written $\boldsymbol{\epsilon} = \begin{bmatrix} \sin(\theta) \\ 0 \\ \cos(\theta) \end{bmatrix}$. Let's compute the three different components of the light shift operator.

Scalar light shift

The contribution of the scalar light shift is straighforward since it is polarisation-independent. We have :

$$V_{\text{scalar}} = U \frac{2J+3}{3(2J+1)} \mathbb{1} \tag{1.20}$$

The scalar contribution is negative (resp. positive) for red (resp. blue) detuned light, leading to a spin-independent attracting (resp. repulsive) term.

Vectorial light shift

For a purely linear polarisation, we have $\boldsymbol{\epsilon}^* = \boldsymbol{\epsilon}$, the cross product involved in the vectorial term thus cancels out. We have :

$$V_{\text{vectorial}} = 0 \tag{1.21}$$

To emulate first-order spin operator with light, the polarisation needs to have some ellipticity.

Tensorial light shift

This term will be the most interesting one, since it is spin-dependent. To compute it, one can use the fact that $\boldsymbol{J}^2 = J(J+1)\mathbb{1}$ (since the light is detuned, the excited state is barely populated, leading to the conservation of the spin J).

$$V_{\text{tensorial}} = -U \frac{(\sin(\theta)J_x + \cos(\theta)J_z)^2}{(J+1)(2J+1)} + U \frac{J}{3(J+1)} \mathbb{1} \tag{1.22}$$

This expression contains two term, the first one being spin-dependent and the second one being spin-independent. By choosing $\theta = \pi/2$ and dropping the term proportional to identity that doesn't play any role on the spin degree of freedom, we recover the famous one-axis twisting Hamiltonian $H \simeq J_x^2$.

As a sidenote, we emphasise that this expression can be simplified to a much easier form, in a regime where the Larmor frequency ω_z is comparable or bigger than U. Indeed, after the gauge transformation $U = \mathrm{e}^{i\omega_z t J_z}$, the operators J_x^2 and $\{J_x, J_z\}$ can be rewritten as :

$$\begin{aligned} J_x^2 &\to \frac{1}{4}\left[\{J_+, J_-\} + \mathrm{e}^{2i\omega_z t} J_+^2 + \mathrm{e}^{-2i\omega_z t} J_-^2\right] \\ \{J_x, J_z\} &\to \frac{1}{2}\left[\mathrm{e}^{i\omega_z t}\{J_+, J_z\} + \mathrm{e}^{-i\omega_z t}\{J_-, J_z\}\right] \end{aligned} \tag{1.23}$$

Within RWA, keeping only the diagonal terms (that don't oscillate), we have :

$$\begin{aligned} J_x^2 &\to \frac{1}{4}\{J_+, J_-\} \\ \{J_x, J_z\} &\to 0 \end{aligned} \tag{1.24}$$

Hence, in this regime, the tensorial contribution can be well approximated by :

$$V_{\text{tensorial}} = \frac{U}{2(J+1)(2J+1)}\left[1 - 3\cos^2(\theta)\right] J_z^2 + U\frac{J}{6(2J+1)}\left[3\sin^2(\theta) - 1\right]\mathbb{1}, \tag{1.25}$$

where we have used the conservation of $\boldsymbol{J}$ to rewrite $\{J_+, J_-\}$ as a linear combination of J_z^2 and $\mathbb{1}$:

$$\begin{aligned} \{J_+, J_-\} &= 2J_x^2 + 2J_y^2 \\ &= 2(\boldsymbol{J}^2 - J_z^2) \\ &= 2\left(J(J+1)\mathbb{1} - J_z^2\right) \end{aligned} \tag{1.26}$$

Example : circular polarisation

We still assume that the quantisation axis is the z axis. We now suppose that the light is propagating along the z axis and that its polarisation is circular : $\boldsymbol{\epsilon} = \frac{1}{\sqrt{2}}\begin{bmatrix} 1 \\ i \\ 0 \end{bmatrix}$

Scalar light shift

The contribution of the scalar light shift is the same as the previous case :

$$V_{\text{scalar}} = U\frac{2J+3}{3(2J+1)}\mathbb{1} \tag{1.27}$$

Vectorial light shift

This time, the vectorial light shift is non-vanishing since the beam polarisation has some ellipticity. The effect of such vectorial term in this configuration is similar to a Zeeman field :

$$V_{\text{vectorial}} = U\frac{2J+3}{2(J+1)(2J+1)}J_z \tag{1.28}$$

Tensorial light shift

Using the conservation of the spin, we have :

$$V_{\text{tensorial}} = \frac{U}{6(J+1)(2J+1)}J_z^2 - U\frac{J}{3(2J+1)}\mathbb{1} \tag{1.29}$$

Again, we were able to implement a second-order spin operator with this polarisation. The key point to note with the circular polarisation is that we can't have a vectorial light shift without having a tensorial light shift. Hence, we can't apply *only* a light Zeeman field without having higher-order spin operators with a single beam.

1.2.3 Advantage over alkali atoms

Light-matter interaction with dysprosium (and more generally, lanthanides) present some advantages compared to the interaction between light and alkali atoms. First, for atoms with $F = 1/2$, the tensorial polarisability is vanishing, implying that spin-dependent light shifts are limited to first-order spin operators. Secondly, the transition landscape of dysprosium is quite favorable. Indeed, it is made of few broad transitions in the near-UV spectrum and of many narrow and well separated transitions in the visible-IR domain. The latter permits to engineer spin-dependent light shifts of order one or two. Moreover, these light shifts don't come together with a strong scattering, thanks to the small linewidth of dysprosium transitions and thanks to the fact that these transitions are far from the broad ones[1].

To summarise, we have seen in this section that the complex electronic structure of dysprosium results in a favorable transition landscape. This transition landscape permits to engineer first and second-order spin-dependent light shift, without suffering too much from scattering. The shape of these light shifts can be tuned with the light polarisation.

1.3 Overview of the experiment

The dysprosium experiment at Collège de France was started in 2013. When I began my thesis, the experiment was already able to produce a cold atomic cloud on the daily basis. We present in this section a quick overview of the experiment, which were already discussed in detailed in thesis [91, 93] and publications [94, 95].

Producing a collimated gaseous dysprosium jet

The experiment starts in an oven heated up to about $10^3\,\mathrm{K}$ and placed in a low-pressure environment ($10^{-8}\,\mathrm{mBar}$). We put in this oven a crucible filled with approximately 15 g of dysprosium cut in small pieces. At such pressure and temperature, dysprosium undergoes a sublimation, and a gaseous jet of dysprosium atoms exits the oven through a small aperture. This atomic jet is diverging, we use a collimator and a transverse cooling apparatus, detailed in [78], to reduce the beam divergence.

Zeeman slower

The atoms in this jet are quite fast, with a typical velocity $v \simeq 500\,\mathrm{m\,s^{-1}}$. In order to trap the atoms in a magneto-optical trap (MOT), we first use a Zeeman slower to reduce their velocity. The Zeeman slower is made with the blue transition of dysprosium at 421 nm. This transition is ideal for the Zeeman slowing because of its large linewidth, that enables to do many absorption/emission cycles in a short amount of time. Our blue laser at 421 nm is locked in frequency on a dysprosium cathode lamp, looking at a Lamb dip signal using modulation transfer spectroscopy.

Magneto-Optical trap

After the Zeeman slower, the atoms are trapped in a magneto-optical trap (MOT) using the red transition at 626 nm of dysprosium. This 626 nm light is obtained by summing two commercial infrared lasers (at 1050 nm and 1550 nm) in a non-linear PPLN crystal. The lock in frequency of this laser is a bit more demanding than the one of the blue laser due to its narrower linewidth $\Gamma \simeq 2\pi \times 135\,\mathrm{kHz}$. It is performed by saturated spectroscopy using fluorescence, on the atomic jet.

[1] Indeed, in the vicinity to a narrow transition, the broad transitions only lead to a small contribution in the imaginary part of the total polarisability

Our narrow-line MOT works in a similar way than other lanthanides MOT, like erbium [96]. In short, the competition between the radiative forces, the magnetic forces (due to a magnetic quadrupole) and the gravity leads to a polarised MOT with $N_{\text{atoms}} \simeq 4\times10^7$ atoms in $|J=8, m=-8\rangle$ at $T \simeq 15\,\mu\text{K}$. Note that the MOT is quite cold thanks to the narrow linewidth of dysprosium's 626 nm transition, but we don't reach the Doppler temperature at this wavelength $T_D \simeq 3\,\mu\text{K}$.

Transport to the science cell

We then transport the atoms in a glass cell, that we call the science cell, to perform evaporative cooling. The purpose of this step is to gain new optical accesses. As we will see later in the thesis, the physics that we probe mainly relies on Raman processes, involving several pairs of counterpropagating beams, but the optics surrounding the MOT chamber are already quite numerous.

The transport stage relies on laser trapping in an optical dipole trap, using a far-detuned infra-red beam at 1070 nm of power $P \simeq 40\,\text{W}$. The beam is initially focused at the MOT position, and the atoms are transferred from the MOT to the dipole trap. We then move the beam focus by changing the length of the optical path after the focusing lens. The duration of the transport is about 1 s. After this stage, we are left with $N_{\text{atoms}} \simeq 3\times10^6$ atoms at a temperature of typically 100 µK.

Loading in the dipole traps

Once transported to the science cell, the atoms are cooled down to increase the collisional rate, which will favor both the loading into the crossed dipole trap and the further evaporative cooling. A single laser beam with circular polarisation performs Doppler cooling, on the 626 nm transition, while the atoms are trapped in the optical dipole trap. This stage is studied in detail in [95].

Two 1064 nm laser beams at respectively 20 W and 3.2 W of waist $w_0 \simeq 25\,\mu\text{m}$ are then shined on the atomic cloud. The horizontal position of the first one is modulated, using an acousto optic modulator (AOM), at $f \simeq 50\,\text{kHz}$ to increase the trapping volume [92]. We typically load $N_{\text{atoms}} \simeq 3\times10^5$ atoms in the crossed dipole trap.

Evaporative cooling

Finally, evaporative cooling is performed by ramping down the optical dipole trap intensities. Bose-Einstein condensates were obtained in our group back in 2018. However, all the works presented in this thesis were performed at a relatively high magnetic fields $|\boldsymbol{B}| > 220\,\text{mG}$ and imply all the Zeeman sublevels. The lifetime of the condensate[1] in these conditions would be small, owing to the dipolar relaxation. As a consequence, we prefer to use a cold thermal cloud of dysprosium, with typically 3×10^4 atoms at $0.1\,\mu\text{K} < T < 0.5\,\mu\text{K}$.

At this stage, the 'preparation' sequence is done. We then apply spin-dependent light shifts and eventual spin rotations to probe different types of physics. Once the experiments have been performed, we need to measure different observables, in particular the magnetisation, that we access by measuring the spin projections in the Dicke basis. This is done using a Stern-Gerlach procedure and absorption imaging.

Stern-Gerlach procedure

A Stern-Gerlach experiment can be performed along the vertical axis. For this, we send a high and short in time (in the ms timescale) current, up to 500 A, in a coil oriented along

[1] in any other state than $|m=-8\rangle$

the gravity direction. To generate such a current pulse, we charge two large capacitors (of capacitance $C \simeq 2.2\,\mathrm{mF}$) during the previous stages. The capacitors are then suddenly discharged in the coil by opening an insulated-gate bipolar transistor (IGBT). The geometry of the coil permits to create a magnetic field gradient of typically $\partial_z B \simeq 50\,\mathrm{G\,cm^{-1}}$ on the cloud position. This procedure permits us to spatially separate the different m sublevels. The magnetic field gradient is applied during a time-of-flight (TOF) expansion of 2.4 ms.

Absorption imaging

We finally use an absorption imaging protocol. The imaging protocol is made of two steps. In the first one, we shine resonant light at 421 nm during about 40 µs. Atoms undergo several cycles of absorption/spontaneous emission during this imaging pulse, the cloud is thus heated up a lot. This is followed by a waiting time of 100 ms so that atoms leave the imaging region. In the second step, we shine a second light pulse, when normally all the atoms have left.

The two light pulses are recorded on a camera. By calculating the optical density (OD) between the first pulse and the second pulse, we can detect the atomic cloud. This imaging process can be performed immediately after our experiments if we want to measure the position of the atoms, or after a TOF if we want to access the atoms velocity.

By combining the Stern-Gerlach procedure and the absorption imaging, we can measure the projection probability in each m state. Suppose we prepare a state $|\psi\rangle$ after the light shifts sequence. This state can be expanded on the Dicke basis $|\Psi\rangle = \sum_m \langle m|\Psi\rangle\,|m\rangle$, the population in each m state being given by $\Pi_m = |\langle\Psi|m\rangle|^2$. From the probability distribution Π_m, we can access different observables such as the magnetisation along z or the variance along z via :

$$\langle J_z\rangle = \sum_m m\Pi_m \;;\; \langle J_z^2\rangle = \sum_m m^2\Pi_m \tag{1.30}$$

By performing spin rotations before the Stern-Gerlach experiment, we can measure the first and second spin moments in any direction (θ, ϕ) of the generalised Bloch sphere [97].

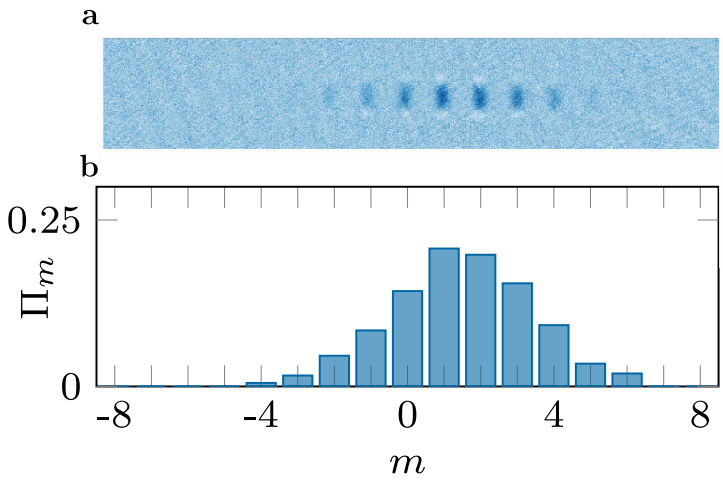

Figure 1.7: Experimental OD. **a** : Example of an OD obtained after Stern-Gerlach and absorption imaging. The state corresponds to a coherent state of average magnetisation $\langle J_z\rangle \simeq 1.45$, experimentally realised by a Rabi oscillation. **b** : Populations in the different m states corresponding to **a**.

As a sidenote, we emphasise that this measurement is performed on a thermal cloud in our system. The fact that we have $N \simeq 3\times10^4$ atoms only acts as an averaged mechanism, that

permits us to access the full probability distribution of the prepared state $|\Psi\rangle$ in a single shot.

We have detailed in this section the preparation and the detection of a cloud of dysprosium atoms. These steps are separated by a timestep where we shine lasers on the atoms, to implement spin-dependent light shifts.

1.4 Laser beam preparation

All the results presented in this thesis rely on the spin-dependent light shifts introduced above. We detail in this section how the different laser beams are prepared and calibrated. As seen earlier, dysprosium presents several transitions to different excited states : $J' = J-1$, $J' = J$, $J' = J+1$. We will only consider here light close to the 626 nm transition that is used throughout the thesis. The preparation of laser beams at other wavelengths would rely on similar techniques.

1.4.1 Optical paths

We currently have four beams at 626 nm focused on the atoms that we use after evaporative cooling. These lasers are fibered to improve the long term stability of the experiment.

The 626 nm light of these four beams is independent from the one used in the MOT and in the Doppler cooling stage. It is also obtained by summing two infrared lasers, at respectively 1050 nm and 1550 nm, in a non-linear PPLN crystal. A wavemeter (precise to 100 MHz) permits to measure the wavelength. By tuning the temperature of one of the IR diodes, we can tune the frequency of the red light, to be either blue or red-detuned, depending on the application. We usually work in the vicinity of the 626 nm transition, being typically red-detuned by $\Delta \simeq -2\pi \times 10\,\mathrm{GHz}$ from the resonance.

The light is then divided into five paths. One is used to monitor the wavelength with the wavelength meter. The four other paths consist in an acousto-optic modulator and a fiber. These AOMs are used to control the beam powers and their frequencies.

After the fiber, we first 'clean' the polarisation with a polarising beamsplitter working in transmission. Then, a tiny fraction of the light is picked-up, using either the transmission through a polished mirror or a beam sampler, and sent to a photodiode. This photodiode permits to monitor the light power going to the atoms, and to calibrate the implemented trap depth. After this cleaning step, the beam is magnified with a telescope and then focused with a lens of long focal length, such that we typically reach a waist of tyically 40 µm on the atoms.

The polarisation of each beam is set with a quarter waveplate and a half waveplate. As demonstrated earlier in this chapter, in the vicinity of a transition, the polarisation of the beam is a critical parameter in the spin-dependent part of the light-matter interaction. In order to improve the control we have on the polarisations of the different laser beams, we install these half and quarter waveplates on motorised mounts that we can tune remotely. Finally, the last mirror before the science cell is usually mounted on a motorised mount, such that we can finely adjust the laser's position, in a reproducible manner.

Once the optical set-up is built, the beams are aligned on the atoms using a protocol that we will explain below. The final steps in the beam preparation consists in setting the polarisation of the laser beams and calibrating their power, using the atoms as a probe.

1.4.2 Alignment on the atoms

Aligning the beam on the atoms is not a straightforward task because the atomic cloud size is small, typically a few micrometers. The way we align the laser beams depend on the sign of the detuning. We present in this paragraph our protocol to align a red-detuned beam.

A red-detuned beam, propagating along y, creates an attractive potential in the xz plane. When the light is shined, if the atoms are not exactly in the propagation axis of the beam, they will undergo oscillations (of both position and velocity) in this attractive potential. This allows to tune the in-plane alignment, because of the the large difference of trapping frequency for the radial and axial directions. Our protocol consists in flashing the beam for various durations, and to measure the in-situ position of the atomic cloud right after. We illustrate this protocol in Fig. 1.8. In the bottom panel, we show an example of oscillations measured for a misaligned beam in the radial direction. We then adjust the laser position in the xz plane with the motorised mount on which is mounted a mirror, such that the amplitudes of the oscillations are minimised. This way, we can align the beam in the radial direction. The alignement in the axial direction is made by measuring the radial trapping frequency.

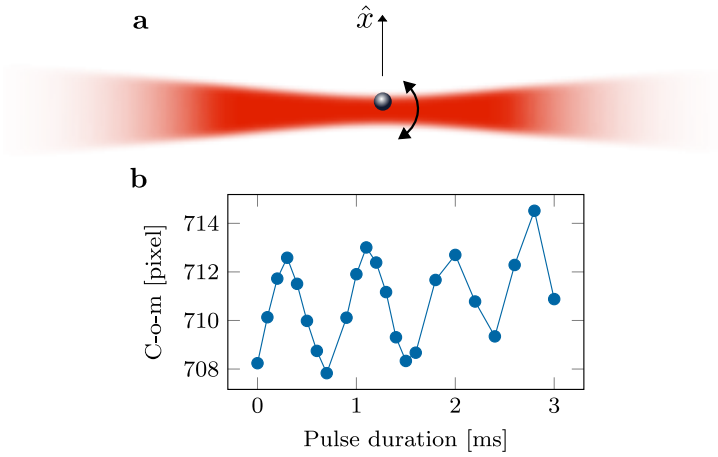

Figure 1.8: Radial alignement of a red-detuned beam. **a** : Experimental scheme. A red-detuned beam misaligned along $\hat{x}$ triggers center-of-mass (c-o-m) and velocity oscillations along $\hat{x}$. **b** : Oscillations of the x-position obtained with a misaligned beam. The alignement is achieved by minimising the amplitude of the oscillations.

1.4.3 Setting the laser polarisation

As stated earlier, the polarisation of our laser beams is a critical parameter. In the results that we will present in the last chapter of the thesis, the requirement on the polarisation precision was below 0.1°. We therefore try to measure the polarisation of the laser beams by different concordant experiments.

An additional constraint is that the polarisation of the beams is dependent on the quantisation axis direction, thus on the exact direction of the magnetic field. In case we need to be extremely precise on the polarisation, we need to calibrate it with the same magnetic field that will be used to perform the experiments. As we will see, it will be a constraint on the type of experiment we can perform to set the beams polarisation. We present here three experiments that were used to set the beams polarisation during this thesis.

Spin dynamics at relatively low magnetic field

Lets assume we want to measure the beam polarisation, for a beam propagating along y, parametrised as $\hat{\boldsymbol{\epsilon}} = \sin(\theta)\hat{\boldsymbol{x}} + \cos(\theta)e^{i\varphi}\hat{\boldsymbol{z}}$, with φ the dephasing between the two components of the polarisation and θ the angle made by the polarisation vector and the z axis. We assume that the magnetic field strength is relatively low : $|\boldsymbol{B}| \leq 80\,\text{mG}$, and that it is oriented along the z axis.[1] The Hamiltonian of a dysprosium atom, considering only the spin degree of freedom, is the following :

$$H = H_{\text{LS}}(\theta, \phi) + \hbar\omega_z J_z, \tag{1.31}$$

where $H_{\text{LS}}(\theta, \phi)$ is the polarisation-dependent light shift Hamiltonian induced by the beam, and ω_z the Larmor frequency.

The atoms are initially at rest in the ground state $|J = 8, m = -8\rangle$. A priori, the Hamiltonian created by this beam on the atoms depends on the polarisation (θ, ϕ). Provided that $|J = 8, m = -8\rangle$ is not an eigen state of this Hamiltonian (this would occur for some particular choices of polarisation), the spin state will evolve under the action of Eq. (1.31). The resulting time evolution of the spin distribution gives access to the polarisation of the beam, via a fit of the spin populations evolution, see Fig. 1.9.

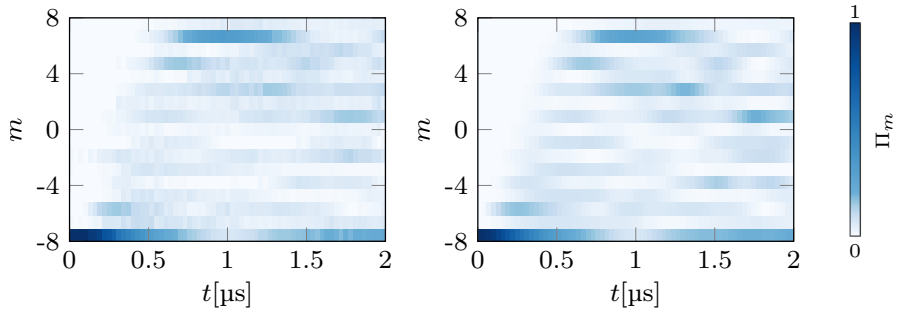

Figure 1.9: Spin dynamics at low magnetic field ($|\boldsymbol{B}| \simeq 50\,\text{mG}$). Left : Time evolution of the populations upon the action of a beam with an unknown polarisation. Right : Fit. Free parameters are the beam polarisation (angle and phase) θ, φ and the trap depth U. The fit permits us to measure any complicated polarisation.

Note that this protocol works only in the regime $\hbar\omega_z < \langle H_{\text{LS}} \rangle$. Indeed, as the magnetic field increases, the rotating wave approximation presented in Section 1.2.2 becomes more and more valid, and the light shift can be more and more approximated by a combination of J_z and J_z^2 operators, that doesn't trigger any evolution of the spin populations since the $|m\rangle$ states are eigenstates of these operators.

Spin dynamics at relatively high magnetic field

As the magnetic field is getting higher, the spin dynamics is suppressed[2] and the above protocol can't be used to calibrate the light polarisation. Some experiments presented in this thesis were performed with a magnetic field of $|\boldsymbol{B}| = 1\,\text{G}$, we thus need to find another protocol to calibrate the polarisation in such a configuration.

[1] This criteria of 'low' magnetic field is a bit arbitrary. What matters here is that the light shift should not be dominated by the Zeeman energy. $|\boldsymbol{B}| \leq 80\,\text{mG}$ roughly corresponds to a good regime, where the spin dynamics doesn't occur on a too short timescale and where we are not limited by the light power.

[2] for reasonable light powers

One option to enhance the spin dynamics is to use amplitude modulation. The light power is modulated in amplitude, via an AOM, at a frequency ω close to the Larmor frequency ω_z. Assuming that the beam is linearly polarised and that its polarisation is making an angle θ with the quantisation axis, the Hamiltonian[1] of a dysprosium atom becomes time-dependent :

$$H(t) = U_0 \frac{1 + R\cos(\omega t)}{2} \left[\cos^2(\theta) J_z^2 + \sin^2(\theta) J_x^2 + \cos(\theta)\sin(\theta)\{J_x, J_z\}\right] + \hbar\omega_z J_z, \quad (1.32)$$

where R is the modulation constrast and U_0 a prefactor containing the light shift for Clebsch Gordan coefficient equal to unity and a scaling factor coming from the tensorial polarisability. Within RWA at ω_z, Eq. (1.32) becomes :

$$H = \frac{U_0 R \sin(2\theta)}{8}\{J_x, J_z\} + U_0 \frac{3\cos^2\theta - 1}{4} J_z^2 - \hbar\delta J_z, \quad (1.33)$$

where we introduced the detuning $\delta = \omega - \omega_z$. Provided that this detuning is small enough, this Hamiltonian permits to trigger spin dynamics, hence to get information on the laser polarisation, even at relatively large magnetic fields.

We show Fig. 1.10 an example on linear polarisation calibration relying on this protocol. On the left pannel, we display theoretical magnetisation evolutions under Eq. (1.33) for various linear polarisations. We reach a maximum in magnetisation for a polarisation $\theta_0 \equiv \arccos\left(1/\sqrt{3}\right)$. On the right panel, we display (dots) the measured maximum magnetisation achieved during the application time of the beam, for various positions of a half waveplate (HWP) disposed on the beam path. The solid line is a fit. From this figure, we can deduce the HWP angle to prepare arbitrary linear polarisation. In particular, the maximum of magnetisation corresponds to an HWP angle leading to $\theta = \arccos\left(1/\sqrt{3}\right)$.

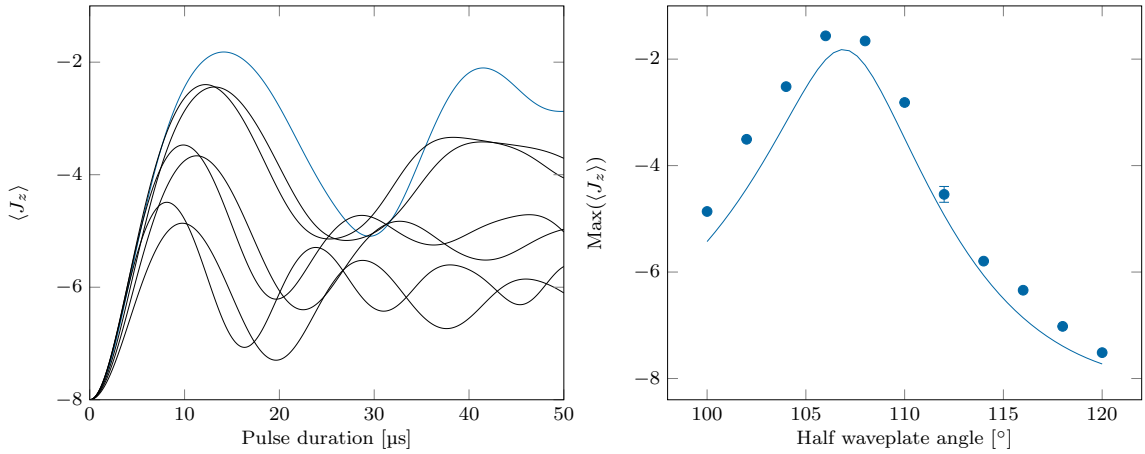

Figure 1.10: Spin dynamics with amplitude modulation. Left : Theoretical evolution for different linear polarisations. Blue curve : polarisation $\theta = \theta_0 = \arccos\left(1/\sqrt{3}\right)$. Black curves : different polarisation angles between $\theta_0 - 10°$ and $\theta_0 + 10°$. Maximal magnetisation is achieved for $\theta = \theta_0$. Right : Experimental measurements. For each half waveplate angle, we display the maximal magnetisation measured during the time evolution. Straight line is a fit, free parameters are polarisation, trap depth, contrast of modulation and detuning.

[1]We drop all the terms proportional to identity because they don't affect the spin degree of freedom.

This experiment could also be used to calibrate an elliptical beam, the relative phase between the components of the polarisation being involved in the spin dynamics.

Spin-dependent light shift measurement

Finally, we present a third experiment to measure the light polarisation, relying on the measurement of the 17 eigenvalues of the light shift operator in the Dicke basis. The method consists in off-centering the understudy laser beam by a quantity $w_0/2$ in one direction[1], w_0 being the waist of the beam. We show a scheme in Fig. 1.11. An atom in the Dicke state $|m\rangle$ will feel a force due to the spatial variation of the light potential :

$$F_m = -\frac{\langle m|\, H_{\mathrm{LS}}(\theta,\phi)\, |m\rangle}{w_0} \exp\left(-1/2\right) \tag{1.34}$$

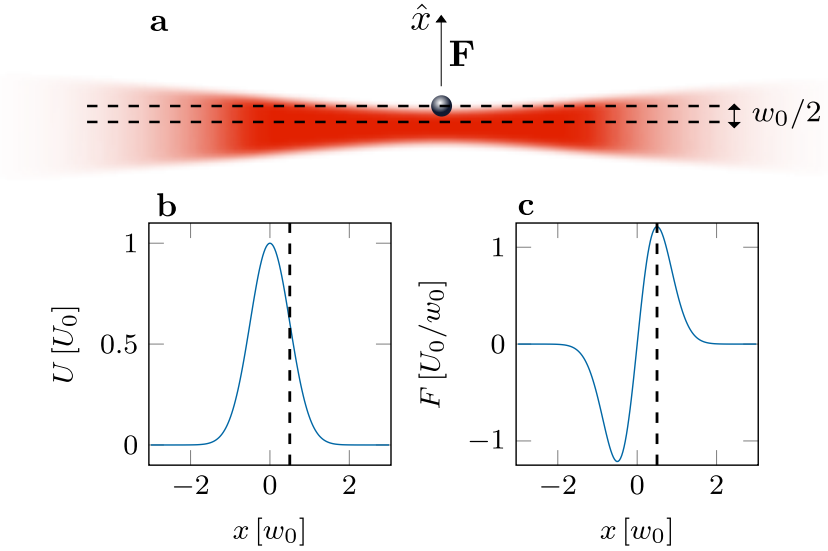

Figure 1.11: Light shift measurement experiment. Assuming a blue-detuned beam leads to a repulsive force. **a** : Experimental scheme. **b** : Potential induced by the laser beam along the radial direction x on a given m state. Dashed line indicates $x = w_0/2$. U_0 is the potential at the waist position. **c** : Force induced by the laser beam along x on a given m state.

Provided the light pulse is applied during a short enough[2] time T_{pulse}, the velocity of each m state after the pulse application is :

$$v_m(T_{\mathrm{pulse}}) = a_0 T_{\mathrm{pulse}} + F_m T_{\mathrm{pulse}}/M, \tag{1.35}$$

where a_0 is a spin-independent acceleration, due to gravity and the spin-independent component of the light shift. Performing a Stern-Gerlach experiment after the light pulse, we can measure the velocity of each spin component, thus accessing F_m.

The experimental sequence is the following. We first prepare a coherent state, using a radio-frequency pulse (see next section), to populate several m states. We then flash the off-centered light beam for a short amount of time. We finally measure the induced velocity for each populated m state via a Stern-Gerlach experiment. We reproduce the experiment

[1]This protocol would work for any beam misalignement, but the maximum force is induced for a misalignement of $w_0/2$ as shown Fig. 1.11

[2]if T_{pulse} is short enough, we can neglect the displacement of the cloud induced by the beam while the light is shined. The atoms thus feel a constant force during the full pulse duration.

for various initial coherent states, in order to measure the induced force on the 17 Zeeman sublevels.

We use this protocol in Fig. 1.12 where we calibrate a linearly polarised beam at a high magnetic field. We recall that, in such a configuration, the average light shift produced by the beam reads[1], within RWA, for a Dicke state $|m\rangle$:

$$\langle m| H_{\mathrm{LS}}(\theta) |m\rangle = \frac{U}{2(J+1)(2J+1)} \left[1 - 3\cos^2(\theta)\right] m^2, \tag{1.36}$$

where U is the value of the light shift for Clebsch-Gordan coefficient equal to unity. We thus expect a parabolic evolution of the force with the magnetic projection m by combining Eq. (1.34) and Eq. (1.36) : $F_m \propto \left[1 - 3\cos^2(\theta)\right] m^2$. This is verified on the left panel of Fig. 1.12, where the 17 forces F_m are measured for a given linear polarisation. The curvature of $F_m = f(m)$ provides a measurement of $\left[1 - 3\cos^2(\theta)\right]$, hence of the polarisation angle θ. We can vary the polarisation with a half waveplate (HWP). We repeat this curvature measurement for various HWP angles, leading to the right panel of Fig. 1.12.

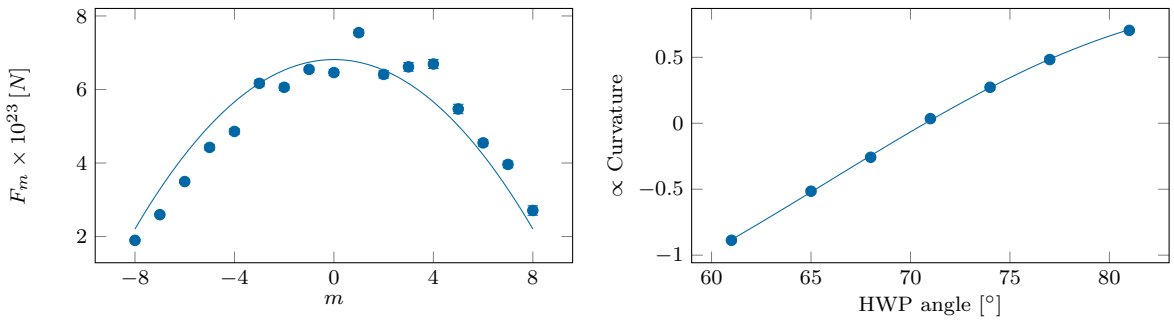

Figure 1.12: Linear polarisation calibration. Left : F_m for a given HWP angle. Solid line is a fit to infer the curvature of $F_m = f(m)$. Right : Measured curvature for various HWP angles. Solid line is a fit with two free parameters : a proportional factor and the offset angle of the HWP.

During this thesis, we often use a linear polarisation making an angle $\theta = \arccos\left(1/\sqrt{3}\right)$ with the quantisation axis. This corresponds to a vanishing curvature, see Eq. (1.36), that can be obtained using the measurements displayed in the right panel of Fig. 1.12.

We have studied in this section different way to precisely set a beam polarisation. In the next section, we focus on the control of the magnetic field, which is also a crucial element in our experiment.

1.5 Magnetic field control

During the experimental sequence, the magnetic field norm and direction are controlled using sets of coils surrounding the experiment. We use mainly two sets of coils on the three axis x, y, z, each of them being made of pairs of coils in Helmholtz configuration. The first set of coils surrounds the whole optical table and create rather small but homogenous magnetic fields. They are, for instance, useful to produce homogenous fields during the transport

[1] We didn't consider here the component of the light shift proportional to identity, which doesn't contribute to F_m (being spin-independent).

stage. However, they don't permit to produce strong magnetic fields, and their response time is slow. We thus have another set of coils surrounding the science cell, allowing to adjust carefully and (relatively) rapidly the magnetic field before shining the laser beams on the atoms.

1.5.1 Magnetic field rotations

As we detailed above, the polarisations of the lasers are quite critical in our experiment. We have four beams aligned on the atomic cloud to perform spin-dependent light shifts, but some of them have better control than other. For example, in the horizontal plane, two beams pass through a dichroic mirror before heading towards the atoms. This optical element affects the polarisation in a non-trivial way. Even if we can compensate for this effect using half and quarter waveplates, we don't reach such a good control than with the top beam, where there is no such optical element just before the glass cell. As a consequence, for experiments that require a fine tuning on the polarisation, we prefere to use the vertical beams. This choice fixes a constraint on the initial magnetic field direction. For instance, if we want to use a π-polarised light with the vertical beams, the magnetic field needs to be in the horizontal plane.

The Stern-Gerlach direction constitutes another constraint. The only coils whose geometry allows a sufficiently strong magnetic field gradient are in the direction of gravity. This means that the magnetic field direction must be vertical before the Stern Gerlach experiment is performed. These two constraints lead to two different experimental sequences, depending on the direction of the quantisation axis we want while shining the beams.

Using a vertical quantisation axis

This is the simplest case. The magnetic field being initially (during the evaporation stage) vertical, we just need to ramp the norm of this field to the desired value (typical value is $|\boldsymbol{B}| \simeq 220\,\mathrm{mG}$). The only thing we need to be careful is to not change the magnetic field sign (avoiding the 0-crossing point). After this ramp down, the lasers can be shined on the atoms to realise the desired Hamiltonian. Then, the Stern Gerlach experiment and the imaging can be performed. We illustrate in Fig. 1.15 the typical experimental timeline for the case of a vertical magnetic field.

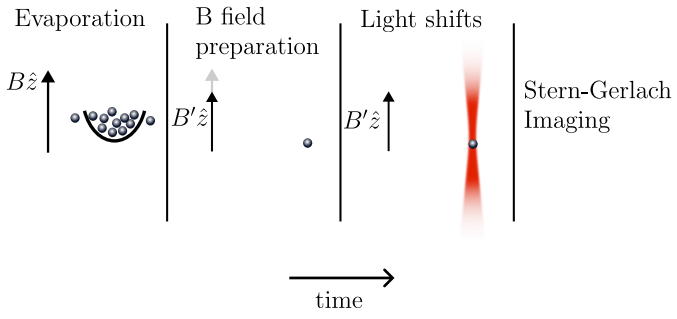

Figure 1.13: Scheme of the experimental sequence, using a vertical magnetic field.

Using an horizontal quantisation axis

This case is more difficult. Indeed, the 'initial' magnetic field is still vertical (during evaporation), so a spin rotation must be performed. After this spin rotation, we can shine the laser beams on the atomic cloud. Before performing the Stern-Gerlach experiment, we need to rotate back the magnetic field towards the vertical axis to measure the state

populations in the good basis. We illustrate in Fig. 1.14 the typical experimental timeline for the case of a vertical magnetic field.

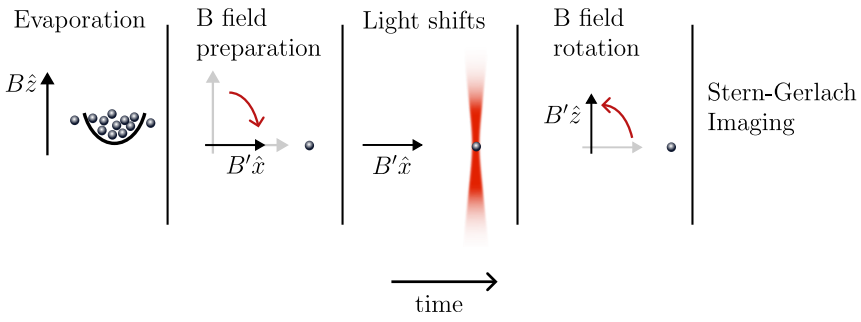

Figure 1.14: Scheme of the experimental sequence, using an horizontal magnetic field.

This rotation must be realised as fast as possible, to avoid any losses (due to dipolar relaxation for example), but the rotation time can't be too small either, to ensure adiabaticity and conserve the spin populations. Typically, the minimum rotation time is given by the inverse of the Larmor frequency. Hence, the minimal time to remain adiabatic at a field of $|\boldsymbol{B}| \simeq 1\,\mathrm{G}$ is roughly $50\,\mu\mathrm{s}$. Experimentally, we perform the rotation in $100\,\mu\mathrm{s}$. We see in Fig. 1.15 the effect of varying the time of the second rotation (from x axis to z axis). For too short rotation times (below $50\,\mu\mathrm{s}$), the magnetisation is not conserved due to non-adiabatic effects.

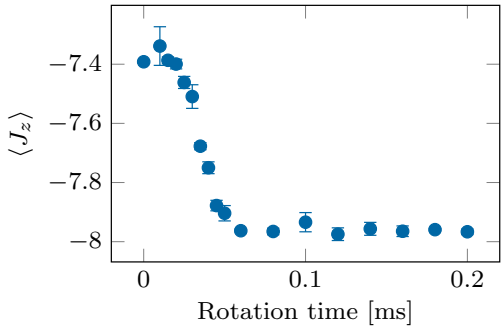

Figure 1.15: Adiabaticity of magnetic field rotations. Initial state is $|-8\rangle_x$ with a magnetic field pointing in the x axis. The magnetic field is then rotated towards the z axis in various durations. Finally, the average magnetisation is measured after a Stern Gerlach experiment.

For an infinitely fast rotation, we would expect to obtain a 0-magnetisation after the Stern-Gerlach. This is not what we measured, because the Stern-Gerlach is performed using only one coil : the gradient of magnetic field comes together with a strong bias along z, which somehow participates to a rotation of the field towards the z axis.

1.5.2 Measuring the magnetic field

We must know precisely the norm of the magnetic field in our experiment. For example, to emulate the quantum Hall systems we will present chapters II to VI, the lasers must be detuned by the Larmor frequency. A magnetic probe measuring magnetic field between $\pm 1\,\mathrm{G}$ on the three axis, with a precision of $1\,\mathrm{mG}$, is installed close to the science cell. However, the field created by the inner coils is not homogeneous on the size of the cell, and differ between the cloud position and the probe. We thus need to use the atoms as a probe to measure the

actual magnetic field.

To measure relatively low magnetic field, ie $|\boldsymbol{B}| \leq 100\,\mathrm{mG}$, a 'DC'-Ramsey-like sequence was previously implemented on the experiment [98]. The idea of this sequence is to rotate the initial state $|m = -8\rangle$ towards the equator of the generalised Bloch sphere, by flashing a magnetic pulse in the x direction. We then wait for various times and apply a second $\pi/2$-rotation around the x axis. After this protocol, the magnetisation of the atoms is measured. The magnetisation undergoes oscillations, whose frequency gives a direct measurement of the Larmor frequency.

However, this protocol doesn't work as well when going to higher fields. Indeed, we are limited by the strength of the magnetic pulses that we can create along the x axis. For high enough bias field along z, the first x-pulse is not strong enough to bring $|-8\rangle$ to the equator of the generalised Bloch sphere. As a result, the amplitude of the Ramsey oscillations is decreased, and the measurement of the frequency is less precise.

To circumvent this difficulty, we installed an antenna nearby the science cell to send radio frequency (RF) signals. This will be used to perform RF-Ramsey sequence. We briefly present here this Ramsey protocol we use to measure precisely relatively high magnetic fields.

The antenna creates an homogeneous time-dependent field $\mathbf{B(t)} = B_0 \cos(\omega t + \phi)\hat{\boldsymbol{x}}$. The following one-particle Hamiltonian is produced on the atoms :

$$H(t) = -\frac{\hbar\Omega}{2}\cos(\omega t + \phi)J_x + \hbar w_z J_z, \tag{1.37}$$

where we introduced the Rabi frequency Ω that describes the strength of the RF-atom coupling. This Hamiltonian is time-dependent. We can make it stationary by doing the gauge transform $U(t) = \mathrm{e}^{i\omega t J_z}$. Within RWA, we are left with a time-independent Hamiltonian, where we introduce $\delta = \omega - \omega_z$, the detuning between the RF-field frequency and the Larmor frequency :

$$H = \frac{\hbar\Omega}{2}\left[\cos(\phi)J_x + \sin(\phi)J_y\right] + \hbar\delta J_z \tag{1.38}$$

We can rewrite this Hamiltonian in a more compact form [99] :

$$\begin{aligned} H &= \frac{\hbar\Omega^{'}}{2}J_{\hat{\boldsymbol{u}}}, \text{ with} \\ \Omega^{'} &= \sqrt{\Omega^2 + \delta^2} \text{ and} \\ \hat{\boldsymbol{u}} &= \frac{\delta\hat{\boldsymbol{z}} + \Omega\cos(\phi)\hat{\boldsymbol{x}} + \Omega\sin(\phi)\hat{\boldsymbol{y}}}{\Omega'} \end{aligned} \tag{1.39}$$

The action of this Hamiltonian is thus a rotation of the spin around the axis $\hat{\boldsymbol{u}}$. There are two regimes depending on the relative strength of the Rabi frequency and the detuning.

If $\delta \geq \Omega^{'}$, $\hat{\boldsymbol{u}}$ points toward an angle located between the equatorial plane and the bottom of the generalised Bloch sphere. Upon application of the RF, the state will undergo a rotation on a small part of the sphere, going between $|-8\rangle$ and $|m\rangle$ where $m \ll 8$ depends on the ratio between the detuning and the Rabi frequency.

On the other hand, if $\delta \ll \Omega^{'}$, $\hat{\boldsymbol{u}} \simeq \cos(\phi)\hat{\boldsymbol{x}} + \sin(\phi)\hat{\boldsymbol{y}}$. The rotation axis lies the equatorial plane : the spin will undergo full rotation around the generalised Bloch sphere, going from $|-8\rangle$ to $|+8\rangle$.

To summarise, by applying the RF pulse, the average magnetisation undergoes oscillations, which amplitude and frequency are given by the detuning δ and the Rabi frequency Ω.

The amplitude of these oscillations are maximised for a $\delta = 0$ detuning. This is the famous Rabi oscillation experiment, see Fig. 1.16.

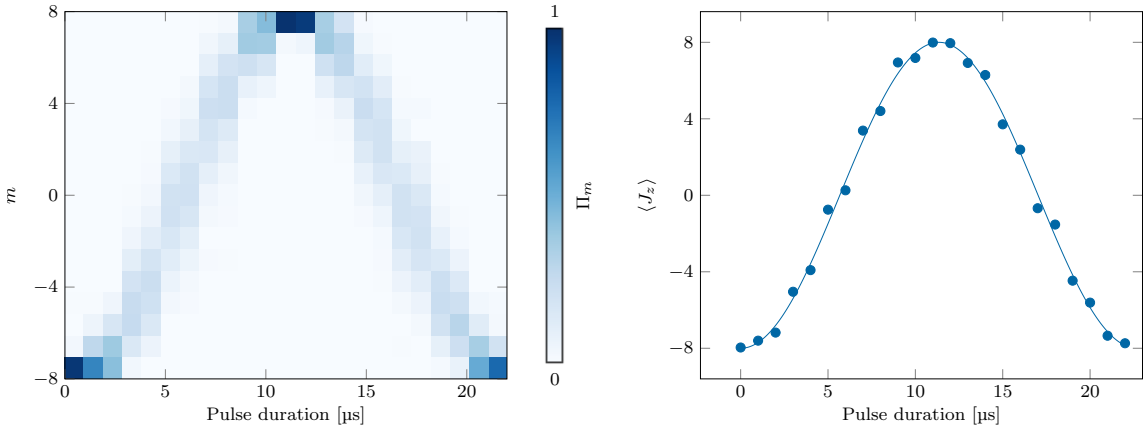

Figure 1.16: Rabi oscillations (experimental) Left : Evolution of the spin populations upon application of a RF pulse. Initial state is $|-8\rangle$. Right : average magnetisation during the Rabi oscillations. Error bars are within the points extent. Fit (in straight line) gives $\Omega = 2\pi \times 14.0(1)\,\mathrm{kHz}$.

For a well chosen interogation time, say $\Omega\tau = \pi$, we can measure the final magnetisation versus the RF detuning. We obtain a Lorentzian peaked on the resonance. The width of this Lorentzian is given by $1/\tau$. This limitation is a pure Fourier transform argument : if the interrogation time lasts for a duration τ, the frequency precision is on the order of $1/\tau$. To get a more precise measurement of the resonance, i.e to reduce the width of the Lorentzian, one strategy is to increase the interrogation time, going to for instance to $\Omega\tau = 10\pi$. However, implementing stable long radio frequency pulses is experimentally challenging.

The famous Ramsey interference protocol is well known to work around this difficulty [100]. The basic idea is to split the π pulse into two $\pi/2$ pulses separated by a waiting time T_{wait}. In this configuration, the width of the Lorentzian scales as $1/T_{\mathrm{wait}}$, again with Fourier transform arguments. We can thus significantly increase the precision on the Larmor frequency measurement just by adding a waiting time between two $\pi/2$ pulses, rather than by implementing long RF pulses.

We show in Fig. 1.17 experimental realisation of a Ramsey interferometry using the RF antenna. We verify that increasing the waiting time between the two $\pi/2$ pulses leads to a sharper Lorentzian, hence a more precise measurement of the Larmor frequency.

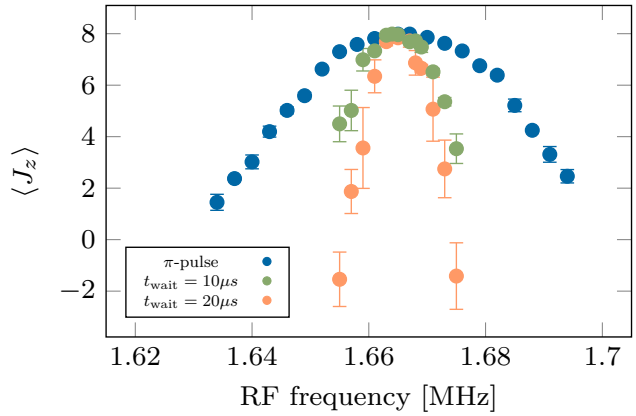

Figure 1.17: Measuring the Larmor frequency. In blue, a π-pulse is applied for various RF frequencies, we measure a broad resonance. In green and orange, Ramsey sequences are performed with (respectively) $t_{\text{wait}} = 10\,\mu\text{s}$ and $t_{\text{wait}} = 20\,\mu\text{s}$. The resonance becomes sharper as the waiting time increases.

1.6 Perspectives and conclusion

All the results that we will present in this manuscript were obtained with a cold thermal gas of dysprosium atoms. Several future projects would require to go to degeneracy to probe more exotic topological phases induced by interactions [78]. However, the dysprosium machine at Collège de France doesn't permit to have a Bose Einstein condensate with a high number of atoms on the daily basis in its current implementation. Hence, the study of interactions is limited.

The main constraints in our experiment to reach quantum degeneracy are the transport from the MOT chamber to the science cell and the loading in the dipole traps, where we typically lose 90% of the atoms. The loading in the dipole traps is poor due to the geometry of our experiment : the transport beam has a very weak confinement in the axial direction ($f \simeq 12\,\text{Hz}$), but a strong confinement in the radial direction ($f \simeq 1.8\,\text{kHz}$). The trap created by the transport beam is thus quite elongated and doesn't fit well with the geometry of the intersection of the dipole traps, which is rather spherical. As a consequence, many atoms are lost in the tails of the transport beam during this stage.

To enhance the axial confinement, one potential avenue is to perform the transport stage using a moving lattice [101], which would lead to a strong axial confinement. Nonetheless, the optical accesses of the current experimental setup complicates the implementation of this proposal. In the following section, we introduce an alternative approach aimed at improving the loading process in the crossed dipole trap. This approach consists in modulating the transport beam to increase its radial size, thereby increasing its overlap with the crossed dipole trap.

1.6.1 Modulating the transport beam

The modulation of dipole traps is a well established technique to increase the trap size. We quickly recall the principle of this modulation. More details can be found in [92]. We denote by x_0 the focus position of the laser in one of the radial direction (for simplicity, we freeze the other direction and assume the modulation is done only along the x axis). The principle

of the modulation is to make this position time-dependent. For instance, for a sinusoidal modulation, the position of the waist is given by $x_0(t) = A\sin(2\pi t/T)$ where T is the period of modulation and A its amplitude. One can show that an arcsinus modulation leads to an averaged trap really close to the usual gaussian trap. On the other hand, a sinus modulation would lead to a double minimum averaged potential, which is not ideal for trapping.

When conducting experiments, it is crucial to ensure that the modulation frequency greatly exceeds the trap's radial frequency f_r. Consequently, the atoms experience an averaged trapping potential, which is shallower but wider than the non-modulated trap. The amplitude of modulation A sets how much the trap is spatially averaged : as A increases, the averaged trap gets broader and broader (see Fig. 1.18). In our experiment, this modulation would be achieved through frequency modulation of the RF going in an AOM. Being diffracted by the AOM, the transport beam position $x(t)$ will follow the RF modulation. The modulation amplitude is limited by both the AOM diffraction range and the optical set-up. Typically, we can go up to $A \simeq 4w_0$, where w_0 is the waist of the beam without modulation.

As seen in Fig. 1.18, an arcsinus modulation leads to an effective gaussian trap, which width is given by the modulation amplitude. From this averaged-trap, one can derive an effective waist and an effective Rayleigh length, describing the potential effectively felt by the atoms. We show Fig. 1.19 these quantities as a function of the modulation amplitude A, as well as the transverse and axial frequencies.

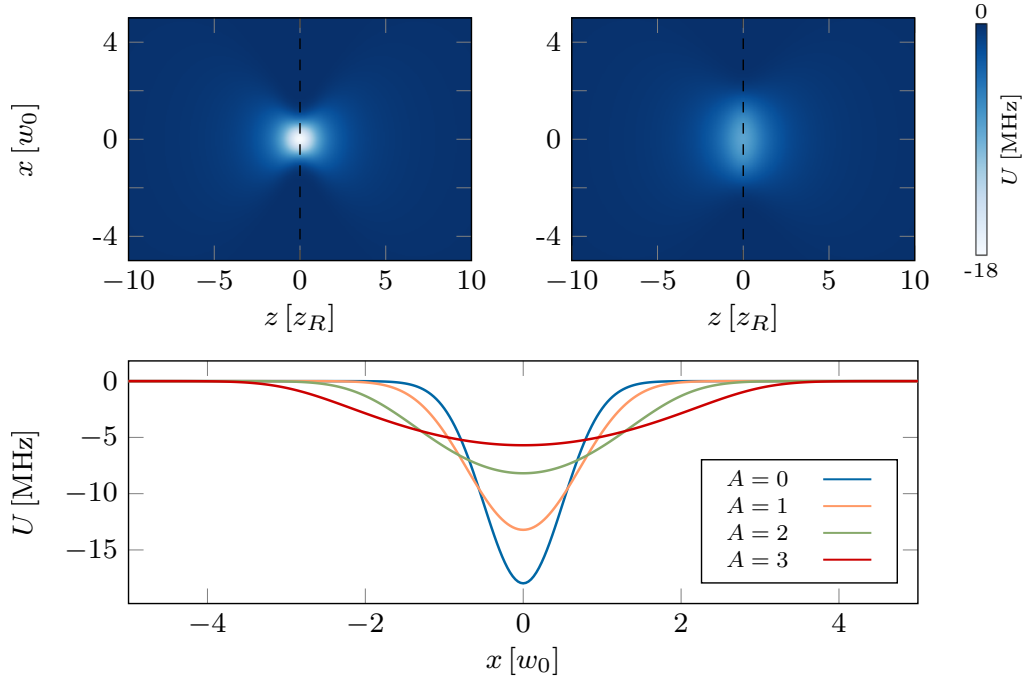

Figure 1.18: Trap depth as a function of the modulation amplitude (arcsinus modulation). Top left: 2D plot of the trap depth when the beam is not modulated. The z axis is the axis of light propagation. The x axis is one of the two radial directions. Top right: 2D plot of the trap depth when the beam is modulated with an amplitude $A = 2w_0$. The dashed lines indicate the 1D cuts at $z = 0$ used for the bottom panel. Bottom: trap depth as a function of the radial position, at $z = 0$, considering four different modulation amplitudes (in unit of w_0).

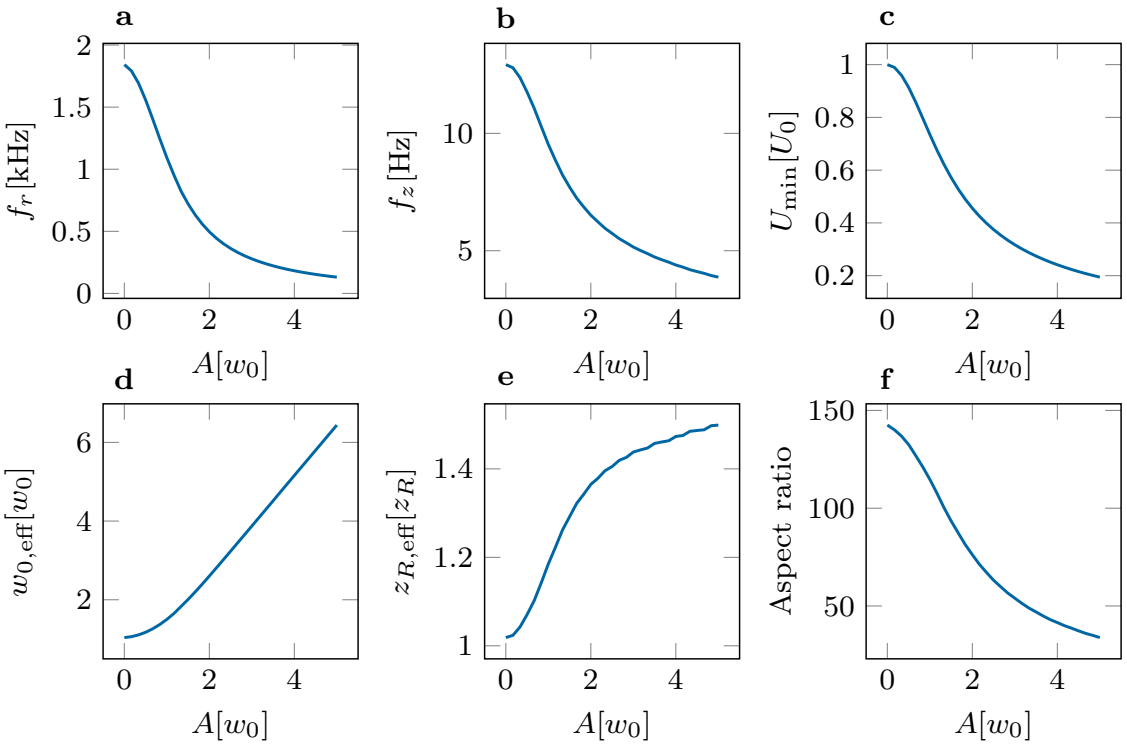

Figure 1.19: Effective trap parameters as a function of the amplitude modulation (arcsinus modulation). **a** : The effective radial frequency decreases with the modulation amplitude. **b** : The effective transverse frequency also decreases with the modulation amplitude. **c**: The effective trap depth $U_{\min}$ at $(x, z) = (0, 0)$ decreases with the modulation amplitude, such that the volume of the trap is constant. **d** : Increase in the effective waist with the modulation amplitude. **e** : Increase in the effective Rayleigh length with the modulation amplitude. **f** : Evolution of the aspect ratio of the trap with the modulation amplitude : the trap is getting more and more spherical as the modulation amplitude increases.

The increase in effective waist with the modulation amplitude corresponds to the desired effect : increasing the overlap between the dipole traps and the transport beam. On the other hand, the increase of the effective Rayleigh length is not intended : the trapping frequency will become even smaller in the transport direction, which means that more atoms will potentially be lost in the tails of the transport beam (at least at the beginning of the evaporation stage, when the cloud is not cooled enough). However, the situation remains favorable as the aspect ratio evolves in the right direction : the trap is getting more and more spherical. To overcome the reduction of the axial frequency, we plan to use a higher power transport beam. We are currently doing some preliminary tests with a 300 W laser at 1070 nm. The strategy is to increase the laser power while the modulation is on, to target a similar axial frequency than the current set-up $f_z \simeq 12\,\text{Hz}$, but with a bigger effective waist. We recall that the axial frequency scales as $f_z \sim \sqrt{P}$ with P the laser power. By imposing the condition that the axial frequency remains unchanged while modulating, this relationship sets an upper threshold on the modulation amplitude that can be used, given the laser power. After the AOM and taking into account losses in the optics and the reflection on the MOT windows, we can typically have 200 W on the atoms. This limits the modulation amplitude to $A \simeq 2.5 w_0$, i.e an effective waist 3 times bigger than the current one, for a similar effective Rayleigh length.

1.6.2 Conclusion

In this chapter, we provided a brief overview of dysprosium's properties. We then delved into the interaction of dysprosium atoms with light, demonstrating how the vectorial and tensorial components of the light shift enable the emulation of a diverse set of Hamiltonians on dysprosium atoms. The pivotal element in this process is the light polarisation.

Afterwards, we presented an overview of the dysprosium machine utilised in our experiments. Following this, we detailed protocols for beam preparation and calibration, emphasising the *precise* control of light polarisation, using the atoms as a probe. We also outline our methodology for controlling the magnetic fields applied to the atomic cloud.

Lastly, we proposed a potential experimental upgrade aimed at increasing the number of atoms captured by the dipole traps, with the ultimate goal of achieving a stable Bose-Einstein condensate with a high number of atoms on a daily basis. This would facilitate the exploration of interacting topological phases.

2 A synthetic quantum Hall ribbon

In this chapter, we briefly recall the particular properties of Hall systems, principally their insulating character in the bulk and the chiral edge modes appearing at their boundaries, insensitive to (small) disorder. We start with the classical Hall effect and move on to the quantum Hall effect afterwards. The quantum Hall effect is illustrated using a toy model made of an array of coupled quantum wires, as proposed by Kane in 2002 [102]. This model is close to the experimental implementation that we will detail later on. Next, we describe the attributes of a quantum Hall system in the context of its topological properties.

In the third section, we look at an experimental realisation of a 2D quantum Hall ribbon using a cold gas of dysprosium atoms. This realisation relies on a *synthetic dimension*, a powerfull tool that we will also introduce in this chapter. Finally, we compare our synthetic quantum Hall system to the quantum wire model.

The experimental findings that we present in this chapter were already obtained in 2020 in our group [103], and are discussed in more details in Thomas Chalopin's thesis [98]. The figures displayed in this chapter are new experimental measurements, realised during my thesis. The motivation for reproducing this system was to consequently create a spatial bipartition of it, with the aim of realising its entanglement Hamiltonian [51]. It will be

addressed in chapter VI. This chapter together with chapter III is also an introduction to the chapters IV and V where we will present the realisation of a synthetic 4D quantum Hall system.

2.1 Introduction to quantum Hall physics

The quantum Hall effect mainly concerns electrons moving in a two-dimensional plane within a perpendicular magnetic field. Despite its apparent simplicity, this system reveals a remarkably rich physics. In this section, we briefly study the classical Hall effect, before focusing on the quantum Hall effect.

The results presented in this section are well established and inspired by [98, 103–105].

2.1.1 Classical Hall effect

We consider an electron moving in a 2D material in the plane xy. A homogeneous magnetic field $\mathbf{B} = B\hat{\boldsymbol{z}}$ is applied orthogonally to this plane. The classical trajectories of the electrons in the bulk of the material are circular and called 'cyclotron orbits'. The frequency of these orbits is the cyclotron frequency, given by $\omega_c = eB/M$, where e is the electronic charge and M the electron mass. If we apply a force along y (for instance, via an electric field), the electrons will start to drift, with a velocity $\boldsymbol{v}_{\text{drift}} = -\boldsymbol{F} \times \boldsymbol{B}/(eB^2)$. This velocity is transverse to the direction of the application of the force. This is the Hall effect. In short, in a magnetic field, the movement of electrons will respond to a force in a direction orthogonal to both the force and the magnetic field. This transverse response can be characterise by the so-called 'Hall mobility' μ, defined by :

$$\mu = \frac{\partial v_x}{\partial F_y}. \tag{2.1}$$

If the force is homogeneous, the mobility is constant in the bulk, and given by :

$$\mu_{\text{bulk}} = -1/(eB). \tag{2.2}$$

In the presence of edges, the reponse of the system is slightly modified. Even in the absence of any external force, the cyclotron orbits bounce off the boundary, leading to the so-called 'skipping orbits', displayed in Fig. 2.1. Macroscopically, they induce the presence of a current at the edges of the sample. Unlike cyclotron orbits in the bulk, these skipping orbits are not affected by any external force, see the right panel of Fig. 2.1. This is a consequence of the fact that the Hall mobility vanishes at the edges of the sample [98].

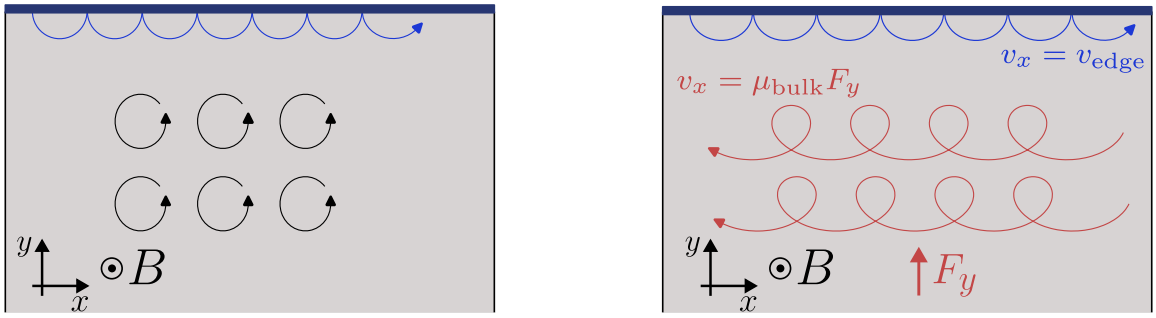

Figure 2.1: Classical Hall effect. Left : Semi-infinite material submitted to an orthogonal magnetic field. Electrons undergo circular orbits in the bulk and skipping orbits close to the edge. Right : Semi-infinite material submitted to an orthogonal magnetic field and to a uniform force F_y. Electrons in the bulk acquire a velocity proportional to the Hall mobility. This is the transverse Hall drift. Close to the edge, the Hall mobility goes to 0 and the velocity of the skipping orbits is not affected by the external force.

Vailidity of the classical approach

In this picture, the electron is a particle with no extension. Its position and velocity are localised in phase-space via the magnetic field, in a region of typical size $\Delta x \Delta p_x \simeq M v_0^2/\omega_c$, where v_0 is the initial velocity of the electron and p_x its momentum. This quantity will get closer and closer to 0 as the magnetic field (and therefore the cyclotron frequency) increases. At high enough magnetic fields, the position and momentum start to saturate Heisenberg inequality $\Delta x \Delta p_x > \hbar$, and the wavy character of matter can't be neglected anymore. We thus rely on quantum mechanics to describe the system is this regime.

2.1.2 Quantum Hall effect

We consider the same system in the context of quantum mechanics. To obtain its properties, we define its Hamiltonian :

$$H = \frac{[\boldsymbol{p} + e\boldsymbol{A}(\boldsymbol{r})]^2}{2M} \tag{2.3}$$

We have introduced the vector potential $\boldsymbol{A}$, such that the magnetic field is obtained by $\boldsymbol{B} = \boldsymbol{\nabla} \times \boldsymbol{A}(\boldsymbol{r})$. Defining new momenta $\Pi_j = p_j + eA_j$ (where $j = x, y$), the Hamiltonian can be rewritten as :

$$\hat{H} = \frac{\Pi_x^2 + \Pi_y^2}{2M} \tag{2.4}$$

These momenta obey the commutation relation $[\Pi_x, \Pi_y] = -i\hbar eB$, meaning that they are canonically conjugated. The Hamiltonian of the system therefore corresponds to that of a harmonic oscillator. Its spectrum can be directly derived, it forms the *Landau levels*. The eigenenergies are given by $E_n = \hbar\omega_c(n+1/2)$ where n is an integer. We illustrate in Fig. 2.2a these Landau levels.

Landau gauge

In the following, we work in the Landau gauge, which is convenient for the geometry that we will study later on. This gauge consists in setting $\boldsymbol{A} = yB\hat{\boldsymbol{x}}$. The translational invariance is thus broken along the y axis but not along the x axis. In this framework, the Hamiltonian becomes :

$$H = \frac{(p_x - eBy)^2}{2M} + \frac{p_y^2}{2M} \tag{2.5}$$

Since the translation operator along x commutes with H, we can look for eigenstates of the system that are also eigenstates of this translation operator, e.g plane waves along the x axis. We are left with the following ansatz for the wavefunction : $\psi_{p_x}(x, y) = \exp[ip_x x/\hbar]\, \phi_{p_x}(y)$, where p_x is the momentum along x. We can plug this ansatz in the Schrödinger equation $H|\psi\rangle = E|\psi\rangle$ to obtain the system's eigenstates and eigenenergies. After a bit of algebra, one can show that the eigenstates are given by the Hermite polynomials. In particular, the ground state of the system (called the lowest Landau level, LLL) can be written as :

$$\psi_{p_x}(x, y) \propto \exp[ip_x x/\hbar] \exp\left[-\frac{(y - p_x \ell_B^2/\hbar)^2}{2\ell_B^2}\right] \quad ; \quad \ell_B = \sqrt{\hbar/(eB)}, \tag{2.6}$$

where we have introduced the magnetic length ℓ_B, characterising the spatial extent of the wavefunction. The position along y of the LLL thus depends on its momentum along x. This is something that we will experimentally verify later on. The LLL is degenerate. Indeed, while an eigenvalue of the Hamiltonian is only labeled by one quantum number n, the eigenstates corresponding to this eigenvalue are labeled by both n and p_x.

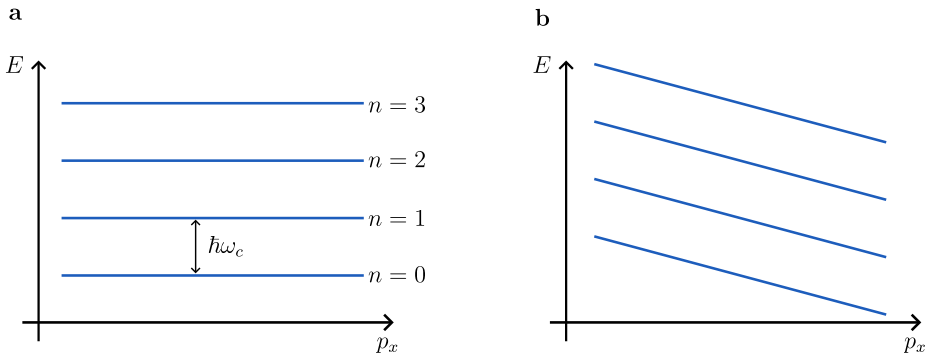

Figure 2.2: Landau levels. **a** : Landau levels without external potential. The energy levels are degenerate and spaced by $\hbar\omega_c$. **b** : Landau levels in the presence of a uniforme force along y (equivalently, a linear potential along y). The Landau levels are tilted, leading to a transverse drift along x.

Transverse response

We assume that a constant force $\boldsymbol{F} = F\hat{\boldsymbol{y}}$ is applied along the direction y. The Hamiltonian of the system is modified and we should consider an additional linear potential $V = -Fy$ in the Hamiltonian :

$$H' = \frac{(p_x - eBy)^2}{2M} + \frac{p_y^2}{2M} - Fy \tag{2.7}$$

After a little algebra, this can be re-expressed as follows :

$$H' = \frac{(p_x - eB(y - y_0))^2}{2M} + \frac{p_y^2}{2M} - \frac{p_x F}{2M} - \frac{F^2 M}{2(eB)^2} \quad ; \text{ with } y_0 = MF/(eB)^2 \tag{2.8}$$

We obtain the inital Hamiltonian without perturbation, shifted by y_0, and with an additional energy term proportional to the momentum p_x (and an energy offset). The eigenvalues

of the perturbed Hamiltonian can be directly obtained from the ones of the unperturbed one :

$$E_n(p_x) = \hbar\omega_c(n + 1/2) - \frac{p_x F}{eB} - \frac{F^2 M}{2(eB)^2} \tag{2.9}$$

Contrary to the previous case, the energy of the Landau levels now depend on the momentum p_x. This dependency comes together with a non-vanishing group velocity. The group velocity of the energy level n is given by:

$$\langle v_x^{(n)} \rangle = \frac{\partial E^{(n)}}{\partial p_x} = \frac{-F}{eB} \tag{2.10}$$

Finally, by derivating this expression with respect to the force, we obtain the mobility in the bulk of a quantum Hall system : $\mu_{\text{bulk}}^{\text{quantum}} = -1/(eB)$. We recover the bulk mobility obtained within the classical picture.

At this stage, the quantum Hall effect seems quite similar to the classical Hall effect. There is, however, a very peculiar property of the quantum Hall effect : the quantised conductivity. In 1980, V.Klitzing et al [1] reported the first measurement of the quantised nature of the transverse conductivity σ_H of a quantum Hall system. More precisely, the conductivity of a quantum Hall system exhibits steps such that $\sigma_H = \nu e^2/h$, where the prefactor ν can take either integer or fractional values. The first case corresponds to the integer quantum Hall effect, the latter to the fractional quantum Hall effect. The width of these steps is robust to disorder or perturbations, and can be used as a universal definition of the Ohm.

One way of understanding the quantisation of quantum Hall conductivity is to invoke topology. In the next section, we study the integer quantum Hall effect in this framework. We will rely on a new model consisting of coupled quantum wire, which is closer to our experimental system that we will present in the third section.

2.2 Quantum Hall effect in an array of quantum wires

In 2002, subsequent to preliminary investigations by Sondhi and Yang [106], Kane et al [102] demonstrated that different quantum Hall states can arrise in a 2D system made of coupled quantum wires, within an orthogonal magnetic field. Inspired by this work, we present a similar model and derive its properties. We will then use it as a support to introduce different topological quantities. Finally, we will leverage these topologial quantities to reinterpret the quantum Hall effect. This model will be an introduction to the topological systems that we realise with our experiment.

2.2.1 Infinite system

We consider a system made of one-dimensional quantum wires infinitely elongated along the x direction. The wires are spacially separated along the other direction, called m, which is discrete and infinite too. We study the dynamics of one particle in this system, thus we don't consider interactions. We suppose that the particle is spinless. We also suppose that there is no trapping potential along x or along m. The different quantum wires are coupled via a tunneling amplitude Ω and a tunneling phase ϕ. We suppose that this tunneling phase depends on the position x, via $\phi(x)$. In the following, we also assume that the phase evolves linearly with x through $\phi(x) = 2kx$, where the wavector k can take any value. This form may seem arbitrary at this stage, but it will be close to the experimental scheme that we will present afterwards. From this wavector k, we can define an energy scale $E_{\text{rec}} = \hbar^2 k^2/2M$,

where M is the mass of the particle, and a momentum scale $p_{\text{rec}} = \hbar k$. Within this picture, the particle evolves freely in a wire along the x direction, and undergoes some hoppings to the neigbouring wires, thereby acquiring a phase that depends on the x.

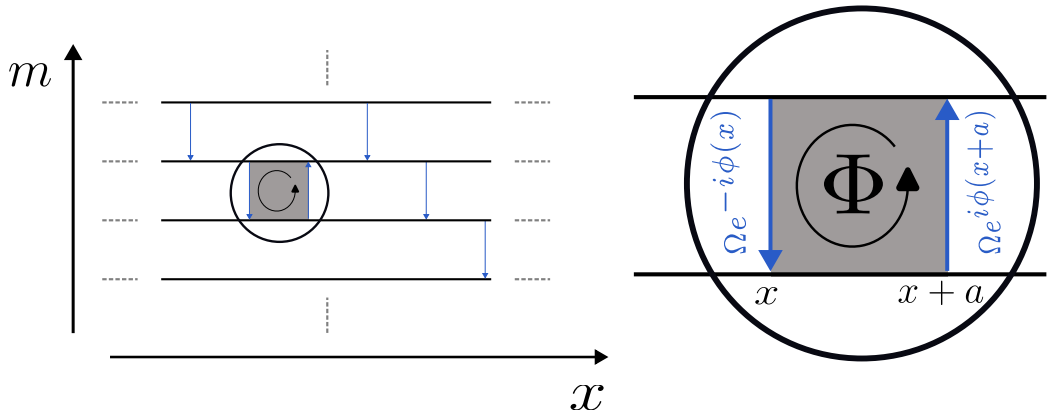

Figure 2.3: Infinite coupled quantum wire system. The quantum wires are infinite along the direction x. Dimension m is discrete and also infinite. A particle can undergo hopping between two neighbouring wires (blue arrows). A particle following the loop surrounding the grey shaded area acquire a phase Φ.

We display in Fig. 2.3 a scheme of the system. A particle undergoing the loop surrounding the grey shaded area acquires a non-vanishing phase Φ. This phase is equal to $\Phi = 2kS = 2ka$ with S the surface of the shaded area and a the distance along x between the two hoppings. It can be interpreted as an Aharonov-Bohm phase, $\Phi_{AB} = qBS/\hbar$, leading to the appearance of an effective magnetic field in the orthogonal direction. This model thus maps to a particle of charge $q = 1$ within a magnetic field $B = 2\hbar k$.

To summarise, we study the motion of a particle evolving in an infinite 2D system. One dimension x is continuous, the other m is discrete. An effective magnetic field in the orthogonal direction arrises from the space-dependent hopping phases. As we will see, this effective magnetic field will be at the origin of a quantum Hall effect. We now discuss the properties of this system.

2.2.2 Ground band properties

The Hamiltonian of the particle is the following :

$$H = \frac{p_x^2}{2M} - \Omega \left(T_m \mathrm{e}^{-2ikx} + \mathrm{h.c} \right), \tag{2.11}$$

where T_m is the hopping operator along the direction m, and Ω is the tunneling amplitude. This system is highly symmetric, with a translation invariance along x of $\mathrm{d}x = \pi/k$, and a translation invariance along m of $\mathrm{d}m = 1$. Bloch theorem thus apply and leads to introduce the quasimomentum : $\mathbf{q} = (q_x, q_m)$. The Brillouin zone is defined by $-\pi \leq q_m < \pi$ and $-k \leq q_x < k$. One way to treat this problem is to replace the translation operator T_m by $T_m = \mathrm{e}^{-iq_m}$. The Hamiltonian becomes :

$$\begin{aligned} H_{q_m} &= \frac{p_x^2}{2M} - \Omega\left(\mathrm{e}^{-i(2kx+q_m)} + \mathrm{h.c}\right) \\ &= \frac{p_x^2}{2M} - 2\Omega\cos\left(2kx + q_m\right) \end{aligned} \tag{2.12}$$

We retrieve the Hamiltonian of a one-dimensional cosine lattice, with a phase depending on q_m. There is thus a degeneracy along q_m. According to Bloch theorem, the eigenstates of the band n can be written as :

$$\psi^{(n)}_{q_x,q_m}(x,m) = \sum_{j\in\mathbb{Z}} C_j^{(n)} \mathrm{e}^{i(q_x+2kj)x} \mathrm{e}^{i(q_m+2\pi j)m}, \tag{2.13}$$

where the coefficients C_j have to be determined. By plugging these wavefunctions into the Schrödinger equation, we recover the famous central equation :

$$C_j^{(n)} \frac{(q_x+2kj)^2}{2M} - \Omega C_{j+1}^{(n)} e^{-iq_m} - \Omega C_{j-1}^{(n)} e^{iq_m} = E C_j^{(n)} \tag{2.14}$$

We can numerically solve this equation to get the ground band and the excited bands over the Brillouin zone. We display the dispersion relation in Fig. 2.5 for various values of the tunneling amplitude. As Ω increases, the bands are getting more and more flat, becoming reminiscent of Landau levels. For all values of Ω, we observe a degeneracy along q_m. Additionally, the system becomes degenerate along q_x too, as Landau levels. The dispersion relation of this system is thus the reminiscent of the one of electrons within a large magnetic field.

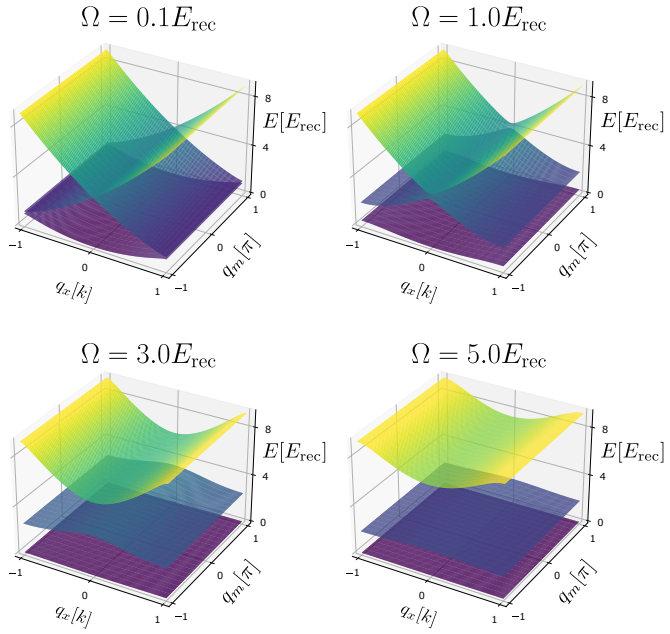

Figure 2.4: Bandstructure of the infinite quantum wire model for various hopping amplitudes Ω. The system is degenerate along q_m. As Ω is increased, the gaps open and the bands flatten, approaching the structure of Landau levels.

2.2.3 The role of topology

In this paragraph, we introduce the Berry connection, the Berry curvature and finally the Chern number, that characterises the topology of the system. We first introduce the Berry connection of the band n [8] :

$$\boldsymbol{\mathcal{A}}^{(n)}_{q_x,q_m} = i\langle\psi^{(n)}_{q_x,q_m}|\boldsymbol{\nabla}\psi^{(n)}_{q_x,q_m}\rangle \tag{2.15}$$

From this quantity, we can define the Berry curvature of the band under consideration :

$$\boldsymbol{F}^{(n)}(q_x,q_m) = i\boldsymbol{\nabla}\times\boldsymbol{\mathcal{A}}^{(n)}_{q_x,q_m} \tag{2.16}$$

It can be shown that, under the application of a weak electric field $\boldsymbol{\mathcal{E}} = \mathcal{E}\boldsymbol{x}$, the velocity of the wavepacket centered at $\boldsymbol{q} = (q_x, q_m)$ in the band n can be computed using the Berry curvature through [107] :

$$\boldsymbol{v}^{(n)}(\boldsymbol{q}) = \frac{\partial E^{(n)}(\boldsymbol{q})}{\partial \boldsymbol{q}} + \frac{1}{\hbar}\boldsymbol{\mathcal{E}}\times\boldsymbol{F}^{(n)}(\boldsymbol{q}), \tag{2.17}$$

where $E^{(n)}$ is the unperturbed energy of the band under consideration. This equation contains two terms. The first one describes the group velocity, due to the band curvature. The second is often referred to as the 'anomalous velocity', and is reminiscent of the drift velocity introduced previously. Since the berry curvature $\boldsymbol{F}$ is orthogonal to the plane xm (Eq. (2.16)), the anomalous velocity is orthogonal to the orientation of the electric field. It thus describes a *transverse* response, reminiscent of the Hall effect. The Berry curvature is the analogue of the Hall mobility introduced in section 1. In the following, we suppose that the electric field $\boldsymbol{\mathcal{E}}$is oriented along m.

In order to derive the transverse conductivity of the system, we compute the current density $\boldsymbol{j}$ induced by the electric perturbation. The current density is defined as :

$$\boldsymbol{j} = \sum_{\boldsymbol{q}} \frac{\boldsymbol{v}(\boldsymbol{q})}{V}, \tag{2.18}$$

where V is the volume of the system. Using Eq. (2.17), we obtain :

$$\boldsymbol{j} = \frac{1}{V}\sum_{\boldsymbol{q}} \frac{\partial E(\boldsymbol{q})}{\partial \boldsymbol{q}} + \frac{\mathcal{E}}{\hbar V}\sum_{\boldsymbol{q}} F(\boldsymbol{q})\hat{\boldsymbol{x}} \tag{2.19}$$

We now replace the discret sum by an integral :

$$\sum_{\boldsymbol{q}} \longleftrightarrow \frac{V}{(2\pi)^2}\int_{\mathrm{BZ}} \mathrm{d}\boldsymbol{q}, \tag{2.20}$$

where the integral is performed over the full Brillouin zone.

After integration upon the Brillouin zone, the group velocity contribution cancels out, due to the bandstructure periodicity. We are left with :

$$\boldsymbol{j} = \frac{\mathcal{E}\boldsymbol{x}}{(2\pi)^2\hbar}\int_{\mathrm{BZ}} F(\boldsymbol{q})\mathrm{d}\boldsymbol{q} \tag{2.21}$$

It is demonstrated that the integral of the Berry curvature over the Brillouin zone is a multiple of 2π [8]. The current density thus reduces to :

$$\boldsymbol{j} = \frac{\nu}{h}\mathcal{E}\hat{\boldsymbol{x}}\,,\ \nu\in\mathbb{Z} \tag{2.22}$$

This results shows that the system transversally responds to the perturbation along m. Moreover, this response is quantised by the integer ν. This number is the topological invariant of the system and is defined by :

$$\nu = \frac{1}{2\pi} \int_{\mathrm{BZ}} \mathrm{d}\boldsymbol{q} F(\boldsymbol{q}) \tag{2.23}$$

This number is an integer, and is topologically *robust*. Indeed, for weak enough perturbations (in the sense that there is no gap closing), it always takes the same value, hence the notion of topology. From Eq. (2.22), we obtain the transverse conductivity of our system : $\sigma = \dfrac{\nu}{h}$. We recover the celebrated quantised Hall transverse conductivity (we recall that we asssume a charge $q = 1$).

We display in Fig. 2.5 the Berry curvature of the infinite quantum wire system for different values of Ω. The Berry curvature is strongly affected by the hopping amplitude. As Ω increases, the Berry curvature flattens. For $\Omega = 5E_{\mathrm{rec}}$, we have $F \simeq 1/(2k)$ on the full Brillouin zone. By integrating this value, we obtain $\int F \mathrm{d}\boldsymbol{q} \simeq (2k) \times (2\pi) \times 1/(2k) = 2\pi$. As expected, the integral of the Berry curvature over the Brillouin zone is a multiple of 2π. Note that this integration leads to the same value for all $\Omega > 0$, howing to the topological robustness.

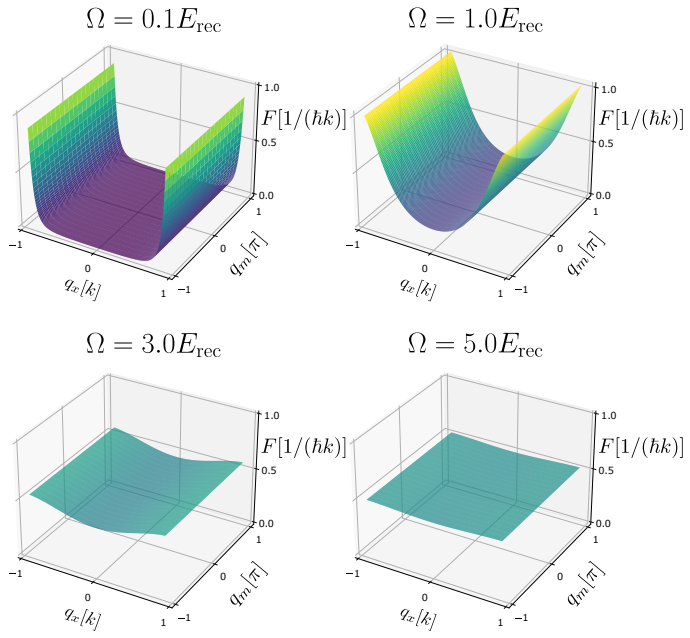

Figure 2.5: Local transverse response : Berry curvature of the infinite quantum wire model for various hopping amplitudes Ω. For low values of Ω, the Hamiltonian is essentialy given by the kinetic energy along x, and the Berry curvature nearly vanishes (at least in the center of the Brillouin zone). When increasing Ω, the Berry curvature homogenises and reaches $\simeq 1/(2k)$ on the full Brillouin zone. Integrating the Berry curvature on the Brillouin zone leads to the same value $\nu = 1$ for all non-vanishing values of Ω.

For now, we have considered an infinite system and have revealed its topology by com-

puting the integral of the Berry curvature on the Brillouin zone. By imposing edges on the sample, howing to the bulk-boundary correspondence [51], one would expect to observe the emergence of chiral edge modes. This concept will be studied more in details in chapter VI. In the next paragraph, we impose edges along the direction m and see how they affect the system's properties.

2.2.4 Finite system

In the presence of boundaries along m, the translation symmetry is broken along this direction. We suppose that we have $2J+1$ wires, whose position m goes from $m=-J$ to $m=+J$. At this stage, J is a positive integer. We will often consider $J=8$ in the following, to match our experimental system. The ground band of the system, originally indexed by (q_x, q_m), maps to a set of $2J+1$ bands indexed by a single momentum. To deal with such a geometry, it is more convenient to use the gauge transform $U=\mathrm{e}^{2ikx}$, leading to :

$$H=\frac{(p-2\hbar k\hat{m})^2}{2M}-\hbar\Omega\left(T_m+T_{-m}\right), \tag{2.24}$$

where we put a hat on the position operator $\hat{m}$, to distinguish it from the m sites. Within this Landau gauge, the Berry curvature and the energy are indexed by a one-dimensional momentum p that can take any values, contrary to the infinite case where it was a function of a two-dimensional quasimomentum $\boldsymbol{q}=(q_x,q_m)$ defined on a Brillouin zone. We compare the finite and the infinite system by looking at their spectrum in Fig. 2.6. The energy bands of the infinite system are degenerate along q_m. When edges are added along m, the degenerated bands indexed by q_m and q_x merge into a single band indexed by p.

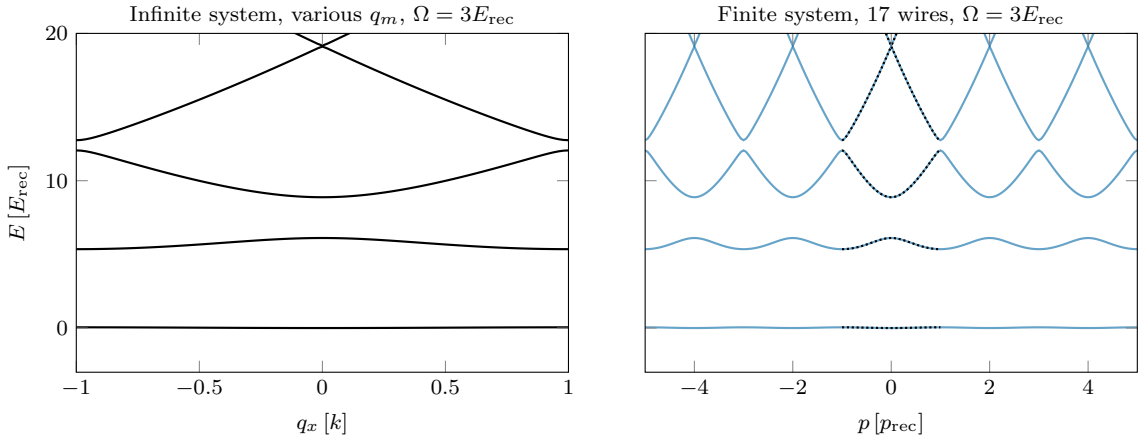

Figure 2.6: Dispersion relation for the finite and the infinite system. Left : Infinite system. There is a degeneracy along q_m. Right : Finite system (with 17 wires). For the range of momenta under consideration, the dispersion relation is reminiscent of the one of the infinite system, that we display with black dashed lines.

We don't see the effect of the edges on Fig. 2.6, because we where here only focuses on momenta close to 0. As seen previously, the m-position of the wavefunctions depend on the momentum p. By looking at larger momenta, the wavefunctions will explore to full range of m, and will start to feel the boundaries at $m=\pm J$.

We show in Fig. 2.7 the dispersion relation of the finite system with 17 wires on a broader range of momenta. We observe the presence of a bulk, defined by $E^{(0)}(p)<E^*$, where E^* lies in the middle of the gap between the ground band and the first excited band. For $\Omega=4E_{\mathrm{rec}}$,

the bulk corresponds to $|p_x| < p^* \simeq 17 p_{\text{rec}}$. In the bulk, the dispersion relation is flat, and matches the one of the infinite system (depicted in dashed black lines). We observe chiral edge modes for $|p_x| > p^*$, where the energy dispersion relation becomes fully kinetic. These edge modes are reminiscent of the chiral edge modes of the Hall effect, and are a direct consequence of the system's non-trivial topology.

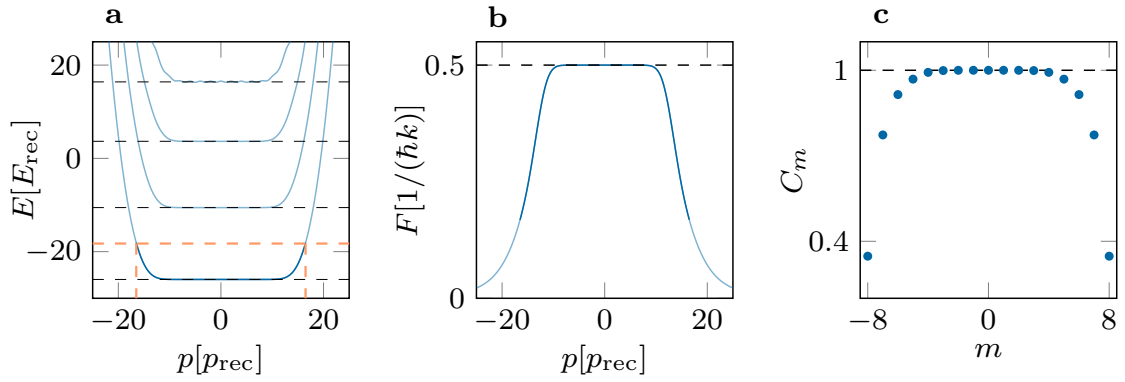

Figure 2.7: Properties of the finite system made of 17 quantum wires at $\Omega = 4E_{\text{rec}}$. **a** : Dispersion relation. The horizontal orange line lies in the middle of the ground band and the first excited band. It defines a bulk and edges. Bands are flat in the bulk, and we recover chiral edge modes on the boundaries. Dashed black lines indicate the eigenenergies of the infinite wires system. There is a good agreement between the two systems in the bulk. **b** : Berry curvature. Close to $p = 0$, the Berry curvature is equal to $0.5\hbar k$. It goes to 0 on the edges, in the same fashion as the Hall mobility. **c** : Local Chern marker. In the bulk of the sample, the local Chern marker is equal to unity, highlighting the non-trivial topology.

The Berry curvature of the ground band in the bulk is equal to the one of the infinite system. It goes to 0 for $|p_x| > p^*$, as a consequence of the presence of edges at $m = \pm J$. This is similar to the decay of the Hall mobility near the system's boundaries. One may wonder if the transverse conductivity is affected by the presence of edges. In this new geometry, the response of the system is not homogeneous due to the edge effects. Considering the response of the whole system is thus not meaningful. To overcome such an issue, we consider the local Chern marker[1] C_m, defined as [108] :

$$C_m = \int \mathrm{d}p \Pi_m(p) F(p), \tag{2.25}$$

where $\Pi_m(p)$ is the squared propability to measure the ground state in the quantum wire m at the momentum p. The local Chern marker characterises the local (in m) transverse response. In the bulk, the local Chern marker of the ground band is equal to unity, similarly to the infinite system, and characterises the non-trivial topology. This number replaces the topological invariant ν for a non-homogeneous system.

In this section we have studied a system of coupled quantum wires, considering both infinite and finite systems. A quantum Hall effect emerges in this model, due to the space-dependent hopping phase between the neighbouring wires, even if the particle under consideration is neutral. This toy model allowed us to introduce the Berry curvature and the Chern number. We interpreted the quantisation of the transverse Hall conductivity through

[1] This quantity is also useful to deal with inhomogeneous systems due to impurities or disorder.

the prism of topological arguments. Subsequently, we introduced boundaries to our system and found that the bulk properties remained unaffected, while the edges exhibited chiral edge modes. We now shift our focus to the experimental realisation of a synthetic quantum Hall ribbon using dysprosium atoms, which is closely related to this quantum wire scheme.

2.3 Realisation of a dysprosium synthetic quantum Hall ribbon

In this section, we present our realisation of a 2D quantum Hall ribbon using dysprosium atoms. This part will be a pedagogical introduction to our protocols, that we have used to realise various topological systems and that we will present in the following chapters. The results presented in this section were already obtained in our group back in 2020 [103]. Recently, we realised again this system, with the aim to study its entanglement Hamiltonian, as we will see in chapter VI. Our protocol to engineer quantum Hall states relies on the use of synthetic dimension [109–111].

2.3.1 Synthetic dimension

A synthetic dimension is a non-spatial dimension treated in the same way than a spatial one. Most of the time, it is made of an internal degree of freedom of a system (its spin state, its momentum state [112, 113], its orbital momentum state [114] ...) that is treated as an effective dimension. This approach has been widely used in photonics [41, 64, 115], and in the ultracold atoms community, where the spin degree of freedom can be considered as an effective dimension [50, 61–63, 109, 111] as we do in our experiment [103].

Synthetic dimensions have several interesting properties. First, they permit to generate artificial gauge fields [109], a key ingredient to emulate topological systems. Secondly, synthetic dimensions permit to engineer particular geometries, such as cylinders [61–63], or systems with sharp edges. Finally, synthetic dimensions can be used to emulate higher-dimensional systems [60, 115, 116] which is something that we will study in the chapters IV and V.

In our experiment, we consider dysprosium's large spin as a synthetic dimension. Hence, the 17 Zeeman sublevels contained in the manifold $J = 8$ will be re-interpreted as a one-dimensional lattice made of 17 sites. This system is large enough to have both edges (at $|m = \pm 8\rangle$) and a bulk. We generate artificial gauge fields by coupling the synthetic dimension to a spatial one, thereby realising a 2D quantum Hall system.

2.3.2 Experimental implementation

Our implementation of a 2D quantum Hall ribbon relies on the scheme drawn Fig. 2.8, involving lasers in Raman configuration. This scheme was detailed in [103], we only provide here a brief idea.

The degeneracy between the different Zeeman sublevels is lifted using a magnetic field along the quantisation axis $\boldsymbol{z}$. These sublevels are separated by the energy $\hbar\omega_z$, where ω_z is the Larmor frequency. We shine a pair of counterpropagating Raman beams on the atoms, that are detuned by $\Delta \simeq -2\pi \times 10\,\mathrm{GHz}$ with respect to the 626 nm transition. This detuning is large compared to the transition linewidth $\Gamma \simeq 2\pi \times 135\,\mathrm{kHz}$, hence the beams do not induce a strong scattering.

The frequency difference between the two lasers is set close to ω_z, so that the atoms can undergo a Raman process : absorbtion of a photon in beam 1 and stimulated emission in beam 2 (and the Hermitian conjugate process). This Raman process is governed by the polarisation of the beams.

The process $|J = 8, m_J\rangle \rightarrow |J' = 9, m_J + 1\rangle \rightarrow |J = 8, m_J + 2\rangle$ that involves two σ_+ photons is not resonant since our Raman beams are detuned by ω_z but not by $2\omega_z$, and can be neglected. We are thus left with the process $|J = 8, m_J\rangle \rightarrow |J' = 9, m_J\rangle \rightarrow |J = 8, m_J + 1\rangle$, and its Hermitian conjugate.

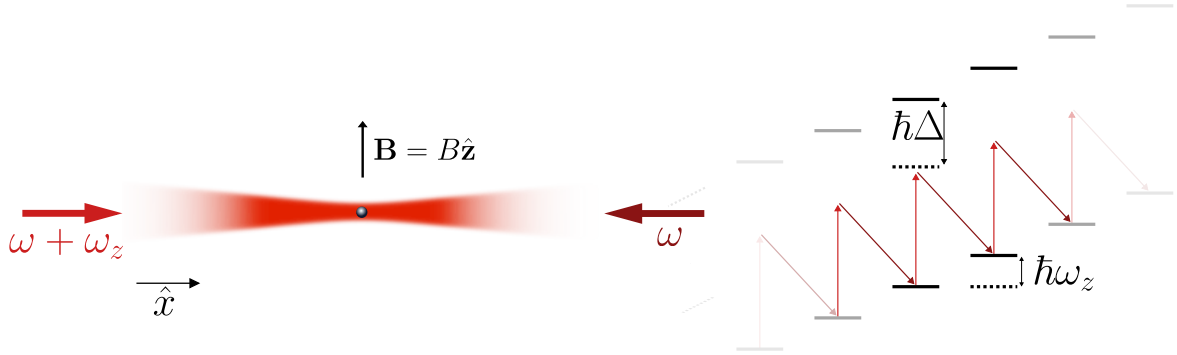

Figure 2.8: Raman configuration. A magnetic field lifts the degeneracy between the Zeeman sublevels. Two counterpropagating beams are shined on a dysprosium atom. They are detuned by Δ with respect to the 626 nm transition. The frequency difference between the two lasers is set close to the Larmor frequency, such that the different Zeeman sublevels are coupled by Raman transitions.

Each Raman transition comes together with a momentum kick. For instance, if a dysprosium atom absorbs one photon from beam 1 and emits one in beam 2, it will aquire a net momentum kick $p = 2\hbar k = 2p_{\text{rec}}$ along the x direction. The internal and the external degrees of freedom of the atoms are thus coupled via the operators : $J_+ \mathrm{e}^{-2ikx}$ and $J_- \mathrm{e}^{2ikx}$. This scheme illustrates how Raman processes and synthetic dimensions lead to the emergence of spin-orbit coupling. It can be shown that [103], within rotating wave approximation and using appropriate gauge transform, this configuration permits to effectively realise the following Hamiltonian :

$$\begin{aligned} H &= \frac{(p - 2\hbar k J_z)^2}{2M} - \frac{\hbar\Omega}{2}(J_+ + J_-) \\ &= \frac{(p - 2\hbar k J_z)^2}{2M} - \hbar\Omega J_x \end{aligned} \tag{2.26}$$

This Hamiltonian is reminiscent of the one studied in Section 2.2. In the next paragraph, we make the link between this Hamiltonian and the one of the quantum wire model considered previously.

2.3.3 Mapping to the quantum wire system

We recall that the quantum wire Hamiltonian derived in Section 2.2 is the following :

$$H_{\text{QW}} = \frac{(p - 2\hbar k\hat{m})^2}{2M} - \hbar\Omega_{\text{QW}}(T_m + T_{-m}), \tag{2.27}$$

where we put a hat on $\hat{m}$, to distinguish the position operator $\hat{m}$ from the spin projection m.

By considering the spin degree of freedom as a dimension, J_z plays the role of a position operator along the direction m, hence it replaces $\hat{m}$. The kinetic term is thus similar for the two systems. The second term plays the role, in both cases, of a translation along m. Indeed, J_+ increases the spin projection m by one unit, while J_- decreases it by one unit. However, we have a slight discrepancy here. On one hand, for the quantum wire model, the matrix element $\langle m+1|\, T_m \,|m\rangle$ is equal to unity for all sites m, the hopping amplitude is thus constant along this direction. On the other hand, we have for the synthetic system $\langle m+1|J_+|m\rangle = \sqrt{J(J+1)-m(m+1)}/2$, see Fig. 2.9c. Hence, the hopping amplitude is not constant in our synthetic system, due to the Clebsch-Gordan variations of the $J_\pm$ operators. To compare the two models, we will adjust the respectives hopping amplitudes Ω such that the matrix elements between $|m=0\rangle$ and $|m=1\rangle$ of the hopping operators are the same in both cases. Thereby, in the following, we use $\Omega_{\text{synthetic}} = 4E_{\text{rec}}$ for the synthetic system and $\Omega_{\text{QW}} = 4E_{\text{rec}}\sqrt{J(J+1)}/2$ for the quantum wire system.

We compare our synthetic system and the finite quantum wire model (with 17 sites) in Fig. 2.9a,b. While the quantum wire model has flat bands in the bulk, reminiscent of Landau levels, the synthetic system provides a non-vanishing curvature in the bulk. Both systems exhibit chiral edge modes, unveiling their topological character. The Berry curvature is also slightly different between the two systems. However, the difference in the hopping matrix elements makes no differences on the topological properties, which are insensitive to small perturbations. This is illustrated by Fig. 2.9f, where we see that the local Chern marker is equal to unity in both cases in the bulk.

Ground band flattening

To compensate for the curvature of the ground band of the synthetic system, an additional spin quadratic term $-J_z^2$ can be added in the Hamiltonian. Indeed, this term plays the role of a quadratic trapping potential along the synthetic dimension, whose shape will counterbalance the dispersion relation of the ground band.

We show in Fig. 2.9d,e,f the effect of an additional quadratic term. We see on the dispersion relation that the quadratic term flattens the ground band in the bulk, making it very close to the one of the quantum wire model. In such situation, the motion is frustrated in the bulk of our synthetic system, reminiscent of the motion of electrons in the bulk of a sample submitted to a strong magnetic field. The J_z^2 term slightly modifies the local transverse response, as seen on the Berry curvature, and make it more close to the one of the quantum wire system. However, the topology is not affected by the quadratic operator, this can be seen on the local Chern marker that is similar in the bulk for the three systems (quantum wire, synthetic system, synthetic system with quadratic spin term), see Fig. 2.9f.

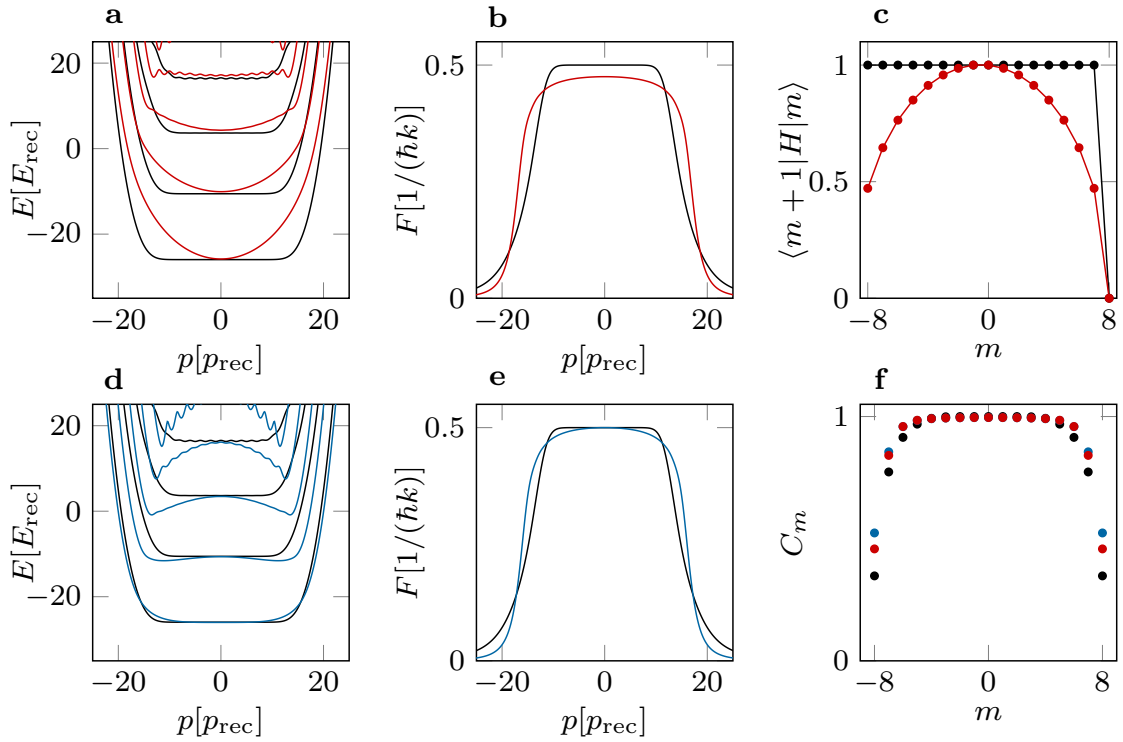

Figure 2.9: Comparison between the synthetic system and the 17-quantum wire system. $\Omega_{\mathrm{synthetic}} = 4E_{\mathrm{rec}}$, $\Omega_{\mathrm{QW}} = 4E_{\mathrm{rec}}\sqrt{J(J+1)}/2$. Black curves refer to the quantum wire system. Red curves refer to the synthetic system. Blue curves refer to the synthetic system with an additional quadratic spin operator $Q = -\Omega/(2J+3)$. **a** : Dispersion relation. **b** : Berry curvature. **c** : Variation of the Clebsch-Gordan coefficients for the operators T_m and J_+. **d** : Dispersion relation. The quadratic spin operator flattens the bands of the synthetic system. **e** : Berry curvature. In the presence of the quadratic operator, the Berry curvature reaches $1/(2\hbar k)$. **f** : Local Chern markers for the quantum wire system (black), the synthetic system without a quadratic term (red) and the synthetic system with a quadratic term (blue). They are all equal to one in the bulk.

2.3.4 Experimental results

We now present some experimental results that we obtained by realising this model. We start by demonstrating the ground band flattening. As seen in chapter I, one way to realise a J_z^2 coupling in our set-up is to shine an additional off-resonant beam linearly polarised, which polarisation is making a well chosen angle θ with the quantisation axis. The frequency of this additional beam must be detuned by several Larmor frequencies from the ones of the two other beams to avoid any new resonant Raman process. Experimentally, we detuned this beam by 10 MHz $\simeq 6\hbar\omega_z$. Such a configuration leads to a vanishing vectorial light shift and to a tensorial light shift equals to :

$$V_{\mathrm{tensorial}} = \frac{U}{2(J+1)(2J+1)}\left[1-3\cos^2(\theta)\right]J_z^2 = Q(U,\theta)J_z^2, \tag{2.28}$$

where U is the light shift for Clebsch-Gordan coefficients equal to unity, introduced in chapter I. Thus, depending on the polarisation angle θ and the detuning (through U), we can implement a positive or negative J_z^2 coupling. Using red-detuned light ($U < 0$) and a polarisation $\theta = \pi/2$, this tensorial light shift leads to a negative J_z^2 term. By

tuning the trap depth U (through the laser power), we can adjust the strength of this quadratic spin term Q, such that it perfectly cancels the curvature of the ground band. It can be shown that a term $-\Omega/(2J+3)J_z^2$ is theoretically optimal to flatten the ground band.

We show in Fig. 2.10 (left) our measurements of the ground band velocity of our synthetic system as a function of the momentum p, for various quadratic spin terms. The curvature of the ground band can be inferred by computing the derivative of the velocity with respect to p. As expected, in the bulk, the curvature is positive for $Q = 0$. Increasing the strength of the quadratic term decreases the curvature and can even make it negative. We present in Fig. 2.10 (right) our measurements of the ground band curvature for various quadratic spin terms. The datas agree well with the theoretical evolution. In the end, for the choice $Q = -\Omega/(2J + 3)$, we recover a (synthetic) 2D quantum Hall system with edges and a flat ground band.

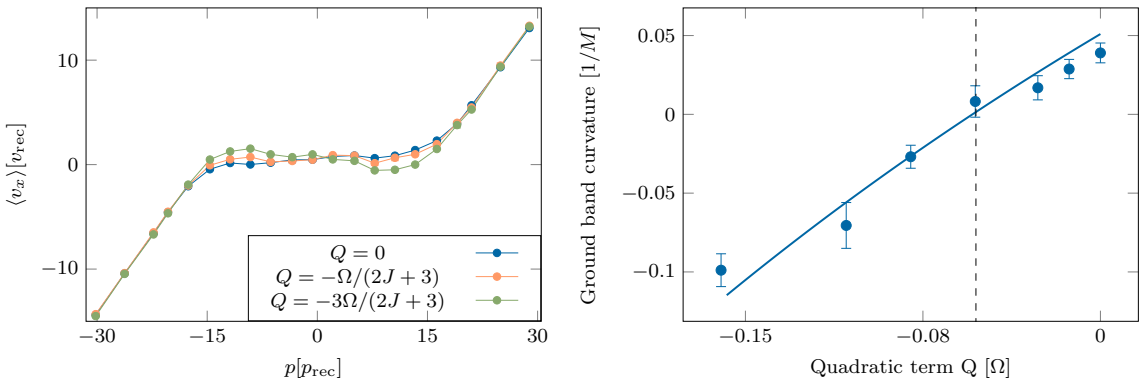

Figure 2.10: Ground band flattening for $\Omega = 4E_{\mathrm{rec}}$. Left : Measurement of the velocity in the ground band of the synthetic quantum Hall system for three different quadratic terms. In the bulk, the velocity is increasing with p for a zero quadratic term (blue curve) and decreasing with p for a strong negative quadratic term (green curve). Note that we measured chiral edge modes for $|p| > 17p_{\mathrm{rec}}$. Right : Curvature of the ground band inferred from the measured velocities for seven different values of Q. Solid lines is the theory. Black dashed line corresponds to $Q = -\Omega/(2J + 3)$ where we theoretically expect a vanishing curvature.

We display in Fig. 2.11 the measured magnetisation and velocity in the ground band and compare them to the theory. The average magnetisation $\langle J_z \rangle$ can be interpreted as a position along the synthetic dimension. We recover the behavior of the LLL : the position of the system along m linearly increases with the momentum p, at least in the bulk. The edges $|m = \pm J\rangle$ are approached for $|p| > 17p_{\mathrm{rec}}$. At these edges, the velocity of the ground band is chiral, unveiling the system's non-trivial topology. In the bulk, the measured velocity is quasi-vanishing, revealing a frustration of motion.

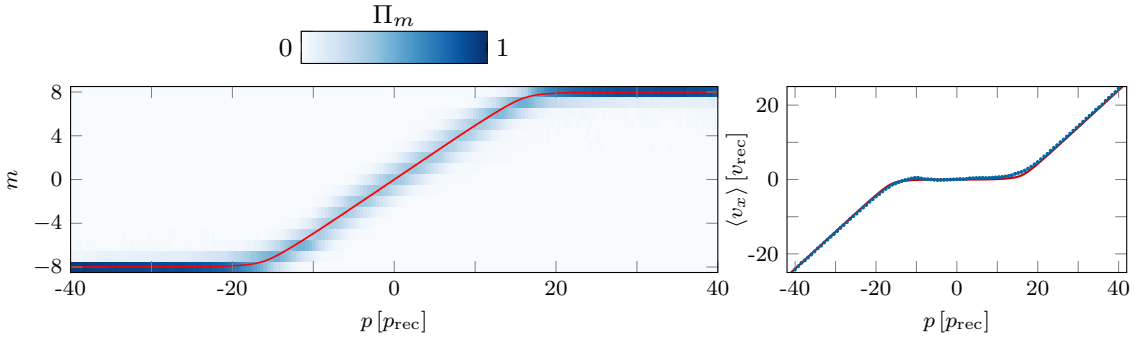

Figure 2.11: Experimental ground band properties for $\Omega = 4E_{\mathrm{rec}}$ and $Q = -\Omega/(2J+3)$. Left : Experimental spin populations. Red curve is the theoretical magnetisation $\langle J_z \rangle$. We see the presences of edges for $|p| > 17p_{\mathrm{rec}}$, where the system starts to be polarised in $m = \pm J$. Right : Velocity in the ground band. Blue dots are experimental points and red line is theory. Error bars are within the dots size. In the bulk, $|p| < 17p_{\mathrm{rec}}$, the velocity is vanishing, exhibiting the frustration of motion. On the boundaries, we observe chiral edges mode.

We then experimentally characterise the topology of our system via a measurement of the Berry curvature and the local Chern marker, see Fig. 2.12. In the bulk, we measure a local Chern marker consistant with unity, hence retrieving the expected quantisation for a quantum Hall system.

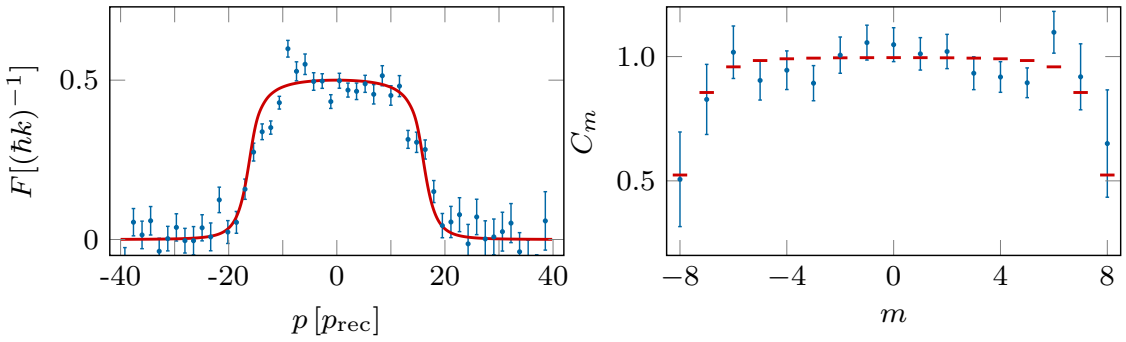

Figure 2.12: Experimental topological properties for $\Omega = 4E_{\mathrm{rec}}$ and $Q = -\Omega/(2J+3)$. Left : Berry curvature F of the ground band. Blue points are experimental data, red line is theory. Error bars are obtained by bootstrapping. The Berry curvature goes to 0 for $|p| > 17p_{\mathrm{rec}}$, due to the presence of edges, similarly to the Hall mobility. Right : Local Chern marker. The measurements are consistent with $C_m = 1$ for $|m| \leq 4$.

2.4 Conclusion

We started this chapter by briefly introducing the classical and the quantum Hall effect. Then, we presented a model made of coupled quantum wires. We have seen that an artificial gauge field can arrise in this model, provided that the hopping terms between the different wires come together with a space-dependent phase. This artificial gauge field is at the origin of a quantum Hall effect, that we interpreted through the prism of topology. This quantum wire model is an introduction to the physical systems that we are producing in our group.

Subsequently, we detailed our experimental realisation of a synthetic quantum Hall ribbon, considering dysprosium's spin as a synthetic dimension. We were able to generate artificial magnetic field on the neutral atoms via spin-orbit coupling. We compared our system to the quantum wire model, and have implementend an additional quadratic spin operator to make the two systems more similar. Finally, we have presented experimental results obtained with our synthetic system. We recovered the typical behavior of the LLL, and we demonstrated the system's non-trivial topology by revealing the existence of chiral edge modes and by the measurement of a local Chern marker consistent with unity in the bulk.

3 Two synthetic dimensions encoded in a large spin

The study of topological systems encourages to consider higher dimensional systems, where a rich physics is expected, such as the 4D [23] and the 6D quantum Hall effect [25], or the 5D Weyl-semimetals [27]. However, in standard materials, going to dimension higher than 3 is not straightforward. The community has developed several tools in the past decades to overcome this problem. One idea relies on connectivity, where the different sites of a system are connected in a clever way, through combination of short and long-range couplings, leading to an effective higher dimensional system (see Fig. 3.1a). This idea has been studied in [115, 116] and experimentally explored using electric circuits [42, 117] or photonics [118].

Synthetic dimensions are another tool to study higher dimensional systems. In this chapter, we propose to apply the connectivity approach to dysprosium's spin synthetic dimension. We will study how a combination of first-order and second-order spin operators applied on

a spin J can lead to an effective two-dimensional synthetic system. We will see that, under the good combination of these spin operators, the synthetic dimension of a spin J can be seen as a cylinder, whose circumference is made of three sites. We will study the conditions under which this picture is valid and the deviations from this ideal case. Subsequently, we will couple the synthetic cylinder to a spatial dimension via Raman processes. We will see that it permits to emulate a cylinder with an artificial magnetic field in both the radial and the longitudinal directions, leading to the emergence of a quantum Hall effect. We will finally expose experimental results of our realisation of a synthetic quantum Hall cylinder made with dysprosium atoms. We were able to vary the quantity of magnetic flux injected through the cylinder, thereby realising Laughlin's thought experiment [119] for the first time. Most of the results presented in this chapter were already extensively discussed in Aurélien Fabre's thesis [78]. This chapter is an introduction to the next two chapters, were we will rely on two synthetic dimensions within dysprosium's spin.

The results presented in this chapter were published in [120, 121].

3.1 The emergence of two dimensions within a large spin

In this section, we show how a combination of first and second-order spin operators can lead to an effective two-dimensional system within a large spin.

3.1.1 Combination of short and long-range couplings

Consider a 1D chain of discrete sites, each of them being couple to their neighbouring : the system is one-dimensional. Now, suppose we add order-4 couplings to the system (Fig. 3.1a). The system is topologically equivalent to the one displayed Fig. 3.1b which is effectively a two-dimensional lattice with a 'screw' geometry. Hence, by combining couplings of different orders, one can effectively emulate higher dimensional systems, where each site is connected to a greater number of sites. We propose here to apply this idea to the $2J+1$ sites of a spin J.

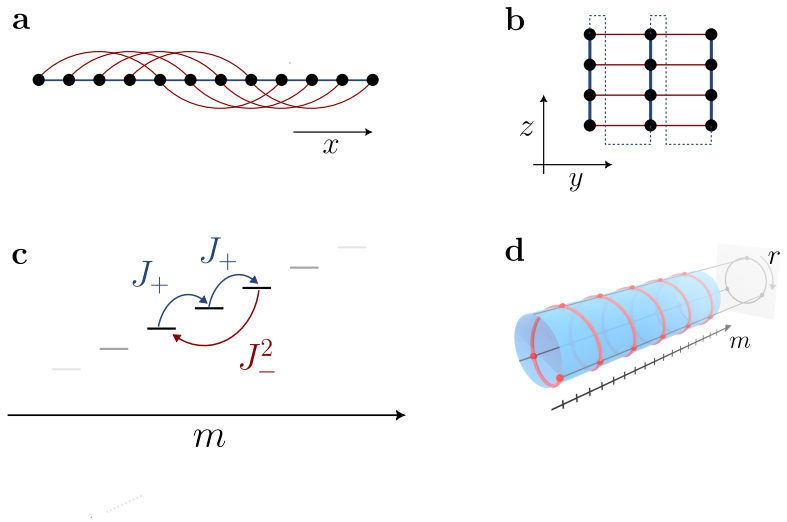

Figure 3.1: Combination of short and long-range couplings. **a** : 1D discrete system, whose sites are combined through short-range couplings (connecting neighbouring sites) and long-range couplings (connecting site n and site $n+4$). **b** : Two-dimensional system, equivalent to the system a. It exhibits a 'screw' geometry. **c** : Synthetic dimension of a spin J, degeneracy being lift with magnetic field. Neighbouring spin states are coupled via J_+ and J_- operator. Next neighbouring ones are coupled via J_+^2 and J_-^2. **d** : Figure from [121]. The system depicted in **c** is equivalent to this cylinder, whose circumference is made of three sites labeled by $r \equiv m \pmod 3$.

3.1.2 The case of a spin system

To apply this idea to a spin, we rely on a combination of rank-1 and rank-2 spin operators (Fig. 3.1c). With well chosen relatives weights, we will see that it leads to an effective two-dimensional systems with a dimension m and a (cyclic) dimension r made of three sites (Fig. 3.1d). We will show that the dynamics between these two dimensions can be decoupled. By applying this combination of spin operators, we can engineer the following Hamiltonian on a spin J:

$$H = -U_a \frac{J_+}{J} - U_b \frac{J_-^2}{J(J-1/2)} + \text{h.c}, \tag{3.1}$$

where U_a and U_b are the hopping amplitudes associated with the two spin operators.

The two transitions involved in the Hamiltonian lead to the emergence of three-sites cycle : $m \to m+1 \to m+2 \to m$, as seen on Fig. 3.1c. Let's treat the magnetic projection m as a position, and consider $r \equiv m \pmod 3$, the reminder of the euclidian division of m by 3. The action of J_+ is to increase m by one unit and to increase r by one unit. The action of J_-^2 is to decrease m by 2 units and to increase r by one unit.

To give an intuition on the condition to have independents dynamics along m and r, we first do an approximate derivation. We consider m and r as continuous variables, and study the effect of the Hamiltonian on the wavefunction $\psi(m,r)$. For the first-order couplings, we have :

$$\begin{aligned} \frac{J_+ + J_-}{J}\psi(m,r) &\simeq \psi(m+1,r+1) + \psi(m-1,r-1) \\ &\simeq \left(2 + \partial_m^2 + 2\partial_m\partial_r + \partial_r^2\right)\psi(m,r), \end{aligned} \tag{3.2}$$

and for the second-order couplings :

$$\begin{aligned}\frac{J_+^2+J_-^2}{J(J-\frac{1}{2})}\psi(m,r) &\simeq \psi(m+2,r-1)+\psi(m-2,r+1)\\ &\simeq \Big(2+4\partial_m^2-4\partial_m\partial_r+\partial_r^2\Big)\psi(m,r).\end{aligned} \tag{3.3}$$

To get these expressions, we have used a Taylor expansion in m and r, keeping only the terms of first-order and second-order. Thereby, Eq. (3.1) can be approximated by :

$$H \simeq -2(U_a+U_b)-(U_a+4U_b)\partial_m^2-(U_a+U_b)\partial_r^2-2(U_a-2U_b)\partial_m\partial_r \tag{3.4}$$

The coupling between m and r comes only from the term $\propto \partial_m\partial_r$, that cancels out for $U_a = 2U_b$. Under this condition, this Hamiltonian describes the motion of a particle on a cylinder, of axial coordinate m and radial coordinate r.

In the following, we assume this condition to be fulfilled, and we define a single coupling amplitude $U \equiv U_a = 2U_b$

3.1.3 Semiclassical analysis

To understand more clearly the dynamics, we perform a semiclassical analysis, which is legitimate for $J \gg 1$.

Variational study

We first carry out a variational study, restricting ourselves to the family of the coherent spin states [122] $|\theta,\phi\rangle$. We calculate the average energy $E(\theta,\phi) \equiv \langle\theta,\phi|H|\theta,\phi\rangle$ in these coherent states. We find $E(\theta,\phi) = -2U\sin(\theta)\cos(\phi) - U\sin^2(\theta)\cos(2\phi)$. We plot Fig. 3.2 this energy landscape. We see that it exhibits three extrema : one minimum located at $(\theta=\pi/2,\phi=0)$ and two minima located at $(\theta=\pi/2,\phi=2\pi/3)$ and $(\theta=\pi/2,\phi=4\pi/3)$. In the following, we perform an Holstein-Primakoff transformation [123] around these maxima and minima to get a more precise description of the system.

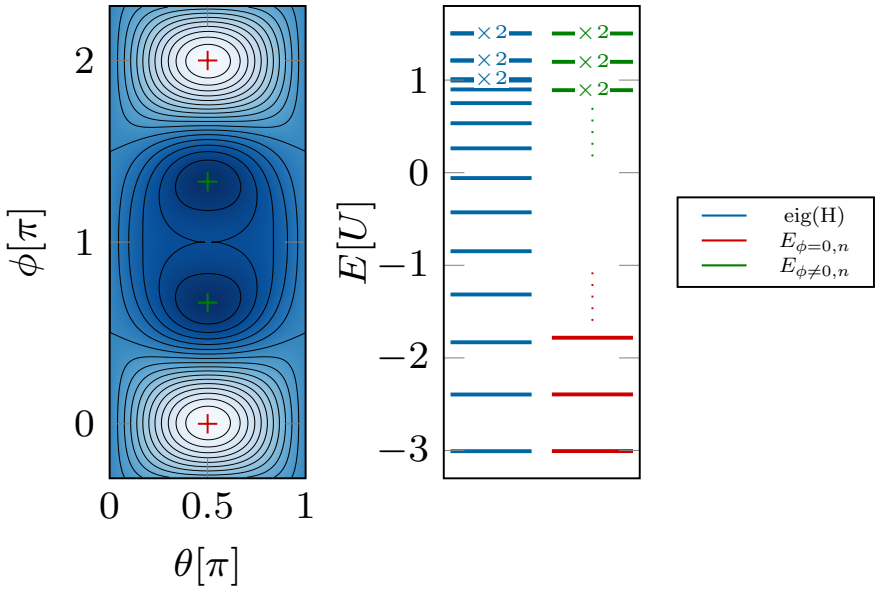

Figure 3.2: Semiclassical approximation. Left : Energy functional as a function of the coherent state angles (θ, ϕ). It exhibits one minimum depicted by the red cross at $(\phi = 0, \theta = \pi/2)$, and two maxima depicted by the green crosses at $(\phi = 2\pi/3, \theta = \pi/2)$ and $(\phi = 4\pi/3, \theta = \pi/2)$. Right : Energy spectrum of the Hamiltonian H (blue) and of the approximated Hamiltonian H_ϕ (red, green). At low energy, the spectrum of H matches the one of $H_{\phi=0}$. At high energy, it matches the ones of $H_{\phi=2\pi/3}$ and of $H_{\phi=4\pi/3}$.

Holstein-Primakoff transformation

By considering the spin J as en ensemble of $2J$ fictitious spins $1/2$ [76], we can perform a Holstein-Primakoff transformation to express the spin operators in term of bosonic creation operator $a^\dagger$ and annihilation operator a as :

$$\begin{aligned} J_x &= J - a^\dagger a, \\ J_z - iJ_y &= \sqrt{2J - a^\dagger a}\, a, \\ J_z + iJ_y &= a^\dagger \sqrt{2J - a^\dagger a}, \end{aligned} \tag{3.5}$$

Assuming J is large enough, we can develop these formula to first-order in $1/J$:

$$\begin{aligned} J_x &= J - a^\dagger a, \\ J_z &= \frac{J}{2}(a + a^\dagger), \\ J_y &= -i\frac{J}{2}(a^\dagger - a), \end{aligned} \tag{3.6}$$

Using these expressions, we can also develop the Hamiltonian in power series of $1/J$. The first-order coupling gives :

$$-U\frac{J_+ + J_-}{J} = -2 + 2\frac{a^\dagger a}{J}, \tag{3.7}$$

The second-order couplings yields :

$$-\frac{U}{2}\frac{J_+^2+J_-^2}{J(J-1/2)} \simeq -\frac{U}{2}\frac{1}{J(J-1/2)}\left[2(a^\dagger a)^2 + J(a^{\dagger 2}+a^2-6a^\dagger a) + 2J(J-1/2)\right] \tag{3.8}$$

In the end, keeping only the terms at first-order in $1/J$, we obtain :

$$H/U \simeq -3 + \frac{10a^\dagger a - a^2 - a^{\dagger 2}}{2J}. \tag{3.9}$$

This quadratic Hamiltonian can be diagonalised using a Bogoliubov transform, by introducing the new bosonic operators :

$$b = ua + va^\dagger \ ; \ b^\dagger = v^* a + u^* a^\dagger, \tag{3.10}$$

under the constraint $\sqrt{u^2+v^2}=1$. For the choice $u=\sqrt{1/2+5/(4\sqrt{6})}$ and $v=-\sqrt{u^2-1}$, the quadratic Hamiltonian can be rewritten :

$$H = E_0 + \hbar\omega b^\dagger b, \tag{3.11}$$

where

$$\begin{aligned} E_0 &= U\left(-3+\frac{2\sqrt{6}-5}{2J}\right), \\ \hbar\omega &= U\frac{2\sqrt{6}}{J}. \end{aligned} \tag{3.12}$$

At first-order in $1/J$, we have shown that, around the minimum of the energy functional, the initial Hamiltonian maps to the one of a harmonic oscillator.

The same calculation can be performed around the two energy maxima, $(\theta=\pi/2, \phi=2\pi/3)$ and $(\theta=\pi/2, \phi=4\pi/3)$. Around these maxima, the dynamics can also be approximated by a harmonic oscillator. Overall, we get the following three Hamiltonians describing the low and the high energy dynamics :

$$H_\phi = (E_0 + \hbar\omega b^\dagger b)\cos(\phi) \ ; \quad \phi \in \left\{0, \frac{2\pi}{3}, \frac{4\pi}{3}\right\}. \tag{3.13}$$

We show in Fig. 3.2 the spectrum of the initial Hamiltonian together with the eigenenergies of these three harmonic oscillators for $J=8$. We see a good agreement for the lower energy states and for the higher energy states.

3.1.4 Domain of validity of the semiclassical approach

We expect this semiclassical approach to be more and more valid as J increases. Moreover, as the spin size decreases, the dynamics starts to be affected the by finite size of the synthetic dimension, and will deviate from the harmonic oscillator. We checked numerically that the number of eigenstates well described by a harmonic oscillator increases with the spin size J, as expected for a semiclassical analysis.

This approach is valid for atoms with a big enough spin, as dysprosium $J=8$, Erbium $J=6$ or Thulium $F=4$. It could also be extended to molecules where spins of even larger sizes could be obtained [124]. In the following, if not stated, we assume that the spin size is $J=8$.

3.1.5 Interpretation as a cylinder geometry

The derivation made here relies on a semiclassical approach, and is relevant only to describe low and high energy states. However, treating on equal footing low and high energy states is unusual. This difficulty will be resolved in the following parts, where one of these synthetic dimensions will be coupled to a spatial degree of freedom, such that only the low energy physics will become relevant. Yet, for now, we still consider the effective spin dynamics restricted to the semiclassical spectrum derived previously.

Eq. (3.13) is reminiscent of the spectrum of a particle evolving on a one-dimensional ring lattice of length L and spacing a : $E(q) \propto -2t\cos(qa)$. The quasimomentum q takes the discrete values $2\pi j/L$, where $j \in \mathbb{Z}$. By analogy, in our model, the angle ϕ plays the role of a momenta, conjugated to the cyclic dimension of length $L = 3$. We can now perform an inverse Fourier transform to define, from these momenta q, the position states in this cylindrical picture :

$$|r, n\rangle = \frac{1}{\sqrt{3}} \sum_{\phi=0,2\pi/3,4\pi/3} \mathrm{e}^{-i\phi r} |\phi, n\rangle \tag{3.14}$$

At this stage, the physical meaning of these $|r, n\rangle$ state may not be obvious. To give more insights, we compute the overlap between such states and the Dicke state m : $\langle m|r, n\rangle$. To do so, we first note that the state $|\phi, n\rangle$ can be obtained by applying a spin rotation of angle ϕ around the z axis on the state $|\phi = 0, n\rangle$. Eq. (3.14) can thus be rewritten [78] as :

$$|r, n\rangle = \frac{1}{\sqrt{3}} \left[|\phi = 0, n\rangle + \mathrm{e}^{-i2\pi r/3}\mathrm{e}^{-i2\pi J_z/3} |\phi = 0, n\rangle + \mathrm{e}^{-i4\pi r/3}\mathrm{e}^{-i4\pi J_z/3} |\phi = 0, n\rangle \right] \tag{3.15}$$

Then, we can easily compute the overlap with $|m\rangle$:

$$\langle m |r, n\rangle = \frac{1}{\sqrt{3}} \left(\sum_{\phi} \mathrm{e}^{-i\phi(r-m)} \right) \langle m |\phi = 0, n\rangle \tag{3.16}$$

In this equation, the term in paranthesis vanishes if $r \neq m \pmod 3$ and is equal to 3 otherwise. We find back the intuition we had at the beginning : each r state only involves the m states equal to r modulo 3. We show in Fig. 3.3 the projection of $|r, n = 0\rangle$, $|r, n = 1\rangle$, $|r, n = 2\rangle$, for the three possible values of r, on the Dicke basis. The overall envelop is given by the eigenstates of the initial Hamiltonian, similar to the eigenstates of a harmonic oscillator. The $|r, n\rangle$ states only involve different classes of m states.

The Hamiltonian can be rewritten in term of these $|r, n\rangle$ states. We first diagonalise it in the $|\phi, n\rangle$ basis :

$$H_{\text{eff}} = \sum_{n\geq 0} \sum_{\phi=0,2\pi/3,4\pi/3} (E_0 + n\hbar\omega) \cos\phi \, |\phi, n\rangle \langle\phi, n| \tag{3.17}$$

Then, using the definitions of the $|r, n\rangle$ states and a bit of algebra, we obtain the following expression :

$$H_{\text{eff}} = \sum_{n\geq 0} \sum_{r=0,1,2} \left(\frac{E_0 + n\hbar\omega}{2} \right) |r + 1, n\rangle \langle r, n| + \text{h.c} \tag{3.18}$$

We recognise the Hamiltonian of a particle on a cylinder of cyclic dimension r, and with a harmonic potential along the axial coordinate m.

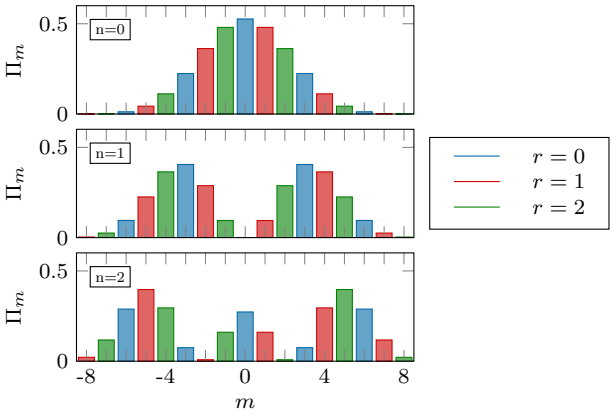

Figure 3.3: Projection of the r states in the Dicke basis. Top : Projection of the three $|r, n = 0\rangle$ states. Middle : Projection of the three $|r, n = 1\rangle$ states. Bottom : Projection of the three $|r, n = 2\rangle$ states. We recognise the ground state of a harmonic oscillator for $n = 0$ and the first two excited states for $n = 1$ and $n = 2$.

3.1.6 Extension to different geometries

In this section, relying on the intuition we had on the three-sites cycles, we demonstrated how the Hamiltonian under study can mimick the Hamiltonian of a particle on a cylinder, whose angular coordinate is made of three sites : $r = m \pmod 3$. We can ask ourself if we could treat this problem with another geometry, for example if the angular direction could have only 2 sites, or n sites with $n > 3$.

2 sites in the dimension r ?

We consider a spin J under the action of the same Hamiltonian and we suppose that the dimension r has only two sites and that it can be defined by $r = m \pmod 2$. In this case, the action of J_+ is still to increase m by one unit and to increase r by one unit. However, the action of J_-^2 is to decrease m by 2 units and to leave r invariant. We can proceed to the same calculation made at the beginning of the section, considering both m and r as continuous variables. The effect of the first-order couplings are

$$\begin{aligned} \frac{J_+ + J_-}{J}\psi(m,r) &\simeq \psi(m+1,r+1) + \psi(m-1,r-1) \\ &\simeq \left(2 + \partial_m^2 + 2\partial_m\partial_r + \partial_r^2\right)\psi(m,r), \end{aligned} \tag{3.19}$$

and the one of the second-order couplings are

$$\begin{aligned} \frac{J_+^2 + J_-^2}{J(J-\frac{1}{2})}\psi(m,r) &\simeq \psi(m+2,r) + \psi(m-2,r) \\ &\simeq \left(2+4\partial_m^2\right)\psi(m,r). \end{aligned} \tag{3.20}$$

There is no combination of U_a, U_b (with $U_a \neq 0$) that cancels out the $\partial_m\partial_r$ term. Thus, in this geometry, the two dimensions m and r can never be considered orthogonal.

More than 3 sites in the dimension r ?

We now consider a spin J under the action of the same Hamiltonian and we suppose that the dimension r exhibits N sites, with $N > 3$. Following the same derivation as the one

made in this section, this approach leads to a decoupled dynamics for $U_b/U_a = 1/2(N-2)$. Then, we can compute the energy functional $E(\theta, \phi)$, using this coupling ratio and assuming the state to be a coherent state. This leads to an energy functional that exhibits only 2 extrema (if $N \neq 3$). Thereby, we can't define easily a basis of 'momentum' states as we did for the case $N = 3$, and the picture of the cylinder with N sites no longer holds.

However, one way to increase the number of sites in the dimension r is to increase the spin operators order. It can be demonstrated that a combination of J_+ and J_-^N (and their Hermitian conjugates) leads to an effective geometry where the cyclic dimension exhibit $N+1$ sites [78]. The realisation of higher order spin operators, as J_-^3, is not straightforward and can't be realised using static light shifts. Indeed, the vectorial and tensorial polarisabilities only provide first-order and second-order spin operators. One way to engineer more sofisticated light-spin couplings is to consider non-static light shifts [125], albeit coming together with a micromotion.

We will illustrate this idea, considering a combination of J_+ and J_-^3 spin operators. The two transitions involved in this Hamiltonian lead to the emergence of four-sites cycles : $m \to m+1 \to m+2 \to m+3 \to m$. This time, we consider $r \equiv m \pmod 4$, the reminder of the euclidian division of m by 4. The action of J_-^3 is to increase r by one unit and to decrease m by three unit. The action of J_+ is unchanged. Similarly to what we did before, we perform a Taylor expansion, treating m and r as continuous variables. This leads to the approximate Hamiltonian :

$$H \simeq -2(U_a + U_b) - (U_a + 9U_b)\partial_m^2 - (U_a + U_b)\partial_r^2 - 2(U_a - 3U_b)\partial_m\partial_r. \tag{3.21}$$

By chosing $U \equiv U_a = 3U_b$, the two dimensions m and r can be decoupled. Again, we consider the family of coherent spin state $|\theta, \phi\rangle$ and perform a variational approach. We get the energy functional :

$$E(\theta, \phi) = -2U \sin(\theta)\cos(\phi) - \frac{U}{3}\sin^3(\theta)\cos(2\phi), \tag{3.22}$$

which exhibits four extrema at the angles : $\theta = \pi/2$ and $\phi = k\pi/2$ where $k = 0, ..., 3$. The exact same derivation that we performed in this section can be generalised to this case, leading to the emergence of a cylinder with four angular coordinates.

3.2 Excitations in the synthetic cylinder

In the following section, we illustrate this picture of two independent dimensions encoded in a large spin J by studying the excitations of the system, either along m or along r. We finally illustrate the deviation from the optimal case, by varying the system's parameters.

3.2.1 Definition of the excitations

Velocities in the synthetic dimension

Starting in an eigenstate of the Hamiltonian, we perform a weak perturbation by inducing a velocity either along the axis m or the axis r. We first define the velocities in the synthetic dimension. To do so, we make an analogy with the definition of velocities in spatial dimension. For instance, the velocity along the spatial coordinate x can be defined as :

$$v_x \equiv \frac{i}{\hbar}[H, x] \tag{3.23}$$

Similarly, by identifying the operator J_z to a position along the axis m, we define the velocity along m as :

$$\begin{aligned} v_m &\equiv \frac{i}{\hbar}\left[H, J_z\right] \\ &= U_a \frac{iJ_+}{J} + U_b \frac{-2iJ_-^2}{J(J-1/2)} + \text{h.c} \end{aligned} \tag{3.24}$$

The definition of the velocity along r is not straightforward. Indeed, the variable r being an angular variable, a definition of the position along r could be $\frac{3}{2\pi}\arg\langle\exp\left(2i\pi J_z/3\right)\rangle$. This operator not being Hermitian, the quantity $\frac{i}{\hbar}\left[H, \exp\left(2i\pi J_z/3\right)\right]$ is not Hermitian either, and can't be used to define the velocity along r through its commutator with H [126, 127]. As demonstrated in [121], the velocity along r can be recovered via :

$$v_r \equiv \frac{i}{\hbar}\frac{1}{\sqrt{3}}\left\{\exp\left(-i\frac{2\pi}{3}J_z\right), \left[H, \exp\left(2i\pi/3J_z\right)\right]\right\}. \tag{3.25}$$

A more intuitive derivation can be realised by replacing in the expression of the velocity along m the -2 prefactor in front of J_-^2 by $+1$. Indeed, under the effect of J_-^2, m decreases by 2 but r increases by 1. The prefactor in front of the term J_+ remains unchanged, since this operator acts the same way on both m and r. These two methods lead to the expression :

$$v_r = U_a \frac{iJ_+}{J} + U_b \frac{iJ_-^2}{J(J-1/2)} + \text{h.c} \tag{3.26}$$

Definition of the perturbations

Now that we have defined velocity operators along the synthetic dimensions, we introduce the perturbations. The following peturbation, creating a linear potential in m, acts only on the m dimension :

$$V_{\text{pert}}^{(m)} = V_m J_z. \tag{3.27}$$

Indeed, for high values of J, the three states $|\phi = 0, n = 0\rangle$, $|\phi = 2\pi/3, n = 0\rangle$, $|\phi = 4\pi/3, n = 0\rangle$ are sufficiently far apart in phase space for the first-order spin operators not to couple them. We recall that our system can be seen as a cylinder, with harmonic trapping along the axis m and cyclic dynamics along r. The action of this perturbation is similar to the one of a linear potential in a harmonic oscillator, which is to shift the equilibrium position. When turning on $V_{\text{pert}}^{(m)}$, the system switches its inital equilibrium position m_0. Once the perturbation is turned off, the system will undergo oscillations around m_0, i.e oscillations of mean magnetisation.

The perturbation along r is more complicated to implement, since it requires a coupling between the three $|\phi, n = 0\rangle$ states, i.e it requires high order spin operators. The following perturbation

$$V_{\text{pert}}^{(r)} = V_r \cos\left(\frac{2\pi}{3}J_z - \alpha t\right) \tag{3.28}$$

couples all the ϕ states since it involves high order spin operators. Moreover, this perturbation is diagonal in the m basis and is $3-$periodic. Its value only depends on r, and can be rewritten as :

$$V_{\text{pert}}^{(r)} = V_r \cos\left(\frac{2\pi}{3} r - \alpha t\right) \tag{3.29}$$

It corresponds to a perturbation moving in r at the velocity $3\alpha/(2\pi)$, leading to $\langle v_r \rangle \neq 0$.

3.2.2 Decoupling of m and r dynamics

We show in Fig. 3.4 the decoupling of the m and r dynamics after application of the two perturbations described above. We consider a spin $J = 8$ and a coupling ratio $U_b/U_a = 1/2$. We also assume that the initial state of the system is the ground state of the Hamiltonian ($|n = 0\rangle$). Note that we would find similar results by considering the system in the highest excited states.

As expected, following the perturbation along m, the mean value $\langle J_z \rangle$ undergoes oscillations, while the populations along r, Π_r, remain constant. This behavior is retrived on the velocities, where v_m undergoes oscillations that are out of phase with the ones of the mean magnetisation. This behavior is similar to the one of a particle in a harmonic trap, moved away from its equilibrium position.

The decoupling between m and r is also illustrated after a perturbation along r, where the evolution of the spin populations leads to a constant value of $\langle J_z \rangle$, but where the average 'position' along r drifts. On the velocities, we see that v_m remains equal to 0, while the velocity along r gets significantly away from 0 after the perturbation. As a sidenote, we emphasise that the velocity along r remains quasi-flat after the perturbation along r, consistent with the absence of any trapping along this direction.

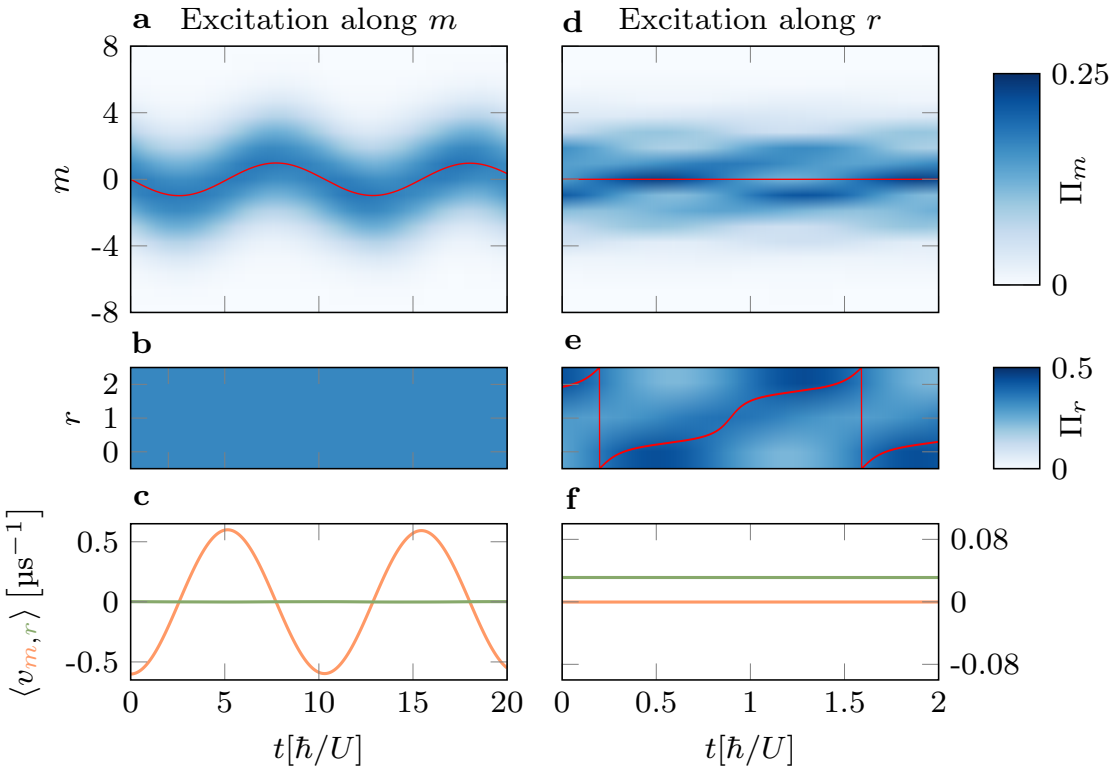

Figure 3.4: Decoupling of m and r dynamics. Left column : Excitation along m. Right column : Excitation along r. **a** : Populations along m. The red line shows the mean magnetisation, which undergoes oscillations. **b** : Populations along r. The three populations are equal and constant, confirming the fact that the system doesn't react along r. **c** : Velocities along the synthetic dimensions after the m excitation. $\langle v_m \rangle$ undergoes oscillations, $\langle v_r \rangle$ is equal to zero. **d** : Populations along m. The red line shows the mean magnetisation, which is constant and equal to 0. **e** : Populations along r. The red line shows the mean value $\langle r \rangle$, which drifts after the perturbation. We see the cyclic aspect of r. **f** : Velocities along the synthetic dimensions after the r excitation. $\langle v_m \rangle$ is equal to 0, contrary to $\langle v_r \rangle$ which exhibits a (constant) non-vanishing value.

3.2.3 Deviation from the ideal case

In the previous paragraph, we set the ratio between the two couplings to be equal to $U_b/U_a = 1/2$. We were considering the case of a spin $J = 8 \gg 1$ validating the semi-classical approximation. Finally, we supposed that the inital state was the ground state of the Hamiltonian. We study in this part the deviation from this 'optimal' situation.

Effect of J

The derivation we performed here relies on a semiclassical approximation, and on a first-order development of the Hamiltonian in $1/J$. We thus expect this model to be more and more valid as J increases. We show in the left column of Fig. 3.5 the velocity along m and r after a perturbation along m, starting in $|n = 0\rangle$. We see that, for $J = 4$, the velocity along r is not strictly zero and undergoes small oscillations (on the inset), that are much higher than the ones obtained with $J = 8$.

Effect of the initial state

We now perform the same perturbation along m, starting in different inital eigenstates of the Hamiltonian, that we labeled by n ($n \in \mathbb{N}$). As seen previously, at low energy, $n = 0$, the two dynamics are decoupled. When increasing n, the picture of synthetic cylinder no longer holds, and the two dynamics are no longer decouple : a perturbation along m induces a response along r (Fig. 3.5 middle column). When going to the highest excited states (Fig. 3.5 right column), $n = 2J$, the dynamics is again decoupled. This was expected since our picture of synthetic cylinder was obtained by doing a Holstein-Primakoff transformation around the energy minima and maxima of the Hamiltonian.

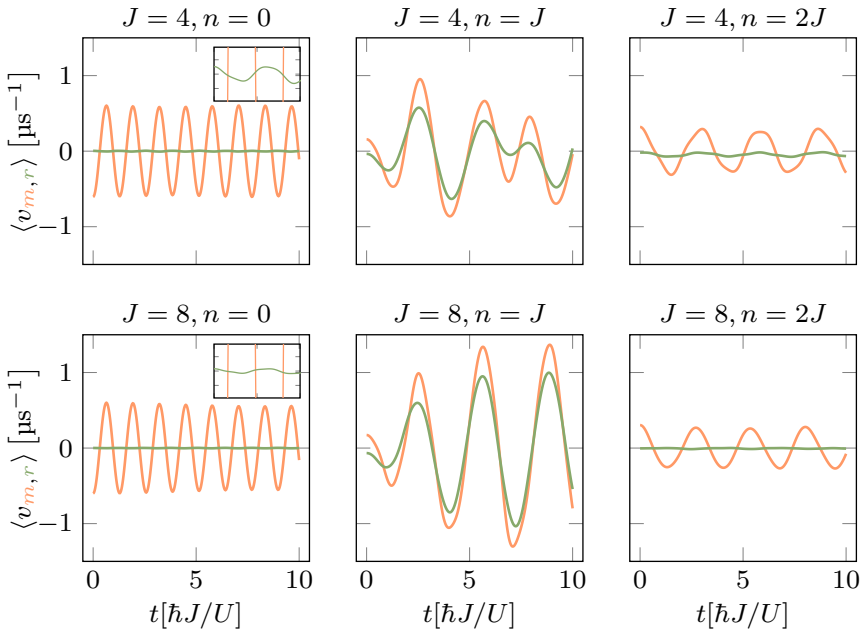

Figure 3.5: Effect of J and n on the decoupling of the dynamics, following an excitation along m. Top row : $J = 4$, increasing n from 0 to $2J$. Bottom row : $J = 8$, increasing n from 0 to $2J$. For the low energy state ($n = 0$) and for the high energy state ($n = 2J$) the dynamics are well decoupled. For the intermediate energy states ($n = J$), the dynamics are no longer decoupled. Insets are zoom made at the beginning of the time evolution, to see more clearly the decoupling between $\langle v_m \rangle$ and $\langle v_r \rangle$.

Effect of U_b/U_a

Finally, we study the effect of varying the coupling ratio U_b/U_a. We keep $J = 8, n = 0$ and U_a fixed, and vary U_b between 0 and U_a. We show in Fig. 3.6a the velocities after a perturbation along m for two different coupling ratios : $U_b/U_a = 1/2$ in solid lines and $U_b/U_a = 1/4$ in dashed lines. For the first case, v_r is equal to 0 and v_m undergoes oscillations. This illustrates the orthogonality of these two dimensions for the ideal ratio U_b/U_a. However, for the latter case, v_r also undergoes oscillation, illustrating the deviation from the decoupled case : in this situation, the two dimensions are no longer orthogonal, and the oscillations of v_r can be interpreted as the projection of the oscillations of v_m along the r axis. A similar behavior can be observed Fig. 3.6b, following an excitation along r. For $U_b/U_a = 1/2$, v_m is equal to 0, but for $U_b/U_a = 1/4$, v_m is not vanishing anymore.

We summarise these observations in Fig. 3.6c, where we plot the velocity ratios v_r/v_m (resp. v_m/v_r) following an excitation along m (resp. along r). In the case of an excitation

along m, we display the ratio of the oscillation amplitudes. In the case an excitation along r, we display the ratio of the mean values. In both cases, the dynamics are decoupled for $U_b/U_a \simeq 0.495$ very close to the 0.5 predicted at the beginning of this chapter. This optimal ratio gets closer and closer to 0.5 as J increases. These results validate our initial picture treating m and r as continuous variables. As soon as the couplings get away from this optimal ratio, the two variables m and r are no longer orthogonal.

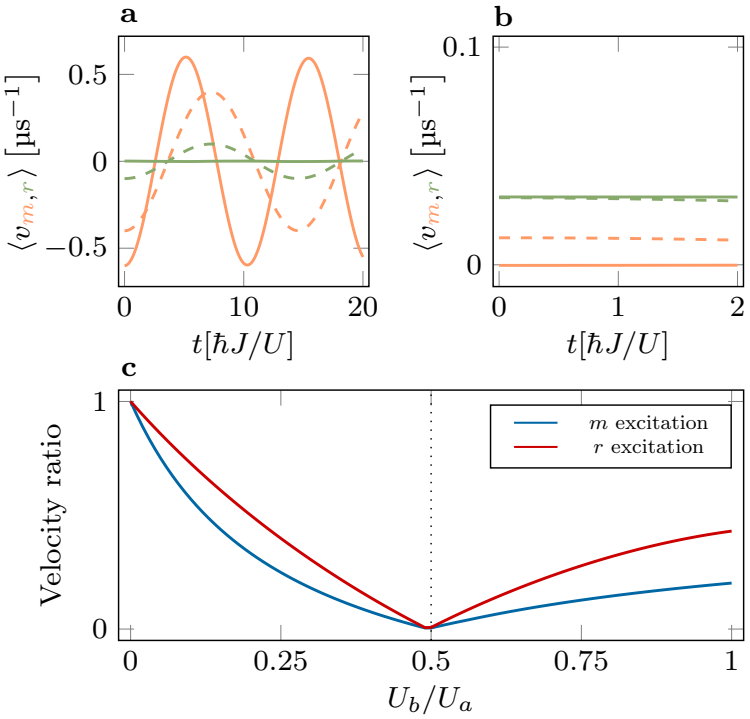

Figure 3.6: Effect of the ratio U_b/U_a on the decoupling of the dynamics. **a** : After an excitation along m. Dashed lines indicate a ratio $U_b/U_a = 1/4$, solid lines indicate a ratio $U_b/U_a = 1/2$. **b** : After an excitation along r. Dashed lines indicate a ratio $U_b/U_a = 1/4$, solid lines indicate a ratio $U_b/U_a = 1/2$. **c** : Decoupling of the two dimensions for different ratios U_b/U_a.

In this section, we studied the perturbations in the synthetic cylinder, validating the picture of two orthogonal dimensions m and r, with harmonic trapping along m and free dynamics along r. We have confirmed the fact that this picture is valid only for the minimum and maxima of the inital Hamiltonian. This way of treating the energy maxima and minima on equal footing is unusual. In the following section, we couple the synthetic cylinder to a spatial coordinate x, in order to create a quantum Hall cylinder in the x, r dimensions. The main difference will be that, in this case, the three ϕ states are involved only at low energy.

3.3 Coupling to a spatial degree of freedom

In order to couple the spin degree of freedom to a spatial degree of freedom, we introduce a space-dependent phase on the couplings J_+ and J_-^2 (and their Hermitian conjugate), similarly to what we presented in chapter II. We thus study the following Hamiltonian :

$$\begin{aligned} H &= \frac{p_x^2}{2M} + V, \\ V &= -\left[U_a \frac{J_+}{J} + U_b \frac{J_-^2}{J(J-1/2)}\right] \mathrm{e}^{-2ikx} + \mathrm{h.c}, \end{aligned} \tag{3.30}$$

where k is a wavector, p_x is the momentum along x of the particle under study and M its mass. We then follow the similar treatment we did in the previous section, performing a semiclassical analysis.

3.3.1 Semiclassical analysis

For each position x, we look for the energy minima of the potential V, assuming the system to be well described by a coherent spin state $|x, \theta, \phi\rangle$. We compute the semiclassical energy functional :

$$\begin{aligned} V_{\mathrm{cl}}(\theta, \phi, x) &\equiv \langle x, \theta, \phi | H | x, \theta, \phi \rangle \\ &= -2U \sin\theta \cos(\phi - 2kx) - U \sin^2\theta \cos(2\phi + 2kx), \end{aligned} \tag{3.31}$$

where we again assumed $U \equiv U_a = 2U_b$. This energy functional exhibits three minima, for the spin orientations $(\theta = \pi/2, \phi = 0)$, $(\theta = \pi/2, \phi = 2\pi/3)$, $(\theta = \pi/2, \phi = 4\pi/3)$. Performing an expansion around these minima, we find the following harmonic spectrum :

$$V_{\phi,n}(x) = (E_0 + n\hbar\omega) \cos(\phi - 2kx) \tag{3.32}$$

We compare Fig. 3.7a this spectrum with the space-dependent potential of Eq. (3.30). We find an excellent agreement for $n = 0$ and $n = 1$, and a slight deviation for $n = 2$. We note that this potential exhibits three minima along x, each of them corresponding to a different $|\theta = \pi/2, \phi\rangle$ state. Contrary to the purely synthetic case, the coupling to a spatial dimension permits to have the three ϕ states involved at low energy only.

Similarly to the previous derivation, the Hamiltonian Eq. (3.30) can be rewritten in term of an effective potential, by diagonalising it in the $|\phi, n\rangle$ basis and in the $|r, n\rangle$ basis :

$$\begin{aligned} H_{\mathrm{eff}} &= \frac{p_x^2}{2M} + \sum_{n\geq 0} \sum_{\phi} (E_0 + n\hbar\omega) \cos(\phi - 2kx) \, |\phi, n\rangle \langle \phi, n| \\ &= \frac{p_x^2}{2M} + \sum_{n\geq 0} \sum_{r} \left(\frac{E_0 + n\hbar\omega}{2}\right) \mathrm{e}^{-2ikx} \, |r+1, n\rangle \langle r, n| + \mathrm{h.c} \end{aligned} \tag{3.33}$$

We recognise the Hamiltonian of a particle evolving on a cylinder, with an axial coordinate x, and a cyclic dimension r. Similarly to our study of the previous chapter, the hopping between r and $r+1$ comes with a space-dependent phase $-2kx$, leading to an artificial gauge field in the xr plane. There is also a third degree of freedom along m with harmonic trapping.

We can validate this effective Hamiltonian by comparing its band structure to the one of the actual Hamiltonian. Both models are invariant upon a translation along x by $\lambda/6$ and a

rotation along z of angle $-2\pi/3$, where $\lambda = 2\pi/k$. These symmetries lead to the conservation of a quasimomentum q :

$$q \equiv \frac{Mv_x}{\hbar} + 2kJ_z \pmod{6k}, \tag{3.34}$$

defined over the Brillouin zone $-3k \leq q < 3k$. The Hamiltonian spectrum thus organises in Bloch bands indexed by q. We compare in Fig. 3.7b the band structure of the actual Hamiltonian and the effective one for different values of n. We see a good agreement at low energy, and a deviation for $n \geq 2$, similarly to the purely synthetic case. Note that the lowest energy bands are completely flat, reminiscent of Landau levels.

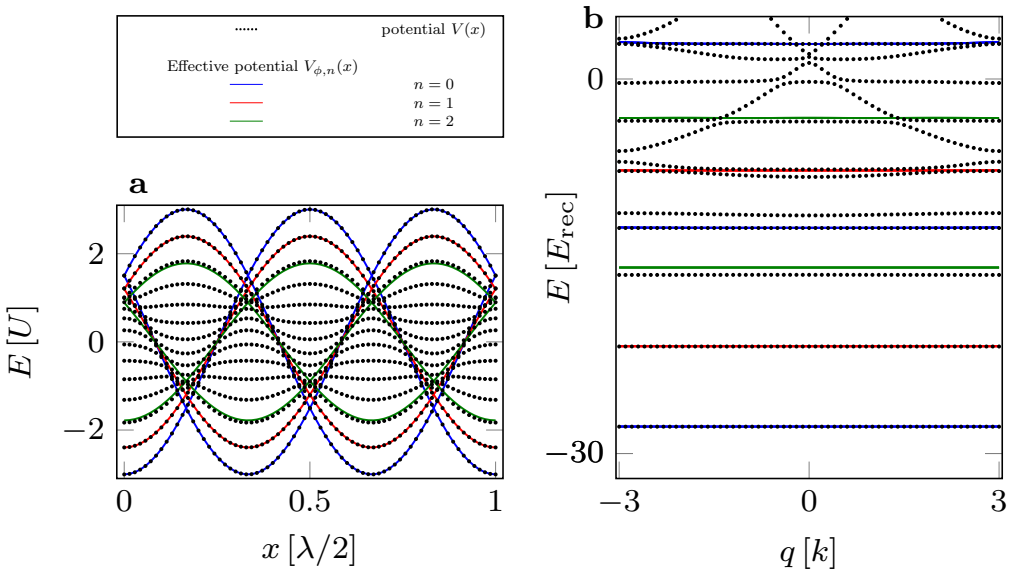

Figure 3.7: Comparison between the effective potential and the actual potential. **a** : Spatial dependene of the semiclassical potential and the actual potential. Blue, red and green lines correspond to the semiclassical potential with $n = 0$, $n = 1$, $n = 2$. Black dashed line correspond to the actual potential. **b** : Band structure computed with either the actual potential (black) or the effective ones (blue, red, green). In both cases, we see a good agreement for $n = 0$ and $n = 1$, and a slight departure for $n = 2$.

3.3.2 Deviation from the optimal ratio

We now study the effect of a departure from the optimal ratio $U_b/U_a = 1/2$. We show in Fig. 3.8 in blue, for each position x, the minimum of the semiclassical energy functional for different coupling ratios, keeping $\overline{U} = \sqrt{U_b U_a}$ constant. The ratio is varied between 0.1 and 3. The functional exhibits three minima, at the positions $x = -\lambda/6, 0, \lambda/6$. The position of these minima does not depend on U_b/U_a. We also indicate in red the minimum of the semiclassical energy functional for the extreme cases $U_b = 0$ and $U_a = 0$. In such cases, the minimum of the energy is space-independent. Indeed, the space component of the Hamiltonian e^{-2ikx} can be gauged away, and the Hamiltonian becomes invariant upon any spatial translation.

We show in Fig. 3.8a,b,c the angles (θ, ϕ) at which these minima are reached as a function of the coupling ratio. As expected, we recover the three states $(\theta = \pi/2, \phi = 4\pi/3)$, $(\theta = \pi/2, \phi = 0)$, $(\theta = \pi/2, \phi = 2\pi/3)$ whatever the coupling ratio. Contrary to the purely

synthetic case, the coupling to the spatial degree of freedom has made these three states to be involved only at low energy. It also means that these three states are relevant to describe the system even when the condition $U_b/U_a = 1/2$ is not satisfied. However, in such case, the picture with a harmonic confinement along m no longer holds and the two synthetic dimensions are not orthogonal anymore, as we will see later on.

We show in Fig. 3.8d the same quantities, for the position $x = \lambda/5$, which doesn't correspond to an energy minimum. In such case, the optimal angle θ remains unchanged, but the optimal angle ϕ acquires a dependence on the coupling ratio, highlighting the fact that the three states $(\theta = \pi/2, \phi = 4\pi/3)$, $(\theta = \pi/2, \phi = 0)$, $(\theta = \pi/2, \phi = 2\pi/3)$ are only relevant to describe the low energy physics.

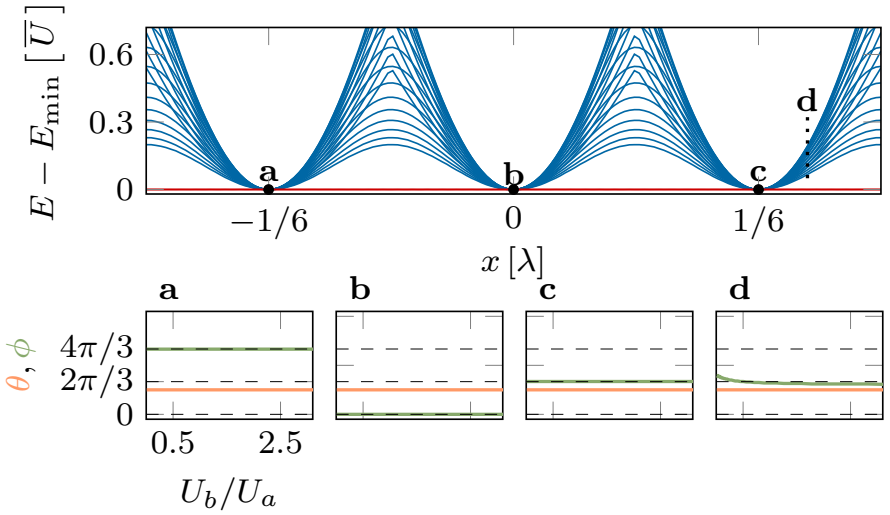

Figure 3.8: Departure from $U_b/U_a = 1/2$. Top panel : (in blue) Energy minimum of the semiclassical potential as a function of the position x for different coupling ratios. The extreme cases $U_b = 0$ and $U_a = 0$ are displayed in red, where the translational invariance leads to a constant energy. Bottom panel **a**, **b**, **c**, **d** : Angles θ and ϕ at which the energy minimum is reached, as a function of U_b/U_a.

In Fig. 3.9, we study the behavior of this system following an excitation along m, for $U_b/U_a = 1/2$ and $U_b/U_a = 1/4$, starting in the ground band of the Hamiltonian at $q = 0$. For the first ratio (left column), the system's velocity along r vanishes while $\langle v_m \rangle$ undergoes oscillations, confirming the orthogonality of m and r. The $\langle v_m \rangle$ oscillations are out of phase with the oscillations in average magnetisation. This illustrates the fact that the picture with the harmonic confinement along m still holds at low energy when coupling the synthetic cylinder to space. We also note that the average value of r remains quasi constant. On the other hand, for a ratio $U_b/U_a = 1/4$ (right column), both $\langle v_r \rangle$ and $\langle r \rangle$ are oscillating after an excitation along m. This shows that m and r are not orthogonal anymore. Moreover, we see some anharmomicity in the oscillations of $\langle v_m \rangle$, indicating that the picture with the harmonic confinement along m breaks down when getting away from $U_b/U_a = 1/2$ if the system is coupled to space.

To conclude, coupling the synthetic cylinder to a spatial coordinate x has made the three states $\phi = 0, 2\pi/3, 4\pi/3$ relevant to describe the physics at low energy. It can be contrasted with the purely synthetic case, where two of the ϕ states were involved at high energy only. These three states are relevant to describe the low energy physics whatever the value of the

coupling ratio U_b/U_a. For $U_b/U_a = 1/2$, the two dimensions m and r are orthogonal, and the system exhibits harmonic confinement along m. For $U_b/U_a \neq 1/2$, the two dimensions m and r are not orthogonal anymore and the confinement along m is no longer harmonic. Yet, the description of our system with two dimensions is still valid. In the next section, we will study an experimental realisation of such space-synthetic cylinder using dysprosium atoms.

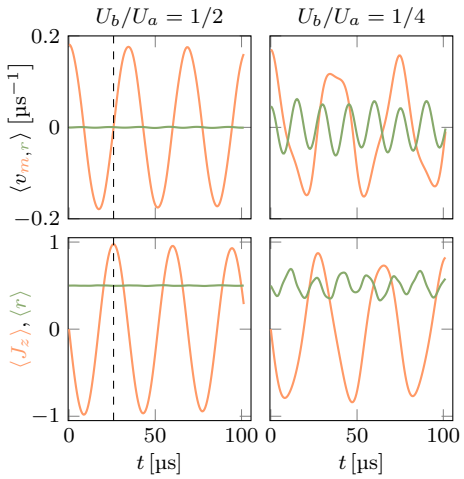

Figure 3.9: Excitation along m in the space-synthetic system, at $q = 0$. Left column : $U_b/U_a = 1/2$. We display the velocities along the synthetic dimension as well as the average values $\langle J_z \rangle$ and $\langle r \rangle$ following an excitation along m. Black dashed lines is a guideline highlighting the $\pi/2$-shift between $\langle J_z \rangle$ and $\langle v_m \rangle$. Right column : $U_b/U_a = 1/4$. The two synthetic dimensions are not orthogonal anymore.

3.4 Application : a synthetic quantum Hall cylinder

Emulating a system in a cylindrical geometry necessitates the capacity to engineer periodic boundary conditions. In one-dimensional system, this can be achieved through the use of quantum rings [128, 129]. In 2D, periodic boundary conditions can be created using carbon nanotubes [130–133]. Nevertheless, realising a quantum Hall system on a cylinder presents a substantially greater challenge, as it requires the capability to generate a radial magnetic field (for instance, via a magnetic field monopole [134]), or to implement a model with breaking of time-reversal symmetry, following Haldane's prescription [10]. Synthetic dimensions permit to circumvent this difficulty by enabling the generation of artificial magnetic fields. By emulating Eq. (3.30) with dysprosium atoms, we were able to realise a quantum Hall system on a cylinder, using the cyclic aspect of the dimension r. The motivation to realise a quantum Hall cylinder was to experimentally implement Laughlin's topological charge pump [120].

3.4.1 Motivation

The first explanation of the robustness of the quantum Hall effect was provided by R.Laughlin in 1981 [119], through a thought experiment. In the latter, Laughlin considered a hollow cylinder submitted to a radial magnetic field $\boldsymbol{B}$ (Fig. 3.10). Under this magnetic field, the single-particle wavefunctions of the electrons organise in Landau levels. Each wavefunction is given by an eigenstate of a harmonic oscilator, centered at a position x_0 depending on the wavevector k_r of the electron along the cyclic direction : $x_0 = \hbar k_r / M\omega_c$, where M is the electron mass and ω_c the cyclotron frequency. Laughlin then considered the insertion of a

varying magnetic flux ϕ through the cylinder. This magnetic flux leads to an electric field along the circumference of the cylinder $\boldsymbol{E} \propto \partial_t(\phi)\boldsymbol{e_r}$, Fig. 3.10, which modifies the electron wavectors k_r, hence shifting the wavefunction center positions x_0. Note that we labeled the angular coordinate by $\boldsymbol{e_r}$, to be consistent with our synthetic cylinder, whose circumference is made of the three r sites. When the flux inserted is equal to one unit of quantum flux $\Phi_0 = h/|e|$, all the electronic wavefunctions are shifted by one site (Fig. 3.10, right), resulting in the pumping of one electron from one edge to the other. We retrieve the quantised Hall conductance. This pumping is robust to the properties of the sample or to the presence of weak disorder, explaining the robustness of the quantisation of the quantum Hall effect. This idea was later generalised by Thouless in 1983 [135] to any system subjected to slow periodic perturbation, leading to the concept of Thouless pumping [136].

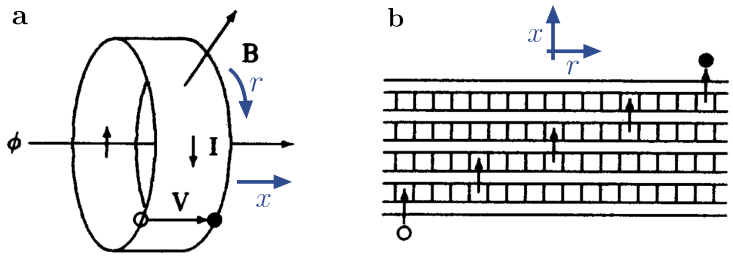

Figure 3.10: Laughlin's thought experiment, adapted from its Nobel prize lecture [137]. **a** : Scheme of the Hall cylinder of axial coordinate **x** and of cyclic coordinate **r**. A magnetic field $\boldsymbol{B}$ pierces the cylinder. A magnetic flux Φ flows through the cylinder. **b** : The one-particle wavefunctions of the electrons are shifted along x due to the flux Φ, resulting in the pumping of one electron from one edge to the other.

So far, the Laughlin pump experiment has remained only a thought experiment, due to the challenge to engineer periodic boundary conditions together with a radial magnetic field in condensed matter systems. Synthetic dimensions permits to lift this difficulty. Some groups have already realised quantum Hall cylinder in cold-atoms experiment [61–63] using the spin of the atoms as a synthetic dimension, but the lack of control on the longitudinal magnetic field $\boldsymbol{B}_{||}$ disabled them from realising Laughlin's topological charge pump.

In this section, we present our quantum Hall cylinder realised with dysprosium atoms. Our protocol permits us to have both a radial effective magnetic field $\boldsymbol{B}_{\perp}$ and a tunable longitudinal one $\boldsymbol{B}_{||}$. We can thus vary the phase $\Phi_{||}$ inserted through the cylinder, enabling us to implement Laughlin's thought experiment.

3.4.2 Experimental protocol

Our experimental protocol is close to the one presented section 3 and relies on a combination of first and second-order spin-orbit couplings. This yields to the emergence of an effective cyclic dimension r in the spin $J = 8$ manifold. Similarly to the experimental scheme presented in chapter II, we shine Raman lasers on an ultracold dysprosium cloud to couple the spin degree of freedom to the spatial degree of freedom. A first pair of lasers is resonant with the transitions $m \to m+1$ and $m \to m-1$, leading to the operators $\mathrm{e}^{-2ikx}J_+$ and $\mathrm{e}^{2ikx}J_-$. Additionally, a second Raman process is made resonant with the transitions $m \to m+2$ and $m \to m-2$. This is done by adding a second frequency detuned by $2\omega_z$ in one of the laser beam, leading to the operators $\mathrm{e}^{-2ikx}J_+^2$ and $\mathrm{e}^{2ikx}J_-^2$. The experimental scheme is summarised Fig. 3.11a.

In the end, the atoms dynamics is described by the Hamiltonian :

$$\begin{aligned} H &= \frac{1}{2}Mv_x^2 + V, \\ V &= -T\mathrm{e}^{-2ikx} + \mathrm{h.c}, \quad T = t_a\mathrm{e}^{i\varphi_a}\frac{J_+}{J} + t_b\mathrm{e}^{i\varphi_b}\frac{J_-^2}{J^2} \end{aligned} \tag{3.35}$$

Using a suitable spin rotation, the phase difference $\varphi_a - \varphi_b$ can be gauged away, such that we can consider only a single phase $\varphi \equiv \varphi_a = \varphi_b$. The potential V can be replaced by an effective potential V_{eff}, following the prescription of the section 3 :

$$V_{\text{eff}} = -t\sum_{r=0,1,2}\left[\mathrm{e}^{i(\varphi-2kx)}\left|r+1\right\rangle\left\langle r\right| + \mathrm{hc}\right], \tag{3.36}$$

where we introduced the total hopping amplitude $t = t_a + t_b$. The atoms is thus evolving on a cylinder, with axial coordinate x and cyclic coordinate r, the dimension m being just playing the role of an additional harmonic potential. Similarly to what we derived in the previous section, this model is invariant upon a translation along x of $\lambda/6$ and a spin rotation along z of angle $2\pi/3$, leading to the conservation of the quasimomentum q :

$$q \equiv \frac{Mv_x}{\hbar} + 2kJ_z \pmod{6k}, \tag{3.37}$$

defined on the Brillouin zone $-3k \leq q < 3k$.

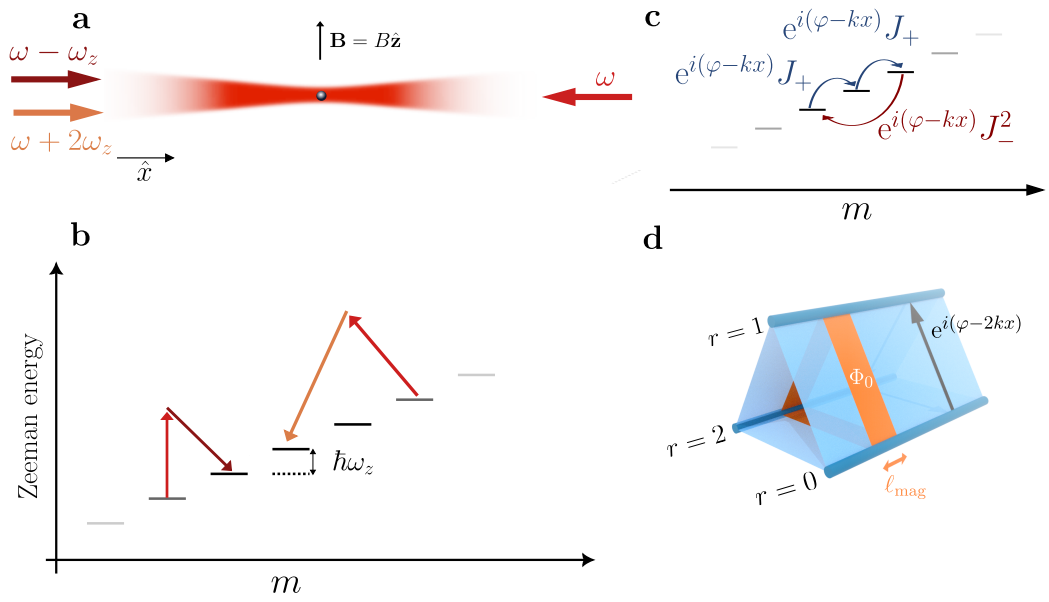

Figure 3.11: Experimental protocol. **a** : Laser configuration, leading to two resonant Raman processes. **b** : Scheme of the two Raman transitions within dysprosium's synthetic dimension. **c** : Appearence of three-sites cycles between different Zeeman sublevels. Only one cycle is depicted here. **d** : Scheme of the quantum Hall cylinder emerging at low energy. The hopping between two $|r\rangle$ states comes together with a phase $\varphi - 2kx$. The $2kx$ term leads to a radial artificial magnetic field, the phase φ to a longitudinal artificial magnetic field.

Effective magnetic fields

In the same way as for the quantum wires model studied previously, the complex phase $2kx$ is at the origin of an artificial magnetic field $B_\perp = 2\hbar k$ in the radial direction of this system (Fig. 3.11d) [120], assuming a particle of charge $q = -1$. This magnetic field defines a magnetic length ℓ_{mag}, such that the flux through the surface $S = R\ell_{\text{mag}}$ (where $R = 3$ is the radius of the cylinder) equals the unit quantum flux Φ_0. This magnetic field is at the origin of the quantum Hall physics in our system. On the other hand, the phase φ leads to an effective magnetic field $\boldsymbol{B}_{||}$ in the axial direction. By varying the phase φ, we can vary the magnetic flux $\Phi_{||}$ threaded through the cylinder, hence implementing Laughlin's topological charge pump.

3.4.3 Experimental results

In the next paragraph, we present experimental results obtained with our protocol. We present only a brief overview of our findings. A more in-depth discussion can be found in [78, 120].

Ground band properties

We present Fig. 3.12 the experimental ground band properties measured as a function of the quasimomentum q (Eq. (3.37)). As expected, the mean magnetisation is equal to zero, confirming the fact that the three coherent states pointing along $\theta = \pi/2$ are relevant to describe the low energy physics. By summing the population modulo 3, we can reconstruct the populations distribution in the three r states. The q-variation of this distribution reveals a chirality typical of quantum Hall effect. When increasing the quasimomentum by $2k$, the probability distribution cycles as $\Pi_r \to \Pi_{r+1}$. Moreover, we measure a vanishing mean velocity in the ground band along x (Fig. 3.12a), as expected for flat Landau levels.

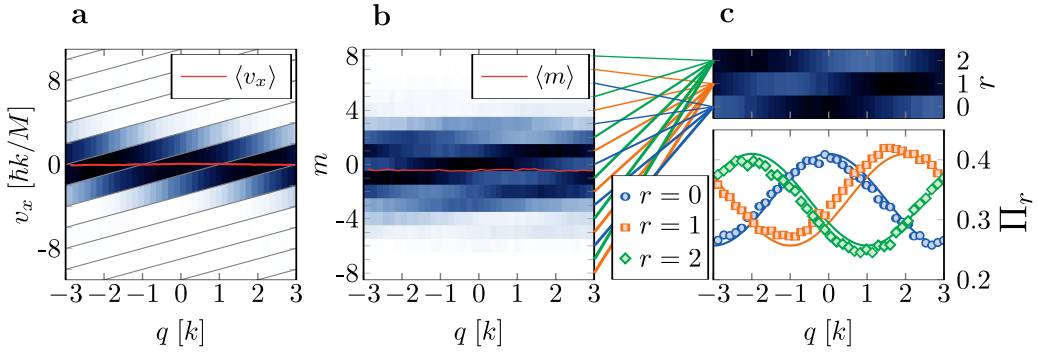

Figure 3.12: Experimental ground band properties. **a** : Velocity along x in the ground band. The average velocity is equal to zero, highlighting the flatness of the ground band. **b** : Populations along m in the ground band. The average magnetisation is vanishing on the full Brillouin zone. **c** : Summing the populations modulo 3 leads to the populations in the three r states. Blue, red and green points refer to, respectively, $r = 0$, $r = 1$, $r = 2$. Solid lines is the theory.

Laughlin's topological charge pump

The chiral drift occuring along r when performing a Bloch oscillation gave us a first hint on the topology of the system. To characterise it fully, we implement Laughlin's topological

charge pump. We prepare the system in a given ground state q and vary the phase φ of the lasers, i.e we vary the magnetic flux $\Phi_{||}$ threaded through the cylinder. We then measure the induced displacement Δx of the atomic cloud. This displacement directly gives us the Berry curvature $F(q)$ of the ground band for this momentum q through $\Delta x = F(q)\varphi$. Experimental results are displayed Fig. 3.13b. The Berry curvature is, within error bars, equal to the theoretical prediction $F(q) = 1/(2k)$. By computing the q-averaged displacement Δx over the Brillouin zone, we can access the Chern number C of the ground band and verifiy Laughlin's prediction via :

$$\frac{\langle \Delta x \rangle}{\ell_{\text{mag}}} = C\frac{\Phi_{||}}{\Phi_0}, \quad C = 1.00(4) \tag{3.38}$$

The measured value of the Chern number is in agreement with the expected quantisation of transport $C = 1$ for a quantum Hall system on a cylinder.

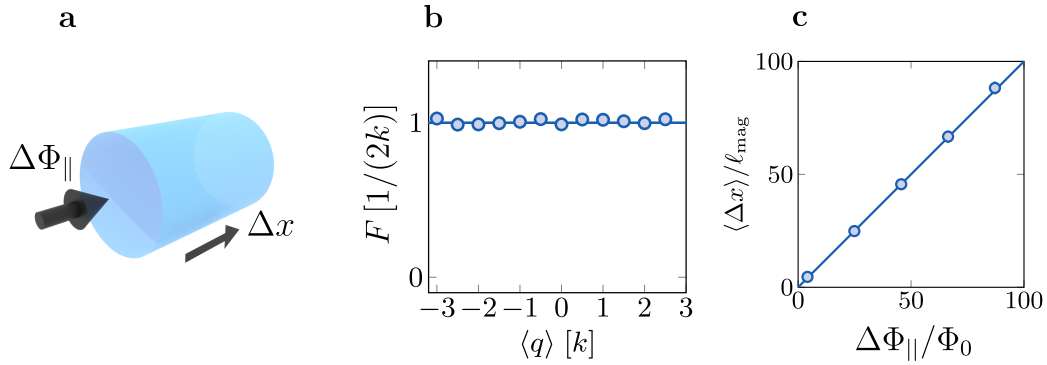

Figure 3.13: Experimental realisation of Laughlin's topological charge pump. **a** : Scheme of the protocol. We insert a flux $\Delta\Phi_{||}$ through the cylinder and measure the induced displacement Δx. **b** : Berry curvature of the ground band inferred from the displacement Δx. **c** : q-averaged displacement over the Brillouin zone. For each unit flux inserted, the system is displaced by one magnetic length, as envisioned by Laughlin in his thought experiment.

3.5 Conclusion

In this chapter, we have seen that we can emulate 2D physics within a large spin J, through a proper combination of first and second-order spin couplings. Moreover, we have seen that one of these dimensions exhibits periodic boundary conditions.

Later on, we have extended this protocol by coupling the synthetic dimensions to space via Raman processes. This led to the appearence of artificial magnetic field in a space-synthetic cylinder, coming together with the emergence of a quantum Hall effect. This was permited by the use of synthetic dimensions, which make possible the generation of an artificial radial magnetic field.

Finally, we have presented experimental results obtained with dysprosium atoms. We were able to emulate a quantum Hall cylinder and to vary the magnetic field flux threaded through this cylinder, implementing Laughlin topological charge pump.

In the latter protocol, one of the two synthetic dimensions was playing no role. In the next chapter, we exploit fully the two dimensions m and r to emulate a 4D quantum Hall systems using dysprosium atoms, two dimensions being synthetic and two being spatial ones.

4 The quantum Hall effect in four dimensions : elements of theory

The study of topological system has started with the discovery of the 2D integer quantum Hall effect [1, 4]. Originally, topological effects were predicted to arise mainly in lower dimensions, but it was discovered that new topological phases can emerge in 3D and 4D [17, 23, 138, 139]. These higher-dimensional topological systems bring new physical phenomena that the community wishes to explore. In particular, the generalisation of the 2D integer quantum Hall effect to 4D exposes a new transport equation, quantised by a novel topological invariant : the second Chern number. Besides being captivating for their topological characteristics, 4D quantum Hall systems are also examined by theoretical researchers, in order to understand the origin of large magnetic field in the early universe [140] or to study quantum gravity [23].

In this chapter, we first present a brief historical review of the study of topological systems, leading to their arrangement in the 'tenfold classification' [19–21]. As we point out, many topological systems remain to be explored, especially in higher dimensions. We then present few properties of 4D quantum Hall systems, that only appear for dimensions higher than 3, namely the non-linear electromagnetic response and the anisotropic chiral edge modes. Following this study, we do a state-of-the-art review about 4D quantum Hall systems. First hints of non-trivial topological in 4D were observed [41, 42, 59]. However, several phenomena inherently related to 4D remain to be detected. Finally, we present our approach to realise for the first time a genuine 4D quantum Hall system in the topological class A. We derive the properties of our model and exhibit its non-trivial topology.

The model presented in the last part of this chapter was experimentally realised and published in [141].

4.1 From 2D topological systems to higher-dimensional topological systems.

4.1.1 Brief historical review of topological insulators and superconductors

The two previous sections focused on experimental realisations of 2D integer quantum Hall systems. Such systems were the first known to exhibit topological states and lead to the developement of the TKKN theory [4]. As the quantum Hall effect is not directly generalisable to 3D [142, 143], topological states were initially limited to low-dimensional systems submitted to a large magnetic field.[1]

In 1988 Haldane, introduced the first modification to this paradigm, suggesting a new model [10] that exhibits quantum Hall effet without the presence of a net magnetic field. In its paper, Haldane showed that the key ingredient to recover such physics is the breaking of time-reversal symmetry. He considered a spinless fermionic system on a honeycomb lattice, with real nearest neighbour hopping terms and complex next-nearest neighbour hopping terms. The latter are responsible for the time-reversal symmetry-breaking, replacing the magnetic field in the integer quantum Hall effect.

A second breakthrough occured in 2005, when Kane and Mele [11, 12] demonstrated that a topological order can arise in a spin fermionic system with time-reversal symmetry. They proved that spin-orbit coupling (a coupling preserving time-reversal symmetry) can lead to the emergence of topological states. These states are known as the quantum spin Hall states, and were soon after realised in 2007 in HgTe quantum wells [14], following a proposal by Bernevig [13]. Such systems are at the origin of the term 'topological insulator'. More particularly, they are the first $\mathbb{Z}_2-$ topological insulators discovered, meaning that their topology is not defined by a Chern number belonging to $\mathbb{Z}$, but by a topological invariant belonging to $\mathbb{Z}_2$. Interestingly, contrary to the integer quantum Hall effect, the quantum spin Hall effect can be directly generalised from $d = 2$ to $d = 3$ [17, 138, 139], and even extended to higher dimensions. In parallel, Zhang and Qi [23] generalised the quantum Hall effect to a four-dimensional system with time-reversal symmetry.

All these studies led to the discovery of new topological phases of matter, even in systems of dimension greater than 2. Around the years 2008-2010, an effort towards a topological

[1] Actually, 3D quantum Hall effect was recently measured in $ZrTe_5$, but its topology, involving three first Chern numbers in three orthogonal planes, is essentially two-dimensional [144].

classification was realised [19–21] to categorise all these new states of matter, from topological insulators to topological superconductors. We introduce this classification in the following.

4.1.2 Topological classification

The topological classification relies on the classification of random matrices, initiated by Zirnbauer and Altland [145, 146], that can be mapped to fermionic non-interacting Hamiltonians without gap closing. It consists in sorting topological systems as a function of the symmetries of their Hamiltonian. A topological insulator or topological superconductor can be characterised by three fundamental symmetries : the time-reversal symmetry Θ, the particle-hole symmetry Ξ and the chiral symmetry Π, and thus assigned to a given topological class. There are in total ten symmetry classes.

The 10 symmetry classes

The time-reversal symmetry operator is an anti-unitary operator Θ. Its square can take two values : $\Theta^2 = +1$ or $\Theta^2 = -1$. If this operator commutes with the Hamiltonian of the system, the latter preserves the time-reversal symmetry. In such case, there are two possible scenarios : either $\Theta^2 = +1$, either $\Theta^2 = -1$. To simplify the notation, we usually write $\Theta = +1$ or $\Theta = -1$. If the time-reversal symmetry operator doesn't commute with the Hamiltonian, the latter doesn't obey time-reversal symmetry and we write $\Theta = 0$. In total, there are three possible values for Θ.

Similarly, for the particle-hole symmetry, there are three possible values for Ξ. The combinations of these two symmetries lead to a total of 9 symmetry classes. Additionally, one should consider the chiral symmetry Π, which is given by the product of the time-reversal and the particle-hole symmetry. It can be demonstrated that for 8 of the 9 possible combinations of Θ and Ξ, the value of Π is uniquely determined. Only the case $(\Theta = 0, \Xi = 0)$ is ambiguious, and can lead either to $\Pi = 0$ or $\Pi = 1$. At the end of the day, the one-particle fermionic Hamiltonians can be categorised in 10 different symmetry classes, leading to the so-called tenfold classification.

The tenfold classification

The tenfold classification proposes to arrange all the topological states, from topological insulators to topological superconductors, using these 10 symmetries combinations. Given the system dimensionality d and its symmetries, the classification provides the topological invariant, highlighting the difference between topologically trivial states ($\nu = 0$) and topologically non-trivial states ($\nu \in \mathbb{Z}$, $\nu \in 2\mathbb{Z}$, $\nu \in \mathbb{Z}_2$).

We show in Fig. 4.1 the topological classification. The first column, sometimes labeled 'AZ', refers to the symmetry class name. The right columns provide the value of the topological invariant for each symmetry class, as a function of the dimension d. We highlight on the figure few well-known observed topological states. The celebrated 2D quantum Hall effect belongs to the symmetry class A (breaking of time-reversal symmetry) in $d = 2$. As seen on the classification, the topological invariant ν is indeed non trivial, $\nu \in Z$. We highlight it in blue. The quantum spin Hall states belong to the symmetry class AII, they are highlighted in red (only for dimension $d \leq 3$). Finally, the famous one-dimensional SSH model [147] belongs to the symmetry class BDI, with a topological invariant $\nu \in \mathbb{Z}$; we highlight it in green. In all the classes, the topological invariant either belong to $\mathbb{Z}_2$ either to $\mathbb{Z}$ or $2\mathbb{Z}$, depending on the dimensionality. This is a consequence of the dimensional hierarchy which

is a general feature of the topological classification [20] that goes beyond the scope of this thesis.

Symmetry				d							
AZ	Θ	Ξ	Π	1	2	3	4	5	6	7	8
A	0	0	0	0	$\mathbb{Z}$	0	$\mathbb{Z}$	0	$\mathbb{Z}$	0	$\mathbb{Z}$
AIII	0	0	1	$\mathbb{Z}$	0	$\mathbb{Z}$	0	$\mathbb{Z}$	0	$\mathbb{Z}$	0
AI	1	0	0	0	0	0	$2\mathbb{Z}$	0	$\mathbb{Z}_2$	$\mathbb{Z}_2$	$\mathbb{Z}$
BDI	1	1	1	$\mathbb{Z}$	0	0	0	$2\mathbb{Z}$	0	$\mathbb{Z}_2$	$\mathbb{Z}_2$
D	0	1	0	$\mathbb{Z}_2$	$\mathbb{Z}$	0	0	0	$2\mathbb{Z}$	0	$\mathbb{Z}_2$
DIII	-1	1	1	$\mathbb{Z}_2$	$\mathbb{Z}_2$	$\mathbb{Z}$	0	0	0	$2\mathbb{Z}$	0
AII	-1	0	0	0	$\mathbb{Z}_2$	$\mathbb{Z}_2$	$\mathbb{Z}$	0	0	0	$2\mathbb{Z}$
CII	-1	-1	1	$2\mathbb{Z}$	0	$\mathbb{Z}_2$	$\mathbb{Z}_2$	$\mathbb{Z}$	0	0	0
C	0	-1	0	0	$2\mathbb{Z}$	0	$\mathbb{Z}_2$	$\mathbb{Z}_2$	$\mathbb{Z}$	0	0
CI	1	-1	1	0	0	$2\mathbb{Z}$	0	$\mathbb{Z}_2$	$\mathbb{Z}_2$	$\mathbb{Z}$	0

Figure 4.1: Topological classification, adapted from [20]. We highlight a few famous topological systems. In blue, the celebrated 2D quantum Hall effect in a time-reversal symmetry breaking system. In green, the famous 1D SSH model. In red, we highlight the quantum spin Hall systems, in dimensions 2 and 3.

Exploring higher-dimensional systems

Similarly to the case of the periodic table of the elements when it was invented, all the entries of the topological classification have not been observed yet. This is in particular the case for higher dimensional ($d > 3$) systems that are by nature more complicated to probe. The work presented in this chapter and the next one consists in the first realisation of a class A topological state in $d = 4$, i.e a generalisation of the 2D quantum Hall effect to four dimensions. We acknowledge a recent realisation of a class AI $d = 4$ topological system realised with electronic circuits [42].

More importantly than filling an entry in the topological classification, exploring a new topological class in higher dimension gives access to a rich and exotic physics, otherwise not present in $d \leq 3$. We highlight in the next section three phenomena specific to the 4D quantum Hall effect : the non-linear electromagnetic response, the peculiar nature of edge modes in 4D and the cyclotron trajectories.

4.2 What does the fourth dimension bring?

In this section, we describe three new phenomena arising in the 4D quantum Hall effect, namely the cyclotron orbits in 4D, the peculiar transport properties through the non-linear electromagnetic response, and the edge modes in 4D. Beforehand, we will describe how the magnetic field should be represented in 4D.

4.2.1 Magnetic field in four dimensions

In 2D and in 3D, the magnetic field if generaly described by a vector, or more precisely by a pseudo-vector. We first stress that the 'usual' definition

$$\boldsymbol{B}(\boldsymbol{r}) = \boldsymbol{\nabla} \times \boldsymbol{A}(\boldsymbol{r}), \tag{4.1}$$

where $\boldsymbol{A}$ is the vector potential and $\boldsymbol{r}$ the positional vector, is not usable in dimensions $d > 3$ since the vectorial product doesn't exist in all higher dimensions, and particularly in

$d = 4$ [148]. A safer definition that can be generalised to any dimensions relies on Einstein's notation, where the $\mu\nu$ component of the magnetic field, can be expressed as :

$$B_{\mu\nu} = \partial_\mu A_\nu - \partial_\nu A_\mu. \tag{4.2}$$

In 3D, labelling the spatial coordinates x, y, z, this equation exhibits three non-zero components : B_{xy}, B_{xz}, B_{yz}, so that the magnetic field can be represented by a vector. In 4D, labelling the spatial coordinates x, y, z, w, this equation leads to six non-zero components : $B_{xy}, B_{xz}, B_{xw}, B_{yz}, B_{yw}, B_{zw}$, and thus can't be represented by a vector anymore. Instead, the magnetic field is depicted by a rank-2 antisymmetric tensor :

$$B = \begin{bmatrix} B_{xx} & B_{xy} & B_{xz} & B_{xw} \\ B_{yx} & B_{yy} & B_{yz} & B_{yw} \\ B_{zx} & B_{zy} & B_{zz} & B_{zw} \\ B_{wx} & B_{wy} & B_{wz} & B_{ww} \end{bmatrix} = \begin{bmatrix} 0 & B_{xy} & B_{xz} & B_{xw} \\ -B_{xy} & 0 & B_{yz} & B_{yw} \\ -B_{xz} & -B_{yz} & 0 & B_{zw} \\ -B_{xw} & -B_{yw} & -B_{zw} & 0 \end{bmatrix}, \tag{4.3}$$

where the antisymmetry, given by Eq. (4.2), forces the diagonal coefficients to vanish. This new description of magnetic field comes together with peculiar classical cyclotron orbits in 4D, that can be explained by the properties of rotations in higher dimensions.

4.2.2 Rotations and classical cyclotron orbits in 4D

Rotations in 4D

In 2D, a rotation occurs in a plane and is defined by one angle θ and one point which is left invariant under the rotation (see Fig. 4.2a). It is described by a 2×2 matrix :

$$R = \begin{bmatrix} \cos\theta & -\sin\theta \\ \sin\theta & \cos\theta \end{bmatrix} \tag{4.4}$$

The 3D case is similar, where a rotation occurs in a plane and is defined by one angle and one axis, which is left invariant under the rotation (see Fig. 4.2b). It is described by a 3×3 matrix :

$$R = \begin{bmatrix} 1 & 0 & 0 \\ 0 & \cos\theta & -\sin\theta \\ 0 & \sin\theta & \cos\theta \end{bmatrix} \tag{4.5}$$

The 4D case is richer. Indeed, let's consider a rotation occuring in the plane xy, of rotation angle α. The plane zw is left invariant by this rotation. This type of rotation is called 'simple rotation' and can be understood as a usual 2D-rotation occuring in a 4D-space. However, we can directly see that more complex rotations can occur, that would only leave one point invariant rather than one plane invariant. These 'double' rotations are defined by two rotation angles and can be seen as two independent rotations, each of them leaving one plane invariant and being define by one angle. The two planes under considerations are orthogonal. For instance, the rotation made of the combination of a rotation of angle α leaving zw invariant and a rotation of angle β leaving xy invariant is a double rotation (see Fig. 4.2c).

In its more general case, rotations in 4D can be described by a 4×4 matrix, that can be written (in the good basis) as :

$$R = \begin{bmatrix} \cos\alpha & -\sin\alpha & 0 & 0 \\ \sin\alpha & \cos\alpha & 0 & 0 \\ 0 & 0 & \cos\beta & -\sin\beta \\ 0 & 0 & \sin\beta & \cos\beta \end{bmatrix}, \tag{4.6}$$

where α and β are the two angles of the rotation. If $\alpha = \beta$, the rotation is called an 'isoclinic' rotation. We have introduced the rotations in 2D, 3D and 4D. We now make the link with the cyclotron orbits.

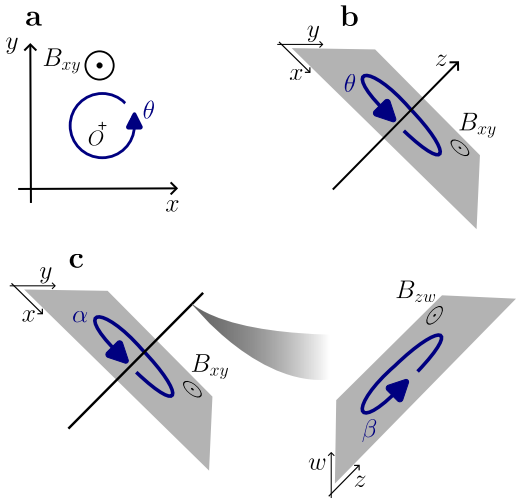

Figure 4.2: Rotations in 2D, 3D and 4D. **a** : Rotation in a 2D space, defined by one angle of rotation and leaving one point invariant. **b** : Rotation in a 3D space, defined by one angle of rotation and leaving one axis invariant. **c** : Rotation in a 4D space. The rotation is composed by a pair of '2D' rotations, each of them being defined by their own angle α and β.

Classical cyclotron orbits

In 2D and 3D, the cyclotron trajectory of a charge q within a magnetic field is planar and can be described by an angle $\theta(t) = \omega_c t$ where ω_c is the Larmor frequency. The position of the particle at time t, $\boldsymbol{r}(t)$, is given by a rotation of angle $\theta(t)$ applied on the initial particle position vector $\boldsymbol{r}(0)$, such that :

$$\boldsymbol{r}(t) = R[\theta(t)]\boldsymbol{r}(0), \tag{4.7}$$

where $R[\theta(t)]$ is the rotation matrix of angle $\theta(t)$ around the axis made by the magnetic field.

This description still holds in 4D, albeit with the possibility of having double rotations. The fact that a rotation in 4D involves two angles means that the magnetic field must be described by two Larmor frequencies, contrary to the lower dimensional cases. The properties of the cyclotron trajectories will directly depend on the ratio between these two Larmor frequencies ω_1 and ω_2. In the following, we define these Larmor frquencies such that $\omega_2 \geq \omega_1$. We also introduce the corresponding periods $T_i = 2\pi/\omega_i$. There are three possible scenarios :

Case 1 : $\omega_2 = \omega_1$

This is the simplest case. This ratio of Larmor frequency leads to circular and closed orbits, reminiscent of the 2D cyclotron orbits. See Fig. 4.3 where we plot the cyclotron trajectory up to four different final times $T_{\max}$. At $T_{\max} = T_1$, the system is back to its initial position. For $T_{\max} > T_1$, the system follows its initial trajectory.

Case 2 : $\omega_2/\omega_1 \in \mathbb{Q}$

If the ratio between the Larmor frequencies is given by a rational number, the cyclotron trajectories are non-planar, but are closed. We illustrate it on Fig. 4.4 where we choose a ratio $\omega_2/\omega_1 = 2$. After a time $T_{\max} = T_1$, the charge is back at its initial position. However, the trajectory is not planar anymore. Similarly to the previous case, for $T_{\max} > T_1$, the system follows its initial trajectory.

Case 2 : $\omega_2/\omega_1 \in \mathbb{R} - \mathbb{Q}$

If the ratio between the Larmor frequencies is an irrational number, the cyclotron trajectory is non-planar and open. We illustrate it on Fig. 4.5, where we use $\omega_2/\omega_1 = \left(1+\sqrt{5}\right)/2$, which is the golden number. After multiple periods T_1, the system doesn't go back to its inital position.

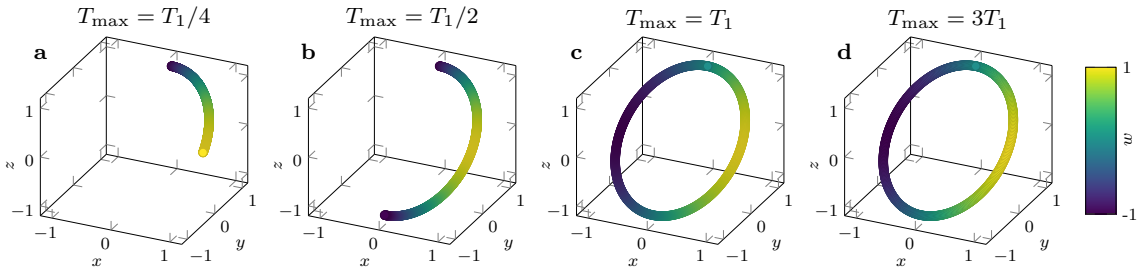

Figure 4.3: Cyclotron trajectories in 4D for $\omega_2/\omega_1 = 1$. We stop the trajectories at four final times from left to right. The fourth spatial dimension is encoded in the color. The trajectory is planar and closed.

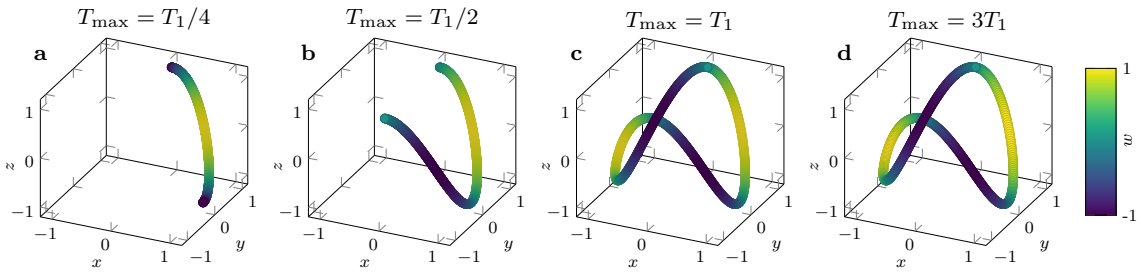

Figure 4.4: Cyclotron trajectories for $\omega_2/\omega_1 = 2$. We stop the trajectories at four final times from left to right. The fourth spatial dimension is encoded in the color. The trajectory is non-planar and closed.

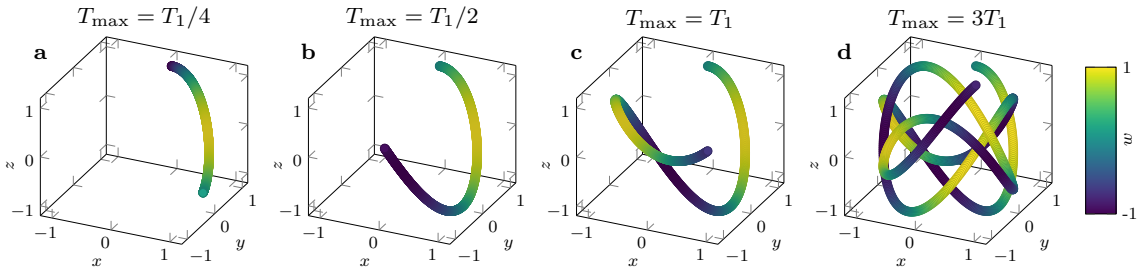

Figure 4.5: Cyclotron trajectories for $\omega_2/\omega_1 = \dfrac{1+\sqrt{5}}{2}$. We stop the trajectories at four final times from left to right. The fourth spatial dimension is encoded in the color. The trajectory is non-planar and open.

4.2.3 Transport properties

In this section, we show that the transport equations are peculiar in 4D. This derivation is greatly inspired from [60] and from [107, 149, 150]. We will not detail the calculations, but rather expose the different key points.

We consider a particle of charge $q = -1$ moving in a four-dimensional space, upon the action of a strong magnetic field leading to a quantum Hall effect. Addtionnaly, the particle is submitted to a space-dependent potential exhibiting translation symmetry (it could mimick electrons in a crystalline potential, or atoms in an optical lattice) such that Bloch formalism is relevant to describe the particle's dynamics. We consider initially an eigenstate $|u_n\rangle$ of the Bloch band n. We study the effect of a weak electromagnetic perturbation, made of an electric field $\boldsymbol{E} = E_\mu e^\mu$ and a magnetic field $B^{\mu\nu} = \partial_\mu A_\nu - \partial_\nu A_\mu$. Our goal is to compute the current density induced by these small electromagnetic fields. We assume that these perturbations are uniform and time-independent. We propose here to follow a semi-classical approach, in which we focus on a wavepacket of center of masse $\boldsymbol{r}$ and momentum $\boldsymbol{k}$.

Assuming that the spatial variation of the potential vector $\boldsymbol{A}(\boldsymbol{r})$ occurs on lengthscale greater than the wavepacket extension, the Hamiltonian of the system can be written, up to second-order in the perturbations, as :

$$H \simeq H_0 + H' + H'', \tag{4.8}$$

where H_0 is the Hamiltonian governing the wavepacket evolution without perturbation and the two other terms are the first and second-order corrections in the perturbations. We will then perform a semiclassical approximation to compute the current density.

The usual semiclassical approximation in 2D relies on the hypothesis that the system follows adiabatically the eigenstate $|u_n\rangle$ upon the application of the perturbations. In 4D, in order to capture fully the specificity of the fourth dimension, one should considers a first-order correction to this assumption. As a consequence, we consider the state $|\tilde{u}_n\rangle$ defined as :

$$|\tilde{u}_n\rangle = |u_n\rangle + |u'_n\rangle\,, \tag{4.9}$$

where $|u'_n\rangle$ takes into account for the band-mixing induced by the perturbations. The state $|\tilde{u}_n\rangle$ can be interpreted as an eigenstate of the perturbed magnetic Bloch band n. Using this

formalism, we suppose that the system adiabatically follows the perturbed magnetic Bloch band n and we drop the index n in the following.

Similarly, the Berry connection $\boldsymbol{\mathcal{A}}$ has to be corrected to first order by $\boldsymbol{\mathcal{A}'}$. $\boldsymbol{\mathcal{A}}$ contains the effect of the strong magnetic field (at the origin of the quantum Hall effect), $\boldsymbol{\mathcal{A}'}$ contains the first order correction in the perturbating fields. They are defined by :

$$\begin{aligned} \mathcal{A}_{k_\mu} &= i\langle u|\partial_{k_\mu}|u\rangle + \text{c.c} \\ \mathcal{A}'_{k_\mu} &= i\langle u|\partial_{k_\mu}|u'\rangle + \text{c.c} \end{aligned} \tag{4.10}$$

Consequently, one has also to consider the correction to the Berry curvature. We define the Berry curvature of the perturbed Bloch band $\tilde{F}^{\mu\nu}$ by :

$$\begin{aligned} \tilde{F}^{\mu\nu} &= F^{\mu\nu} + F'^{\mu\nu} \\ F'^{\mu\nu} &= \partial_{k_\mu}\mathcal{A}'_{k_\nu} + \partial_{k_\nu}\mathcal{A}'_{k_\mu}, \end{aligned} \tag{4.11}$$

where $F^{\mu\nu}$ is the Berry curvature of the unperturbed band, and $F'^{\mu\nu}$ describes its first-order correction. This modified Berry curvature can be used to recover the semiclassical equations of motion :

$$\dot{r}^\mu(\boldsymbol{k}) = \frac{\partial\tilde{E}(\boldsymbol{k})}{\partial k_\mu} - \dot{k}_\nu\tilde{F}^{\mu\nu}(\boldsymbol{k}), \tag{4.12}$$

$$\dot{k}_\mu = -E_\mu - \dot{r}^\nu B_{\mu\nu}, \tag{4.13}$$

where we have introduced the correction to the band energy $\tilde{E}(\boldsymbol{k})$ to second order in the perturbating fields. In order to compute the mean group velocity of the wavepacket, one can plug Eq. (4.13) into Eq. (4.12), keeping only terms of order 2 or less in the perturbations.

Finally, the current density j^μ is obtained by summing the group velocity of each occupied states $\boldsymbol{k}$, and by dividing by the system size V :

$$j^\mu = \frac{1}{V}\sum_k \dot{r}^\mu(\boldsymbol{k}). \tag{4.14}$$

This equation is not easy to express in a compact way. We can substitute the discrete summation by an integral, using the phase space density of states. One needs to be careful to the system dimensionality when performing this operation. Indeed, as shown in [149], the 4D phase space density should be replaced by its corrected version, in second-order to the perturbations.

Performing this substitution, one obtains a heavy expression for the current probability that we don't display here but that can be found in [60]. The mentioned expression can be greatly simplified, mainly using the antisymmetric properties of the magnetic field and the Berry curvature tensors, and assuming a filled band. Under these hypothesis, the current density can be expressed as :

$$j^\mu = \frac{E_\nu}{(2\pi)^4}\int_{\text{BZ}} F^{\mu\nu}d\boldsymbol{k} + \frac{\nu_2}{(2\pi)^2}\epsilon^{\mu\nu\gamma\delta}E_\nu B_{\delta\gamma}, \tag{4.15}$$

where we have introduced the second Chern number of the considered band ν_2, that can be obtained by a non linear combination of the Berry curvature components :

$$\nu_2 = \frac{1}{4\pi^2}\int_{\text{BZ}}\left[F^{\mu\nu}F^{\gamma\delta} + F^{\delta\mu}F^{\gamma\mu} + F^{\gamma\mu}F^{\nu\delta}\right]d\boldsymbol{k}. \tag{4.16}$$

This number is the topological invariant of the system, and is thus robust to any smooth perturbation or to a relatively weak disorder. It can take only integer values.

The transport equation Eq. (4.15) is the main result of this section. It contains two terms. The first one is similar to the 2D quantum Hall effect, resulting in a transverse response proportional to the electric field, albeit without quantisation in 4D. The second term is more interesting, and vanishes in dimension smaller than 4. This term is proportional to both the electric and the magnetic perturbations and is referred to as the 'non-linear electromagnetic response'. It is quantised by the second Chern number ν_2. We illustrate it in Fig. 4.6. In short, the magnetic perturbation B_{yw} lead to the emergence of a 2D quantum Hall effect in the plane xz. Hence, together with B_{yw}, the perturbative electric field E_z gives rise to a current j^x.

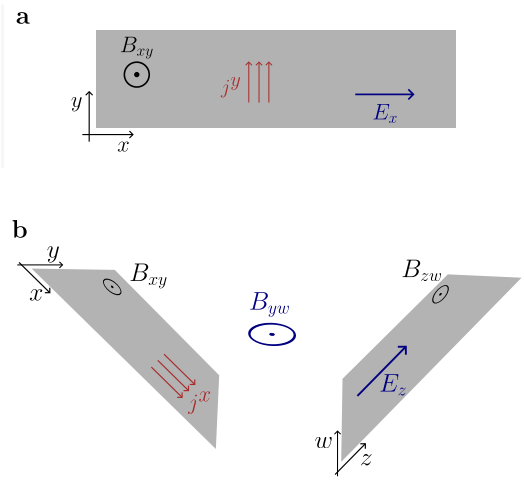

Figure 4.6: Quantum Hall effect in 2D and 4D. **a** : Linear response in a 2D quantum Hall system. The strong magnetic field B_{xy} leads to a 2D quantum Hall effect in the xy plane. The electric perturbation E_x leads to a quantised current j^y in the transverse direction. **b** : Non-linear response in a 4D quantum Hall system. The strong magnetic field components B_{xy} and B_{zw} give rise to a 4D quantum Hall effect. The electromagnetic perturbations B_{yw} and E_z generate a quantised current j^x in the fourth direction.

As as sidenote, we stress that Eq. (4.15) doesn't invoke the corrected Berry curvature nor the corrected band energy. This is a consequence of the band filling assumption. However, the consideration of the first-order correction to the Berry connection and to the Berry curvature, as well as the second-order correction to the eigenenergy are necessary to fully grasp the anomalous Hall drift occuring in 4D for a partially filled band.

4.2.4 Anisotropic edge modes

The non-linear response quantised by the second Chern number occurs in the bulk of the system. If we consider boundaries, the system is expected to exhibit edge modes at these boundaries, via the bulk-boundary correspondence [21], similarly to the chiral edge modes occuring in 2D quantum Hall effect. However, their behaviors is quite different in low and high-dimensional systems.

In 2D, the boundary of the system is one-dimensional. The edges modes are chiral and are constrained to propagate in 1D, by construction. In 4D, the boundary is three-dimensional. However, it was shown that the edge modes doesn't propagate on this 3D hyperedge, but are still propagating through one-dimensional channels [151–153], thus not exploring the full boundary. They are anisotropic. Moreover, this foliation is extremely sensitive to the trapping potential, and can lead to very different behaviors, from integrable trajectories to chaotic ones [151].

4.3 State-of-the-art review

In this section, we briefly review experimental realisations of 4D quantum Hall systems. We start by describing a few proposals, and then study some realisations based on topological charge pumping, or implementation of a genuine 4D system.

4.3.1 Proposals

As seen previously, the study of high-dimensional topological systems is quite motivating, particularly because it allows the discovery of new physical phenomena. To push forward research in this direction, many proposals have been submitted to experimentally realise four-dimensional systems.

Emulating a genuine 4D system

Emulating a four-dimensional system is not straightforward, spatial dimensions being limited to three. Several ideas permit to circumvent this difficulty. The first one relies on connectivity and was studied in the previous chapter. More particularly, in [154], the author proposes the realisation of a four-dimensional quantum Hall system on a lattice using only real hopping operators, thus not breaking time-reversal symmetry. This proposal was soon after realised using electric circuits [42]. The idea of connectivity could also be used in photonics system to emulate higher-dimensional systems [115, 116].

Another strategy to emulate a four-dimensional system is to use, on top of the three spatial dimensions, a synthetic dimension. Again, proposals have been made to extensively describe realistic experiments. In, [60] the authors propose to use ultracold atoms on a 3D lattice, the fourth dimension being provided by the internal states of the atoms and adressed with Raman transitions. Similarly, this idea can be extended to photonics, where [155] proposes to use a 3D array of ring resonators, the fourth dimension being encoded in the modes of each resonator.

Mapping to a 2D topological charge pump

An alternative approach to emulate higher-dimensional systems relies on the correspondence between a topological charge pump and a higher dimensional system [156]. Soon after Laughin's thought experiment, Thouless [135] proposed another approach to realise topological charge pumping, not requiring periodic boundary conditions, thus easier to realise experimentally. We quickly describe below how a Thouless topological charge pump can be mapped onto a higher-dimensional system, inspired by [157].

In its celebrated paper [135], Thouless considered a 1D spinless fermionic system upon a perodic potential. It could for instance be a particle in a 1D-optical superlattice[1] [157]:

$$V_{\mathrm{SL}}(x,\varphi) = V_1 \cos^2\left(\frac{2\pi x}{a}\right) + V_2 \cos^2\left(\frac{\pi x}{a} + \varphi\right), \tag{4.17}$$

where x is the spatial coordinate, a is the smaller lattice spacing and φ corresponds to the dephasing between the two sublattices. He then showed that if one parameter of the potential is adiabatically changed, returning to its initial value after a time T, the induced current integrated over T is quantised by the Chern number. In the case of our superlattice, it corresponds for instance to ramping the phase φ from 0 to 2π. Going to momentum

[1] Superlattices are obtained by superimposing lattices with different periodicities.

space, the Hamiltonian of the particle can be replaced by a Bloch Hamiltonian verifying the following invariances :

$$\begin{aligned} H(k_x, \varphi) &= H(k_x + 2\pi/a, \varphi) \\ H(k_x, \varphi) &= H(k_x, \varphi + 2\pi), \end{aligned} \tag{4.18}$$

where k_x is the wavector along x. We can hence define a Brillouin zone $-\pi \leq \varphi < \pi$, $-\pi/a \leq k_x < \pi/a$, on which the Berry curvature can be computed. The Hamiltonian being fully gapped in the Brillouin zone, we can obtain the ground band Chern number by integrating the Berry curvature over the Brillouin zone, leading to a Chern number equal to 1. As shown by Thouless, the first Chern number quantises the charge transport through the 1D system, similarly to the quantised transport in a 2D quantum Hall system. He also demonstrated that, in both cases, the transport is topologially protected against disorder or impurities. This idea is called 'dimensional extension' and has been implemented several times experimentally in 1D topological charge pumps [158–162].

In parallel to these realisations, [156] proposed to implement a 2D-topological charge pump. Following the same prescription, a 2D topological charge pump could be mapped onto a four-dimensional system through dimensional extensions, the two pumps parameters being interpreted as two additional momenta. Even though the proposal only realises a dynamical version of a 4D quantum Hall effect, it predicts the ability to measure a charge transport quantised by a second Chern number, something only possible in 4D. Subsequent to these proposals, a few experiments have probed some aspects of 4D physics. We quickly describe their findings in the next section.

4.3.2 Experimental realisations of 4D quantum Hall system

A 2D topological charge pump in an optical superlattice

In [59], the authors implemented a 2D topological charge pump using ultracold atoms in an optical superlattice, hence realising a dynamical version of the 4D quantum Hall effect. Their system, Fig. 4.7a, can be mapped to a pair of 2D quantum Hall systems in a cylinder geometry via dimensional extension. Their experimental set-up provided them the ability to probe the non-linear electromagnetic response (detailed in the previous section) occuring in 4D, and the ability to measure the second Chern number. The measured value is in agreement within error bars with $\nu_2 = 1$.

A 2D topological charge pump in photonic waveguides

At the same time, Zilberberg et al [41] presented a 2D topological charge pump made with photonics waveguides, realising also a dynamical version of a 4D topological system (see Fig. 4.7b). They tracked the propagation of light in their sample induced by the scan of the pump parameters. Their main result consists in the observation of peculiar surface states, that implies the existence of a non-trivial second Chern number in the bulk of their system. This experiment, together with the experiment presented above [59], provides the first evidence (and the measurement) of a non-trivial second Chern number.

A 4D topological insulator using electronic circuits

In [42], following the prescription of [154], the authors realised a 4D topological lattice using appropriate connections between electronic constituents. This way, they realised for the first

time a genuine 4D-topological system with time-reversal symmetry, thus belonging to the class AI. Interestingly, this class is topologically trivial in dimension $d \leq 3$ (see Fig. 4.1). However, going to 4D leads to a non-trivial topology, coming together with a non-vanishing topological invariant : $\nu_2 \in \mathbb{Z}_2$. In their experiment, they could switch from a topologically trivial phase to a topologically non-trivial phase by adjusting a parameter. The non-trivial topology manifests itself by the appearence of 3D edge modes. In Fig. 4.7c, we display the local density of states they measured in the non-trivial phase. We see the existence of a bulk (made of 16 sites), where the local density of states is low, and edges (made of the remaining 128 sites), where the local density of states is way higher. Moreover, the authors emphasise that these edge modes are robust to disorder as expected for a topological system, since each electronic components had a $\simeq 10\%$ deviation in their inductance or conductance. We also point out that these edge modes are not anisotropic. They are related to Weyl points, that host 3D topological surface states. These edge modes thus have a completely different nature than the ones expected for the generalisation of the 2D quantum Hall effect to 4D, which belongs to the topological class A.

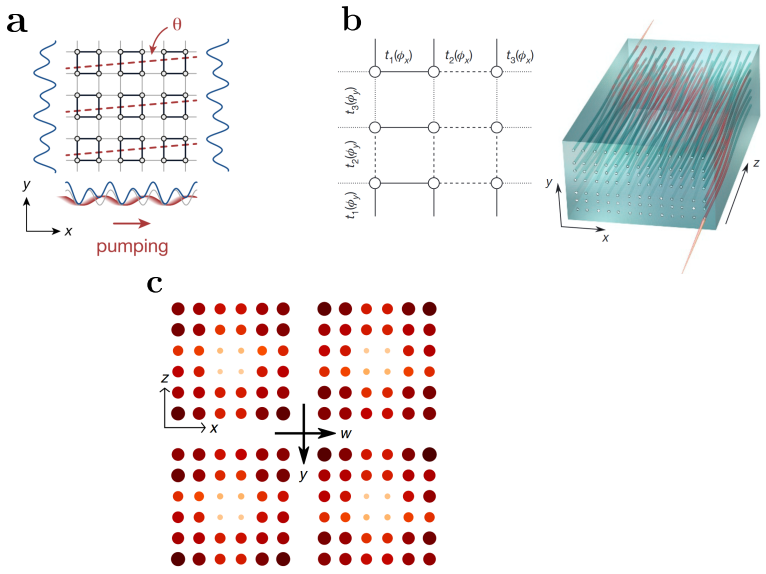

Figure 4.7: Experimental measurements of 4D quanutm Hall physics. **a** : Reference from [59]. A 2D topological charge pump is implemented on a optical superlattice, realising a dynamical version of the 4D quantum Hall effect. **b** : Reference from [41]. An array of photonics wires is used to implement a 2D topological charge pump, leading to a dynamical version of the 4D quantum Hall effect. **c** : Reference from [42]. A genuine 4D Hamiltonian is implemented on a a lattice made of electrical components. We display here the measured local density of states.

The observation of these 3D edge modes is the main result of the paper, and is a direct consequence of the non-trivial topology occuring in 4D. Their experimental set-up is the first topological insulator observed in class AI, and the first system where the non-trivial topology comes hand in hand with the higher dimensionality. However, no direct evidence of transport quantisation has been reported.

These important realisations are the first steps towards the experimental exploration of higher-dimensional systems. However, some 4D phenomeons still need to be probed. In the following section, we present our model that led to the realisation of a genuine synthetic

4D quantum Hall system in class A, using dysprosium atoms. To our knowledge, it is the first observation of this topological class in 4D. It is also the first measurements of cyclotron orbits in 4D, the first measurement of the second Chern number for a genuine 4D system and the first measurements of the anisotropic edge modes.

4.4 Synthetic quantum Hall effect in four dimensions : elements of theory

In this section, we describe our model to realise a quantum Hall system in four dimensions. We will mainly focus on the theory, our experimental results will be presented in the next chapter.

4.4.1 Description of the model

Implementation with dysprosium atoms

The realisation of a 4D quantum Hall system relies on the same ingredients presented in the two previous chapters. Counterpropagating Raman lasers are used to couple dysprosium's spin degree of freedom to its momentum. The four dimensions of our system are made of two spatial dimensions, labeled x, z and two synthetic dimensions m, r, where m is the projection of the spin along the quantisation axis and $r \equiv m \pmod 3$ is the reminder of the euclidian division of m by 3, as introduced in previously. In order to make the r dimension relevant, we again combine two types of spin operators J_+ and J_-^2, leading to an effective two-dimensional system within dysprosium's spin. The two spatial dimensions x, z are infinite[1] but the synthetic dimension m exhibits edges at $m = -J$ and $m = +J$. Finally, the dimension r provides only three sites, albeit coming together with periodic boundary conditions, so no edge effects are expected along this direction.

A magnetic field $\boldsymbol{B} = B\hat{\boldsymbol{z}}$ lifts the degeneracy within the synthetic dimension of dysprosium. A first pair of Raman lasers propagating along $\hat{\boldsymbol{x}}$ is shined on dysprosium atoms. Their polarisation is linear and set to $\theta = \arccos\left(1/\sqrt{3}\right)$. They are respectively detuned by $\Delta + \omega_z$ and by Δ with respect to the 626 nm transition, such that the process $m \to m + 1$ (and its Hermitian conjugate) is resonant, while $\Delta \simeq -2\pi \times 7\,\mathrm{GHz}$ is big enough to limite incoherent scattering. This Raman transition comes together with a net momentum kick $-2k\hat{\boldsymbol{x}}$ (resp. $+2k\hat{\boldsymbol{x}}$). We label this process (x).

Similarly, a second pair of Raman lasers propagating along $\hat{\boldsymbol{z}}$ is sent on the atoms. These beams are respectively polarised σ_+ and σ_-. They are detuned by $\Delta' - 2\omega_z$ and by Δ', such that the process $m \to m - 2$ (and its Hermitian conjugate) is resonant. Again, this Raman transition comes together with a net momentum kick $-2k\hat{\boldsymbol{z}}$ (resp. $+2k\hat{\boldsymbol{z}}$). We label this process (z).

The detunings Δ' and Δ differ by several Larmor frequencies $\simeq 50\omega_z$, such that there is no interference between the two pairs of Raman lasers. We summarise the experimental scheme in Fig. 4.8. As for the previous chapter, k refers to the wavector associated to a photon of wavelength $\lambda = 626\,\mathrm{nm}$. The recoil momentum p_{rec} and recoil energy E_{rec} are defined with respect to this wavector.

[1] Effectively, they are limited by the extent of the laser beam. The latter can be assumed big enough compared to the system dynamics such that edge effects along x, z can be neglected.

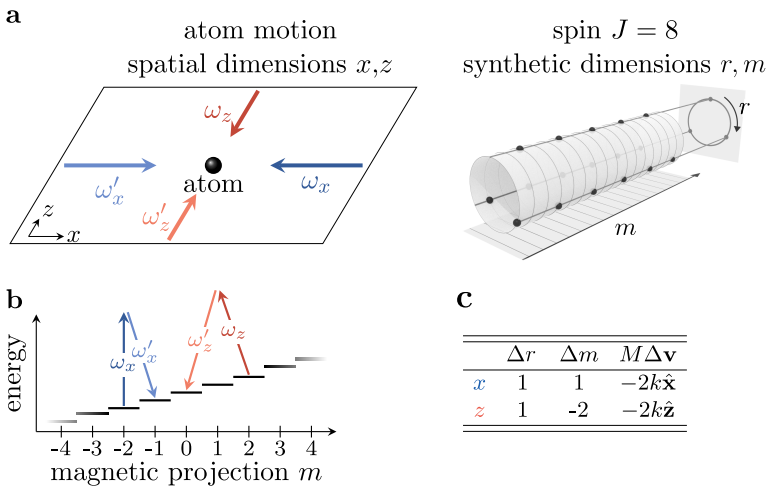

Figure 4.8: Experimental scheme leading to a 4D quantum Hall system. **a** : A pair of counterpropagating Raman beams couple the spatial degrees of freedom (x, z) to the spin degrees of freedom (m, r). **b** : A magnetic field lifts the degeneracy between the Zeeman sublevels. We display the two Raman transitions. **c** : Summary of the Raman transitions. The first two columns provide the hopping along the synthetic dimensions. The last column provides the net momentum kick.

As we will show in the next chapter, within rotating wave approximation, the combination of these two processes leads to the following single-particle Hamiltonian :

$$H = \frac{Mv^2}{2} - \left(t_x e^{i\phi_x} \frac{J_+}{J} + t_z e^{i\phi_z} \frac{J_-^2}{J^2} + \text{h.c} \right) + \beta \frac{J_z^2}{J^2}. \tag{4.19}$$

This Hamiltonian is made of three terms. The first one is the kinetic energy in real space (x, z). The second one describes the Raman processes, where the phases $\phi_x = -2kx$ and $\phi_z = -2kz$ are space-dependent. The last one is due to the tensorial component of the atomic polarisability and influence the curvature of the energy dispersion. The hopping amplitudes t_x, t_z and the quadratic term β are controlled via the laser intensities.

At first glance, its not obvious that Eq. (4.19) describes the motion of a particle in a 4D space. We will make it more obvious at the end of the section by describing our system with a continuous model. However, we will first give an intuition of why this model describes a 4D quantum Hall system in the next paragraph.

Interpretation as a four-dimensional quantum Hall system

We consider linear combinations of the processes (x) and (z) to define new Raman processes.

The combination $(\mu) \equiv \frac{1}{3}[(x) - (z)]$ leads to :

$$\begin{aligned} \Delta m &= 1 \\ \Delta r &= 0 \\ \Delta p_x &= -2k/3 \\ \Delta p_z &= 2k/3. \end{aligned} \tag{4.20}$$

Similarly, the combination $(\nu) \equiv \frac{1}{3}\left[2(x) + (z)\right]$ leads to :

$$\begin{aligned} \Delta m &= 0 \\ \Delta r &= 1 \\ \Delta p_x &= -4k/3 \\ \Delta p_z &= -2k/3. \end{aligned} \tag{4.21}$$

Contrary to the processes (x) and (z), (μ) and (ν) act independently on the two spin degrees of freedom. The process (μ) increases m by one unit and leaves r unchanged, while imparting a net momentum kick $\hbar \boldsymbol{k_\mu} = 2\hbar k \left(\hat{\boldsymbol{x}} - \hat{\boldsymbol{z}}\right)/3$. On the other hand, the process (ν) increases r by one unit and leaves m unchanged, while imparting a net momentum kick $\hbar \boldsymbol{k_\nu} = 2\hbar k \left(2\hat{\boldsymbol{x}} + \hat{\boldsymbol{z}}\right)/3$. We introduce in this paragraph two new directions : $\hat{\boldsymbol{\mu}} = (\hat{\boldsymbol{x}} - \hat{\boldsymbol{z}})/\sqrt{2}$ and $\hat{\boldsymbol{\nu}} = (2\hat{\boldsymbol{x}} + \hat{\boldsymbol{z}})/\sqrt{5}$. Similarly, we introduce the wavectors corresponding to the 'virtual' Raman processes $\boldsymbol{k_\mu} = k_\mu \hat{\boldsymbol{\mu}}$ and $\boldsymbol{k_\nu} = k_\nu \hat{\boldsymbol{\nu}}$, where the norms of these vectors are given by $k_\mu = 2\sqrt{2}k/3$ and $k_\nu = 2\sqrt{5}k/3$. We illustrate these new directions Fig. 4.9a (the direction $\hat{\boldsymbol{\xi}}$ displayed on this figure will be introduced later on).

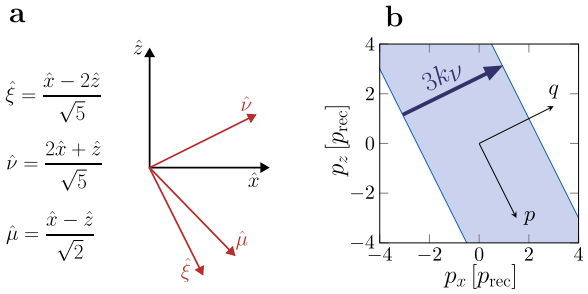

Figure 4.9: Geometry of the Raman transitions and Brillouin zone. **a** : We display the orientation of $\hat{\boldsymbol{\nu}}, \hat{\boldsymbol{\mu}}, \hat{\boldsymbol{\xi}}$ in the (xz) plane. **b** : Brillouin zone, shaded in blue, in the p_x, p_z plane. It is of finite extent along $\hat{\boldsymbol{\nu}}$ and of infinite extent along $\hat{\boldsymbol{\xi}}$.

Similarly to what we presented in chapter II, each of these mechanism can be interpreted as 2D quantum Hall system, respectively in the plane (μ, m) and in the plane (ν, r). Overall, our system can be seen as a generalisation of the 2D quantum Hall effect to four dimensions, thus belonging to the topological class A in $d = 4$.

The two directions μ and ν are not orthogonal. We can go back to the basis (x, z, r, m) to define the magnetic tensor of our system, by interpreting the complex phases ϕ_x and ϕ_z as Peierls phases. Assuming a unit charge, these Peierls phase provide an expression for an effective potential vector through

$$\phi_\alpha = A_r \Delta r^{(\alpha)} + A_m \Delta m^{(\alpha)}, \tag{4.22}$$

where α refers to (x, z). We recall that the process (x) increases both m and r by 1 unit, while process (z) decreases m by 2 but increases r by 1. We thus have :

$$\begin{aligned} \phi_x &= A_r + A_m \\ \phi_z &= A_r - 2A_m. \end{aligned} \tag{4.23}$$

We obtain the following explicit expression for the potential vector in the basis (x, z, r, m):

$$\boldsymbol{A} = \frac{1}{3}\left(0, 0, 2\phi_x + \phi_z, \phi_x - \phi_z\right). \tag{4.24}$$

Finally, through Eq. (4.2), we obtain the expression of the antisymmetric tensor describing the magnetic field :

$$B = \frac{2k}{3}\begin{bmatrix} 0 & 0 & -2 & -1 \\ 0 & 0 & -1 & 1 \\ 2 & 1 & 0 & 0 \\ 1 & -1 & 0 & 0 \end{bmatrix}. \tag{4.25}$$

In this paragraph, we have given the Hamiltonian of our model, and have explained how it can mimick the Hamiltonian of a charged particle evolving in a four-dimensional space in the presence of a magnetic field. We have derived the corresponding magnetic field tensor. In the following, we describe the Hamiltonian properties.

Hamiltonian invariances

The Hamiltonian Eq. (4.19) conserves the quasimomentum $\boldsymbol{p} = M\boldsymbol{v} + 2\hbar k m\,(\boldsymbol{k_\mu} + \boldsymbol{k_\nu}) \pmod{3\boldsymbol{k_\nu}}$. Indeed, upon the action of process (x), the change of momentum is :

$$\boldsymbol{dp} = -2\hbar k\hat{\boldsymbol{x}} + 2\hbar\,(\boldsymbol{k_\mu} + \boldsymbol{k_\nu}) = \overrightarrow{0}. \tag{4.26}$$

Similarly, upon the action of process (z), the change of momentum is :

$$\boldsymbol{dp} = -2\hbar k\hat{\boldsymbol{z}} - 4\hbar\,(\boldsymbol{k_\mu} + \boldsymbol{k_\nu}) = 3\hbar\boldsymbol{k_\nu} = \overrightarrow{0} \pmod{3\boldsymbol{k_\nu}} \tag{4.27}$$

Within Bloch's formalism, the energy bands of the Hamiltonian are indexed by $\boldsymbol{p}$. We can decompose this quasimomentum in the following way :

$$\boldsymbol{p} = p\hat{\boldsymbol{\xi}} + q\hat{\boldsymbol{\nu}}, \tag{4.28}$$

in which we introduced the direction ξ orthogonal to ν (see Fig. 4.9a) and where p can take any real value while we have $|q| < 3k_\nu/2$. This defines the Brillouin zone of the system, that we draw in Fig. 4.9b. Additionally, we emphasise that the direction ξ is not canonically conjugated to either m or either r.

The system exhibits a continuous translational invariance along $\hat{\boldsymbol{\xi}}$ and a discrete translational invariance along $\hat{\boldsymbol{\nu}}$ of period $2\pi/(3k_\nu)$. We stress that the reciprocal lattice is only defined on a 2D space, contrary to what we could expect for a 4D system on a lattice. This is similar to the case of chapter II, where we saw that a 2D system made of quantum wires in the plane (x, m) were described by a one-dimensional momentum in Fourier space. Similarly, we saw in chapter III a 2D cylinder described by a one-dimensional quasimomentum in Fourier space. The model under study can be seen as a combination of these two systems, leading to a 2D quasimomentum.

To summarise, we have defined three new directions ξ, ν, μ. μ and ν are the directions canonically conjugated to, respectively, m and r. The Hamiltonian translational invariances are described by the directions ξ and ν that are orthogonal to each other. It exhibits a continuous translational invariance along ξ and a discrete translational invariance along ν. These invariances lead to a 2D Brillouin zone, infinite in the direction ξ and finite in the direction ν, of extent $3k_\nu$. The quasimomentum $\hat{\boldsymbol{p}} = p\hat{\boldsymbol{\xi}} + q\hat{\boldsymbol{\nu}}$ is conserved, and we use it within Bloch's formalism in the following to index the magnetic Bloch bands.

4.4.2 Energy spectrum

We display in Fig. 4.10 the energy spectrum of the Hamiltonian Eq. (4.19), for the couplings $t_x, t_z = 5.69E_{\text{rec}}, 5.1E_{\text{rec}}$ and $\beta = -2t_z$, which corresponds to the ones studied experimentally. p is varied between $-12p_{\text{rec}}$ and $12p_{\text{rec}}$ while seven values of q uniformly spaning the Brillouin zone are used. We observe a quasi-degeneracy of the bands with respect to q, especially for the lowest energy ones. The band structure exhibits two main regions. First, a bulk that we define by $|p| < p^* \equiv 7p_{\text{rec}}$, $q \in [-3k_\nu, 3k_\nu]$, where the momentum cutoff p^* is chosen such that the ground band energy at p^* approximately lies in the middle of the gap at $p = 0$. In the bulk, the ground band is nearly flat, revealing a frustation of motion. The second region concerns the momentum in the intervals $|p| > p^*$, $q \in [-3k_\nu, 3k_\nu]$. As seen on the figure, this region hosts chiral edge modes : the ground band energy strongly increases with the momentum projection p, leading to a negative velocity for $p < -p^*$ and a positive velocity for $p > p^*$. In our system, the boundaries are provided by the dimension m, exhibiting one edge at $m = -J$ and one at $m = +J$.

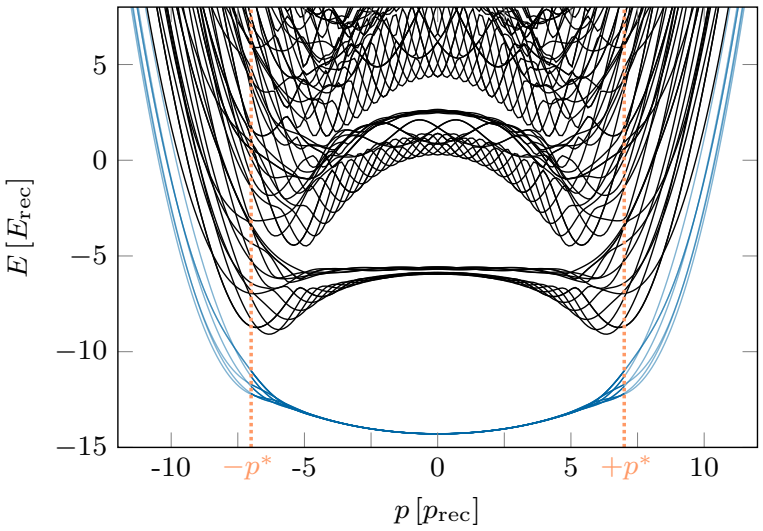

Figure 4.10: Spectrum of the Hamiltonian for $t_x, t_z = 5.69E_{\text{rec}}, 5.1E_{\text{rec}}$ and $\beta = -2t_z$. The ground band is displayed in blue, the bulk region being displayed in dark blue and bounded by $\pm p^* = \pm 7p_{\text{rec}}$. The excited bands are displayed in black.

The energy spectrum Fig. 4.10 is reminiscent of Landau levels with boundaries. In the bulk, the ground band and the first excited bands are nearly flat, mimicking the flat landau levels of a charged particle in a magnetic field. We will detail this aspect in the last paragraph of this section.

The ground band flatness is not perfect in the bulk due to the variations of the Clebsch-Gordan coefficients of J_+ and J_-^2 with m, that are not entirely compensated by the ones of the quadratic term J_z^2. The flattening of the ground band can be improved by adjusting the parameter β of Eq. (4.19), such that the Clebsh-Gordan coefficients of J_z^2 perfectly compensate the ones of J_+ and J_-^2 in the bulk. Using the same couplings t_x, t_z as before and $\beta = -2.456t_z$ yields to the band structure displayed in Fig. 4.11, which is flatter than the one presented in Fig. 4.10. Another way to flatten the ground band could be to adjust the ratio between t_x and t_z. However, as we will see in the last section of the chapter, we can't change too much the range of the couplings t_x, t_z in order to remain in a regime where our

model can be well described by a direct sum of 2D Landau levels.

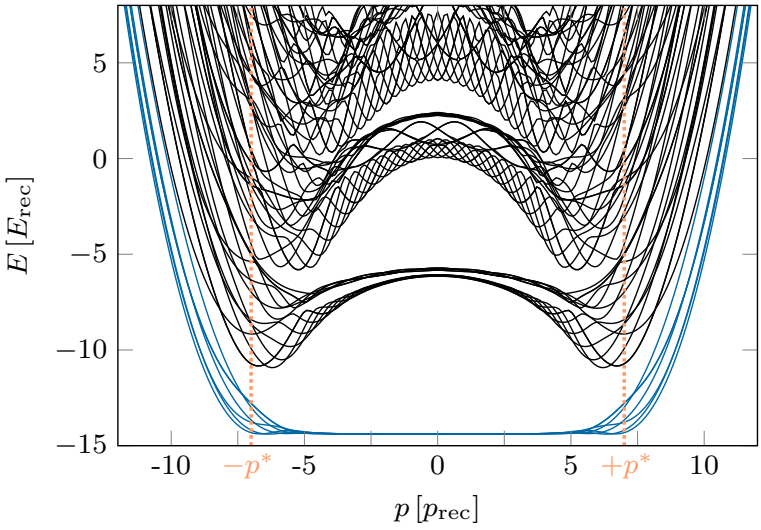

Figure 4.11: Ground band flattening. Using coupling values $t_x, t_z, \beta = 5.69E_{\mathrm{rec}}, 5.1E_{\mathrm{rec}}, \beta = -2.456t_z$ results in a very flat ground band in nearly all the bulk.

In the following, if not mentioned, we stick to the couplings $t_x, t_z, \beta = 5.69E_{\mathrm{rec}}, 5.1E_{\mathrm{rec}}, -2t_z$ corresponding to Fig. 4.10. Indeed, changing the quadratic term to $\beta = -2.456t_z$ would require experimentally the addition of an off-resonant fifth beam, using its tensorial polarisability. Since the experimental apparatus is already quite involved with four beams and since the small curvature does not affect the topology of our system, we decided to not implement this fifth beam.

4.4.3 Theoretical ground band properties

This paragraph is dedicated to the properties of the ground band as a function of $\boldsymbol{p}$, starting by the spin degree of freedom.

Spin degree of freedom

We display in Fig. 4.12 the value of the two spin dimensions, namely $\langle m \rangle$ and $\langle r \rangle$, in the ground band and in the center of the Brillouin zone.[1] As expected, the system exhibits edges along the dimension m. The edge $m = -J$ is approached for $p < -p^*$, and the edge $m = +J$ is approached for $p > p^*$. For $p > p^*$, the system starts to polarise itself in $m = +J$, resulting in a polarisation in $r = +2$.[2] A similar behavior is observed on the opposite edge. In the bulk, the mean magnetisation remains close to 0, while r explores its full dynamical range. We also display in this figure the directions $\hat{\boldsymbol{\mu}}$ and $\hat{\boldsymbol{\nu}}$, which are canonically conjugated to m and r.

[1] As seen in chapter III, the position in the dimension r is ill-defined being cyclic. In the following, we adress $\frac{3}{2\pi}\arg\langle e^{2i\pi/3J_z}\rangle$ to the mean value $\langle r \rangle$

[2] This behavior means that the two synthetic dimensions are correlated when the system is close to the edges $m = \pm J$. As we will see later on, this correlation falls down in the bulk, where one of the two synthetic dimensions can drift while leaving the second one unchanged.

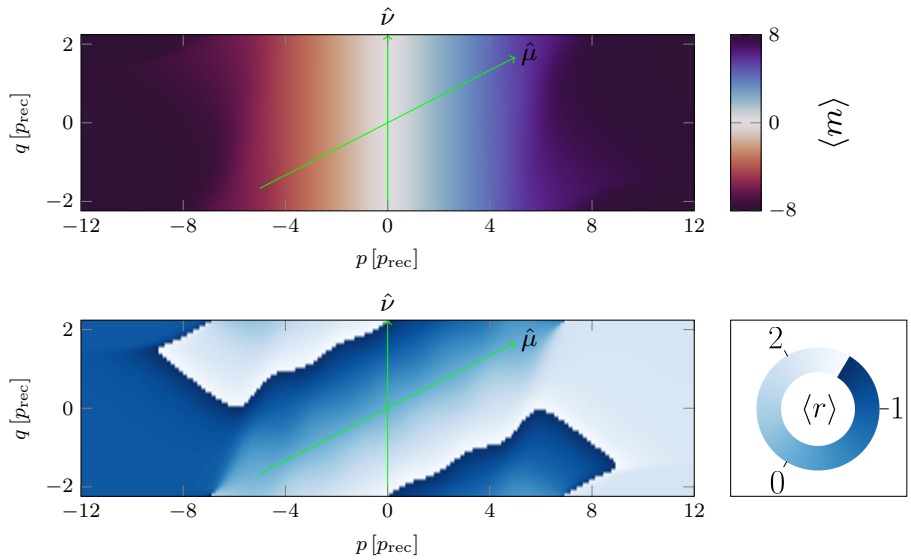

Figure 4.12: Spin properties in the ground band. Top : Evolution of $\langle m \rangle$. The latter is constant along $\hat{\boldsymbol{\nu}}$ but not along $\hat{\boldsymbol{\mu}}$. Bottom : Evolution of $\langle r \rangle$. It is constant along $\hat{\boldsymbol{\mu}}$ but not along $\hat{\boldsymbol{\nu}}$.

We show on Fig. 4.13 the populations along m and along r along the direction $\hat{\boldsymbol{\mu}}$. As expected, the mean magnetisation linearly evolves when the quasimomentum is changed along this direction, as a consequence of the Raman process (μ) introduced earlier. On the other hand, even if the populations along m are changing, their foliation into the population modulo 3 leads to a constant value of $\langle r \rangle$ in this direction. This figure illustrates the fact that the momentum along $\hat{\boldsymbol{\mu}}$ is indeed canonically conjugated to m, while leaving r unchanged.

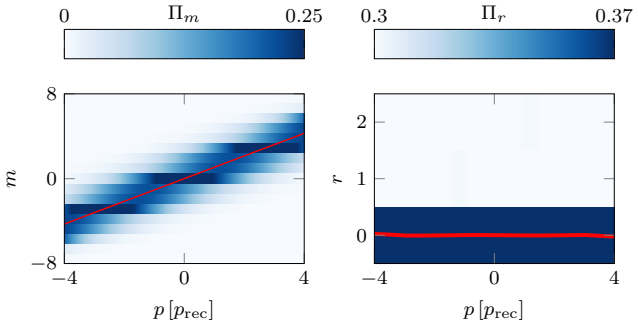

Figure 4.13: Evolution of $\langle m \rangle$ and $\langle r \rangle$ along $\hat{\boldsymbol{\mu}}$ in the ground band. Left : Populations along m are displayed and the average value $\langle m \rangle$ is plotted in red. Right : Populations modulo 3 deduced from Π_m. The average value $\langle r \rangle$ is plotted in red and is quasi-constant.

Similarly, we display in Fig. 4.14 the populations along m and r following a cut along the direction $\hat{\boldsymbol{\nu}}$. The spin probabilities evolve as a function of q in such a way that the mean magnetisation is constant, while $\langle r \rangle$ exhibits a drift. We also observe the cyclic aspect of r, exhibiting a jump when crossing $q \simeq -0.8 p_{\mathrm{rec}}$. This figure illustrates the fact that the momentum along the direction $\hat{\boldsymbol{\nu}}$ is canonically conjugated to r, while leaving m unchanged.

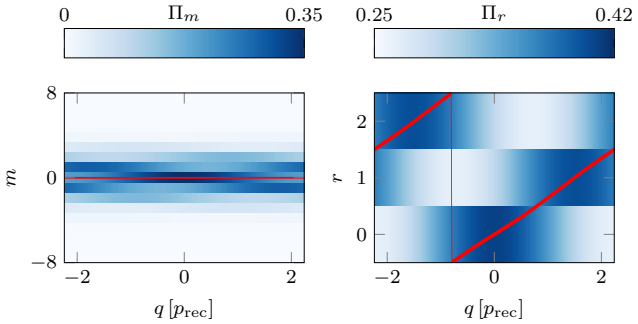

Figure 4.14: Evolution of $\langle m \rangle$ and $\langle r \rangle$ along $\hat{\boldsymbol{\nu}}$ in the ground band. Left : Populations along m are displayed and the average value $\langle m \rangle$ is plotted in red. Even though the populations exhibit some features, their average value leads to a constant value $\langle m \rangle = 0$. Right : Sum of spin distribution modulo 3 deduced from Π_m. The average value $\langle r \rangle$ is drifting. We observe the cyclic aspect of r.

The two previous figures are remindful of two systems that we previously studied in this manuscript. First, Fig. 4.13 is reminiscent of the properties of the 2D synthetic quantum Hall ribbon presented in chapter II, the ribbon being encoded in the dimensions (μ, m). Secondly, Fig. 4.14 is reminiscent of the synthetic quantum Hall cylinder presented in chapter III. The axial dimension of the cylinder being oriented along ν and its angular dimension being encoded by r.

Similarly to what we studied before, the evolutions of $\langle m \rangle$ and $\langle r \rangle$ can be interpreted as Hall drifts occuring in the (m, μ) plane and in the (r, ν) plane, these two Hall drifts being independent from each other. Indeed, the change of momentum can be interpreted as the action of an adiabatic force on a ground band wavepacket. When a force is applied along μ, the drift occurs along $\langle m \rangle$, while when a force is applied along ν, it occurs along $\langle r \rangle$. We will detail this Hall drift later on, invoking the Berry curvature.

Equivalently, these evolutions can be understood as a consequence of the spin-momentum locking provided by the Raman processes. To simplify, one can consider the virtual Raman processes (μ) and (ν). The first process leads to an increase of m by 1 and a momentum kick $-\hbar \boldsymbol{k_\mu}$. The second process leads to an increase of r by 1 and a momentum kick $-\hbar \boldsymbol{k_\nu}$. Within this picture, the conserved quasimomentum can be rewritten as :

$$\boldsymbol{p} = M\boldsymbol{v} + \langle m \rangle \hbar \boldsymbol{k_\mu} + \langle r \rangle \hbar \boldsymbol{k_\nu} \ (\mathrm{mod}\ 3\boldsymbol{k_\nu}). \tag{4.29}$$

Considering the bulk only, we can neglect the velocity since the ground band energy dispersion is weak. It leads to a simpler expression :

$$\boldsymbol{p} = \langle m \rangle \hbar \boldsymbol{k_\mu} + \langle r \rangle \hbar \boldsymbol{k_\nu} \ (\mathrm{mod}\ 3\boldsymbol{k_\nu}). \tag{4.30}$$

This equation can be projected along ν or along μ, permitting to give an analytical expression for the drifts presented in Fig. 4.13 and Fig. 4.14, valid in the bulk only :

$$\begin{aligned} \langle r \rangle &= \boldsymbol{p} \cdot \hat{\boldsymbol{\nu}} / (\hbar k_\nu) \\ \langle m \rangle &= \boldsymbol{p} \cdot \hat{\boldsymbol{\mu}} / (\hbar k_\mu) \end{aligned} \tag{4.31}$$

Spatial degree of freedom

We now consider the spatial degree of freedom of the ground band. We display Fig. 4.15 the velocities along $\hat{\boldsymbol{\xi}}$ and along $\hat{\boldsymbol{\nu}}$. In the bulk of the system, both velocities vanish, which was expected from the ground band dispersion displayed in Fig. 4.10. We recover the behavior of the bulk of a quantum Hall system. For $|p| > p^*$, the situation is different, where we see a non-zero velocity mainly oriented along the direction $\hat{\boldsymbol{\xi}}$. This non-zero velocity is a consequence of the presence of edges along m, and reveals the topology of our system. The velocity along $\hat{\boldsymbol{\nu}}$ becomes more and more negligible compared to its orthogonal counterpart when going closer and closer to the system boundaries, so that the edge modes are essentially pointing along $\hat{\boldsymbol{\xi}}$. As anticipated in the previous section for a four-dimensional system, the edge modes are anisotropic : they don't propagate in all the directions of the 3D boundaries. Moreover, we recognise a chirality reminiscent of quantum Hall systems : the velocity is oriented along $+\hat{\boldsymbol{\xi}}$ close to the edge $m = +J$ (corresponding to $p > p^*$) but is oriented along $-\hat{\boldsymbol{\xi}}$ close to the edge $m = -J$ (corresponding to $p < -p^*$).

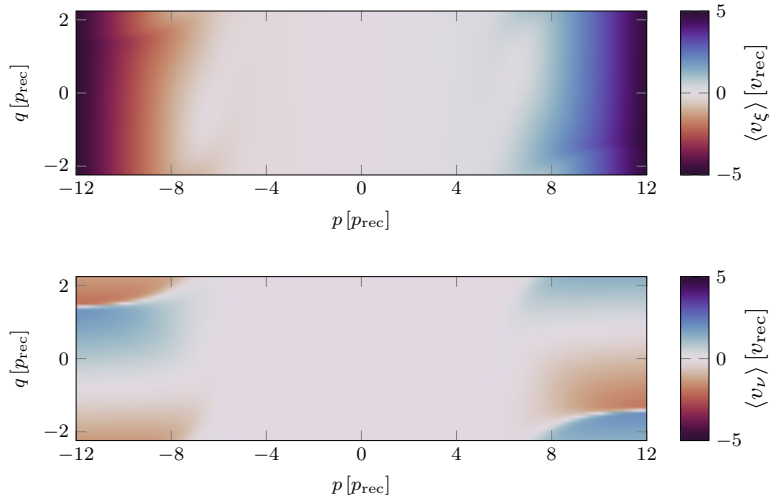

Figure 4.15: Spatial velocities in the ground band. Top : Velocity along $\hat{\boldsymbol{\xi}}$. Bottom : Velocity along $\hat{\boldsymbol{\nu}}$. The two velocities vanish in the bulk. For $|p| > p^*$, the velocity is non-zero, mainly pointing along $\pm\hat{\boldsymbol{\xi}}$.

Anistropic edge modes

We illustrate these anisotropic chiral edge modes in Fig. 4.16 and in Fig. 4.17. To do so, we initially consider a wave packet at $(p, q) = (0, 0)$ in the ground band of the system. We then apply a weak force on the system $\boldsymbol{F}$ pointing along $-(\hat{\boldsymbol{\xi}} + \hat{\boldsymbol{\nu}})/\sqrt{2}$, such that the system's quasimomentum is adiabatically changed towards $(p, q) = (-25p_{\text{rec}}, -25p_{\text{rec}})$ in a time $t = T_{\max}$. We chose this time to be long enough compared to the gap to the first excited band, so that the system remains in the ground band. We compute the spatial velocities and spin degree of freedom of the wavepacket while evolving the momentum. We integrate the spatial velocities to compute the system's position. While the momentum is increasing, the mean magnetisation get close to the edge $m = -J$ as seen in Fig. 4.16a, and reach it at $t \simeq T_{\max}/2$.

We display on Fig. 4.16b the system's position on the 3D hyperplane (ξ, ν, r) as a function of the time. The spatial positions are displayed in arbitrary unit, and the time is encoded in the color. At the beginning of the evolution ($t < T_{\max}/2$), the spatial positions remain very close to 0, as a consequence of the insulating character of the bulk. Meanwhile, the system's

position along r is greatly changing. More interestingly, for the times ($t > T_{\max}/2$) where the 3D hyperedge is reached, the system starts to drift in an anisotropic manner, its motion being limited to the direction $-\hat{\boldsymbol{\xi}}$ and thus not fully exploring the 3D hyperedge.

Similarly, we display in Fig. 4.17 the system's position when going towards the edge $m = +J$, by applying a weak force pointing along $+(\hat{\boldsymbol{\xi}}+\hat{\boldsymbol{\nu}})/\sqrt{2}$, such that the system's quasi momentum (p, q) is adiabatically evolving from $(0, 0)$ to $(+25p_{\text{rec}}, +25p_{\text{rec}})$. This time, the system is drifting towards $+\hat{\boldsymbol{\xi}}$ only, illustrating the chiral aspects of the edge modes.

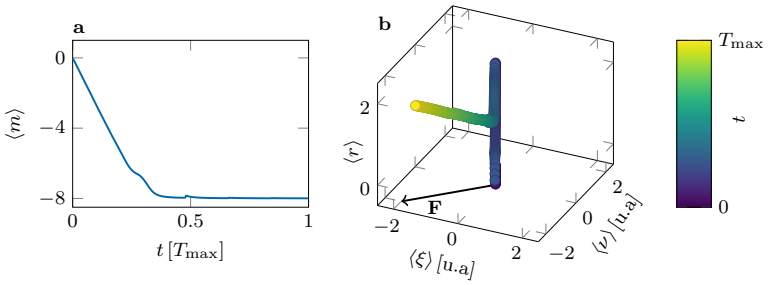

Figure 4.16: Anistropic edge mode at $m = -J$. **a** : $\langle m \rangle$-variation as the system is exploring the ground band. $m = -J$ edge is reached after $t \simeq T_{\max}$. **b** : Trajectory on the 3D hyperedge (ξ, ν, r). Time is encoded in color. The edge mode is pointing towards $-\hat{\boldsymbol{\xi}}$.

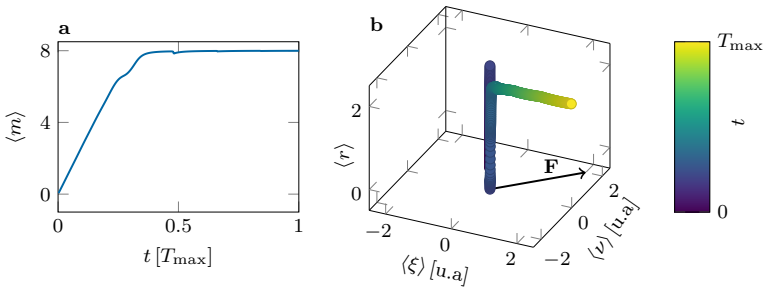

Figure 4.17: Anistropic edge mode at $m = +J$. **a** : $\langle m \rangle$-variation as the system is exploring the ground band. $m = +J$ edge is reached after $t \simeq T_{\max}$. **b** : Trajectory on the 3D-hyperedge (ξ, ν, r). Time is encoded in color. The edge mode is pointing towards $+\hat{\boldsymbol{\xi}}$.

Berry curvature

The ground band bulk properties can be interpreted as anomalous Hall drifts by invoking the Berry curvature. Indeed, the semiclassical equation of motion, in the absence of perturbation, yields in the bulk of the system :

$$\mathrm{d}r^{\mu} = F^{\mu\nu}\mathrm{d}p_{\nu}. \tag{4.32}$$

where we neglected the dispersion of the ground band, the latter being quasiflat. This equation shows that increasing the momentum along, for example, ν leads to a response along r given by $F^{r\nu}$. The six Berry curvature components can be computed via Kubo formula [107], using the velocities along the spatial and the synthetic dimensions, already introduced in the previous chapter. We display the six Berry curvatures compontents over the Brillouin zone in Appendix C. At the couplings t_x, t_z, β under considerations, the latter

are quasiflat in the bulk of the system. We display in Fig. 4.18 their q-averaged value as a function of p. Three Berry curvature components are vanishing. $F^{m\nu} = 0$ illustrates that the application of a force along ν doesn't induce a Hall response in m, as seen on Fig. 4.14. Similarly, $F^{\xi\nu} = 0$ is expected from Fig. 4.14. Finally, $F^{mr} = 0$ indicates that applying a force along m, for instance a perturbative Zeeman field, doesn't lead to any drift of r.

In a simpler manner, the bulk Berry curvature components can be derived directly from the conservation of the quasimomentum Eq. (4.30). By projecting the latter on $\hat{\boldsymbol{\gamma}} \perp \hat{\boldsymbol{\mu}}$ and on $\hat{\boldsymbol{\xi}}$, we obtain :

$$\begin{aligned} \frac{1}{\sqrt{10}} p_\xi - \frac{3}{\sqrt{10}} p_\nu &= -\frac{3}{\sqrt{10}} \hbar k_\nu \langle r \rangle \\ p_\xi &= \frac{3}{\sqrt{10}} \hbar k_\mu \langle m \rangle. \end{aligned} \tag{4.33}$$

Plugging these equations in Eq. (4.32), we can compute the Berry curvature components, valid in the bulk only. We obtain : $\{F^{m\xi}_{\text{bulk}}, F^{m\nu}_{\text{bulk}}, F^{r\xi}_{\text{bulk}}, F^{r\nu}_{\text{bulk}}\} = \{\sqrt{5}/(2k), 0, -1/(2\sqrt{5}k), 3/(2\sqrt{5}k)\}$. We plot these values in Fig. 4.18 in dashed lines. We see a good agreement in the bulk with the components derived from the Kubo formula for $F^{m\nu}, F^{r\xi}$ and $F^{r\nu}$. There is though a slight discrepancy for the component $F^{m\xi}$. The latter comes from the fact that, with the couplings t_x, t_z, β we are using, the ground band is not perfectly flat. As a consequence, the assumption $\boldsymbol{v} = 0$ is not rigorously valid and Eq. (4.33) is not exact. One can show that using couplings that flatten the ground band (Fig. 4.11) leads to a good agreement between the two methods to compute $F^{m\xi}$. Interestingly, even though the quadratic term $\beta J_z^2/J^2$ affects the local properties of the ground band via the Berry curvatures, it doesn't change the system topology, as we will see in the next paragraph.

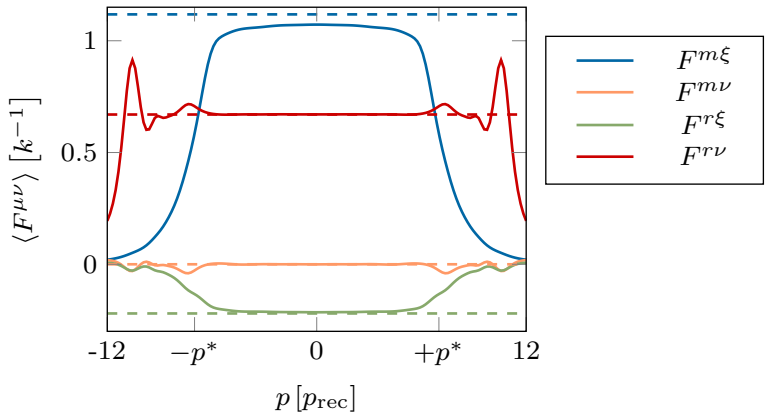

Figure 4.18: Berry curvatures of the ground band. Four Berry curvature components are displayed, the two other being $F^{mr} = F^{\xi\nu} = 0$. We plot in dashed lines the values derived from the spin-momentum locking relation.

4.4.4 Topological properties

The presence of a gap in the bulk together with the existence of edge modes gave us some hints about the topology of the system. As seen previously, in 4D, the transport is quantised by the second Chern number ν_2, which is expected to be equal to 1 for the topological class A in dimension 4. Our system exhibiting edges along m, considering its topological response as a whole is not meaningfull. We rather focus on the bulk response of the system

considering the local second Chern marker. In the bulk, the latter should match the second Chern number. The local second Chern marker is defined by [108] :

$$C_2(\boldsymbol{r}) = 2\pi^2 \epsilon_{\xi,\nu,r,m} \langle \boldsymbol{r} | Pr^{\xi} Pr^{\nu} Pr^{r} Pr^{m} P | \boldsymbol{r} \rangle , \tag{4.34}$$

where $\epsilon_{\xi,\nu,r,m}$ is the Levi-Civita symbol, P refers to the projector on the ground band and $\boldsymbol{r} = (\xi, \nu, r, m)$ is the 4-dimensional position vector. This expression can be rewritten, such that it involves observables experimentally accessible with our experiment. We detail the derivation in [141]. In the end, Eq. (4.34) can be rewritten as :

$$C_2(m) = \frac{1}{3} \int_{\text{bulk}} \mathrm{d}p\mathrm{d}q \Pi_m(p,q) \rho_2(p,q), \tag{4.35}$$

where the integral is performed on the bulk only. We introduce in Eq. (4.35) the second Chern character ρ_2 that can be obtained via a non-linear combination of Berry curvature components (Eq. (4.16)) :

$$\rho_2(p,q) = F^{\xi\nu} F^{rm} + F^{m\xi} F^{r\nu} - F^{r\xi} F^{m\nu}, \tag{4.36}$$

where the first contribution vanishes since both $F^{\xi\nu}$ and F^{rm} are zero.

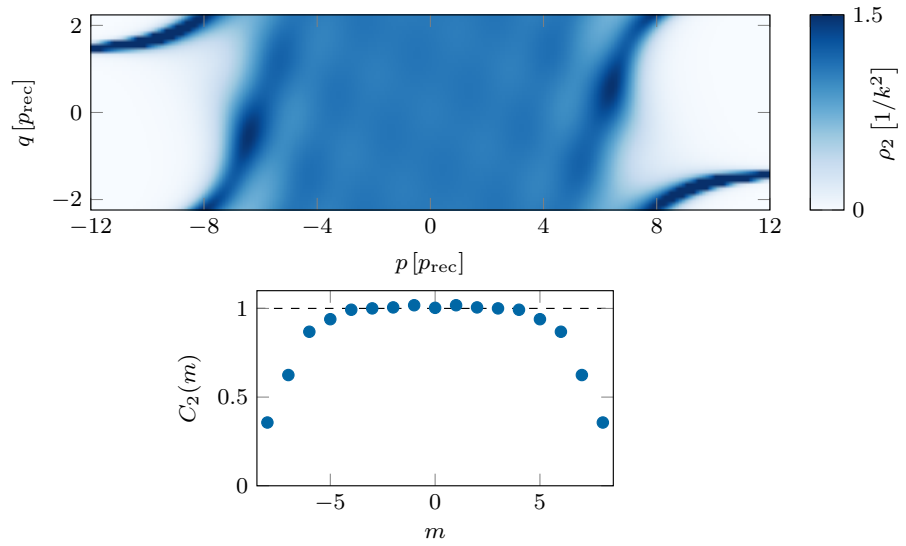

Figure 4.19: Topological properties of the ground band. Top : Second Chern character ρ_2 in the ground band. It is quasiflat in the bulk. Bottom : Local second Chern marker. It equals unity in the bulk, highlighting the topological character of the system.

We display Fig. 4.19 the second Chern character over the Brillouin zone. It is constant in the bulk, its value being given by $\rho_2^{bulk} \simeq 3/(4k^2)$. Weighting it by the m populations and integrating over the bulk lead to the local second Chern marker, also displayed Fig. 4.19. This quantity is constant in the bulk and is equal to 1, as expected for a topological system in the class A in $d = 4$. The decrease of $C_2(m)$ for $|m| \geq 5$ is a consequence of the boundaries at $m = \pm J$. As a sidenote, we point that similarly to what was presented in chapter II, the local second Chern marker is topologically protected. We will illustrate this in the next section.

We have studied properties of our system and have interpreted it as a pair of 2D quantum Hall system. In the following paragraph, we propose a continuous model to make this interpretation more clear.

4.4.5 Effective continuous model in the bulk

Derivation of the continuous model in the bulk

We have studied in the previous paragraph the properties of the Hamiltonian Eq. (4.19). Even though the 4D character of this Hamiltonian was not immediately apparent, we have seen that we can interpret it as a pair of two independent 2D Landau levels. In this paragraph, we derive a semiclassical model, in the bulk of the system, to make this analogy more obvious.

We start by replacing the spin ladder operators by translation operators along m and r, involving the momenta along these directions : p_m and p_r. By considering these directions continuous, and recalling that J_+ increases both m and r by one unit, we obtain :

$$J_+ \simeq \mathrm{e}^{-i(p_m+p_r)}\sqrt{J(J+1)-m(m+1)}. \tag{4.37}$$

We also assume that the states under consideration are in the bulk only, so that $|m/J| << 1$. We can develop Eq. (4.37) at second order in m/J, leading to :

$$J_+ \simeq \mathrm{e}^{-i(p_m+p_r)}\left(J-\frac{m^2}{2J}\right). \tag{4.38}$$

Similarly, we obtain :

$$J_-^2 \simeq \mathrm{e}^{-i(p_r-2p_r)}\left(J^2-m^2\right). \tag{4.39}$$

We can now plug these expressions in Eq. (4.19), leading to the approximated Hamiltonian :

$$H \simeq \frac{p_x^2+p_z^2}{2M} - \left[t_x\left(1-\frac{1}{2}\left(\frac{m}{J}\right)^2\right)\mathrm{e}^{-i(p_m+p_r-2kx)} + t_z\left(1-\left(\frac{m}{J}\right)^2\right)\mathrm{e}^{-i(p_r-2p_m-2kz)} + \mathrm{h.c}\right] + \beta\frac{J_z^2}{J^2}. \tag{4.40}$$

This expression can be simplified by Taylor expanding the exponentials and keeping only the order 2 terms in all dynamical variables. It leads to :

$$H \simeq \epsilon_0 + H_{\mathrm{kin}} + \beta'\left(\frac{m}{J}\right)^2. \tag{4.41}$$

The first term of Eq. (4.41) is an energy offset given by $\epsilon_0 = -2t_x - 2t_z$. The last term is a quadratic energy shift, with $\beta' = \beta + t_x + 2t_z$. In the following, we are interested in the kinetic term, defined by :

$$H_{\mathrm{kin}} = \frac{p_x^2+p_z^2}{2M} + t_x\left(p_m+p_r-2kx\right)^2 + t_z\left(p_r-2p_m-2kz\right)^2 \tag{4.42}$$

Generalised Landau levels

By introducing the inverse mass tensor $1/M$ (in the basis (x,z,r,m)) :

$$1/M = \begin{bmatrix} 1/M & 0 & 0 & 0 \\ 0 & 1/M & 0 & 0 \\ 0 & 0 & 2t_x+2t_z & 2t_x-4t_z \\ 0 & 0 & 2t_x-4t_z & 2t_x+8t_z \end{bmatrix} \tag{4.43}$$

and the artifical potential vector derived earlier :

$$\boldsymbol{A} = \frac{-2k}{3}\left(0,0,2x+z,x-z\right), \tag{4.44}$$

Eq. (4.42) can be rewritten :

$$H_{\text{kin}} = \frac{1}{2}\left(\frac{1}{M}\right)^{\alpha\beta}(p_\alpha - A_\alpha)(p_\beta - A_\beta)\,. \tag{4.45}$$

This Hamiltonian corresponds to the Hamiltonian of a charged particle submitted to a magnetic field in four dimensions.

As seen previously in this chapter, the magnetic field in 4D is described by two Larmor frequencies. In order to compute the Larmor frequencies of our model, we re-express Eq. (4.42) as :

$$H_{\text{kin}} = \frac{p_x^2}{2M} + 4k^2 t_x \left(x - \frac{1}{2k}(p_m + p_r)\right)^2 + \frac{p_z^2}{2M} + 4k^2 t_z \left(z - \frac{1}{2k}(2p_m - p_r)\right)^2. \tag{4.46}$$

We recognise a direct sum of two harmonic oscillators, one in the plane $(x, m+r)$ and one in the plane $(z, 2m-r)$.

From Eq. (4.46), we identify the two Larmor frequencies : $\omega_x = 4\sqrt{E_{\text{rec}} t_x}/\hbar$ describes the motion of the particle in the $(x, m+r)$ plane and $\omega_z = 4\sqrt{E_{\text{rec}} t_z}/\hbar$ in the $(z, 2m-r)$ plane. For the couplings considered in this section, we have $\omega_x \simeq 2\pi \times 30\,\text{kHz}$ and $\omega_z \simeq 2\pi \times 28.4\,\text{kHz}$.

The spectrum of H_{kin} corresponds to generalised Landau levels of energies : $E_{n_x,n_z} = \omega_x(n_x + 1/2) + \omega_z(n_z + 1/2)$. These generalised Landau levels are macroscopically degenerated and are respectively indexed by $p_m + p_r$ and $2p_m - p_r$.

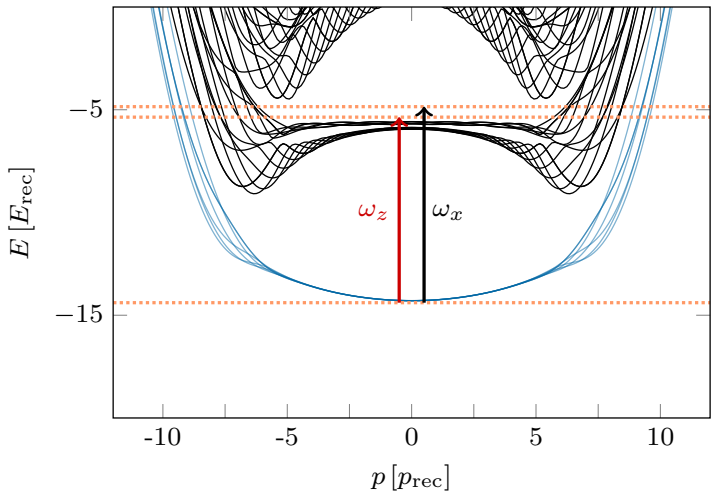

Figure 4.20: Mapping to a direct sum of 2D Landau levels. We display in blue the ground band of the initial Hamiltonian and in black its excited bands. The three first eigenvalues of H_{kin} (continuous model) are displayed in orange. The first gap corresponds to $\hbar\omega_z$, the second to $\hbar\omega_x$.

We compare in Fig. 4.20 the spectrum of the initial Hamiltonian and the first eigenenergies of the generalised Landau levels. We see a good agreement in the bulk for the first two excited bands. The first gap corresponds to excitations in the $(z, 2m-r)$ plane, the second in the $(x, m+r)$ plane. We note that the curvature of the Hamiltonian is not captured by the generalised Landau levels. It is a consequence of the fact that we considered only H_{kin}, which doesn't influence our discussion and would only add a dispersion to the generalised Landau levels.

Equation of motions

The continuous model can be used to derive the cyclotron trajectories, providing another derivation of the Larmor frequencies, using the equation of motion :

$$\partial_t \boldsymbol{v} = \frac{1}{M} B \boldsymbol{v}, \tag{4.47}$$

where B is the magnetic field tensor. It leads to :

$$\partial_t \boldsymbol{v} = \begin{bmatrix} 0 & 0 & -4v_{\text{rec}}/3 & -2v_{\text{rec}}/3 \\ 0 & 0 & -2v_{\text{rec}}/3 & 2v_{\text{rec}}/3 \\ 4kt_x/\hbar & 4kt_z/\hbar & 0 & 0 \\ 4kt_x/\hbar & -8\ kt_z/\hbar & 0 & 0 \end{bmatrix} \boldsymbol{v}. \tag{4.48}$$

By derivating this equation with respect to the time, we obtain the following equations governing the velocity in the (x, z) plane :

$$\begin{aligned} \partial_t^2 v_x &= -16 E_{\text{rec}} t_x v_x/\hbar^2, \\ \partial_t^2 v_z &= -16 E_{\text{rec}} t_z v_z/\hbar^2. \end{aligned} \tag{4.49}$$

After integration, we obtain the projection of the 4D cyclotron trajectory in the (x, z) plane, which involves the two Larmor frequencies defined previously :

$$\begin{aligned} x(t) &= A_x \cos\left(\omega_x t + \varphi_x\right), \\ z(t) &= A_z \cos\left(\omega_z t + \varphi_z\right), \end{aligned} \tag{4.50}$$

where A_i, φ_i respectively refer to an amplitude and a phase that we don't detail here.

We have derived a continuous model in this paragraph from the initial Hamiltonian. The latter permitted us to make the analogy with a direct sum of a pair of 2D Landau levels more clear. We have computed the corresponding Larmor frequencies, and have seen that they are in good agreement with the Hamiltonian bandstructure. In the following paragraph, we study the domain of validity of this continuous model.

Domain of validity of the continuous model

We expect the continuous model to be less accurate in a regime where the discrete nature of synthetic dimension cannot be neglected anymore. It occurs when the width of the ground band orbitals is smaller than the spacing between the different sites. We show in Fig. 4.21 the populations along m for various couplings strengths in the ground band, at $\boldsymbol{p} = \overrightarrow{0}$. We see that the population widths increase with t_x, t_z. We observe clearly the discretisation for the lower couplings case, where the probability distribution is peaked around $m = 0$. Note that a similar behavior occurs along r, albeit more difficult to quantify since this dimension only exhibits three sites.

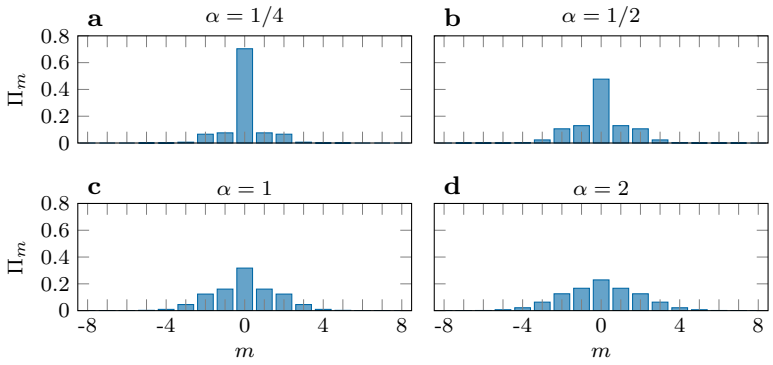

Figure 4.21: Orbital widths along m in the ground band at $p = q = 0$, for different couplings $t_x, t_z = \alpha \times 5.69E_{\text{rec}}, \alpha \times 2.55E_{\text{rec}}$. $\boldsymbol{a}$: $\alpha = 1/4$. $\boldsymbol{b}$: $\alpha = 1/2$. $\boldsymbol{c}$: $\alpha = 1$. $\boldsymbol{d}$: $\alpha = 2$.

As a consequence, when decreasing the coupling, we expect our picture of a direct sum of two 2D Landau levels to fall down. We illustrate it on figure Fig. 4.22, where we display $\langle r \rangle$ in the ground band for two values of the couplings. For the values $t_x, t_z = 5.69E_{\text{rec}}, 5.11E_{\text{rec}}$, as shown earlier, the direction μ is not coupled to r. This is no longer the case for half of these couplings, where we see a modulation of $\langle r \rangle$. We also highlight this effect on the second Chern character ρ_2 that exhibits a modulation in the bulk for the lower couplings (Fig. 4.23). Even though our system cannot be decomposed anymore as a direct sum of a pair of 2D Landau levels, its topological properties are conserved. We illustrate it in Fig. 4.23, where we demonstrate that the local second Chern marker remains equal to unity in the bulk.

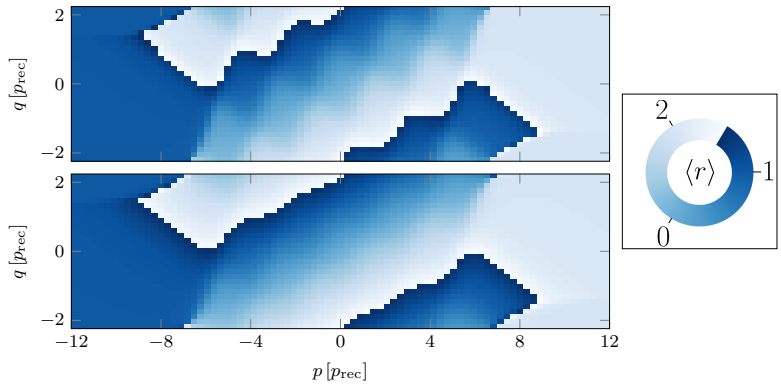

Figure 4.22: Validity of the continuous model. Top : $\langle r \rangle$ in the ground band for $t_x, t_z = 2.85, 2.55E_{\text{rec}}$. We see oscillations of $\langle r \rangle$ in the bulk along $\boldsymbol{\mu}$. Bottom : $\langle r \rangle$ in the ground band for $t_x, t_z = 5.69, 5.1E_{\text{rec}}$. $\langle r \rangle$ is quasiflat in the bulk along $\boldsymbol{\mu}$.

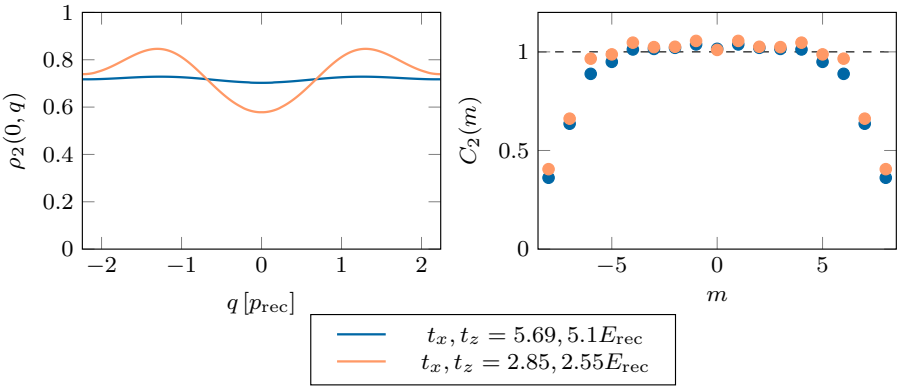

Figure 4.23: Topological properties and coupling strengths. Left : Second Chern character ρ_2 in the ground band for $p = 0$ and various q, for two different coupling strengths. Right : Local second Chern marker. For both coupling strengths, $C_2(m)$ is equal to unity in the bulk, showing that the topological properties remain similar in the two situations.

The choice of laser couplings

As seen before, our model becomes closer to a direct sum of two 2D Landau levels as the couplings t_x, t_z increase. This provides us a lower bound for the choice of these couplings. However, we can't use either too strong couplings.

The first reason is experimental. Using higher couplings means using higher light power, hence more heating from spontaneous emission while the Raman processes are occuring. The second reason is actually related to the orbitals widths : likewise what we displayed in Fig. 4.21, the orbital width along r also increases with the coupling strengths. However, since the r dimension only provides three sites, the probability distributions along r will be less and less peaked, and our definition $\langle r \rangle = \frac{3}{2\pi} \arg\langle \mathrm{e}^{2i\pi J_z/3} \rangle$ no longer holds. Finally, the enlargement of orbital extent along m leads to more rapid manifestation of the edges. Consequently, the transport is quantified over a decreasing bulk size. In the end, the choice of the couplings t_x, t_z results from a compromise.

4.5 Conclusion

We have started this chapter by doing a brief historical review of the exploration of topological systems. The latter leads to the tenfold classification, classifying topological insulators and superconductors as a function of their symmetries and dimensionality. All the entries of this classification have not been explored yet, and it is particularly the case in higher dimensions, where exciting physical phenomena are expected.

We illustrated this on four-dimensional quantum Hall systems, demonstrating their rich physics by invoking the anisotropic chiral edge modes and the peculiar nature of cyclotron orbits. We also derived the transport equation in 4D, involving the notable non-linear response, quantised by the second Chern number. This study motivated the experimental exploration of four-dimensional systems.

Subsequent to this, we went back to experiments, discussing the proposals and experimental realisations of four-dimensional quantum Hall systems. The second Chern number was measured, but in a dynamical realisation using 2D topological charge pump. On the other hand, a genuine 4D system was realised (in topological class AI), albeit without direct measurement of transport quantisation.

Finally, we described our approach using dysprosium atoms to realise a 4D quantum Hall system in topological class A. We derived the ground band properties of our system and showed its non-trivial topology. By doing a continuous approximation, we interpreted our system as a direct sum of 2D Landau levels.

We present our experimental realisation of this protocol in the next chapter. To our knowledge, it consists in the first experimental realisation of a 4D topological system in the class A.

5 Realisation of a four-dimensional synthetic quantum Hall system

We described in the previous chapter how a particuliar Raman laser scheme can emulate a 4D quantum Hall system. We show in this chapter the experimental realisation of this scheme. We start by deriving the Hamiltonian

$$H = \frac{p_x^2 + p_z^2}{2M} - t_x \left[\mathrm{e}^{-2ikx} \frac{J_+}{J} + \mathrm{h.c} \right] - t_z \left[\mathrm{e}^{-2ikz} \frac{J_-^2}{J^2} + \mathrm{h.c} \right] + \beta J_z^2, \tag{5.1}$$

characterising our system. Then, we detail the experimental protocol to prepare the ground state of this Hamiltonian and describe the data analysis. Subsquently, we show experimental results, starting from the spin and velocity properties in the ground band. In particular, we unveil the anisotropic chiral edge modes, a peculiar feature of the 4D quantum Hall physics. In the next section, we show our measurements of cyclotrons orbits in four dimensions.

We recover the peculiar trajectories described in the previous chapter, which properties are closely related to the choice of Larmor frequencies. Finally, we probe the topology of our system. We first measure the second Chern number from a non-linear combination of experimental Berry curvature component. We then explore the non-linear response and propose a new protocol to exhibit the system's non-trivial topology.

The results presented in this chapter are published in [141].

5.1 Hamiltonian derivation

We start this chapter by deriving the 4D Hamiltonian that we investigated previously. This Hamiltonian consists in the combination of two Raman processes : one occuring along x and one along z. The different beam frequencies are chosen to ensure that these two Raman processes are not interfering with each other. A magnetic field $|\boldsymbol{B}| \simeq 220\,\mathrm{mG}$ oriented along z lifts the degeneracy between the different Zeeman sublevels. We recall the experimental scheme in Fig. 5.1.

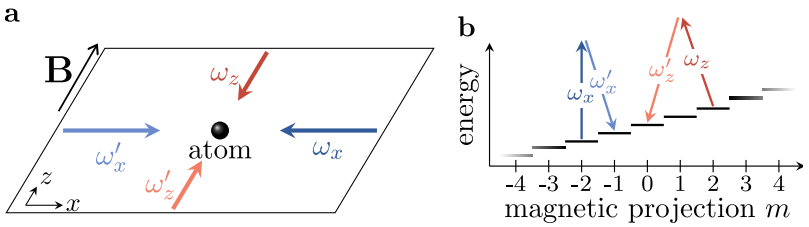

Figure 5.1: Experimental scheme. **a** : Experimental scheme used to emulate the 4D quantum Hall system. The beams involved in the process (x) are displayed in blue, the one involved in the process (z) in red. A magnetic field **B** oriented along $\hat{\boldsymbol{z}}$ lifts the degeneracy between the Zeeman sublevels. **b** : Raman transitions governed by the process (x) and the process (z).

5.1.1 Process (x) only

Deriving the time-dependent Hamiltonian

The frequencies of the beams propagating along x are given by : $\omega_x = \Delta$ and $\omega_{x'} = \Delta + \omega_z$, where ω_z is the Larmor frequency and $\Delta \simeq -2\pi \times 7\,\mathrm{GHz}$ an overall detuning such that the single photon processes are off-resonant. The polarisation of the two beams are assumed to be linear, hence we write the electric fields as :

$$\begin{aligned} \boldsymbol{E_{x'}} &= \sqrt{I_{x'}} \mathrm{e}^{i(kx-\omega_{x'}t)} \begin{bmatrix} 0 \\ \sin(\theta_{x'}) \\ \cos(\theta_{x'}) \end{bmatrix}, \\ \boldsymbol{E_x} &= \sqrt{I_x} \mathrm{e}^{i(-kx-\omega_x t)} \begin{bmatrix} 0 \\ \sin(\theta_x) \\ \cos(\theta_x) \end{bmatrix}, \end{aligned} \tag{5.2}$$

where $\theta_x, \theta_{x'}$ define the polarisation of the beams. We now compute the AC-stark shift induced by these two beams on a Dysprosium atom. We thus consider the total electric field : $\boldsymbol{E} = \boldsymbol{E_x} + \boldsymbol{E_{x'}}$. Its important to note that the light shift induced by $\boldsymbol{E}$ is different from the sum of the light shift induced by $\boldsymbol{E_x}$ and $\boldsymbol{E_{x'}}$ due to the intereference terms. We compute

the scalar light shift, vectorial light shift and tensorial light shift, given by the following equation as seen in chapter I :

$$\begin{aligned} H &= H_{\text{scalar}} + H_{\text{vectorial}} + H_{\text{tensorial}} \\ &= V\left[\alpha_0 \boldsymbol{E}^2 \mathbb{1} - i\alpha_1 \left(\boldsymbol{E}^* \times \boldsymbol{E}\right) \cdot \frac{\boldsymbol{J}}{2J} + \alpha_2 \frac{3\left[\left(\boldsymbol{E}^* \cdot \boldsymbol{J}\right)\left(\boldsymbol{E} \cdot \boldsymbol{J}\right) + \left(\boldsymbol{E} \cdot \boldsymbol{J}\right)\left(\boldsymbol{E}^* \cdot \boldsymbol{J}\right)\right] - 2J(J+1)\boldsymbol{E}^2 \mathbb{1}}{2J(2J-1)}\right]. \end{aligned} \tag{5.3}$$

In Eq. (5.3), $\alpha_0, \alpha_1, \alpha_2$ are the scalar, vectorial and tensorial polarisability associated with the transition under study (in our case, the 626 nm transition) and V is a scaling factor, also introduced in the first chapter.

Scalar light shift

We start by computing $|\boldsymbol{E_x} + \boldsymbol{E'_x}|^2$:

$$\begin{aligned} |\boldsymbol{E_x} + \boldsymbol{E_{x'}}|^2 &= \boldsymbol{E_x}.\boldsymbol{E_x^*} + \boldsymbol{E_x}.\boldsymbol{E_{x'}^*} + \boldsymbol{E_{x'}}.\boldsymbol{E_x^*} + \boldsymbol{E_{x'}}.\boldsymbol{E_{x'}^*} \\ &= I_x + I_{x'} + 2\sqrt{I_x I_{x'}} \cos\left[2kx + \omega_z t\right] \cos(\theta_{x'} - \theta_x). \end{aligned} \tag{5.4}$$

We can deduce the scalar component of the light shift, H_{scalar} using the light shifts for Clebsch-Gordan coefficient equal to unity $U_x, U_{x'}$ and the scalar polarisability α_0 for the 626 nm transition :

$$H_{scalar}(t) = \alpha_0 U_x \mathbb{1} + \alpha_0 U_{x'} \mathbb{1} + 2\alpha_0 \sqrt{U_x U_{x'}} \cos(\theta_{x'} - \theta_x) \cos\left[2kx + \omega_z t\right] \mathbb{1}. \tag{5.5}$$

Vectorial light shift

We compute $\boldsymbol{E}^* \times \boldsymbol{E}$:

$$\boldsymbol{E}^* \times \boldsymbol{E} = \boldsymbol{E_{x'}^*} \times \boldsymbol{E_{x'}} + \boldsymbol{E_x^*} \times \boldsymbol{E_x} + \boldsymbol{E_{x'}^*} \times \boldsymbol{E_x} + \boldsymbol{E_x^*} \times \boldsymbol{E_{x'}} \tag{5.6}$$

Since the beams don't have any ellipticity, the first two terms cancel out. After computing the remaining two vectorial products, we get :

$$\boldsymbol{E}^* \times \boldsymbol{E} = -2i\sqrt{I_x I_{x'}} \sin(\theta_{x'} - \theta_x) \sin\left[2kx + \omega_z t\right] \hat{\boldsymbol{x}}. \tag{5.7}$$

We can deduce from this equation the vectorial component of the light shift, $H_{\text{vectorial}}$, using the vectorial polarisability α_1 for the 626 nm transition :

$$H_{\text{vectorial}}(t) = -\alpha_1 \sqrt{U_x U_{x'}} \sin(\theta_{x'} - \theta_x) \sin\left[2kx + \omega_z t\right] J_x \tag{5.8}$$

Tensorial light shift

The tensorial light shift is a bit more complicated to obtain. It contains two terms. The first term is proportional to identity and involves $|\boldsymbol{E_x} + \boldsymbol{E_{x'}}|^2$, already derived above. It leads to :

$$H^{(1)}_{\text{tensorial}} = -\alpha_2 \frac{J+1}{2J-1} \left[U_x + U_{x'} + 2\sqrt{U_x U_{x'}} \cos(\theta_{x'} - \theta_x) \cos\left[2kx + \omega_z t\right]\right] \mathbb{1}, \tag{5.9}$$

where α_2 is the tensorial polarisability for the 626 nm transition. The second term is proportional to the operator $T \equiv \left(\boldsymbol{E}^*.\boldsymbol{J}\right)\left(\boldsymbol{E}.\boldsymbol{J}\right) + \left(\boldsymbol{E}.\boldsymbol{J}\right)\left(\boldsymbol{E}^*.\boldsymbol{J}\right)$, that we can rewrite as :

$$T = 2|E_y|^2 J_y^2 + 2|E_z|^2 J_z^2 + 2\text{Re}\left[E_y E_z^*\right]\{J_y, J_z\}, \tag{5.10}$$

where we used the projections of $\boldsymbol{E}$ on the basis (x, y, z), given by :

$$\begin{aligned}
|E_z|^2 &= I_{x'}\cos^2(\theta_{x'}) + I_x\cos^2(\theta_x) + 2\sqrt{I_x I_{x'}}\cos(\theta_{x'})\cos(\theta_x)\cos\left[2kx + \omega_z t\right] \\
|E_y|^2 &= I_{x'}\sin^2(\theta_{x'}) + I_x\sin^2(\theta_x) + 2\sqrt{I_x I_{x'}}\sin(\theta_{x'})\sin(\theta_x)\cos\left[2kx + \omega_z t\right] \\
\mathrm{Re}\left[E_y E_z^*\right] &= I_x\sin(\theta_x)\cos(\theta_x) + I_{x'}\sin(\theta_{x'})\cos(\theta_{x'}) + \sqrt{I_x I_{x'}}\cos\left[2kx + \omega_z t\right]\sin(\theta_x + \theta_{x'}).
\end{aligned} \tag{5.11}$$

Using these projections, the operator T can be decomposed as $T = T_x + T_{x'} + T_{x,x'}$. The first two terms correspond to the contributions of the two beams considered alone. The last term corresponds to the intereference component. These terms are given by :

$$\begin{aligned}
T_x &= 2I_x\left[\cos^2(\theta_x)J_z^2 + \sin^2(\theta_x)J_y^2\right] + 2I_x\sin(\theta_x)\cos(\theta_x)\{J_y, J_z\} \\
T_{x,x'} &= 4\sqrt{I_x I_{x'}}\cos\left[2kx + \omega_z t\right]\left[\cos(\theta_x)\cos(\theta_{x'})J_z^2 + \sin(\theta_x)\sin(\theta_{x'})J_y^2\right] \\
&\quad + 2\sqrt{I_x I_{x'}}\cos\left[2kx + \omega_z t\right]\sin(\theta_x + \theta_{x'})\{J_y, J_z\},
\end{aligned} \tag{5.12}$$

$T_{x'}$ being obtained by the same equation than T_x, replacing x by x'.

The total Hamiltonian derived from these three components is time-dependent. In particular, it oscillates at a frequency ω_z. We can remove the time-dependency by performing a rotating wave approximation.

Rotating wave approximation

In order to simplify the Hamiltonian, we consider the gauge transform $U = \mathrm{e}^{i\omega_z t J_z}$ and remove the fast oscillating terms within rotating wave approximation (RWA). In our system, we have two energy scales. The first one is the Zeeman energy, leading to a typical frequency $\omega_z \simeq 2\pi \times 380\,\mathrm{kHz}$. The second one is the energy scale provided by the Raman processes. Experimentally, we are typically using coupling amplitudes t_x, t_z of a few recoil energy, leading to the typical frequency $\omega_{\mathrm{LS}} \simeq 2\pi \times 10\,\mathrm{kHz}$. Hence, $\omega_z \gg \omega_{\mathrm{LS}}$. After the gauge transformation, the RWA will consist in removing the terms oscillating at multiple values of ω_z, whose contribution would otherwise averaged out. In the rotating frame, the Hamiltonian becomes :

$$H \to UHU^\dagger + i\hbar\frac{\mathrm{d}U}{\mathrm{d}t}U^\dagger. \tag{5.13}$$

The second term is equal to $-\hbar\omega_z J_z$ and cancels out with the Zeeman energy. The first term is more complicated to compute. It requires the derivation of $UJ_xU^\dagger$, $UJ_y^2U^\dagger$, $U\{J_y, J_z\}U^\dagger$ that can be performed using the Baker-Hausdorff formula[1]. We obtain :

$$\begin{aligned}
UJ_xU^\dagger &= \frac{\mathrm{e}^{i\omega_z t}}{2}J_+ + \frac{\mathrm{e}^{-i\omega_z t}}{2}J_- \\
UJ_z^2U^\dagger &= J_z^2 \\
UJ_y^2U^\dagger &= \frac{1}{4}\left[\{J_+, J_-\} - \mathrm{e}^{2i\omega_z t}J_+^2 - \mathrm{e}^{-2i\omega_z t}J_-^2\right] \\
U\{J_y, J_z\}U^\dagger &= \frac{1}{2i}\left[\mathrm{e}^{i\omega_z t}\{J_z, J_+\} - \mathrm{e}^{-i\omega_z t}\{J_z, J_-\}\right].
\end{aligned} \tag{5.14}$$

Then, we use these expressions to get the Hamiltonian in the rotating frame, neglecting the fast oscillating terms (ie, terms oscillating at multiple values of ω_z).

[1] $\mathrm{e}^A B\mathrm{e}^{-A} = B + [A, B] + \frac{1}{2!}[A, [A, B]] + ...$

We are left with :

$$H = H^{\text{static}} + H^{\text{spin-changing}}. \tag{5.15}$$

The first term of Eq. (5.15) conserves the spin of the state under study, and can be written as a combination of the operators $\mathbb{1}$ and J_z^2 :

$$\begin{aligned} H^{\text{static}} = &\left[U_x \frac{5+4\cos^2(\theta_x)}{2J+1} + U_{x'} \frac{5+4\cos^2(\theta_{x'})}{2J+1}\right] \mathbb{1} \\ &+ \left[U_x \frac{1-3\cos^2(\theta_x)}{2(J+1)(2J+1)} + U_{x'} \frac{1-3\cos^2(\theta_{x'})}{2(J+1)(2J+1)}\right] J_z^2. \end{aligned} \tag{5.16}$$

Within RWA, this term doesn't involve any interference term between the two beams.

The second term of Eq. (5.15) contains spin-changing term :

$$\begin{aligned} H^{\text{spin-changing}} = &\sqrt{U_x U_{x'}} \sin(\theta_{x'} - \theta_x) \frac{J(2J+3)}{4(J+1)(2J+1)} \left[i\mathrm{e}^{2ikx} \frac{J_-}{J} + \text{h.c}\right] \\ &+ \sqrt{U_x U_{x'}} \sin(\theta_{x'} + \theta_x) \frac{J^2}{2(J+1)(2J+1)} \left[i\mathrm{e}^{-2ikx} \frac{\{J_+, J_z\}}{2J^2} + \text{h.c}\right]. \end{aligned} \tag{5.17}$$

The term proportional to $\{J_+, J_z\}$ is not symmetric under the transformation $m \to -m$ and would lead to asymmetric Bloch bands. As a consequence, we choose $\theta_x = -\theta'_x$ such that this term cancels out. In particular, we choose $\theta_x = \text{acos}\left(1/\sqrt{3}\right)$ such that the quadratic spin term of H^{static}, that would lead to an important curvature of the ground band, also cancels out. For simplicity, we use $U_x = U_{x'}$.

We finally obtain the Hamiltonian induced by the beams propagating along the direction x, within RWA[1] :

$$\begin{aligned} H^{(x)} &= \frac{p_x^2}{2M} - t_x \left[\mathrm{e}^{-2ikx} \frac{J_+}{J} + \text{h.c}\right], \\ \text{with } t_x &= \frac{J(2J+3)}{4(J+1)(2J+1)} \sin(2\theta_x) U_x. \end{aligned} \tag{5.18}$$

5.1.2 Process (z) only

The derivation of the Hamiltonian created by the process (z) is similar. This time, we assume that the beams propagating along (z) are polarised σ_- and σ_+. They are detuned by Δ' and by $\Delta' - 2\omega_z$, where $\Delta' \simeq \Delta + 2\pi \times 20\,\text{MHz} \simeq \Delta + 50\omega_z$. We also suppose that the intensities of the two beams are equal.

Under the RWA at ω_z, we obtain in the rotating frame :

$$\begin{aligned} H^{(z)} &= \frac{p_z^2}{2M} - t_z \left[\mathrm{e}^{-2ikz} \frac{J_-^2}{J^2} + \text{h.c}\right] + \beta J_z^2, \\ \text{with } t_z &= -\frac{J^2}{2(J+1)(2J+1)} U_z, \\ \text{and } \beta &= -2t_z. \end{aligned} \tag{5.19}$$

[1] We dumped in this formula the term proportional to identity, which just creates an attractive potential on the atoms independent on the spin degree of freedom, thus not relevant for the physics we probe. Note that we also removed the $\pm\pi/2$ phase factor in front of J_-, J_+, that can be absorbed by changing the origin of times before performing RWA.

5.1.3 Combination of process (x) and process (z)

Combining the two previous Hamiltonian, we recover the Hamiltonian presented in the previous section :

$$\begin{aligned} H &= H^{(x)} + H^{(z)} \\ &= \frac{p_x^2 + p_z^2}{2M} - t_x \left[\mathrm{e}^{-2ikx} \frac{J_+}{J} + \mathrm{h.c} \right] - t_z \left[\mathrm{e}^{-2ikz} \frac{J_-^2}{J^2} + \mathrm{h.c} \right] + \beta J_z^2 \end{aligned} \tag{5.20}$$

This Hamiltonian results from the sum of the two contributions. It assumes no interferences between the x-propagating and the z-propagating beams. Experimentally, this condition is ensured by detuning the horizontal beams by 20 MHz with respect to the vertical beams. Indeed, the interferences between a x-propagating beam and a z-propagating beam lead to light shifts oscillating at typically $50\omega_z$, that are completely supressed within RWA.

We have shown in this paragraph how our Raman apparatus can create the Hamiltonian studied in the previous chapter. We will now describe our typical sequence to study this Hamiltonian experimentally.

5.2 Experimental sequence

The typical experimental sequence starts with the cold cloud preparation described in chapter I. After evaporative cooling, we are left with a cold cloud of $3.0(3) \times 10^4$ atoms at temperature $T = 260(10)$ nK under a magnetic field $|\boldsymbol{B}| \simeq 220$ mG. We then ramp up the Raman beams to emulate the 4D quantum Hall system.

The strength of our protocol relies in the ability to prepare individually any quasimomentum state $\boldsymbol{p} = (p, q)$ in the ground band. We detail it in the following paragraph.

5.2.1 Preparation of arbitrary momentum state in the ground band

The preparation of any quasimomentum in the ground band is performed in two steps. First, the atoms are loaded in the ground band at a given initial quasimomentum $\boldsymbol{p}_\mathrm{i}$. Secondly, the quasimomentum is adiabatically modified. Each of these steps requires to precisely control the system's quasimomentum.

Control of the quasimomentum

The control of the quasimomentum is enabled by considering an additional detuning ω_1 along x and ω_2 along z. These detunings are small compared to ω_z : their value is typically set by the recoil energy $\omega_\mathrm{rec} \simeq 2\pi \times 3$ kHz, much smaller than the Larmor frequency $\omega_z \simeq 2\pi \times 380$ kHz. As a consequence, we can't neglect within RWA the terms oscillating at ω_1 or at ω_2. The Hamiltonian becomes :

$$H = \frac{\boldsymbol{p}^2}{2M} - t_x \left[\mathrm{e}^{-i(2kx - \omega_1 t)} \frac{J_+}{J} + \mathrm{h.c} \right] - t_z \left[\mathrm{e}^{-i(2kz - \omega_2 t)} \frac{J_-^2}{J^2} + \mathrm{h.c} \right] + \beta \frac{J_z^2}{J^2} \tag{5.21}$$

For $\omega_1 = \omega_2 = 0$, this Hamiltonian is time-independent and associated with a stationnary wave. If $\omega_1 \neq 0$ or $\omega_2 \neq 0$, this Hamiltonian is time-dependent and is associated with a running wave. For given detunings, we can define a moving lattice in which the Hamiltonian is time-independent. This lattice has a velocity $\boldsymbol{v}_\mathrm{frame}$ in the lab frame :

$$\boldsymbol{v}_\mathrm{frame} = \frac{\omega_1 \hat{\boldsymbol{x}} + \omega_2 \hat{\boldsymbol{z}}}{2k} \tag{5.22}$$

By imposing detuning ramps, we can make the frame velocity time-dependent. Hence, the atomic motion in the moving frame is affected by an inertial force $\boldsymbol{F}(t) = -M\mathrm{d}\boldsymbol{v}_{\mathrm{frame}}/\mathrm{d}t$. Invoking Newton's second law, the change of quasimomentum in the moving frame is given by : $\mathrm{d}\boldsymbol{p} = -M\mathrm{d}\boldsymbol{v}_{\mathrm{frame}}$. Overall, any quasimomentum can be reached by changing the frame velocity via :

$$\boldsymbol{p} = \boldsymbol{p}_{\mathrm{i}} + M\boldsymbol{v}_{\mathrm{frame,i}} - M\boldsymbol{v}_{\mathrm{frame}}, \tag{5.23}$$

where $\boldsymbol{p}_{\mathrm{i}}$ and $\boldsymbol{v}_{\mathrm{frame,i}}$ are the initial momentum and the initial frame velocity.

The choice of the initial frame velocity should ensure a good overlap between the initial state $|m = -J\rangle$ and the ground state of the Hamiltonian at the initial quasimomentum (corresponding to the initial frame velocity). We propose to use initial detunings $\omega_1 = -\omega_2/2 \simeq 15E_{\mathrm{rec}}$, corresponding to an initial frame velocity $\boldsymbol{v}_{\mathrm{frame,i}} \simeq 8.38v_{\mathrm{rec}}\hat{\boldsymbol{\xi}}$. Before ramping up the Raman beams, the atoms are polarised in $|m = -J\rangle$ and are at rest in the lab frame, their velocity in the moving frame is thus given by $-\boldsymbol{v}_{\mathrm{frame,i}}$. Using the quasimomentum definition, $\boldsymbol{p} = M\boldsymbol{v} + 2\hbar k\langle J_z\rangle(\boldsymbol{k_\mu} + \boldsymbol{k_\nu}) \pmod{3\boldsymbol{k_\nu}}$, we obtain the initial value $\boldsymbol{p}_{\mathrm{i}} \simeq -15.5p_{\mathrm{rec}}\hat{\boldsymbol{\xi}} - 0.89p_{\mathrm{rec}}\hat{\boldsymbol{\nu}}$. As seen in the previous chapter, the ground state of the Hamiltonian for this quasimomentum is indeed very close to $|m = -J\rangle$. Using $\boldsymbol{v}_{\mathrm{frame,i}} \simeq 8.38v_{\mathrm{rec}}\hat{\boldsymbol{\xi}}$ is thus a good choice of initial frame velocity to load the atoms in the ground band.

Adiabatic preparation of a quasimomentum in the ground band

The Raman detunings are initially set to $\omega_1 = -\omega_2/2 \simeq 15E_{\mathrm{rec}}$ as seen before. Their intensities are then ramped up during $T_1 = 200\,\mu\mathrm{s}$ to $t_x = 8.2(6)E_{\mathrm{rec}}, t_z = 7.4(1)E_{\mathrm{rec}}$. This ramp in intensity should be slow enough to adiabatically load the atoms in the ground band. At this stage, we are in the ground band of the Hamiltonian, at the quasimomentum $\boldsymbol{p}_{\mathrm{i}} = -15.5p_{\mathrm{rec}}\hat{\boldsymbol{\xi}} - 0.89p_{\mathrm{rec}}\hat{\boldsymbol{\nu}}$.

We then apply detuning ramps (hence frame velocity ramps) to vary $\boldsymbol{p} = (p, q)$ to the desired value. We first ramp p up to $p = -2p_{\mathrm{rec}}$ in a time T_2. We then ramp q to the targeted value in a time T_3 and p to the desired value in T_4. Finally, we ramp down the couplings to reach $t_x = 5.69(6)E_{\mathrm{rec}}, t_z = 5.1(1)E_{\mathrm{rec}}$.[1] The durations T_3 and T_4 depend on the final values (p, q) we want to reach. The purpose of this sequence is to avoid as much as possible to cross the gap minima located on the edges of the Brillouin zone and depicted in figure Fig. 5.2 (in white) that could lead to a transfer towards excited bands via avoided crossing.

[1]The preparation could be done by directly ramping up the couplings during T_1 to $t_x = 5.69(6)E_{\mathrm{rec}}, t_z = 5.1(1)E_{\mathrm{rec}}$. However, we found out that it was more beneficial to perform the p, q-ramps at higher couplings. Indeed, the gaps are also higher in such case, which permits to perform adiabatic ramps at reduced times.

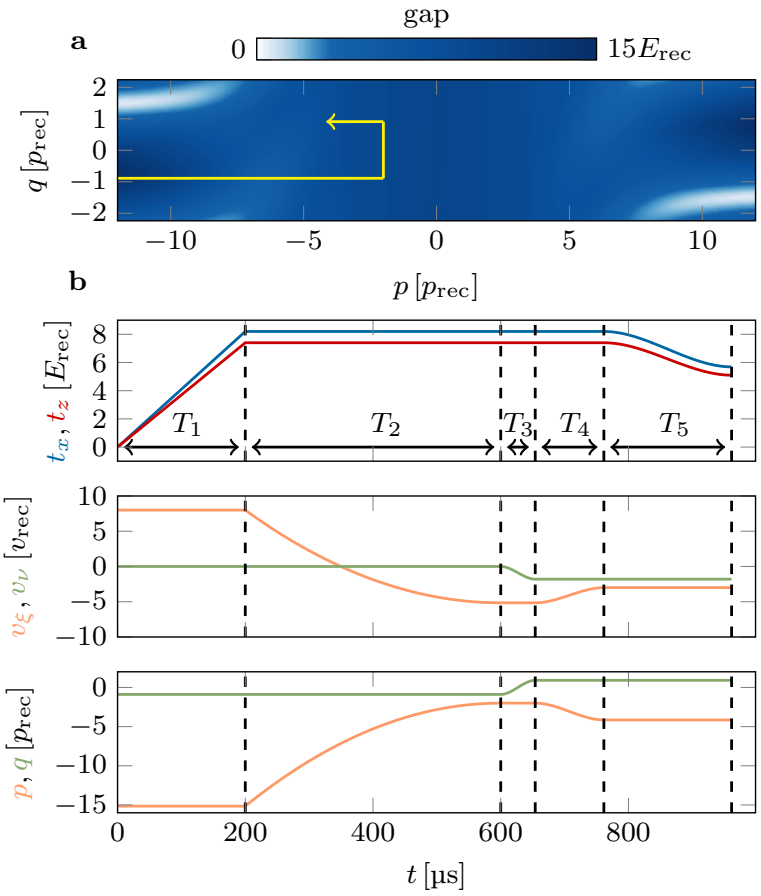

Figure 5.2: Loading in the ground band. **a** : We display the gap to the first excited band as a function of p and q. We display on yellow a typical evolution of p, q during the loading to a given quasimomentum. **b** : Experimental sequence corresponding to the yellow arrow drawn above. The first plot shows the evolution of the coupling values, the second the evolution of the frame velocity along the axis ξ and ν, and the final one shows the corresponding quasimomentum, in the moving frame.

Adiabaticity of the ramps

The ramp profile is adjusted so that the rate of momentum change is small compared to the band gaps, ensuring that the atoms remain in the ground band during the whole procedure. Interestingly, the gap is not constant over the Brillouin zone in our system, as seen Fig. 5.2. A diabatic change of (p, q) will gradually populate the excited bands. We check this in Fig. 5.3 by numerically simulating the preparation of a given state and computing the fidelity of the prepared state with the ground state, while ramping the quasimomentum from p_i, q_i to $-2p_{\mathrm{rec}}, q_i$ for different ramp durations. Moreover, the p and q-variations are smoothened to avoid any cusps that could lead to diabatic effects.

We choose the duration of the ramps by performing numerical simulations of adiabaticity, see Fig. 5.3. In the end, we use the following ramp durations. The first ramp in p is performed in $T_2 = 400\,\mu\mathrm{s}$. The ramp in q lasts for $T_4 = 30\,\mu\mathrm{s} \times \Delta q/p_{\mathrm{rec}}$, where Δq is the change of q-quasimomentum. The final ramp in p is made in $T_6 = 50\,\mu\mathrm{s} \times \Delta p/p_{\mathrm{rec}}$, where Δp is the change of p-quasimomentum.

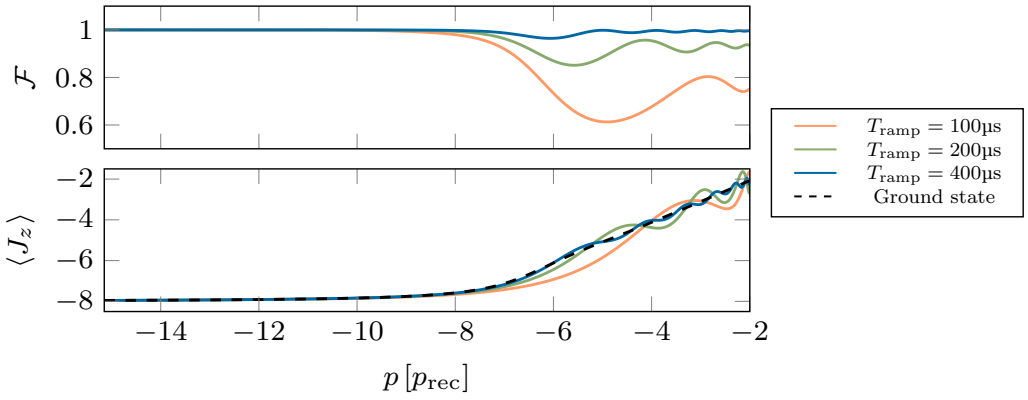

Figure 5.3: Adiabaticity of the loading (simulations). Top : Simulated fidelity between the prepared state and the ground state, during the first ramp in p, for three different ramping times. Bottom : Evolution of the mean magnetisation while the quasimomentum is changed. Non-adiabatic ramps result in a deviation between the mean magnetisation of the prepared state and the one of the ground state. We use in the simulations $t_x = 5.69E_{\mathrm{rec}}, t_z = 5.1E_{\mathrm{rec}}, \beta = -2t_z$.

To summarise, we use detuning ramps to control the system's quasimomentum. The protocol consists in interpreting the atomic motion in a moving frame, which velocity is controled by detuning ramps. In this moving frame, the Hamiltonian is time-independent and the atoms quasimomentum is changed by the inertial force associated with the frame acceleration.

5.2.2 Imaging and data analysis

Imaging

At the end of the preparation, we turn off the Raman beams and let the atomic cloud freely expand during 2.4 ms. A gradient of magnetic field is applied simultaneously (as described chapter I) and separates the different m states along the z axis. We then image the atoms and perform an algorithm to enhance the images quality (this algorithm is detailed in [78]). A typical experimental image is displayed in Fig. 5.4.

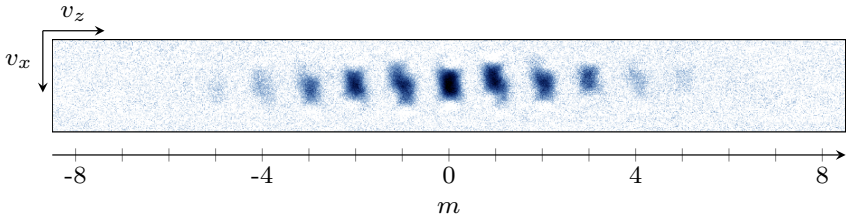

Figure 5.4: Exemple of absorption image after loading in the ground band. Detuning are chosen such that the atoms are in the state $\langle \boldsymbol{p} \rangle = \overrightarrow{0}$, corresponding to $\langle J_z \rangle \simeq 0$.

The Stern-Gerlach apparatus permits us to spatially separate the different m-sublevels. We can thus measure the populations in the m states and, by summing the population modulo 3, access the populations in the r states. We can obtain this way the average values $\langle m \rangle$ and $\langle r \rangle$. Moreover, the time-of-flight expansion probes the momentum distribution of the atomic cloud by recording the spatial distribution after a free fall. We can thus

infer the system's final mean velocity from the mean position of the cloud after time-of-flight.

Thermal broadening

As such, Fig. 5.4 is not easy to interpret. The reason is that Fig. 5.4 actually doesn't involve a single quasimomentum, but rather a distribution of quasimomenta, due to the cloud temperature. The width of the quasimomentum distribution, after the loading in the ground band, is typically $\sigma \simeq 1.4 p_{\text{rec}}$. The mean value of the distribution, $\langle \boldsymbol{p} \rangle = \overrightarrow{0}$ in the case of Fig. 5.4, is given by the detuning ramps.

Taking into account the thermal broadening, the conservation of the quasimomentum reads :

$$\langle \boldsymbol{v} \rangle = \frac{1}{M} \left[\langle \boldsymbol{p} \rangle - 2\hbar k m \hat{\boldsymbol{x}} + 3j\hbar \boldsymbol{k_\nu} \right], j \in \mathbb{Z} \tag{5.24}$$

Eq. (5.24) shows that the distribution of quasimomentum is reflected into a velocity distribution, leading to typical image displayed Fig. 5.4. If our atoms were at a much lower temperature after the detuning ramp, we should be able to detect after the Stern-Gerlach a discrete set of velocities, in agreement with :

$$\boldsymbol{v} = \frac{1}{M} \left[\boldsymbol{p} - 2\hbar k m \hat{\boldsymbol{x}} + 3j\hbar \boldsymbol{k_\nu} \right], j \in \mathbb{Z} \tag{5.25}$$

We propose to show some simulations of expected images to understand in more details this effect. For this, we numerically prepare the atoms in the ground band of the Hamiltonian under consideration. We set the detunings so that, on average, the atoms are in $\langle \boldsymbol{p} \rangle = \overrightarrow{0}$. We take into account the thermal broadening by considering a distribution of quasimomenta, centered around $\langle \boldsymbol{p} \rangle$. We also simulate the Stern-Gerlach experiment, which separated the Zeeman sublevels along the z axis.

Fig. 5.5a shows a simulated image with a quasimomentum distribution's width $\sigma \simeq 0.35 p_{\text{rec}}$. For a given m state, the quasimomentum conservation imposes that only a certain velocity class is accessible. Theoretically, this velocity class contains an infinite number of velocities, all separated by $3\hbar \boldsymbol{k_\nu}/M$. However, the probability to populate these velocity components is significant for only a few of them, explaining why we see typically 2 or 3 velocity components per m states in Fig. 5.5a. Then, we increase the width of the quasimomentum distribution (mimicking the effect of a temperature increase) in Fig. 5.5b,c,d. As the width of the quasimomentum distribution increases, all the clouds expand. They end up merging in Fig. 5.5d, which actually corresponds to the same quasimomentum distribution width that we have in the experiment. In the end, Fig. 5.5d is a numerical simulation of the experimental image displayed in Fig. 5.4.

The thermal broadening due to the finite temperature can be understood by the Doppler effect. Indeed, from the atoms point of view, the Raman beam frequencies are slightly shifted by the atom's velocities. If an atom is at rest in the lab frame, it feels the same light detunings than the one we expect, and he ends up in the desired quasimomentum state $\boldsymbol{p}_{\text{target}}$ after the detuning ramps. If an atom has a non-zero velocity (in the lab frame), he feels slightly different detunings, and ends up in a different quasimomentum state $\boldsymbol{p}_{\text{target}} + \Delta \boldsymbol{p}_{\text{thermal}}$.

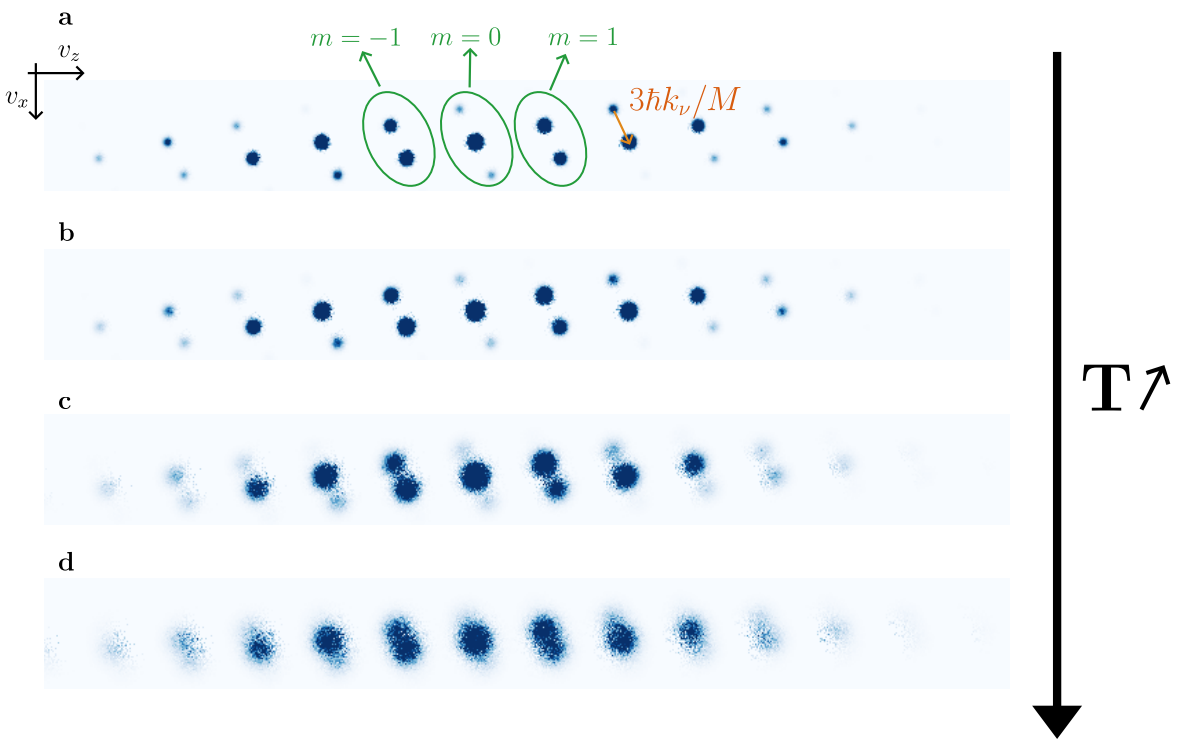

Figure 5.5: Numerical simulations of images after Stern-Gerlach. Effect of thermal broadening. Atoms are initially prepared in the ground band, for the same couplings used in the experiment, and at $\langle \boldsymbol{p} \rangle = \overrightarrow{0}$. **a** : The width of the quasimomentum distribution is $\sigma \simeq 0.35 p_{\text{rec}}$. We encircle in green the clouds belonging to $m = -1$, $m = 0$, $m = 1$. A given m state can be expanded on different velocities, separated by multiple of $3\hbar \boldsymbol{k_\nu}/M$, depicted in orange in the figure. **b** : $\sigma \simeq 0.47 p_{\text{rec}}$. **c** : $\sigma \simeq 0.93 p_{\text{rec}}$. **d** : $\sigma \simeq 1.4 p_{\text{rec}}$. The last situation corresponds to the typical exprimental conditions.

The effect ot thermal broadening is to blur the measured ground band properties, namely the spatial velocities on the spin populations along m and r, which is not ideal. However, as we will see later on, this thermal broadening can be deconvolve using the quasimomentum conservation.

Correction of experimental offsets

To interpret the image after time-of-flight correctly, we need to perform a few corrections. The first one consits in correcting the reached quasimomentum. Indeed, during the state preparation, the atoms feel the gravitational force, which modifies their quasimomentum (along the gravity direction, i.e $\hat{\boldsymbol{z}}$), so that the actual quasimomentum results from both the effect of the detuning ramps and gravity. The second correction consists in substracting the Stern-Gerlach contribution to measure accurately the system's mean velocity. This is done by independent calibrations of our Stern-Gerlach apparatus. Finally, we need to apply a more subtle correction which consists in substracting the drifts occuring during the state preparation. Indeed, during the state preparation, the atoms acquire a non-zero velocity in the lab frame due to the non-vanishing ground band curvature and to the change of frame. It leads to a displacement of the cloud *during* the state preparation, in the lab frame. As a consequence, the mean displacement of the cloud after time-of-flight doesn't directly provide the mean velocity of the system. To suppress this contribution, we take, for each final detunings, an image of the cloud without time-of-flight. We then use it as a reference to measure the cloud velocity after taking, for the same detunings, an image after time-of-flight.

We also emphasise that the measurements of the system velocity are performed in the lab frame. We then infer the system velocity in the relevant moving frame by performing, a posteriori, the relevant change of frame.

Deconvolution of the thermal broadening

As stated earlier, the thermal broadening blurs the measured ground band properties. It can be deconvolve via the quasimomentum conservation. Before implementing this deconvolution, we need to check the validity of the quasimomentum conservation in our experiment. To do so, we prepare the system in various states in the ground band, and infer, from the absorption imaging, the average velocity $\langle \boldsymbol{v} \rangle$ and the mean magnetisation $\langle m \rangle$ corresponding to these states. We then compute $\langle \boldsymbol{p} \rangle \equiv M\langle \boldsymbol{v} \rangle + 2\hbar k \langle m \rangle \pmod{3\boldsymbol{k}_{\boldsymbol{\nu}}}$ and compare it to the expected values of p and q inferred from the detuning ramps. The latter are given by $p = p_i - M\boldsymbol{v}_{\text{frame}} \cdot \hat{\boldsymbol{\xi}} + p_{\text{corr}}$ and $q = q_i - M\boldsymbol{v}_{\text{frame}} \cdot \hat{\boldsymbol{\nu}} + q_{\text{corr}}$. Here, we summarised in p_{corr} and q_{corr} the corrections to the targeted momentum due to gravity and experimental imperfections. We then compare the measured average momenta to the expected one. We display the results in Fig. 5.6. We observe a good agreement between the measured average momenta and the targeted momenta, showing that the conservation of thee quasimomentum is respected.

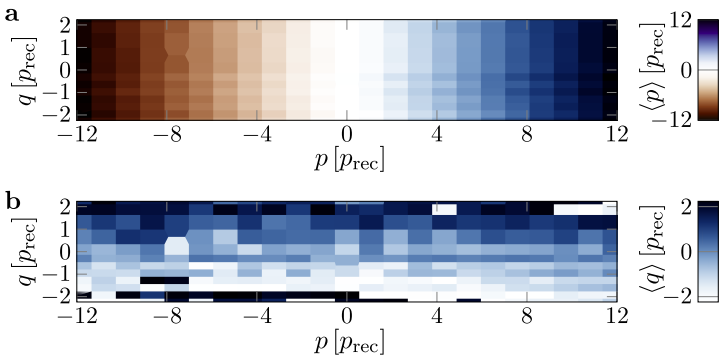

Figure 5.6: Experimental verification of the quasimomentum conservation. **a** : Measured value of $\langle p \rangle$ as a function of the expected p, q given by the detunings. **b** : Measured value of $\langle q \rangle$.

The deconvolution of the thermal broadening starts by measuring the spin-velocity density of states in the ground band. To obtain it, we sum the spin-resolved velocity distributions for various quasimomenta (uniformely spanning the Brillouin zone) to treat all the momenta on equal footing. We thus access to the averaged spin-resolved velocity distribution $\mathcal{D}_{\boldsymbol{p}}(m, \boldsymbol{v})$. By integrating these distributions over all momenta, we obtain the spin-velocity density of states of the ground band (see Fig. 5.7).

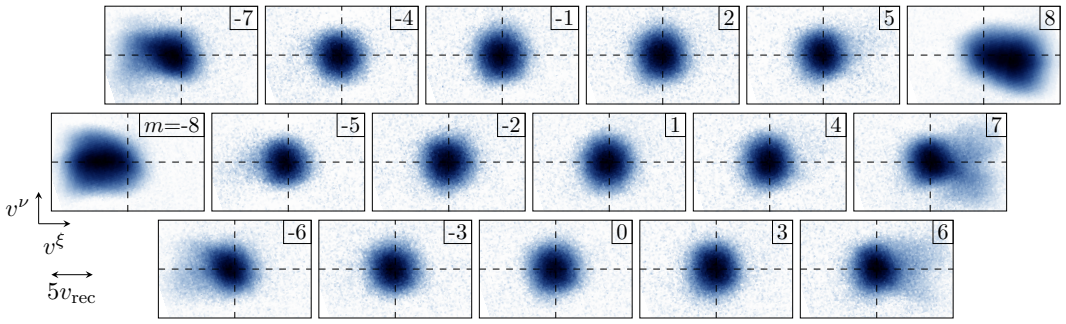

Figure 5.7: Experimental density of state, as a function of the velocity $\boldsymbol{v}$ and the magnetic projection m. The density of state is obtained by integration of the spin-resolved density of state over the momentum $\boldsymbol{p}$. Horizontal (resp. vertical) dashed lines indicate $v^\xi = 0$ (resp. $v^\nu = 0$).

Now that we have the density of states, we can implement the deconvolution. As seen earlier, the conservation of the quasimomentum imposes that each quasimomentum expends on a discrete set of velocities :

$$\boldsymbol{v} = \frac{1}{M}\left[\boldsymbol{p} - 2\hbar k m \hat{\boldsymbol{x}} + 3j\hbar \boldsymbol{k_\nu}\right], j \in \mathbb{Z} \tag{5.26}$$

Hence, for a given $\boldsymbol{p}$, we can sum all the contributions in the density of states to access the spin projections probability for this momentum $\Pi_m(\boldsymbol{p})$. By iterating this procedure for all momenta, we access to the spin projections probability in the full Brillouin zone.

We illustrate this in Fig. 5.8, considering only three m states (for simplicity). We first consider (in red) the quasimomentum $\boldsymbol{p} = (0, 0)$. Eq. (5.26) imposes that the velocity can take only certain values, depicted by red dots on the figure[1]. We see that this quasimomentum will have an important probability to be measured in $|m = 0\rangle$, and to a weak probability to be measured in $|m = \pm 8\rangle$, which was expected from our theoretical study of the previous chapter. Similarly, we show in green (resp. in orange) the velocities accessible to $\boldsymbol{p} = (1p_{\mathrm{rec}}, 0)$ (resp. to $\boldsymbol{p} = (0, 1p_{\mathrm{rec}})$). As anticipated, the respective contributions of the three quasimomenta in the density of state can be perfectly distinguished.

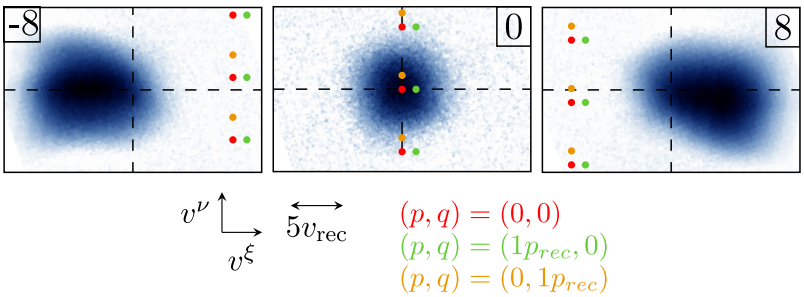

Figure 5.8: Illustration of the deconvolution of the quasimomentum. We display the density of states as a function of three values of m. Red dots correspond to the velocity class accessible to the quasimomentum $(p, q) = (0, 0)$. Similarly, green and orange dots respectively correspond to the velocity classes accessible to $(p, q) = (1p_{\mathrm{rec}}, 0)$ and $(p, q) = (0, 1p_{\mathrm{rec}})$.

Additionally, we show in Fig. 5.9 the velocities accessible to $(p, q) = (\pm 8p_{\mathrm{rec}}, 0)$. As expected, for negative values of p, the system is more likely to be measured in $|m = -8\rangle$ than in $|m = 0\rangle$ or $|m = 8\rangle$.

[1]Theoretically, an infinite number of velocities are accessible via Eq. (5.26). However, some velocities are more probable than others, which is why only a few of them are depicted on Fig. 5.8

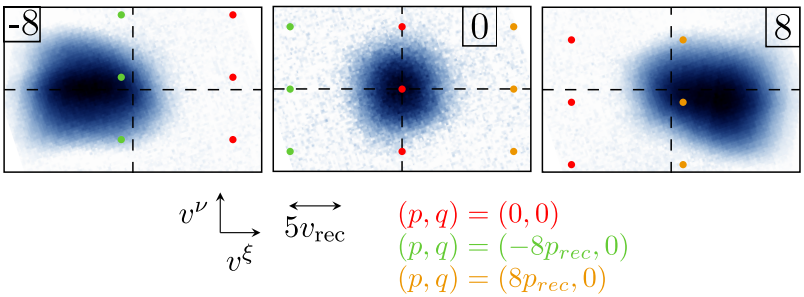

Figure 5.9: Illustration of the deconvolution of the quasimomentum for three other values of $\boldsymbol{p} = (p, q)$. We see that $(p, q) = (-8p_{\mathrm{rec}}, 0)$ have a higher probability to be in $|m = -8\rangle$ than in $|m = 0\rangle$ or $|m = 8\rangle$.

The measured spin projections probability Π_m provides a direct measurement of the mean spin projection $\langle m\rangle$ through :

$$\langle m\rangle \equiv \sum_m m\Pi_m. \tag{5.27}$$

We can also measure the mean value along the cyclic coordinate r via :

$$\langle r\rangle \equiv \frac{2\pi}{3}\left\langle \exp\left(i\frac{2\pi}{3}m\right)\right\rangle. \tag{5.28}$$

Following this method, we reconstruct the experimental ground band properties, that we display in the next paragraph.

As a sidenote, we stress that we can already see typical properties of a quantum Hall system on the spin-resolved density of states Fig. 5.7. Indeed, for $|m| \leq 5$, the density of states are centered around vanishing velocities, meaning that our system induces a frustration of motion in the bulk. Its not the case anymore on the edges $|m\rangle = \pm J$, where the density of states are shifted along $\pm v_\xi$ showing the existence of chiral edge modes on the boundaries. Moreover, these edge modes are anisotropic : the density of states are only shifted along ξ, while remaining around $v_\nu = 0$.

5.3 Experimental ground band properties

We display in the following the experimental ground band properties measured in the ground band as a function of p and q.

5.3.1 Spin properties

Fig. 5.10c shows the experimental spin projections, measured for the couplings $t_x = 5.69(6)E_{\mathrm{rec}}$, $t_z = 5.1(1)E_{\mathrm{rec}}$, $\beta = -2t_z$. Our measurement matches well with the theoretical predictions presented in the previous chapter. We present in Fig. 5.10a the spin projections along the direction $\hat{\boldsymbol{\mu}}$. As expected, $\langle m\rangle$ is evolving along this direction, while $\langle r\rangle$ is constant. Conversely, we present in Fig. 5.10b the spin projections along $\hat{\boldsymbol{\nu}}$. While $\langle m\rangle$ is constant, $\langle r\rangle$ is drifting when performing a Bloch oscillation. We also observe experimentally the chirality of r with the winding occuring at $q \simeq -0.9p_{\mathrm{rec}}$. This measurement shows that, in our experimental system, μ is indeed conjugated to m and ν is conjugated to r.

The evolution of the mean spin projections in the ground band can be interpreted as anomalous Hall drift via :

$$\mathrm{d}\langle r^\mu\rangle = F^{\mu\nu}\mathrm{d}p_\nu \tag{5.29}$$

By fitting the spin mean projection evolutions with p and q in the bulk, we measure the following Berry curvature components :

$$\{F^{rx}, F^{rz}, F^{mx}, F^{mz}\} = \{-1.00(2), -0.98(2), -0.98(2), 1.96(2)\}/(2k). \tag{5.30}$$

These values are consistent with the expected Berry curvature tensor in the bulk, obtained by inverting the magnetic field tensor [151], defined in the previous chapter :

$$F_{\text{bulk}} = B^{-1} = \frac{1}{2k}\begin{bmatrix} 0 & 0 & 1 & 1 \\ 0 & 0 & 1 & -2 \\ -1 & -1 & 0 & 0 \\ -1 & 2 & 0 & 0 \end{bmatrix} \tag{5.31}$$

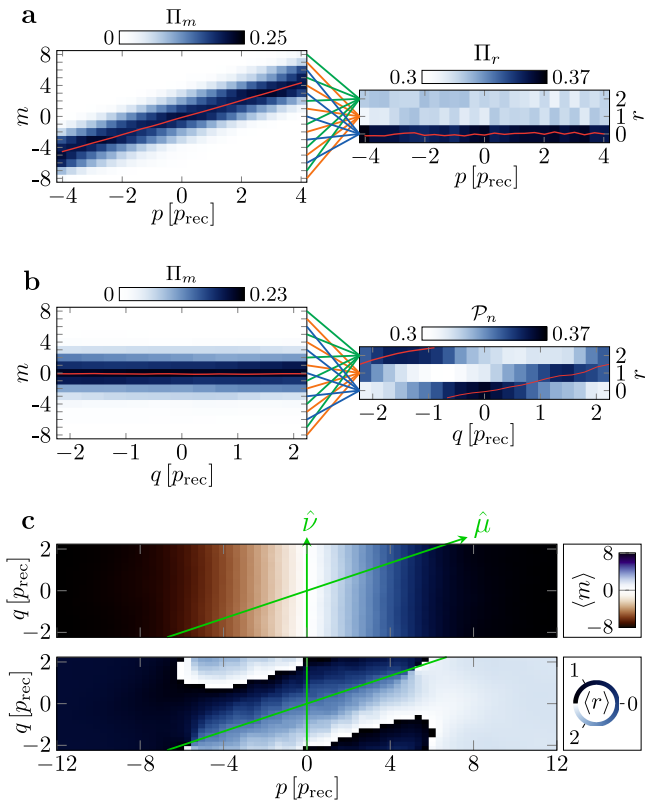

Figure 5.10: Experimental ground band spin properties. **a** : Evolution of the populations along m and along r while the quasimomentum is evolving along $\hat{\boldsymbol{\mu}}$. Mean values $\langle m \rangle$, $\langle r \rangle$ are displayed in red. **b** : Evolution of the populations while the quasimomentum is evolving along $\hat{\boldsymbol{\nu}}$. **c** : Experimental mean values $\langle m \rangle$, $\langle r \rangle$ as a function of p, q.

5.3.2 Velocity properties

Fig. 5.11a shows the measured velocities in the ground band. For $|p| < p^* = 7p_{\text{rec}}$ we measured a vanishing velocity, illustrating that there is a frustration of motion in the bulk of our system. It is consistent with the theoretical dispersion relation presented in the previous chapter. This is not the case anymore on the boundaries $m = \pm J$, that are approached for $|p| > p^*$ (see Fig. 5.10), where the velocity is, mostly, pointing along $\pm\hat{\boldsymbol{\xi}}$. Additionally, these edge modes are chiral : they are oriented along $+\hat{\boldsymbol{\xi}}$ for $p > p^*$ and along $-\hat{\boldsymbol{\xi}}$ for $p < -p^*$. We highlight this behavior Fig. 5.11b where we plot the q-averaged velocity as a function of p.

The measured velocities of these edge modes can be interpreted considering a fermionic quantum Hall insulator. The edge modes typically arise at the Fermi momentum $p_F \simeq p^*$ corresponding to a Fermi energy equal to the bulk gap : $E_{\mathrm{F}} \simeq 5E_{\mathrm{rec}}$. Assuming a ballistic motion, the corresponding Fermi velocity can be obtained by $v_{\mathrm{F}} \simeq \pm\sqrt{2E_{\mathrm{F}}/M} \pm 2.2v_{\mathrm{rec}}$. This value is consistent with the measured value at this momentum : $\langle v\rangle = -1.4(2)v_{\mathrm{rec}}$ at $p = -p^*$ and $\langle v\rangle = 1.6(2)v_{\mathrm{rec}}$ at $p = p^*$.

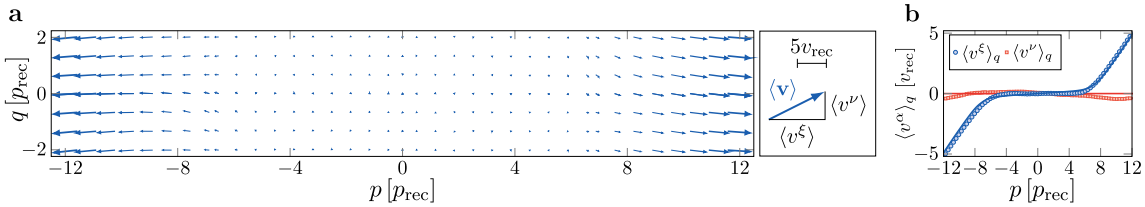

Figure 5.11: Experimental ground band velocities. **a** : Measured velocity as a function of p, q. **b** : q-averaged velocities. The averaged velocity along ν remains close to 0, while the averaged velocity along ξ is vanishing in the bulk but exhibit ballistic behavior on the edges.

To summarise, as anticipated in the previous chapter, we detected anisotropic chiral edge modes at the boundaries of our 4D quantum Hall system. This measurement is a typical feature of 4D physics. Moreover, the velocity of these edge modes can be easily interpreted considering a fermionic 4D quantum Hall insulator.

5.3.3 Berry curvatures

The velocity properties of the ground band provide an other measurement of the Berry curvature components, considering the $\boldsymbol{p}$-variations of the measured velocities. The idea consists in considering additional gauge fields A_m, A_r along the synthetic dimensions and in computing the induced spatial displacement due to these additional gauge fields. We detail the derivation in [141]. It leads to the following expression of Berry curvature components, after considering a projection along $\hat{\boldsymbol{\xi}}$ and $\hat{\boldsymbol{\nu}}$:

$$\begin{aligned}
F^{\xi r} &= \frac{1}{2\sqrt{5}k}\left[1 - M\frac{\partial\langle v^\xi\rangle}{\partial p} + 3M\frac{\partial\langle v^\xi\rangle}{\partial q}\right] \\
F^{\nu r} &= \frac{1}{2\sqrt{5}k}\left[-3 - M\frac{\partial\langle v^\nu\rangle}{\partial p} + 3M\frac{\partial\langle v^\nu\rangle}{\partial q}\right] \\
F^{\xi m} &= \frac{\sqrt{5}}{2k}\left[-1 + M\frac{\partial\langle v^\xi\rangle}{\partial p}\right] \\
F^{\nu m} &= \frac{\sqrt{5}}{2k}M\frac{\partial\langle v^\nu\rangle}{\partial p}
\end{aligned} \tag{5.32}$$

From these expressions and from Fig. 5.11, we can access the experimental Berry curvature components. We display figure Fig. 5.12 their $q-$averaged value. We also display in solid lines the theoretical bulk values, obtained by putting to 0 the derivatives of the velocity components. We obtain a good agreement between the measurements and the expected bulk values.

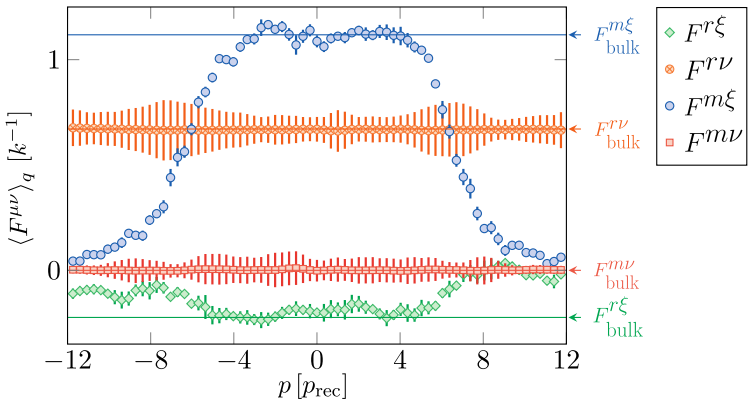

Figure 5.12: Experimental Berry curvature components. The Berry curvature components are deduced from the measured velocity. We display in straight line the theoretical value in the bulk. $F^{r\nu}$ and $F^{m\nu}$ are quasi-flat because the velocity along ν itself exhibits only very little variations in the Brillouin zone.

Equivalently, after proceeding to a projection along $\hat{\boldsymbol{x}}$ and $\hat{\boldsymbol{z}}$, and considering the bulk only, we recover the values inferred by inverting the magnetic field tensor, i.e : $\{F^{rx}_{\mathrm{bulk}}, F^{rz}_{\mathrm{bulk}}, F^{mx}_{\mathrm{bulk}}, F^{mz}_{\mathrm{bulk}}\} = \{-1, -1, -1, 2\}/(2k)$.

The good agreement between the experimental ground band properties and Eq. (5.29) shows that our system can be, up to a good approximation, understood as a direct sum of 2D Landau levels, as detailed previously with our continuous model.

5.4 Cyclotron orbits

We have studied theoretically in the previous chapter the peculiar cyclotron orbits in 4D. We show in this paragraph our experimental realisation of such orbits, starting with the protocol to trigger these orbits.

5.4.1 Experimental Protocol

Experimentally, we prepare analogues to the cyclotron orbits by preparing excitations of the systems, that are referred to as magneto-plasmons [44]. They consist in a coherent superposition of different Landau levels and their dynamics is governed by the Larmor frequencies.

We induce excitations of the system by performing a quench of the Raman detunings, i.e a quench of the quasimomentum. The experimental sequence starts by preparing the system in a given momentum $\boldsymbol{p}$ as described previously. We then quench $\boldsymbol{p}$ by $\boldsymbol{p}_{\mathrm{quench}}$. As a consequence, the system is not anymore in the ground state of the Hamiltonian and can be described as a coherent superposition of contributions from the different energy bands. The quench strength and direction need to be carefully adjusted.

The quench strength controls the number of populated bands after the excitation. If it is too weak, the system remains essentially in the ground band and we don't observe cyclotron trajectory given our signal-to-noise ratio. If it is too strong, many bands are populated and the resulting dynamics is quite complicated to interpret.

On the other hand, the quench direction dictates which excited band is mostly populated. Indeed, as seen on the continuous model developed in the previous chapter, the first two excited bands concern independently excitations in the $(x, m + r)$ plane and excitations in

the $(z, 2m - r)$ plane. Consequently, quenching the quasimomentum along x or along z independently triggers oscillations of v_x or v_z, of respective frequency ω_x, ω_z.

We propose Fig. 5.13 a scheme of the protocol to trigger cyclotron oscillations.

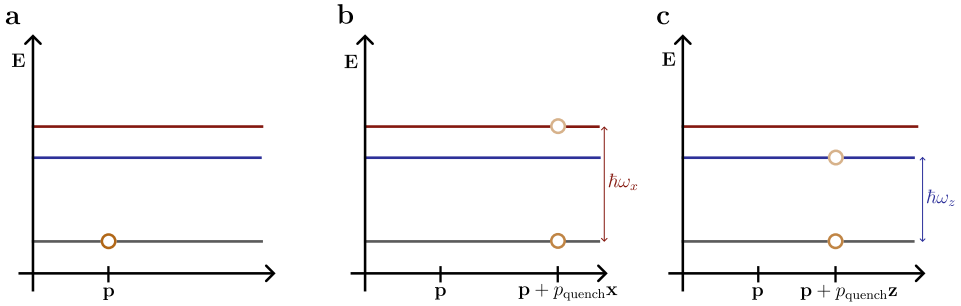

Figure 5.13: Cyclotron orbits protocol. **a** : The system is initially prepared in the ground state of the Hamiltonian in a given quasimomentum $\boldsymbol{p}$. **b** : After a quench of the quasimomentum along $\hat{\boldsymbol{x}}$, the state of the system is a coherent superposition of the ground band and of the second excited band. **c** : After a quench of the quasimomentum along $\hat{\boldsymbol{z}}$, the state of the system is a coherent superposition of the ground band and of the first excited band.

5.4.2 Independent excitations

We first show experimental results of independent excitations in Fig. 5.14. We prepare the system in the ground band of the Hamiltonian, and then quench in three different directions to reach $(p, q) = (0, 0)$. We then hold for various waiting times, and measure the spatial velocity of the system. For the left column, $\boldsymbol{p}$ is quenched by $(p_{\text{rec}}/\sqrt{2})\hat{\boldsymbol{z}}$. For the middle column, $\boldsymbol{p}$ is quenched by $\sqrt{2}p_{\text{rec}}\hat{\boldsymbol{x}}$. The right column results from a quench of the quasimomentum by $(p_{\text{rec}}/\sqrt{2})\hat{\boldsymbol{x}} + \sqrt{2}p_{\text{rec}}\hat{\boldsymbol{z}}$. We adjust the light couplings such that the two hopping amplitudes differ a lot : $t_x \simeq 16.5E_{\text{rec}}$ and $t_z \simeq 5E_{\text{rec}}$. The purpose of this adjustement is to make more clear the existence of two different Larmor frequencies.

After a quench along $\hat{\boldsymbol{z}}$ (Fig. 5.14, left column) the system mostly oscillates along $\hat{\boldsymbol{z}}$, the fitted amplitude being 10 times higher for v_z than for v_x. The fitted frequency $f = 46(1)\,\text{kHz}$ is in good agreement with $f_z = 4\sqrt{E_{\text{rec}}t_z}/h \simeq 51\,\text{kHz}$. The discrepency can be explained by the fact that the measured oscillations are damped[1] while the fitting is performed with a pure sinusoidal function, and by the fact that the continuous model doesn't perfectly match the Hamiltonian dispersion relation (see Fig.20 of the previous chapter).

Similarly, after a quench along $\hat{\boldsymbol{x}}$ (Fig. 5.14, middle column), the system mostly oscillates along $\hat{\boldsymbol{x}}$. This time, the frequency of the oscillations is much smaller and given by $f = 23(1)\,\text{kHz}$. We were expecting a frequency of $\omega_x = 4\sqrt{E_{\text{rec}}t_z}/h \simeq 29\,\text{kHz}$. As before, the discrepency can be explained by the damping of the oscillations and by the imperfection of the continuous model.

When quenching along a mixed direction (Fig. 5.14, right column), namely $(\hat{\boldsymbol{x}} + \hat{\boldsymbol{z}})/\sqrt{2}$, both velocities are excited. v_x is oscillating at f_x and v_z at f_z, with similar amplitudes than the case of the independent oscillations.

These experiments show that our system has two Larmor frequencies, determined by the hopping amplitudes t_x, t_z. As expected, each of these Larmor frequencies is involved in a different plane, one including the x direction, the other including the z direction. It illustrates that our system can be seen as a direct sum of a pair of 2D Landau levels.

[1] the damping is not expected at this level theoretically. Experimentally it could be due to inhomogeneous light intensity profile or small diabatic effect in the initial state preparation.

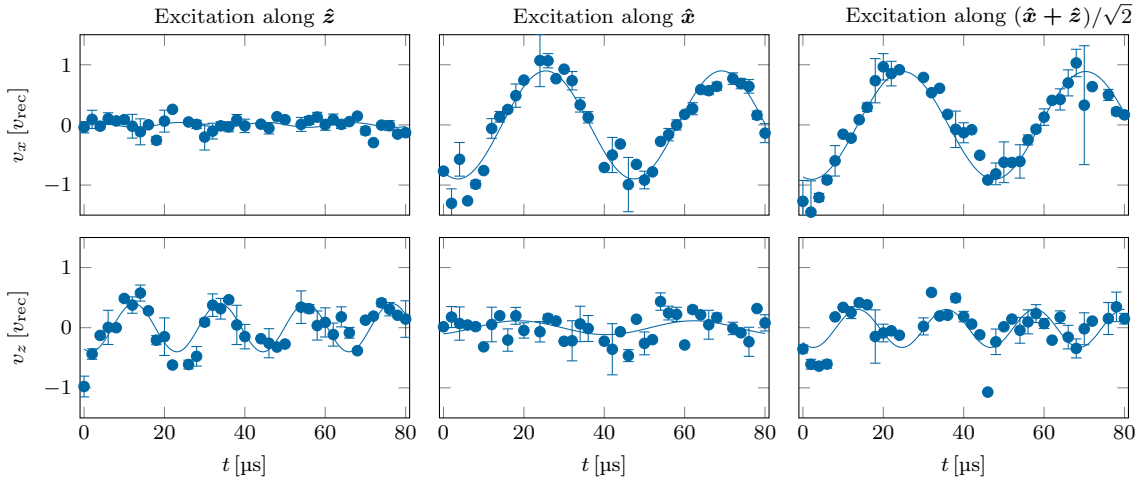

Figure 5.14: Experimental cyclotron trajectory in the (x, z) plane. The data are fitted with damped oscillations. The cyclotron trajectory are measured for $t_x \simeq 16.5E_{\mathrm{rec}}$ and $t_z \simeq 5E_{\mathrm{rec}}$. Left : Response of the system after a quench of the quasimomentum along $\hat{\boldsymbol{z}}$, only v_z is oscillating. Middle : After a quench of the quasimomentum along $\hat{\boldsymbol{x}}$, only v_x is oscillating. Right : after a quench along $(\hat{\boldsymbol{x}} + \hat{\boldsymbol{z}})\sqrt{2}$, both v_x and v_z oscillate.

5.4.3 Lissajous orbits

As seen in the previous chapter, the cyclotron trajectories in 4D are richer than their 2D and 3D counterparts, involving two frequencies in two different planes. We show in Fig. 5.15 such 4D orbits, for two different sets of Larmor frequencies. The experimental realisation of these orbits follows the protocol described above. The atoms are initially prepared in the center of the Brillouin zone, and the quasimomentum is quenched in a mixed direction $(\hat{\boldsymbol{x}}+\hat{\boldsymbol{z}})/\sqrt{2}$, such that the two excitations are triggered. The initial state is prepared with the desired coupling strengths. The center-of-mass positions in the spatial dimensions are recovered by time-integrating the measured velocities.

We first adjust the coupling such that the Larmor frequencies are roughly equal $\omega_z \simeq \omega_x$, see Fig. 5.15a,b. We are in the regime of an 'isoclinic' rotation, the trajectory is quasi-closed.

We then adjust the couplings such that the Larmor frequencies are separated by a ratio of 2 : $\omega_z \simeq 2\omega_x$, see Fig. 5.15c,d. The trajectory is still closed, but not planar anymore. After two periods $T = 2\pi/\omega_z$, the four coordinates x, z, m, r are roughly back to their initial values.

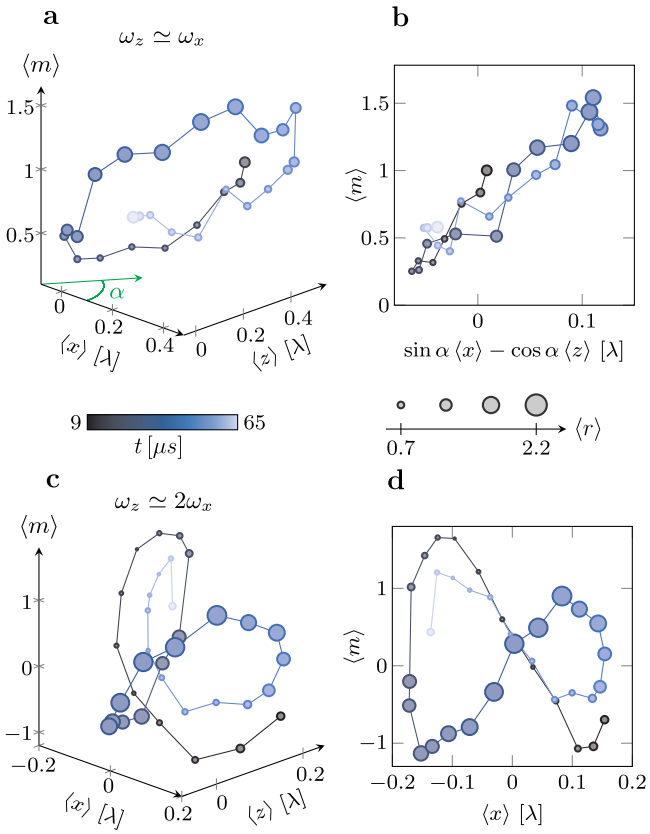

Figure 5.15: Cyclotron dynamics. Evolution of the atoms position in the 4D space (x, z, r, m) following a quasimomentum excitation for two different ratio of Larmor frequencies. Time is encoded in color and $\langle r \rangle$ is encoded in the size of the points. **a** : Cyclotron trajectory for $\omega_z \simeq \omega_x$. The green arrow shows the viewpoint for the planar projection shown in **b**. **b** : Two-dimensional projection illustrating the planar nature of the orbit, viewed from the side. **c** : Cyclotron trajectory for $\omega_x \simeq 2\omega_x$. **d** : Two-dimensional projection in the ${}^{x}m$ plane, illustrating the closed aspect of the trajectory, after two periods $T \simeq 2\pi/\omega_z$.

To our knowledge, these measurements consist in the first observation of the complex nature of the cyclotron orbits in four dimensions, which have no equivalent in lower dimensions.

In the next paragraph, we study experimentally the topology of our system and reveal properties closely related to its higher dimensionality.

5.5 Non-trivial topology

The non-trivial topological aspect of our system was unveiled by the existence of edge modes at the system boundaries, via the bulk-edge correspondence [51]. In this section, we propose an other evidence of the non-trivial topological properties of our system, focusing on the bulk region.

5.5.1 Second Chern number measurement

The second Chern number C_2 can be inferred from the measured Berry curvature. As seen in the previous chapter, our system being gapless, we should not consider the system as a whole

to consider its topological response but focus on the bulk region, via the local second Chern marker $C_2(m)$ [108]. Its measurement relies on a non-linear combination of the measured Berry curvatures. The second Chern marker can be measured using the measured Berry curvature components and spin projection probabilities via [141]:

$$C_2(m) = \frac{1}{3}\int_{\text{bulk}} \mathrm{d}p\mathrm{d}q\Pi_m(p,q)\rho_2(p,q), \tag{5.33}$$

where the second Chern character ρ_2 is obtained by a non-linear combination of the measured Berry curvature components.

We show Fig. 5.16a the experimental second Chern character in the Brillouin zone. We measure a constant second Chern character in the bulk $\rho_2 \simeq 0.75(7)/k^2$, consistent with the theoretical value $3/(4k^2)$. Using this measurement together with the spin population measurements, we can access the local second Chern marker. We display its value Fig. 5.16b. In the region $|m| \leq 5$, we get $C_2(m) \simeq 0.97(6)$, in agreement with the expected value $C_2 = 1$ for a quantum Hall system of class A in dimension 4.

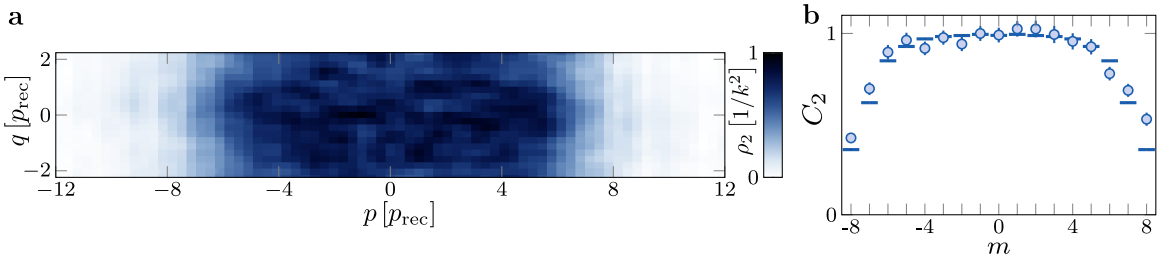

Figure 5.16: Topology of the ground band. **a** : Second Chern character in the ground band, deduced from the measured Berry curvature components. **b** : Local second chern number deduced from **a**. Experimental values are displayed with the dots, theory with the horizontal lines.

5.5.2 Non-linear electromagnetic response

As seen in the previous chapter, the transport, via the non-linear electromagnetic response, is quantised in 4D by the second Chern number. We recall that this response consists, for a filled band, in an additional term in the current density induced by an electromagnetic perturbation :

$$j^\mu = \frac{E_\nu}{(2\pi)^4}\int_{BZ} F^{\mu\nu}\mathrm{d}\boldsymbol{k} + \frac{C_2}{2\pi^2}\epsilon^{\mu\nu\gamma\delta}E_\nu B_{\gamma\delta}, \tag{5.34}$$

where E_ν and $B_{\gamma\delta}$ are the electromagnetic perturbation. The standard topological experiment to probe this non-linear response would be to have a fermionic insulator filling the ground band of our system and to apply an electric perturbation along a direction, orthogonal to a magnetic field perturbation. We would expect to measure a current proportional to the electric and the magnetic perturbation along the fourth direction. However, as seen before, we use bosons and prepare wavepackets centered at a given quasi momentum $\langle \boldsymbol{p} \rangle$. Thus, we can't probe the non-linear response as described in Eq. (5.34).

We propose in this paragraph to detect a modified version of the non-linear response, assuming that our system is homogeneous. This hypothesis was theoretically verified in the last part of the previous chapter, and is valid for high enough coupling strengths. We also assume that the magnetic perturbation contains only two components : $B_{rm} = -B_{mr}$ and that the electric perturbation is fully oriented along $\hat{\boldsymbol{\nu}}$.

The Berry curvature is modified by the magnetic perturbation and can be expressed, at first-order, as $\tilde{F} = F + F^{(1)}$, where $F^{(1)}$ is the contribution due to the magnetic perturbation. The Berry curvature tensor can be obtained by inverting the magnetic field tensor [151]. It becomes :

$$\begin{aligned} \tilde{F} &= F + F^{(1)} \\ \tilde{F} &= \frac{1}{2k}\begin{bmatrix} 0 & 0 & 1 & 1 \\ 0 & 0 & 1 & -2 \\ -1 & -1 & 0 & 0 \\ -1 & 2 & 0 & 0 \end{bmatrix} + \frac{3}{4k^2}\begin{bmatrix} 0 & -B_{rm} & 0 & 0 \\ B_{rm} & 0 & 0 & 0 \\ 0 & 0 & 0 & 0 \\ 0 & 0 & 0 & 0 \end{bmatrix} \end{aligned} \tag{5.35}$$

We will now re-express Eq. (5.34) under these hypothesis.

As detailed in [60], the current density is given by :

$$j^{\mu} = \int_{BZ} \mathrm{d}\boldsymbol{k} D\left(\boldsymbol{r}, \boldsymbol{k}\right) v^{\mu}\left(\boldsymbol{k}\right), \tag{5.36}$$

where $D\left(\boldsymbol{r}, \boldsymbol{k}\right)$ is the modified phase-space density of states and $\boldsymbol{r}$ the 4D positional vector. The general expression of the modified phase-space density of states in four dimensions can be expressed as [60, 149] :

$$D\left(\boldsymbol{r}, \boldsymbol{k}\right) = \frac{1}{(2\pi)^4}\left[1 + \frac{1}{2}B_{\mu\nu}\tilde{F}^{\mu\nu} + \frac{1}{64}\left(\epsilon^{\alpha\beta\gamma\delta}B_{\alpha\beta}B_{\gamma\delta}\right) \times \left(\epsilon^{\mu\nu\lambda\rho}\tilde{F}^{\mu\nu}\tilde{F}^{\lambda\rho}\right)\right], \tag{5.37}$$

Eq. (5.37) can be greatly simplified assuming that the only components of the magnetic perturbation are B_{rm} and B_{mr}. We are left with :

$$\begin{aligned} D\left(\boldsymbol{r}, \boldsymbol{k}\right) &= \frac{1}{(2\pi)^4}\left[1 + \frac{1}{2}B_{rm}\tilde{F}^{rm} + \frac{1}{2}B_{mr}\tilde{F}^{mr}\right] \\ &= \frac{1}{(2\pi)^4}, \end{aligned} \tag{5.38}$$

where we have used $\tilde{F}^{mr} = \tilde{F}^{rm} = 0$.

For our system, the transport equation thus reads :

$$j^{\xi} = \int_{\mathrm{BZ}} \mathrm{d}\boldsymbol{k}\frac{v^{\xi}}{(2\pi)^4} = \frac{E_{\nu}}{(2\pi)^4}\int_{\mathrm{BZ}} F^{\xi\nu}\mathrm{d}\boldsymbol{k} + \frac{1}{(2\pi)^4}\int_{\mathrm{BZ}} \rho_2 E_{\nu} B_{mr}, \tag{5.39}$$

where there is no implicit summation on the indices ξ, ν. In our plateform, we have only access to the response of individual wavectors $\boldsymbol{k}$. We thus focus on the integrands in the following. This choice is also motivated by the fact that, at our laser couplings, our system can be considered as homogeneous, at least in the bulk. Using the fact that $F^{\xi\nu} = 0$, we obtain a *local* expression that illustrates the non-linear response contribution for a given wavevector :

$$v^{\xi}_{NL}(\boldsymbol{k}) = \rho_2(\boldsymbol{k}) E_{\nu} B_{mr} \tag{5.40}$$

In order to unveil this local non-linear response experimentally, we need to add an electromagnetic field perturbation. We propose to add a perturbative B_{rm} field to our experimental system. The electric perturbation is simulated by the detuning ramps, leading to a force that we can interpret as a Lorentz force $\boldsymbol{F} = q\boldsymbol{E}$, which orientation can be carefuly chosen by the choice of the detuning ramps.

Implementation of a B_{rm} field

Similarly to the B_{mx} field arising from x-dependent phase when hopping from m to $m+1$, we can emulate a B_{rm} field when making the hoppings $r \to r+1$ coming together with a phase dependent on m.

To do so, we propose to change the polarisation of one of the two Raman beams propagating along x to circular polarisations $\sigma_\pm$. The spin-dependent light shift induced by the pair propagating along x becomes :

$$V_{x'} = -t'_x \mathrm{e}^{-2ikx} \frac{J_+ + (\gamma + i\epsilon)\{J_+, J_z\}/2}{J} + \mathrm{h.c} + \beta' \frac{J_z^2}{J^2}, \tag{5.41}$$

where $t'_x = 3t_x/4$, $\beta' = J^2 t'_x/(4\sqrt{2}(2J+3))$, $\epsilon = \pm 4\sqrt{2}/(3(2J+3))$ and $\gamma = |\epsilon|/\sqrt{8}$. The spin operator J_+ is thus changed to $J_+ + \dfrac{\gamma + i\epsilon}{2}\{J_+, J_z\}$.

The effect of this new spin-hopping term on a Dicke state $|m\rangle$ is :

$$\begin{aligned}\left[J_+ + \frac{\gamma + i\epsilon}{2}\{J_+, J_z\}\right]|m\rangle &= a_m \left[1 + \frac{\gamma}{2}(2m+1) + i(\epsilon m + \epsilon/2)\right]|m+1\rangle \\ &\simeq a_m \mathrm{e}^{i(\epsilon m + \epsilon/2) + \gamma(2m+1)/2}|m+1\rangle,\end{aligned} \tag{5.42}$$

where we Taylor-expanded the exponential term, using $\epsilon \ll 1$ and $\gamma \ll 1$. We also introduced $a_m = \sqrt{J(J+1) - m(m+1)}$, the hopping amplitude due to the ladder spin operator. The phase component $\mathrm{e}^{i\epsilon/2}$ can be gauged away, such that we are left with :

$$\left[J_+ + \frac{\gamma + i\epsilon}{2}\{J_+, J_z\}\right]|m\rangle \simeq a_m \mathrm{e}^{\gamma(2m+1)/2}\mathrm{e}^{i\epsilon m}|m+1\rangle. \tag{5.43}$$

The phase ϵm is at the origin of a B_{rm} field. Indeed, using this new algebra of spin transitions and interpreting the phase of these spin transitions as Peierls phase, we can obtain the new potential vector $\boldsymbol{A}$ via :

$$\begin{aligned}\phi_x &= A_r + A_m = 2kx + \epsilon m \\ \phi_z &= A_r - 2A_m = 2kz,\end{aligned} \tag{5.44}$$

leading to $\boldsymbol{A} = (0, 0, 4kx + 2kz + 2\epsilon m, 2kx - 2kz + \epsilon m)/3$.

We finally obtain the magnetic perturbation B_{rm} via $B_{rm} = \partial_r A_m - \partial_m A_r = -2\epsilon/3$. The sign of this perturbation can be flipped by switching the polarisation from σ_- to σ_+. When the polarisation is set back to a linear polarisation, the perturbation goes to 0.

Modified ground band dispersion

The dispersion relation is slightly modified by this new spin algebra, see Fig. 5.17. More particularly, the ground band is now tilted in the bulk. The band deformation is due to the terms $\beta' J_z^2$ and $\gamma\{J_+, J_z\}$. We emphasise that this band deformation is not a consequence of the B_{rm} perturbation itself, but is rather a consequence of the way we implement this perturbation in our system. The band dispersion is similar for the cases $B_{rm} \simeq \pm 0.0661$. It can be explained by the fact that, for the two possible circular polarisations, the terms $\beta' J_z^2$ and $\gamma\{J_+, J_z\}$ are the same, whereas the value of the artificial B_{mr} field is only given by the term $i\epsilon\{J_+, J_z\}$, whose sign doesn't affect the dispersion relation.

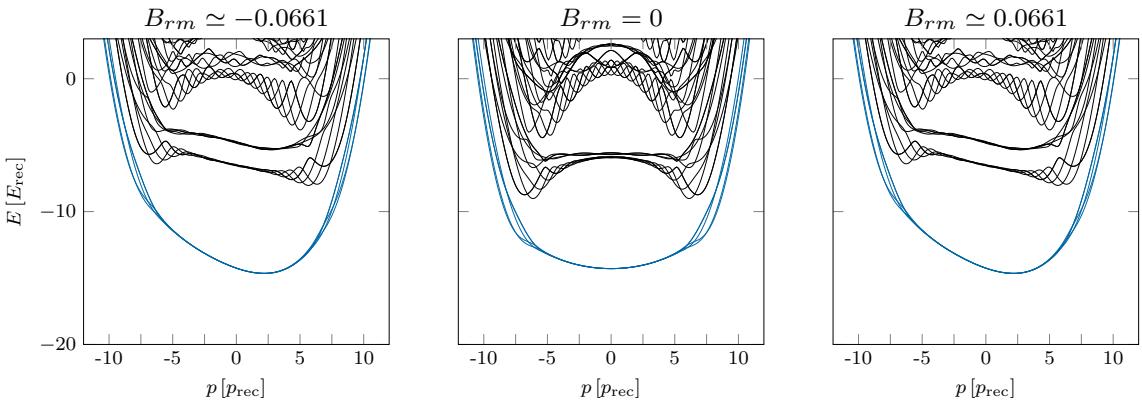

Figure 5.17: Theoretical dispersion relation as a function of the B_{rm} perturbation. For the left and the right columns, the couplings are rescaled to $t_x = 4/3 \times 5.69 E_{\rm rec}, t_z = 5.1 E_{\rm rec}$, such that the gap to the first excited band is not affected by the perturbation. For the center column, the couplings are $t_x = 5.69 E_{\rm rec}, t_z = 5.1 E_{\rm rec}$.

A non-linear response experiment?

We have all the tools to illustrate the non-linear response in our experimental system by applying a force along a spatial direction (say along $\hat{\boldsymbol{\nu}}$) and by measuring the induced displacement along the orthogonal direction (in this case, $\hat{\boldsymbol{\xi}}$) in the presence and in the absence of a B_{rm} perturbation.

However, one need to be cautious when performing this measurement. Indeed, there are several sources of possible displacements of the atoms along $\hat{\boldsymbol{\xi}}$ while applying a force along $\hat{\boldsymbol{\nu}}$. The first one is the curvature of the ground band. As seen Fig. 5.17, when the B_{rm} field is turned on, the derivative of the dispersion relation is not vanishing at $p = 0$, leading to a non-zero velocity along $\hat{\boldsymbol{\xi}}$. We recall that this non-vanishing velocity is not a marker of the non-linear response and is not a consequence of the perturbative B_{rm} field, but is due to the term $\gamma\{J_z, J_+\}$. As a consequence, we expect a non-zero velocity component along $\hat{\boldsymbol{\xi}}$ when the perturbation is on, which is partly due to the modified ground band dispersion and not only to the electromagnetic perturbation. We correct Eq. (5.40) to take into account this new dispersion :

$$\begin{aligned} v^{\xi} &= v^{\xi}_{NL} + v^{\xi}_{GB} \\ v^{\xi} &= \rho_2 E_\nu B_{mr} + \frac{\partial \mathcal{E}}{\partial p}, \end{aligned} \tag{5.45}$$

where $\mathcal{E}$ is the ground band energy.

The second cause of displacement along $\hat{\boldsymbol{\xi}}$ is the change of frame. Indeed, we measure the position of the atoms in the lab frame, but we should interpret it in the moving frame. Finally, the last source of displacement along $\hat{\boldsymbol{\xi}}$ is the the non-linear response itself, which provides an additional drift in the presence of a perturbating magnetic field B_{rm} and a perturbating electric field along $\hat{\boldsymbol{\nu}}$.

We generate a perturbating electric field by applying an (inertial) perturbative force on the atoms via the change of frame velocity. Provided this force is applied adiabatically along $+\hat{\boldsymbol{\nu}}$, it will increase the ν-projection of the quasimomentum by $+\Delta q$. Assuming we start in $(p = p_i, q = q_i)$, the force will change the system's quasimomentum to $(p = p_i, q = q_i + \Delta q)$.

The velocity of the atoms at $(p = 0, q = +\Delta q)$ in the lab frame is given by :

$$\boldsymbol{v}_{\text{lab}}(+\Delta q) = \boldsymbol{v}_{\text{GB}}(+\Delta q) + \boldsymbol{v}_{\text{frame}}(+\Delta q) + \boldsymbol{v}_{\text{NL}}(+\Delta q), \tag{5.46}$$

where $\boldsymbol{v}_{\text{GB}}$ stands for the contribution coming from the ground band dispersion, $\boldsymbol{v}_{\text{frame}}$ is the contribution due to the change of frame and $\boldsymbol{v}_{\text{NL}}$ is the contribution due to the non-linear response, that we wish to measure.

One way to distinguish the component $\boldsymbol{v}_{\text{NL}}$ from the two other components is to perform a second experiment where the force is applied towards $-\hat{\boldsymbol{n}}\boldsymbol{u}$ and to project Eq. (5.46) along $\hat{\boldsymbol{\xi}}$. Indeed, the projections of the velocity along $\hat{\boldsymbol{\xi}}$ obey the following equations :

$$\begin{aligned} v^{\xi}_{\text{frame}}(+\Delta q) &= v^{\xi}_{\text{frame}}(-\Delta q) \\ v^{\xi}_{\text{GB}}(+\Delta q) &= v^{\xi}_{\text{GB}}(-\Delta q) \\ v^{\xi}_{\text{NL}}(+\Delta q) &= -v^{\xi}_{\text{NL}}(-\Delta q) \end{aligned} \tag{5.47}$$

we can thus isolate v^{ξ}_{NL} with :

$$v^{\xi}_{\text{lab}}(+\Delta q) - v^{\xi}_{\text{lab}}(-\Delta q) = 2v^{\xi}_{\text{NL}}(+\Delta q). \tag{5.48}$$

The displacements of the cloud in the lab frame while evolving the q-component of the quasimomentum by $+\Delta q$ and $-\Delta q$ are given by time-integration of the velocities in the lab frame:

$$\begin{aligned} \delta\xi(+\Delta q) &= \int v^{\xi}_{\text{lab}}(q(t))\mathrm{d}t \\ \delta\xi(-\Delta q) &= \int v^{\xi}_{\text{lab}}(q(t))\mathrm{d}t \end{aligned} \tag{5.49}$$

Hence, the difference in ξ-displacement between the two experiments is given by :

$$\Delta\xi = \delta\xi(+\Delta q) - \delta\xi(-\Delta q) = 2\int v^{\xi}_{\text{NL}}(q)\mathrm{d}t. \tag{5.50}$$

This expression only involves the non-linear response velocity component. As a consequence, we expect this quantity to vanish when there is no B_{rm} field. On the other, the latter should be positive (resp. negative) when the B_{rm} field is positive (resp. negative).

We show in Fig. 5.18 simulations of the difference in ξ-displacement given by Eq. (5.50). In these simulations, the initial state of the system is $p_i = 0, q_i = -0.89p_{\text{rec}}$. We then perform a parabolic ramp of q towards $q = q_i \pm 20p_{\text{rec}}$ in 600 µs with and without B_{rm} field. We display the difference in displacement in the lab frame (Eq. (5.50)) following the two experiments. The laser couplings are $t_x = 5.69E_{\text{rec}}, t_z = 5.1E_{\text{rec}}, \beta = -2t_z$ for the case without B_{rm} field. When the B_{rm} field is turned on, t_x is rescaled by 4/3 such that the gap at the center of the Brillouin zone is similar with and without the magnetic perturbation. As expected, $\Delta\xi^{\text{NL}}$ is vanishing for $B_{rm} = 0$. It also changes sign when the direction of the magnetic field perturbation is flipped.

We show in dashed lines the displacement induced by integrating the expected relation derived earlier for a homogeneous system, $v^{\text{NL}} = \rho_2 B_{rm} F(q)$, from q_i to $q_i \pm 20p_{\text{rec}}$. We see a good agreement between the prediction given by the simulation and the theoretical non-linear reponse, confirming that our implemented B_{rm} field can indeed by considered as a perturbation and that the continuous approximation of our system is valid for the chosen couplings. We checked numerically that this agreement breaks down for lower coupling values.

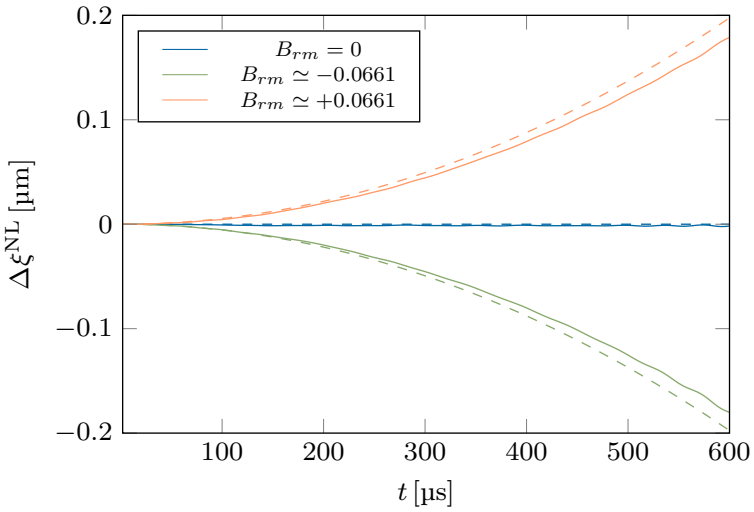

Figure 5.18: Non-linear response (simulations). We display in straight line the difference in ξ-displacement after applying a force during 600 µs along $+\hat{\boldsymbol{\nu}}$ and along $-\hat{\boldsymbol{\nu}}$, as a function of time and for three different values of the B_{rm} perturbation. The dashed lines correspond to the theoretical non-linear response.

As seen on Fig. 5.18, the signal of the non-linear response is very weak (approximately 0.2 µm), and is at the limit of our detection precision. Moreover, we recall that this signal is obtained after substracting measurements from two experiments (one when the electric perturbation is applied towards $+\Delta q$ and one when its applied towards $-\Delta q$) and that it supposes that these two experiments could be realised in a completely symmetric way, which is not rigurously true in practice. Other source of noises that we don't control perfectly can also degrade this small signal, such as imperfection in the intensity profil of the beams and noise in frequency in the detuning ramps (that would lead to imperfect frame velocity ramps). Taking all these factors into account makes this effect quite difficult to detect experimentally.

Options to enhance the signal would be to apply the perturbation for a longer time or to increase its strength. However, these strategies are not straightforward to implement. First, $B_{rm} \simeq \pm 0.0661$ is already the maximum value we can reach by changing the polarisation of one of the x-propagating Raman beams, since its polarisation is already maximally circular. Secondly, the increase in the electric perturbation (equivalently, in the force) is limited by the adiabatic criterion since we want to remain in the ground band. Finally, applying the electric perturbation for a longer time is complicated since it comes together with additional drifts along $\hat{\boldsymbol{\nu}}$, ultimately leading to an offcentering of the atomic cloud with respect to the Raman beams. As a consequence, we were not able to detect the non-linear electromagnetic response through this transport experiment.

In the following, we propose a new protocol to unveil the non-trivial topology, by performing quenches of the system in the presence of a magnetic perturbation.

5.5.3 Precessions

The non-trivial topology of our system can be illustrated by the modified cyclotron orbits in the presence of a magnetic perturbation. We present in this paragraph this idea, and show its experimental realisation.

Cyclotron orbits in the presence of a B_{rm} field.

We consider again the continuous model developed in the previous chapter where the magnetic field tensor contains the B_{rm} contribution. The equation of motion reads :

$$\begin{aligned}\partial_t \begin{bmatrix} v_x \\ v_z \\ v_r \\ v_m \end{bmatrix} &= \frac{1}{M} B \begin{bmatrix} v_x \\ v_z \\ v_r \\ v_m \end{bmatrix} \\ &= \begin{bmatrix} 0 & 0 & -4v_{\mathrm{rec}}/3 & -2v_{\mathrm{rec}}/3 \\ 0 & 0 & -2v_{\mathrm{rec}}/3 & 2v_{\mathrm{rec}}/3 \\ 4kt_x/\hbar & 4kt_z/\hbar & -2B_{rm}(t_x-2t_z)/\hbar & 2B_{rm}(t_x+t_z)/\hbar \\ 4kt_x/\hbar & -8kt_z/\hbar & -2B_{rm}(t_x+4t_z)/\hbar & 2B_{rm}(t_x-2t_z)/\hbar \end{bmatrix} \begin{bmatrix} v_x \\ v_z \\ v_r \\ v_m \end{bmatrix},\end{aligned} \tag{5.51}$$

where we have developed the product of the inverse mass tensor and the magnetic field tensor. The second equation can be simplified by rewritting $\frac{1}{M}B$ in terms of 2×2 block matrices :

$$\frac{1}{M} B = \begin{bmatrix} 0 & E \\ F & G \end{bmatrix} \tag{5.52}$$

We thus obtain :

$$\begin{aligned}\partial_t \begin{bmatrix} v_x \\ v_z \end{bmatrix} &= E \begin{bmatrix} v_r \\ v_m \end{bmatrix} \\ \partial_t \begin{bmatrix} v_r \\ v_m \end{bmatrix} &= F \begin{bmatrix} v_x \\ v_z \end{bmatrix} + G \begin{bmatrix} v_r \\ v_m \end{bmatrix},\end{aligned} \tag{5.53}$$

leading to the following equation in the xz plane :

$$\partial_t^2 \begin{bmatrix} v_x \\ v_z \end{bmatrix} = EF \begin{bmatrix} v_x \\ v_z \end{bmatrix} + EGE^{-1} \begin{bmatrix} v_x \\ v_z \end{bmatrix}. \tag{5.54}$$

Using the expressions of the matrices E, F, G, we have :

$$\begin{aligned}\partial_t^2 v_x &= -\omega_x^2 \left(v_x + M B_{rm} \rho_2^{\mathrm{bulk}} \partial_t v_z \right) \\ \partial_t^2 v_z &= -\omega_z^2 \left(v_z - M B_{rm} \rho_2^{\mathrm{bulk}} \partial_t v_x \right),\end{aligned} \tag{5.55}$$

We recover the equation of a Foucault pendulum in the xz plane when assuming that the two Larmor frequencies are equal $\omega_x = \omega_z \equiv \omega$:

$$\partial_t^2 \boldsymbol{v} = -\omega^2 \boldsymbol{v} + 2\omega_p \hat{\boldsymbol{n}} \times \boldsymbol{v}, \tag{5.56}$$

where $\hat{\boldsymbol{n}}$ is normal to the xz plane and where $\omega_p = M\rho_2 B_{rm}\omega^2/2$. We allow ourselves to use a vectorial product in Eq. (5.56) by considering only a 3D space made of the degrees of freedom x, z and an orthogonal direction to define the normal vector to the xz plane.

Eq. (5.56) shows that, in the presence of a B_{rm} field, the projections of the cyclotron orbits in the xz plane undergo a precession reminiscent of a Foucault pendulum. The precession rate is proportional to the bulk second Chern character, thus providing a direct measurement of the non-trivial topology.

Experimental measurements

We measured experimentally such precessions. To do so, we follow the same protocol described in the previous section, adjusting the light intensities of the x-propagating beams in the presence of the modified polarisation, such that the two experimental Larmor frequencies ω_x, ω_z are equal. The atoms are adiabatically prepared in the ground band in the bulk of the system. This preparation is made with the modified polarisation of one of the Raman beam, such that the effective magnetic field contains the desired value of the perturbation B_{rm}. We then quench the quasi-momentum along the direction $\hat{\boldsymbol{x}}$ by quenching the detuning of the Raman beams. Finally, we hold for various time and measure the spatial velocities following the excitation.

We display Fig. 5.19 our experimental results following such protocol. On Fig. 5.19b, in the absence of magnetic field perturbation, the system mainly responds along $\hat{\boldsymbol{x}}$. This is similar to the case studied in the previous section, where we initially quench the system either along $\hat{\boldsymbol{\xi}}$ either along $\hat{\boldsymbol{\nu}}$. This is no longer the case on Fig. 5.19a,c where the magnetic perturbation connects the two spatial degrees of freedom. Equivalently, the magnetic perturbation leads to the appearence of a Hall effect in the xz plane. The measured evolution is reminiscent of a Foucault pendulum trajectory. As expected from the continuous model, the precession rate flips its sign when changing the sign of the magnetic field perturbation. We compare on Fig. 5.19d the measured precession rate (dots) for three different magnetic field perturbations and the theoretical prediction (blue line). Our measurements are consistent with a second Chern character $\rho_2^{\text{bulk}} = 0.65(2)/k^2$, in good agreement with the value inferred from the Berry curvature components $0.75(7)/k^2$ and with the theoretical predictions $\rho_2 = 3/(4k^2)$.

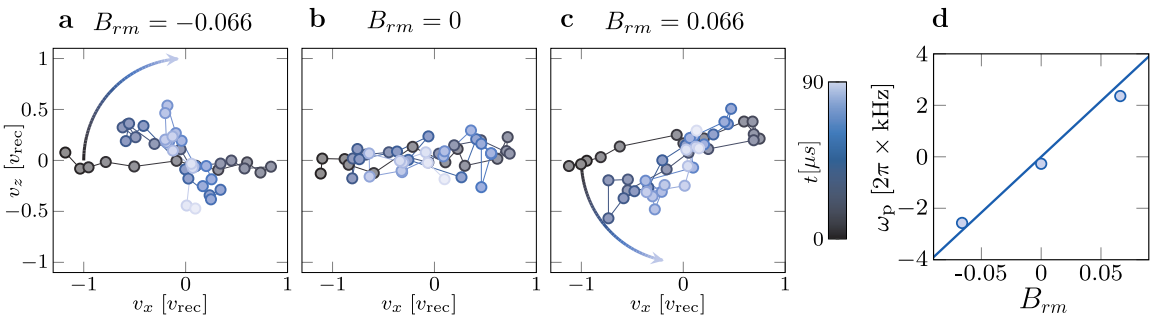

Figure 5.19: Magnetic field perturbation : cyclotron precessions in the plane (x, z). **a, b, c** : Precessions for magnetic field perturbation $B_{rm} = -0.066, 0, 0.066$. Time is encoded in color. **d** : Dots : Measured precession rates for the three magnetic field perturbation. Straight line : theory. The measured precession rates are in good agreement with the theoretical prediction $\rho_2 = 3/(4k^2)$.

This experiment is a new illustration of the non-linear response. It is not specific to our synthetic system and could be generalised to any 4D quantum Hall system. By reproducing this protocol for many quasimomenta $\boldsymbol{p}$ spanning the Brillouin zone, we could reconstruct the local second Chern marker, hence accessing the topology of our system with another experiment.

5.6 Conclusion

We have presented in this chapter our experimental realisation of a 4D quantum Hall system. Four mains results were obtained. First, the ground band properties were measured, unveiling the existence of the anisotropic chiral edge modes at the system boundaries - a feature specific to the 4D quantum Hall effect and a directe consequence of the system's topology. Then, we measured cyclotron orbits in the bulk of our system, showing the existence of two Larmor frequencies and the complex nature of these orbits in 4D. Subsequently, we confirmed the the non-trivial topology of our system by measuring a second Chern marker equals to unity in the bulk. Finally, we illustrated the non-linear electromagnetic response using a new protocol made of excitations in the presence and in the absence of a magnetic perturbation. This protocol provided us a new measurement of the second Chern character.

6 Realising the entanglement Hamiltonian of a quantum Hall system

In the previous chapters, we studied quantum Hall systems in different geometries and with different dimensionalities. The guideline for all these chapters were the topological properties of the systems under consideration. All these systems were non-interacting, and their topological character was related to their bandstructure. In a sense, their topology was a '*classical topology*' [163].

In some many-body systems, one can recover a '*quantum topology*', which is often referred to as a topological order [163]. Microscopically, the topological order is deeply connected to the notion of long-range entanglement [164]. One of its macroscopic manifestations is the ground state degeneracy. This degeneracy is robust upon any local perturbations, including those that break symmetries, hence the notion of topology.

The detection of topological order is a challenging task because no local order parameter can probe it. Numerically, its identification is also complicated, because it involves strongly correlated systems, that are difficult to fully characterise when their size is increasing. Different tools were developed to determine the topological order of any system, mainly the topological entanglement entropy [165, 166] and the entanglement Hamiltonian. The latter was introduced by Li and Haldane in their seminal paper [51] considering fractional quantum Hall states and can be generalised to non-interacting systems, such as Chern insulators or integer quantum Hall states [167].

This chapter relates the experimental realisation of the entanglement Hamiltonian of a non-interacting quantum Hall system. We start by introducing the von Neumann entropy and the entanglement Hamiltonian, and motivate the use of the latter by the bulk-edge

correspondence. Then, we briefly present our experimental findings and propose a guideline to extend our protocole to interacting systems.

The results presented in this chapter are published in [168].

6.1 Topological entropy and entanglement Hamiltonian

6.1.1 Topological entropy

In 2006, a first link was made between topological ordering and an entanglement measurement via the von Neumann entropy [165, 166]. The idea consists in considering a bipartition in A and B of a quantum many-body system in its ground state $|\Psi\rangle$. The von Neumann entropy provides a measurement of the entanglement between A and B :

$$S\left[\rho_A\right] \equiv -\mathrm{Tr}\left[\rho_A \log \rho_A\right], \tag{6.1}$$

where ρ_A is the reduced density matrix obtained by tracing out the B subsystem.

For an infinite system, the von Neumann entropy can be expressed as :

$$S\left[\rho_A\right] = \alpha \mathcal{L}^{d-1} - \gamma, \tag{6.2}$$

where d is the system's dimension, α a non-universal constant and γ a universal constant characterising the topological order. γ is called the *topological entanglement entropy*. This quantity connects the topological ordering of a many-body system to the long-range entanglement of its ground state.

Hence, topological order can be inferred for an infinite system by a deviation to the area law $S\left[\rho_A\right] = \alpha \mathcal{L}^{d-1}$. However, the von Neumann entropy suffers from three main issues. First, Eq. (6.2) is true only in the limit of infinite systems, and a non-universal additive correcting term should be considered when dealing with finite-size systems. Secondly, its accurate calculation is difficult, because it relies on scaling arguments [169, 170]. Finally and more importantly, it doesn't uniquely identify topological order.

In 2008, Li and Haldane in their celebrated paper [51] proposed a new tool to detect topological ordering, the entanglement Hamiltonian.

6.1.2 Entanglement Hamiltonian

Originally introduced for non-abelian fractional quantum Hall states, the entanglement Hamiltonian is a powerful tool to identify topological order that can be generalised to non-interacting systems.

Definition

We consider a pure quantum many-body system in its ground state, and a spatial bipartition of it in two subsystems A and B. The many-body ground state wave function can be written, performing a Schmidt decomposition, as :

$$|\Psi\rangle = \sum_{\alpha} \mathrm{e}^{-\xi_\alpha/2} \left|\Phi_\alpha^A\right\rangle \otimes \left|\Phi_\alpha^B\right\rangle. \tag{6.3}$$

Using this decomposition, the reduced density matrix of the subsystem A can be expressed as :

$$\begin{aligned} \rho_A &= \mathrm{Tr}_B\left[|\Psi\rangle\langle\Psi|\right] \\ \rho_A &= \sum_{\alpha} \mathrm{e}^{-\xi_\alpha} \left|\Phi_\alpha^A\right\rangle\left\langle\Phi_\alpha^A\right|. \end{aligned} \tag{6.4}$$

We introduce the entanglement (or modular) Hamiltonian $\widetilde{H}_A$:

$$\rho_A = \sum_\alpha \mathrm{e}^{-\xi_\alpha} \left|\Phi_\alpha^A\right\rangle \left\langle\Phi_\alpha^A\right| \equiv \mathrm{e}^{-\widetilde{H}_A} \tag{6.5}$$

The coefficients $\{\xi_\alpha\}$ are thus the eigenvalues of the entanglement Hamiltonian. They form the 'entanglement spectrum'. The information about the entanglement between A and B is contained in the values of the coefficients ξ_α. Indeed, if there is only one non-vanishing $\mathrm{e}^{-\xi_\alpha}$, the ground state can be written as a product state : $|\Psi\rangle = |\Phi_\alpha^A\rangle \otimes |\Phi_\alpha^B\rangle$, and the two subsystems are not correlated. On the other hand, if several coefficients are non-vanishing, the two subsystems are entangled. As a sidenote, we point out that the entanglement Hamiltonian could also be defined via a partition cut in momentum space [171, 172].

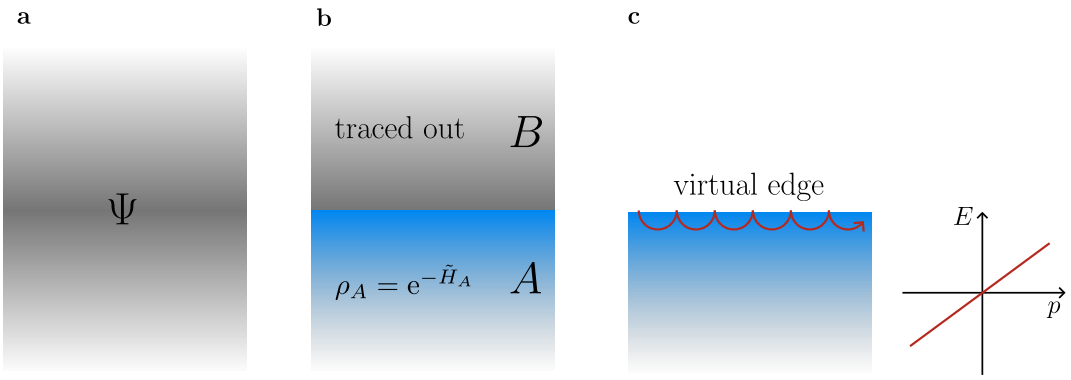

Figure 6.1: Entanglement Hamiltonian and bulk-edge correspondence. **a** : The system, whose topology is unknown, is in its ground state Ψ. **b** : We perform a bipartition on this system, defining the entanglement Hamiltonian $\widetilde{H}_A$. **c** : The entanglement spectrum shows a chiral dispersion relation, revealing the existence of a virtual edge at the cut position. Via the bulk-edge correspondence, it unveils the non-trivial topology of the state Ψ.

The entanglement Hamiltonian contains more information than the von Neumann entropy. In particular, via the Li-Haldane conjecture [51], the entanglement Hamiltonian reveals the edges excitations of the system, see Fig. 6.1. Hence, by measuring or computing a chiral dispersion relation in the entanglement spectrum, one can identify wheter or not the system is topologically ordered. This correspondence between the edge behavior of the entanglement Hamiltonian and the bulk of the original Hamiltonian is called the bulk-edge correspondence. In short, it means that all the information about the edges of a topological system is encoded in its bulk.

State-of-the art

Despite growing theoretical interests, the experimental measurement of the entanglement spectrum has remained challenging. It was directly measured by tomography [173] using the IBM quantum computer, but this method is limited to small systems. Indeed, the exponential increase of the Hilbert space dimensionality with the system size generally prohibites the full tomography of the entanglement Hamiltonian. As a consequence, for most of the interacting systems, the entanglement Hamiltonian remains unknown. Some protocols avoiding the full tomography were proposed [174], but remain extremely demanding to implement. Similarly, its numerical computation for interacting systems is limited by the exponential

growth of the Hilbert space size.

An other approach has recently emerged [175, 176] to experimentally realise an approximation of the entanglement Hamiltonian as a physical Hamiltonian [176]. This approach relies on the Bisognano-Wichmann (BW) theorem [177, 178]. This theorem states that the entanglement Hamiltonian of an infinite, continuous and Lorentzian invariant system can be well approximated by a spatial deformation of the initial Hamiltonian H. Considering a partition cut along the y direction at $y = 0$, the BW theorem gives the following approximation for the entanglement Hamiltonian $\widetilde{H}_A$:

$$\widetilde{H}_A \simeq H_{\mathrm{BW}} \equiv yH + C, \tag{6.6}$$

where the constant C ensures the good normalisation. The BW theorem can be adaptated to lattice system [179, 180], making it of particular interest for cold atom experiments.

In the next section, we propose a protocol relying on the BW theorem to realise, as a physical Hamiltonian, the entanglement Hamiltonian of a single-particle 2D quantum Hall system using dysprosium atoms. We will then present our experimental findings, mainly focusing on the bulk-edge correspondence.

6.2 Experimental realisation

The protocol introduced in this section relies on the same toolbox used throughout all this thesis, namely using Raman transitions and synthetic dimensions to emulate single-particle quantum Hall systems.

6.2.1 System under study

The topological system we study in this section is a non-interacting synthetic 2D quantum Hall ribbon, that was presented in chapter II. Our system is discrete along the synthetic direction m and continuous along x. We will study its topological properties by performing a 'spatial' partition cut at $m^* = 0.5$, leading to two subregions. The subregion A corresponds to $m \leq 0$ and arbitrary x while the subregion B corresponds to $m \geq 1$ and arbitrary x, see Fig. 6.2.

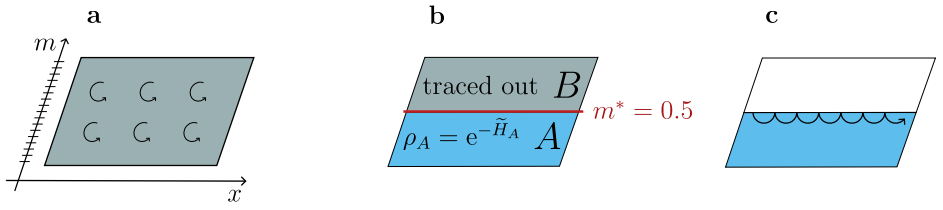

Figure 6.2: Entanglement Hamiltonian adapted to our system. **a** : Topological system under study : a synthetic 2D Quantum Hall ribbon. **b** : Definition of the subsystems A, B and of the bipartition at $m^* = 0.5$. **c** : Appearance of an edge after the partition cut, as a consequence of the bulk-edge correspondence.

6.2.2 Principle of the protocol

Our strategy to implement the entanglement Hamiltonian of the 2D quantum Hall ribbon is made of three steps. First, we prepare the single-particle ground state and measure its properties (spin distribution, dispersion relation). We artificially introduce a partition by

tracing out the subsystem B from our data to characterise the entanglement Hamiltonian of our system (both its spectrum and its eigenvectors). Then, guided by the BW theorem, we prepare a family of deformed Hamiltonians H_A^{var} acting only on the subregion A. We measure their eigenstates and eigenenergies, that we compare to the target state (obtained after the first step) to realise an approximation of $\widetilde{H}_A$. Finally, we measure the energy spectrum of this approximation of $\widetilde{H}_A$, and reveal the topological character of the initial system by the detection of a chiral dispersion relation. We detail these three steps in the following.

6.2.3 Entanglement Hamiltonian characterisation

The first step of the protocol requires the realisation of the ground state of the single-particle Hamiltonian that we want to study. The experimental scheme to realise the Hamiltonian of a 2D quantum Hall ribbon was already described in chapter II. A Raman configuration, see Fig. 6.3a, leads to the following Hamiltonian

$$H = \frac{(p_x - \hbar k J_z)^2}{2M} - \hbar\Omega J_x + Q J_z^2, \tag{6.7}$$

where the coupling amplitude Ω is given by the laser powers and where Q is chosen to flatten the ground band. The bandstructure of the Hamiltonian Eq. (6.7) is indexed by the momentum p_x.

We first measure the spin projection probabilities in the ground state as a function of p_x, Fig. 6.3c. As demonstrated in [168], they permit to access the quasi-energy spectrum $E_A(p_x)$ of $\widetilde{H}_A$ via :

$$E_A(p_x) = -\log\left[\frac{1 - P_A(p_x)}{P_A(p_x)}\right], \tag{6.8}$$

where $P_A(p_x)$ is the probability to measure the ground state in the subsystem A at the momentum p_x. We expect this quasi-energy to vanish when the probabilities to measure the ground state in the subsystem A and in the subsystem B are the same. This occurs at a momentum $p_x^* = 2\hbar k m^* = \hbar k$. By definition, we have :

$$E_A(p_x^*) = 0 \tag{6.9}$$

We obtain a chiral dispersion close to p_x^*, see Fig. 6.3e, which is in agreement with the expected dispersion [181] :

$$E_A(p_x) \simeq \frac{4}{\pi}(p_x - p_x^*)\ell_x, \tag{6.10}$$

where ℓ_x is the magnetic length along x, deduced from Fig. 6.3c.

By projecting the spin projection probabilities on the subsystem A, we can access to the eigenstates of $\widetilde{H}_A$, Fig. 6.3d.[1] We observe a virtual edge[2] at $m = 0$. In parallel, we evaluate the dispersion relation of the original Hamiltonian, Fig. 6.3b, by integrating the ground band velocity. We obtain the first excited bands by measuring the cyclotron oscillation frequencies, following a momentum kick, as seen in the previous chapter.

[1] We don't measure the phase of the state with this method. However, the original Hamiltonian being real, we can assume that the ground band wave functions are real too. In such case, the projection probabilities provide a measurement of the ground state.

[2] Actually, the virtual edges is located at $m = m^* = 0.5$, but the discrete nature of the synthetic dimension causes this virtual edge to appear at $m = 0$.

To summarise, we have measured the ground band spin projection probabilities Π_m and the dispersion relation of the initial system, recovering flat Landau levels. From the Π_m we deduced, for each momentum p_x, the probability to measure the ground state in the subregion A. We have then inferred the eigenvalues E_A of the entanglement Hamiltonian corresponding to the bipartition via Eq. (6.8). We also measured the ground state $|\Psi_A(p_x)\rangle$ of the entanglement Hamiltonian.

Our measurements of $|\Psi_A(p_x)\rangle$ and E_A provide an illustration of the Li-Haldane conjecture [51]. Near the cut, the dispersion relation of the entanglement Hamiltonian is chiral, revealing the existence of chiral edge modes at the system's boundaries.

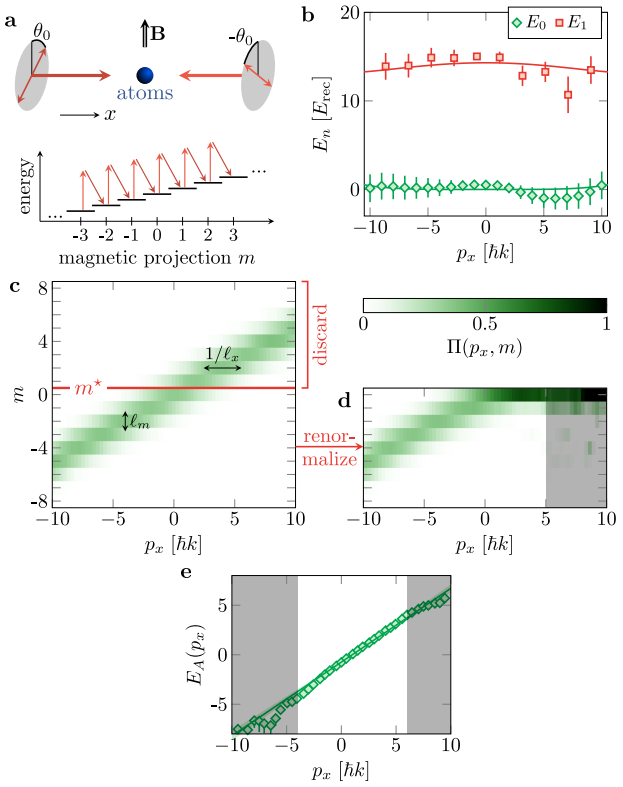

Figure 6.3: Entanglement Hamiltonian characterisation. **a** : Experimental scheme to realise the 2D quantum Hall ribbon. Polarisations are set such that the Raman coupling reads J_x. **b** : Measured ground band and first excited band. The ground band energy is inferred from the ground band velocity. The first excited band is obtained by measuring cyclotron orbit frequencies at different momenta. **c** : Experimental spin projections probabilities. We can infer the magnetic lengths along m and along x : ℓ_x, ℓ_m. **d** : By discarding the subsystem $m > m^* = 0.5$, we obtain the spin projections probabilities (hence the eigenstates, since the Hamiltonian is real) of the entanglement Hamiltonian of our system. We observe a virtual edge at $m = 0$. **e** : From the spin projection probabilities, we deduce the quasi-energy spectrum of the entanglement Hamiltonian. We observe a chiral dispersion, reminiscent of a virtual edge mode that would occur at the virtual boundary $m^* = 0.5$. Solid line is the expected evolution given by Eq. (6.10).

6.2.4 Approximate realisation of the entanglement Hamiltonian

We then implement a family of Hamiltonians guided by the BW theorem. The application of BW theorem to our system would imply the realisation of $H_{\mathrm{BW}} = J_z H$. Indeed, interpreting m as a spatial coordinate, J_z plays the role of a position within the direction of the partition cut. However, this expression is not strictly valid, since J_z doesn't commute with J_x, hence with H. We rather consider the anticommutator of J_z and H [168], leading to :

$$H_{\mathrm{BW}} = \frac{4}{\sqrt{\pi}} \left\{ \frac{m^* - J_z}{\ell_m}, \frac{H - \epsilon_0}{\hbar \omega_c} \right\}, \tag{6.11}$$

where ω_c is the Larmor frequency of our system and ϵ_0 an energy shift.

Engineering Eq. (6.11) with Raman transitions and spin-dependent light shifts is challenging. In particular, it would require the ability to emulate a J_z^3 term, that we can't produce with a two-photon process. We rather propose to follow a variational approach, implementing a family of Hamiltonians :

$$H_A^{\mathrm{var}} = \frac{(p_x - \hbar k J_z)^2}{2M} - \hbar \Omega^{\mathrm{var}} \left(J_+ J_z + J_z J_- \right) + b^{\mathrm{var}} J_z + Q^{\mathrm{var}} J_z^2, \tag{6.12}$$

where the parameters Ω^{var}, b^{var} and Q^{var} are experimentally varied via laser powers and detunings. The choice of this family of Hamiltonians is inspired from the BW theorem, even though it doesn't contain the exact BW Hamiltonian. However, we checked numerically that we can obtain a very good approximation of the BW Hamiltonian with this method. Interestingly, the term $J_+ J_z + J_z J_-$ realises the partition cut at $m^* = 0.5$. Indeed, we have :

$$\langle m = 1 | \, J_+ J_z + J_z J_- \, | m = 0 \rangle = 0 \tag{6.13}$$

As a consequence, the family of Hamiltonians realised by Eq. (6.12) separates the two subsystems $m \geq 1$ and $m \leq 0$, thus mimicking the effect of the entanglement Hamiltonian that acts only on one of the two subsystems.

The $J_+ J_z + J_z J_-$ operator is obtained by changing the Raman beam linear polarisation, θ_1, θ_2, to a configuration where $\theta_1 \neq -\theta_2$. Additionally, we want to get rid of any J_+ or J_- terms, that would couple the subspaces $m \leq 0$ and $m \geq 1$. This can be done by the choice of relative polarisation $\theta_1 - \theta_2 \simeq 2.8°$, as shown in [168]. The polarisations must be tuned as precisely as possible, such that our variational Hamiltonians indeed decouple the two subspaces.

We detail the variational optimisation in [168]. In the end, we obtain in Fig. 6.4 a good approximation of the entanglement Hamiltonian of our system, that we 'learnt' in the first part of the protocol.

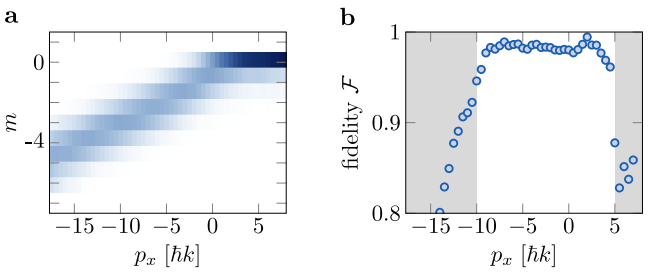

Figure 6.4: Approximate realisation of $\widetilde{H}_A$. **a** : Measured spin projection probabilities. We observe an edge at $m = 0$. **b** : Fidelity between **a** and the entanglement Hamiltonian characterised in Fig. 6.3d. We obtain a very good fidelity for momenta $-10\hbar k \leq p_x \leq 5\hbar k$, which is the region over which we performed the variational approach. The grey shaded area corresponds to the momenta where the variational optimisation is not performed, leading to a smaller fidelity.

6.2.5 Inferring topological properties

We can then measure the dispersion relation of the optimised Hamiltonian, see Fig. 6.5. The good agreement between the measured ground band energy and the quasi-energy E_A for momenta around p_x^* is the main result of our work. It unveils the non-trivial topology of our system via the bulk-edge correspondence.

The agreement is only valid for the momenta close to p_x^*, and a strong deviation occurs for $p_x \ll p_x^*$ or $p_x \gg p_x^*$. This is due to the discrete nature of the synthetic dimension and its finite size : for $p_x \gg p_x^*$ and for $p_x \ll p_x^*$, the system is fully polarised in either $m = 0$ or $m = -8$, leading to a quadratic dispersion. This deviation would not occur for a continuous Hall system.

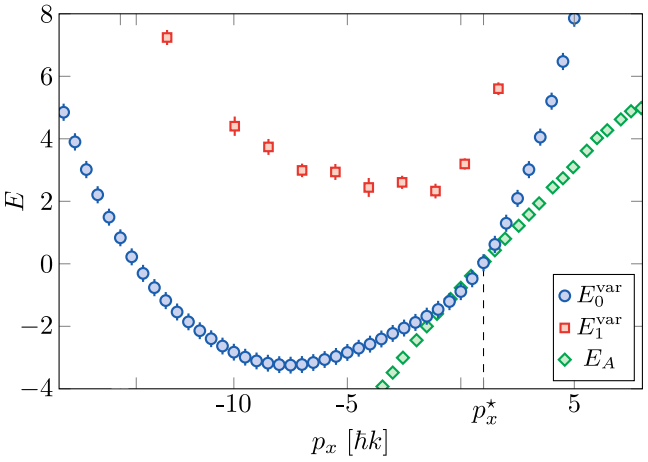

Figure 6.5: Revealing topological properties of our system. We measure the dispersion relation of our approximated entanglement Hamiltonian. We display in blue the ground band and in red the first excited band (measured with cyclotron excitations). We obtain a good agreement with the quasi-energy E_A (in green, measured previously) around the momentum p_x^*.

To summarise, we have first characterised the entanglement Hamiltonian $\widetilde{H}_A$ of our system by realising a posterior partition cut on the ground state of the full system. Then, we performed a variational approach to emulate an Hamiltonian which approximates well

$\widetilde{H}_A$. This variational approach was guided by the BW theorem. Finally, we measured the ground band dispersion of this optimised Hamiltonian, revealing the non-trivial topology of the bulk of our system, by recognising a chiral dispersion relation. This measurement is an illustration of the Li-Haldane conjecture.

6.3 Discussion

To our knowledge, this realisation, together with [182], consists in the first experimental implementation of the BW theorem, and the first physical realisation of an entanglement Hamiltonian. However, our system is non-interacting, which makes the notion of entanglement Hamiltonian less useful. For such non-interacting systems, we can generally fully characterise the system theoretically, thereby knowing its topological properties in advance. In particular, this is the case in our study, where the topological properties could be known a priori.

Our group is currently doing a theoretical work together with Leonardo Mazza's team to generalise this protocol to interacting systems. The goal is to show that, for some quantum many-body states[1], the non-interacting component of the entanglement Hamiltonian is not affected by the presence of interactions. Hence, our protocol could be generalised to any quantum simulator where the interactions can be controlled, such as arrays of interacting Rydberg atoms [183–186]. In such case, the measurement of the entanglement spectrum of an interacting system would consist of four steps:
(i) One should turn off the interactions and measure the ground state of the non-interacting system.
(ii) Secondly, one should realise a posterior bipartition of the measured ground state, providing a target state, that would be close to the ground state of the entanglement Hamiltonian of the non-interacting system.
(iii) Then, by performing an experimental variational approach on the Hamiltonian parameters, guided by BW theorem, one could realise a state as close as possible to the target state. For the optimal parameters, the implemented Hamiltonian would be a very good approximation of the single-particle entanglement Hamiltonian.
(iv) Finally, the interactions could be turned back on, keeping the parameters found in the previous step. The resulting Hamiltonian would be a good approximation of the entanglement Hamiltonian of this interacting system (even considering uniform interactions!). The measurement of the dispersion relation of this final Hamiltonian would reveal wheter or not the system possesses a topological order.

[1] such as some Laughlin states

7 Conclusion and outlook

7.1 Summary

This thesis was dedicated to the experimental realisation of topological quantum Hall systems using an ultracold gas of dysprosium atoms. By encoding synthetic dimensions in dysprosium's spin, and by coupling these synthetic dimensions to momentum via Raman transitions, we were able to engineer artificial magnetic fields, at the origin of the quantum Hall effect in our systems.

We started the manuscript by describing our experimental apparatus and by describing the rich interactions between a dysprosium atom and a photon. We then introduced several protocols aimed at controlling precisely the light polarisation.

In chapter II and III, we studied two-dimensional quantum Hall systems on two different geometries, a quantum Hall ribbon and a quantum Hall cylinder. We implemented, for the first time, Laughlin's topological charge pump within this cylinder.

Chapter IV and V present the main result of this thesis : the realisation of a 4D quantum Hall system combining two synthetic dimensions and two spatial ones. We observed a few typical properties related to 4D quantum Hall physics. First, we unveiled the anisotropic chiral edge modes occuring at the system's boundaries, revealing a non-trivial topology. We then characterised this non-trivial topology by measuring a second Chern number equal to unity in the bulk. We also measured cyclotron orbits in the center of the Brillouin zone, and observed a non-planar cyclotron trajectory, a direct consequence of the four-dimensional aspect of our system. Finally, we detected a revisited version of the non-linear electromagnetic response by examining the system's response to excitations in the presence of a magnetic perturbation.

In the last chapter, we briefly described an ongoing experiment focusing on the entanglement spectrum of a two-dimensional single-particle quantum Hall system. We experimentally realised its entanglement Hamiltonian by following the prescription from Bisognano and Wichmann [178]. We finally provided a roadmap to extend our protocol to interacting systems.

7.2 Perspectives

7.2.1 Many-body topological states

All the results presented in this thesis are related to single-particle physics. Exotic properties are expected to arise in topological interacting systems [187–191], and our plateform would

be a good candidate to explore these new phases of matter. For instance, we could realise fractional quantum Hall states and probe the anyonic nature of the excitations [30, 192].

Several challenges must be met to study topological interacting systems with our experiment. First, we need to have a robust and stable Bose-Einstein condensate on the daily basis. This is an ongoing work with the modulation of the transport beam presented chapter I, that should significantly increase the number of atoms loaded in the dipole traps. Secondly and more importantly, we should adapt our protocols to lower magnetic fields, in order to avoid any dipolar relaxation effects that would deteriorate the condensate on the timescales of our experiments. Then, all the scattering lengths of dysprosium should be measured to fully grasp the interactions within the synthetic dimensions [193]. Finally, the interactions within synthetic dimensions being infinite-range[1], we should find a protocol to control their range, for example using multiple Feshbach resonances [194].

7.2.2 Vortices in 4D

Another exciting direction permitted by the interactions would be the study of vortices in 4D. Recently [195–197] studied theoretically the behavior of vortices in a 4D superfluid. They demonstrated that vortices in 4D have exotic properties, which are directly linked to the peculiar nature of rotations in higher dimensions, as seen in chapter IV.

General 4D rotations involve two rotation frequencies (or two rotation angles) ω_{xy} and ω_{zw}, which induce rotations in the xy-plane and the zw-plane, respectively. The arrangement of vortices in a 4D superfluid depends on the relative values of these rotation frequencies. When they are equal, two vortices living in two orthogonal planes, thus intersecting at a point, are in a stable configuration [195] (contrary to the 3D case, where the intersection between two vortices would be a line and would lead to the reconnection phenomenon [198–200]).

For unequal rotation frequencies, each of the vortices wants to align itself with the highest rotation frequency (in order to minimise its rotational energy), and the two vortices don't remain in an orthogonal configuration. Consequently, they start to tilt and to interact repulsively. The relative equilibrium orientation of the two vortices thus results from a compromise between the interaction energy and the rotational energy, leading to a 'skewed vortex surface'. Interestingly, such 'skewed vortex surface' can be recovered for equal rotation frequencies under certain hypothesis [197], via a sophisticated phenomenon that we don't detail here.

These theoretical predictions have no equivalent in lower dimensions, and would represent an exciting area for experimental exploration. The study of vortices in our 4D system would come naturally in the presence of interactions, since the artificial magnetic field[2], by mimicking a rotation, would stabilise the vortices [44, 55, 109, 201]. The findings of [195–197] are based on a minimalistic model assuming, among other things, rotational invariance and local interactions. In our system, we could expect to observe an even richer family of vortices. Indeed, the hardwall boundary conditions, imposed by the synthetic dimension m, break the SO(4) symmetry. We could also consider engineering various boundary conditions along the spatial x, z dimensions via repulsive or attractive light shifts, and study how the 4D arrangement of the vortices would be modified.

[1] which could disable us from emulating certain systems, such as Bose-Hubbard models that require only on-site interactions

[2] induced by the Raman processes

Appendix A : Partitioning dysprosium's electronic spin to reveal entanglement in nonclassical states

We provide the reference [76] published during my thesis, that is not described in the manuscript. In short, we considered dysprosium's large spin $J = 8$ as 16 virtual qubits, and studied the non-classical correlations between these qubits.

Partitioning dysprosium's electronic spin to reveal entanglement in nonclassical states.
T. Satoor*, A. Fabre*, J.-B. Bouhiron, A. Evrard, R. Lopes, S. Nascimbene
Physical Review Research 3 (1), 043001 (2021)
* These authors contributed equally

Partitioning dysprosium's electronic spin to reveal entanglement in nonclassical states

Tanish Satoor,* Aurélien Fabre,* Jean-Baptiste Bouhiron, Alexandre Evrard, Raphael Lopes, and Sylvain Nascimbene†
Laboratoire Kastler Brossel, Collège de France, CNRS, ENS-PSL University, Sorbonne Université, 11 Place Marcelin Berthelot, 75005 Paris, France

(Received 30 April 2021; revised 9 July 2021; accepted 20 August 2021; published 1 October 2021)

Quantum spins of mesoscopic size are a well-studied playground for engineering nonclassical states. If the spin represents the collective state of an ensemble of qubits, its nonclassical behavior is linked to entanglement between the qubits. In this paper, we report on an experimental study of entanglement between two subsystems of dysprosium's electronic spin. Its ground state, of angular momentum $J = 8$, can formally be viewed as a set of $2J$ qubits symmetric upon exchange. To access entanglement properties, we partition the spin by optically coupling it to an excited state $J' = J - 1$, which removes a pair of qubits in a state defined by the light polarization. Starting with the well-known W and squeezed states, we extract the concurrence of qubit pairs, which quantifies their nonclassical character. We also directly demonstrate entanglement between the 14- and 2-qubit subsystems via an increase in entropy upon partition. In a complementary set of experiments, we probe decoherence of a state prepared in the excited level $J' = J + 1$ and interpret spontaneous emission as a loss of a qubit pair in a random state. This allows us to contrast the robustness of nonclassical pairwise correlations of the W state with the fragility of the coherence involved in a Schrödinger cat state. Our findings open up the possibility to engineer novel types of entangled atomic ensembles, in which entanglement occurs within each atom's electronic spin as well as between different atoms. Qubit ensembles with large entanglement depth could then be realized with a few atoms only, facilitating the scaling up of quantum-enhanced sensors.

DOI: 10.1103/PhysRevResearch.3.043001

I. INTRODUCTION

Entanglement is a hallmark of nonclassical behavior in compound quantum systems. Minimal entangled systems of qubit pairs, as realized with correlated photon pairs, play a central role in testing the foundations of quantum mechanics [1,2]. Entanglement can also be engineered in many-particle systems [3], such as an ensemble of interacting atoms [4]. In this case, the atoms are not individually addressable, and quantum correlations are indirectly revealed by measuring global properties, such as a squeezed spin projection quadrature [5–8] or via the quantum enhancement of magnetic sensitivity [9–11]. State-of-the-art experiments on photonic systems [12], superconducting qubits [13], trapped ions [14], and Rydberg atom arrays [15] can now produce highly entangled states of tens of individually identifiable qubits, in which entanglement is more readily observable.

Besides quantum state tomography, a wide array of methods have been developed for the detection of entanglement [16,17]. In two-qubit systems, the degree of entanglement is quantified by the concurrence [18,19]. Its direct measurement remains challenging since it requires nonlinear operations on the prepared state [20–23], and it was so far only achieved for photon pairs in pure quantum states [21]. In the case of multipartite systems, the study of entanglement is cumbersome due to the existence of distinct classes of entanglement [24]. It is often revealed using entanglement witnesses, by measuring the fidelity with respect to a given entangled state [25]—the method being limited to simple enough target states.

In this paper, we study quantum entanglement between subsystems of the electronic spin of dysprosium atoms, of angular momentum $J = 8$ in its ground state and prepared in nonclassical spin states. Quantum states with nonclassical correlations have been extensively studied in single large-spin systems, including photon qutrits [26], ground-state atomic spins [27,28], molecules [29], and Rydberg atoms [30]. In the formal analogy between a spin J and a set of $2J$ qubits symmetric upon exchange [31], nonclassicality goes hand in hand with entanglement between the virtual qubits. However, as long as the angular momentum J is conserved, the qubit ensemble cannot be partitioned, and the relevance of entanglement is disputable. Here, we use an optical coupling to an excited electronic state of angular momentum $J' = J - 1$ to partition the 16-qubit ensemble associated with the spin J, giving access to entanglement. The virtual absorption of a photon is interpreted as the annihilation of a qubit pair in a state defined by the light polarization, leaving a set of 14 qubits in the excited electronic level [see Fig. 1(a)]. This process thus realizes a partition of the electronic spin J in two subsystems—the excited electronic spin $J' = J - 1$ and the photon angular momentum $L = 1$. We use this partition to probe entanglement in nonclassical spin states, either by characterizing nonclassical behavior of qubit pairs via the

*These authors contributed equally to this work.
†sylvain.nascimbene@lkb.ens.fr

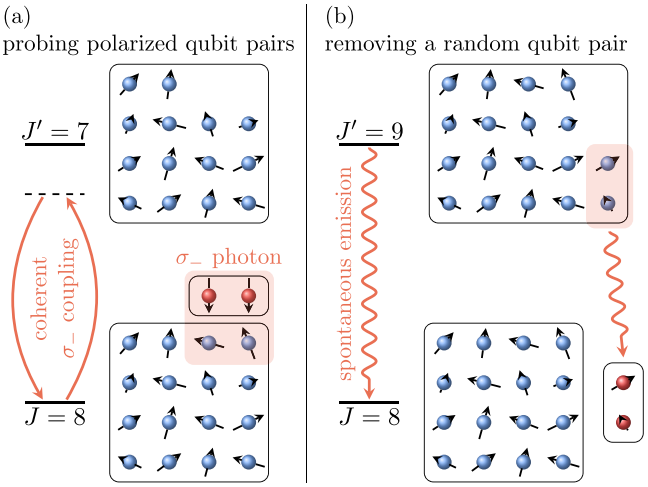

FIG. 1. Scheme of the experiments manipulating qubit pairs in the electronic spin of dysprosium. An electronic spin of angular momentum J can be viewed as a set of $2J$ virtual qubits symmetric upon exchange. (a) The coherent coupling to an excited state $J' = J - 1$ with σ_- polarized light probes the probability to find a qubit pair polarized in $|\uparrow\uparrow\rangle_z$. (b) The spontaneous emission from an excited state $J' = J + 1$ removes a random pair of qubits.

measurement of concurrence or by revealing an increase in entropy upon partition. We extend this protocol to probe decoherence in states prepared in an excited electronic level $J' = J + 1$ [see Fig. 1(b)]. There, the spontaneous emission of a photon drives the system to the electronic ground state J, which corresponds to the removal of a qubit pair randomly drawn from the initial state. We reveal the robustness of nonclassical pairwise correlations with respect to qubit loss, as well as the fragility of coherence in Schrödinger cat states.

This paper is organized as follows. We present in Sec. II the experimental protocol used to measure the properties of qubit pairs extracted from the electronic spin, based on the polarization dependence of the light-spin interaction. In Sec. III, we investigate the nonclassical character of these qubit pairs via the measurement of the concurrence of the reduced two-qubit density matrix and apply it to a W state and a squeezed state. In Sec. IV, we investigate the increase of entropy upon the 14|2 partition as a proof of entanglement for W and Schrödinger cat states, by studying the mixed nature of the reduced two-qubit density matrix. In Sec. V, we study the decoherence upon the loss of a qubit pair triggered by spontaneous emission. We show that nonclassical pairwise correlations are robust with respect to the extraction of qubits. In contrast, the coherence of a Schrödinger cat state is completely destroyed upon qubit loss, due to the complete *which path* information carried by the spontaneously emitted photon's polarization. In another superposition state, we show the existence of a quantum jump leaving the path information hidden, such that maximal-order coherence remains visible. Finally, we present a possible extension of our work to ensembles of dysprosium atoms entangled together using an optical resonator. Such systems would combine entanglement between atoms and within each electronic spin, allowing one to scale up entanglement depth and its application to quantum-enhanced sensing.

II. PAIR HUSIMI FUNCTION MEASUREMENT

A. Probing pairs via light coupling

The electronic ground state $J = 8$ can be interpreted as the sum of $2J = 16$ virtual spin-1/2s, in a state symmetric upon exchange. We discuss here the partition of this qubit ensemble, prepared in a state ρ, through the coupling to an excited electronic level, of angular momentum $J' = 7$. As sketched in Fig. 1(a), the coupling to the excited manifold is induced by light close to the optical transition, via the absorption of a photon. The photon polarization $\boldsymbol{\epsilon}$ defines an $L = 1$ quantum state $|\boldsymbol{\epsilon}\rangle$ that can be considered as a symmetric two-qubit state. We restrict ourselves here to the case of a circular polarization σ_-, which corresponds to qubits polarized in $|\downarrow\downarrow\rangle_z$. Since the excited state contains only $2J' = 14$ qubits, two qubits are removed upon photon absorption. The conservation of angular momentum requires these removed qubits to be polarized in $|\uparrow\uparrow\rangle_z$, the time-reversed state of the absorbed photon's polarization. The excited state ρ' can be then written as a projected state $\rho' = \langle\uparrow\uparrow|_z \rho |\uparrow\uparrow\rangle_z$. The probability for a pair chosen from the 16 qubits to be polarized in $|\uparrow\uparrow\rangle_z$ then reads

$$Q_{\text{pair}}(\mathbf{e}_z) = \text{Tr}\rho',$$

defining the pair Husimi function along the direction $\mathbf{e}_z$. Hence the light absorption properties of the electronic spin J can be linked to the properties of its two-qubit reduced density matrix.

To probe this behavior, we measure the light shift V induced by an off-resonant light beam close to the considered optical transition. The light shift, being induced by virtual photon absorption processes, is proportional to the pair Husimi function, as

$$V/V_0 = Q_{\text{pair}}(\mathbf{e}_z), \quad V_0 = \frac{(dE)^2}{\hbar\Delta},$$

where $d = \langle J-1||\mathbf{d}||J\rangle$ is the reduced dipole matrix element, E is the light electric field amplitude, and Δ is the detuning from resonance.

B. Application to Dicke states

We illustrate our method by measuring the value of the Husimi function $Q_{\text{pair}}(\mathbf{e}_z)$ for an arbitrary Dicke state $|m\rangle$ (with $-J \leqslant m \leqslant J$), which we denote Q_m hereafter.

All our experiments are performed on a cloud of $1.0(1) \times 10^5$ dysprosium atoms (of the bosonic isotope ^{162}Dy), held in an optical dipole trap at a temperature $T = 0.54(3)\ \mu$K. The results described in this paper can be understood by considering a single atom, with the ensemble acting as an averaging mechanism only. The experimental scheme for the Q_m measurement is shown in Fig. 2(a). We prepare the atoms in a coherent state $|m = J\rangle_{\mathbf{n}}$ polarized along a direction $\mathbf{n}$, parametrized by the spherical angles (θ, ϕ). The polar angle θ determines the projection probabilities Π_m along the Dicke states $|m\rangle$, which are significant for values of m close to $J\cos\theta$. We then push the atomic cloud by applying an off-centered laser beam, with circular σ_- polarization and blue detuning with respect to an optical transition at 696 nm. The intensity gradient then leads to a force along x proportional to the light shift [Fig. 2(a)]. After this kick, a magnetic

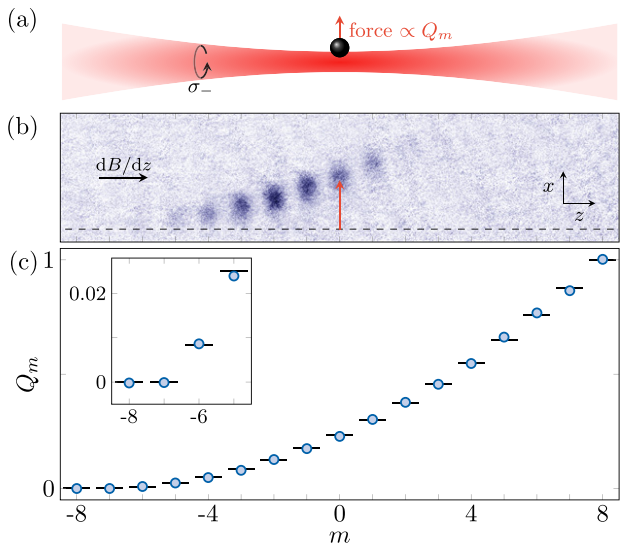

FIG. 2. Husimi function measurement for Dicke states. (a) Scheme of the light shift measurement. We measure the force induced on the atoms by an off-centered laser beam, blue detuned with respect to the optical resonance. (b) Image of an atomic gas prepared in a coherent state of polar angle $\theta \simeq 100°$. The atoms are kicked along x by the laser beam. Subsequently, we apply a magnetic field gradient separating the magnetic sublevels $|m\rangle$ along z during time of flight. The dashed line indicates the mean x position in the absence of the repulsive laser beam. (c) Probability Q_m for a qubit pair taken in the Dicke state $|m\rangle$ to be in $|\uparrow\uparrow\rangle_z$, deduced from the kick amplitudes. In all figures, error bars represent the 1σ statistical uncertainty (here smaller than the blue circles). The black lines are the theoretical values of Eq. (1).

field gradient is applied to spatially separate the different m components along z, which allows us to retrieve the light shift experienced by each Dicke state independently. After a 2.3-ms time of flight, we image the atoms and measure the x displacement for each Dicke state $|m\rangle$ that is significantly populated, and hence their values Q_m. A typical absorption image is shown in Fig. 2(b). Repeating this measurement for various angles θ, we measure the light shifts for all projections m and infer the Q_m values shown in Fig. 2(c) [32].

Our measurements are consistent with an absence of light shift for the states $|m = -J\rangle$ and $|m = -J+1\rangle$; that is, these states are dark with respect to the $J \to J' = J-1$ optical transition for σ_- polarized light. In terms of the underlying qubits, the state $|m = -J\rangle$ only contains $|\downarrow\rangle_z$-polarized qubits, while the state $|m = -J+1\rangle$ has a single qubit in $|\uparrow\rangle_z$. In both cases, a qubit pair cannot be found polarized in $|\uparrow\uparrow\rangle_z$; hence $Q_{-J} = Q_{-J+1} = 0$.

More generally, a Dicke state $|m\rangle$ is composed of $J-m$ qubits in $|\downarrow\rangle_z$ and $J+m$ qubits in $|\uparrow\rangle_z$ [33]. The probability to pick a pair $|\uparrow\uparrow\rangle_z$ simply reads

$$Q_m = \binom{J+m}{2} \Big/ \binom{2J}{2} = \frac{(J+m)(J+m-1)}{2J(2J-1)}, \qquad (1)$$

in good agreement with our measurements.

We use these measurements to probe the Husimi function of states lacking z rotation symmetry. For this, we measure their projection probabilities $\Pi_m(\mathbf{n})$ along $\mathbf{n}$ by combining a spin rotation and a Stern-Gerlach projective measurement along z. We then infer the Husimi function by weighting these probabilities with the Q_m values, as

$$Q_{\text{pair}}(\mathbf{n}) = \sum_m Q_m \Pi_m(\mathbf{n}). \qquad (2)$$

In the following, we use the theoretical values of Eq. (1) rather than the measured ones to avoid propagating systematic errors.

C. Coherent and W states

We first apply the above protocol to the quasiclassical coherent spin state $|m = -J\rangle$ and the W state $|m = -J+1\rangle$. The coherent state can be viewed as a set of $2J$ qubits polarized in $|\downarrow\rangle_z$, forming a nonentangled product state. The W state, which hosts a single qubit in $|\uparrow\rangle_z$, is a paradigmatic state of a fundamental class of entanglement [24], which has been realized and studied in various settings [34–41].

In our experiment, the atoms are initially spin polarized in the coherent state $|m = -J\rangle$. To produce the W state, we confine the system to the two spin states $|m = -J\rangle$ and $|m = -J+1\rangle$ by applying a strong quadratic light shift acting on the other spin states only, leading to a constrained quantum Zeno dynamics [42–44]. An additional resonant radio-frequency π pulse then brings the system to $|m = -J+1\rangle$. The quadratic light shift is produced using the 696-nm laser beam with a σ_- polarization, leading to positive energy shifts for all Dicke states $|m\rangle$, except for $m = -J$ and $-J+1$. We reach a maximum W-state fidelity of 0.91(1), with residual overlaps on other Dicke states below 4% [45].

We report in Figs. 3(a) and 3(b) the measured projection probabilities $\Pi_m(\theta)$ for these two states. For a given projection m, the coherent-state probabilities feature a single peak centered on the expected maximum at $\theta_m = \arccos(m/J)$, shown as red lines. For the W-state probabilities, we observe a double-peaked distribution for all nonstretched states $m \neq \pm J$. This behavior results from the interference between two processes, depending on whether the spin $|\uparrow\rangle_z$ is projected on $|\uparrow\rangle_\theta$ or $|\downarrow\rangle_\theta$. The first (second) process dominates for $\theta \simeq 0$ ($\theta \simeq \pi$), and the two processes destructively interfere at θ_m, as observed in our data.

We combine these measurements to infer the pair Husimi functions using Eq. (2), finding good agreement with theory for both states [see Fig. 3(c)]. In particular, for the coherent state, our data match well the probability $Q_{\text{pair}}(\theta) = \sin^4(\theta/2)$ that two qubits in $|\downarrow\rangle_z$ are projected in $|\uparrow\rangle_\theta$. In the following sections we use these measurements to probe entanglement properties.

III. NONCLASSICALITY OF QUBIT PAIRS

Our first characterization of entanglement of the $2J$-qubit state consists in revealing the nonclassical character of qubits pairs extracted from it.

A. Measure of nonclassicality via the concurrence

The collective state ρ_{pair} of a qubit pair symmetric upon exchange can be written as the state of an angular momentum

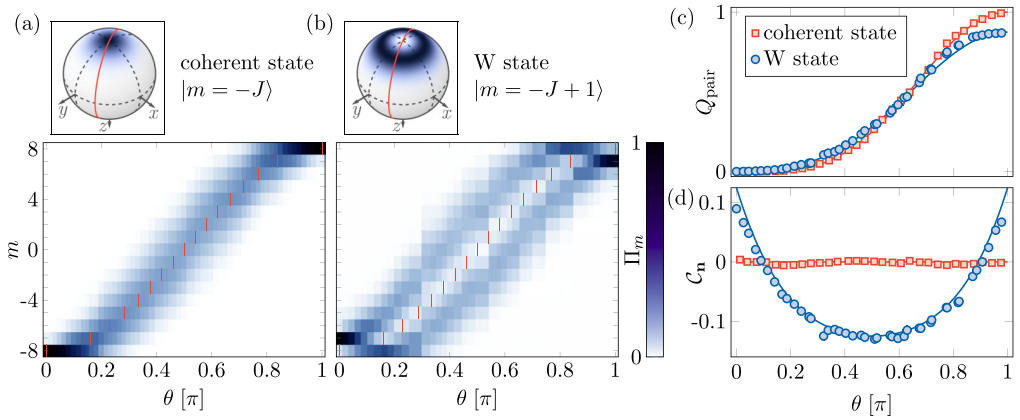

FIG. 3. Qubit pair properties of coherent and W states. (a) and (b) Measured spin projection probabilities Π_m as a function of the polar angle θ, for a coherent spin state (a) and for the W state (b). The red vertical lines indicate the expected maxima for the coherent state, also corresponding to minima for the W state. The top panels represent the considered spin-J states on the Bloch sphere, where the red circles indicate the spanned measurement projection axis. (c) Pair Husimi function Q_{pair} computed from the (a) and (b) data (blue circles and red squares, respectively). The lines correspond to the expected functions $Q_{\text{pair}}(\theta)$ for the coherent and W states (red and blue lines). (d) Distribution $\mathcal{C}_{\mathbf{n}}$ of nonclassical correlations as a function of the polar angle θ. The points $\mathcal{C}_{\mathbf{n}} > 0$ measured for the W state evidence nonclassicality.

$L = 1$. Drawing an analogy with quantum optics [46,47], it will be called classical if it can be expressed as a statistical mixture of quasiclassical coherent states [48], as

$$\rho_{\text{pair}}^{(\text{classical})} = \sum_{\mathbf{n}} w_{\mathbf{n}} ||\mathbf{n}\rangle\langle\mathbf{n}||, \tag{3}$$

where $||\mathbf{n}\rangle$ is a spin-1 coherent state pointing along $\mathbf{n}$, and $w_{\mathbf{n}} \geqslant 0$, $\sum_{\mathbf{n}} w_{\mathbf{n}} = 1$. Coherent states are the only pure states that satisfy the equality

$$Z(\mathbf{n}) \equiv 2\langle L_{\mathbf{n}}^2\rangle - \langle L_{\mathbf{n}}\rangle^2 - 1 = 0 \tag{4}$$

for arbitrary measurement axis $\mathbf{n}$. Then it follows by convexity that $Z(\mathbf{n}) \geqslant 0$ for classical states. As shown in Ref. [48], the existence of a strictly negative value $Z(\mathbf{n})$ constitutes a necessary and sufficient criterion of nonclassicality.

To apply this criterion to our system, we use the connection between the mean values of spin projection and the Husimi function of qubit pairs extracted from the electronic spin J,

$$\langle L_{\mathbf{n}}\rangle = Q_{\text{pair}}(\mathbf{n}) - Q_{\text{pair}}(-\mathbf{n}),$$
$$\langle L_{\mathbf{n}}^2\rangle = Q_{\text{pair}}(\mathbf{n}) + Q_{\text{pair}}(-\mathbf{n}),$$

leading to the expression $Z(\mathbf{n}) = \alpha\,\mathcal{C}_{\mathbf{n}}$, where we introduce the coefficient $\alpha = (\sqrt{Q_{\text{pair}}(-\mathbf{n})} - \sqrt{Q_{\text{pair}}(\mathbf{n})})^2 - 1$ and the distribution

$$\mathcal{C}_{\mathbf{n}} = 1 - (\sqrt{Q_{\text{pair}}(-\mathbf{n})} + \sqrt{Q_{\text{pair}}(\mathbf{n})})^2.$$

The parameter α being negative, nonclassicality is characterized by the existence of a direction $\mathbf{n}$ for which $\mathcal{C}_{\mathbf{n}}$ is strictly positive. This criterion of nonclassicality is equivalent to the bipartite entanglement witness established in Ref. [49].

We show in Fig. 3(d) the distribution $\mathcal{C}_{\mathbf{n}}$ computed from the measured Husimi functions, for the coherent and W states. For these states, symmetric upon rotations around z, we expect $\mathcal{C}_{\mathbf{n}}$ to only depend on the polar angle θ of the measurement axis [50]. For the coherent state, the measured $\mathcal{C}_{\mathbf{n}}$ remains close to zero for all angles θ. Indeed, qubit pairs drawn from this state form themselves a spin-1 coherent state, for which $\mathcal{C}_{\mathbf{n}}$ vanishes according to Eq. (4). For the W state, $\mathcal{C}_{\mathbf{n}}$ takes significantly positive values for θ close to 0 and π, showing a nonclassical character.

We now show that the distribution $\mathcal{C}_{\mathbf{n}}$ can be used to quantify the degree of nonclassicality of a quantum state, defined by its distance from the set of nonclassical states [51]. For a system of two qubits, this geometrical measure can be directly expressed in terms of the concurrence $\mathcal{C}$ [52], the most common measure of pairwise entanglement [18,19]. In our system, qubit pairs should be considered as indivisible quantum objects, such that the concurrence only measures the amount of nonclassical correlations. The concurrence can be explicitly written in terms of the density matrix, but it does not correspond to a directly accessible physical observable. Remarkably, the distribution $\mathcal{C}_{\mathbf{n}}$ can be used to retrieve the concurrence, as

$$\mathcal{C} = \max\left[0, \max_{\mathbf{n}} \mathcal{C}_{\mathbf{n}}\right].$$

This relation was conjectured and numerically checked for randomly generated states in Ref. [53].

For the W state realized in the experiment, the measured $\mathcal{C}_{\mathbf{n}}$ takes its maximum for $\theta = 0$ leading to a concurrence $\mathcal{C} = 0.089(5)$. This value is about 71% of the maximum possible value $\mathcal{C} = 1/J = 0.125$ in a system of $2J$ qubits symmetric upon exchange [54], which would be reached for the W state in the absence of experimental imperfections. In our system, the concurrence is limited by the residual population $\Pi_{-J+2} \simeq 0.03$ in the Dicke state $|m = -J + 2\rangle$ that originates from spin-changing collisions between atoms in $|m = -J + 1\rangle$.

B. Pairwise correlations in a squeezed state

Nonclassical correlations between qubit pairs play a central role in the squeezing of a spin projection quadrature [55]. In this section we extend the measurement of qubit pair properties to a squeezed spin state, which we produce via a nonlinear

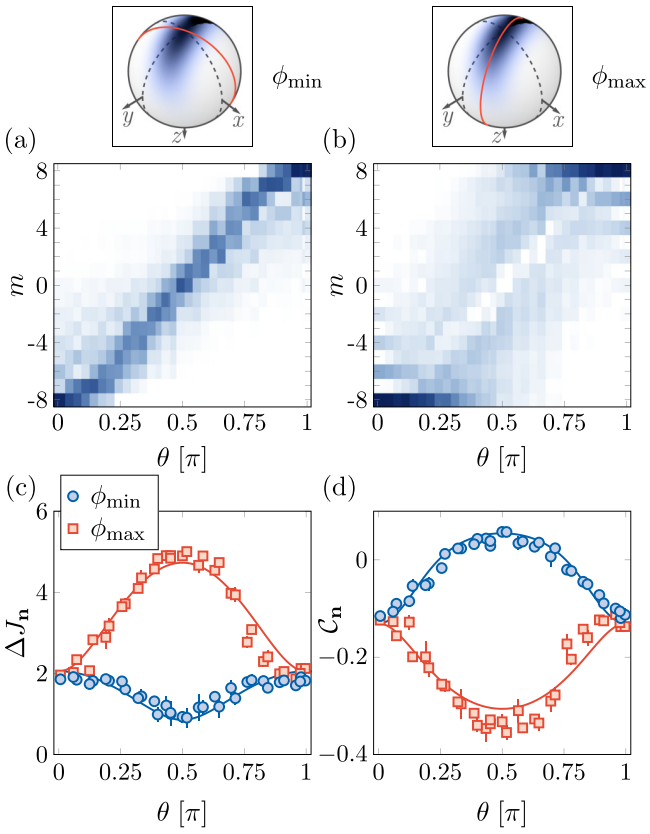

FIG. 4. Qubit pair properties for a squeezed state. (a) and (b) Measured spin projection probabilities Π_m for a squeezed spin state, as a function of the polar angle θ with azimuthal angles $\phi_{\min}$ (a) and $\phi_{\max}$ (b). (c) Spin projection uncertainty $\Delta J_{\mathbf{n}}$ computed from the (a) and (b) data (blue circles and red squares, respectively). The lines correspond to the projection uncertainties expected for the targeted spin state. (d) Distribution $\mathcal{C}_{\mathbf{n}}$ of nonclassical correlations as a function of θ.

spin dynamics. We apply a $\hbar\chi J_x^2$ spin coupling, generated by the spin-dependent light shift of the 696-nm laser beam, using a linear polarization $\mathbf{e}_x$ [56]. This coupling induces a twisting of the spin distribution, leading to the squeezing of a spin projection quadrature [55], as first implemented in atomic Bose-Einstein condensates [8,9]. In our experiment, we apply a nonlinear coupling of strength $\chi = 2\pi \times 32.1(4)$ kHz for a duration $t \simeq 700$ ns, in the presence of a z magnetic field $B = 75(1)$ mG.

In contrast to the Dicke states discussed above, the spin projection probabilities are no longer invariant around z. We show in Figs. 4(a) and 4(b) the probabilities $\Pi_m(\theta, \phi)$ for two azimuthal angles $\phi_{\min} = -0.4(2)$ rad and $\phi_{\max} = \phi_{\min} + \pi/2$, which feature minimal and maximal spin projection uncertainties, respectively. For $\theta = \pi/2$, a minimum spin projection uncertainty $\Delta J_{\min} = 0.92(16)$ is measured at $\phi_{\min}$ [see Fig. 4(c)], in agreement with the value $\Delta J_{\min} = 0.85$ expected for an optimally squeezed state (within the one-axis twisting dynamics). We report in Fig. 4(d) the corresponding distribution $\mathcal{C}_{\mathbf{n}}$. The measured $\mathcal{C}_{\mathbf{n}}$ takes its maximum for $\theta = \pi/2$ and $\phi = \phi_{\min}$, i.e., along the squeezed quadrature direction. This maximum gives a value for the concurrence $\mathcal{C} = 0.058(6)$, in agreement with the expected value of 0.055.

Our measurements can be used to check the direct link between quadrature squeezing and nonclassical pairwise correlations [57]. Indeed, for the states reached via the one-axis twisting dynamics, one expects the concurrence to be expressed in terms of the minimum spin projection uncertainty, as

$$\mathcal{C} = \frac{1 - 2\Delta J_{\min}^2/J}{2J - 1}. \tag{5}$$

From the measured projection quadrature, we calculate a value of 0.053(5) for the right-hand side of Eq. (5), in agreement with the direct measurement of the concurrence.

IV. PROBING ENTANGLEMENT VIA THE SUBSYSTEM ENTROPY

So far, we studied the entanglement of $2J$-qubit states via the nonclassical character of their qubit pairs. In this section, we access entanglement more directly, by probing whether a given state of the spin $J = 8$ is separable with respect to the 14|2 partition performed by the photon absorption. For this, we use the fact that for a separable state, the global state is more disordered than its parts [58]. More precisely, we quantify disorder via the Rényi entropy of infinite order (also called the min-entropy), defined as [59]

$$S_\infty(\rho) = -\ln \lambda_{\max}(\rho),$$

where $\lambda_{\max}$ is the maximum eigenvalue of the density matrix ρ. This eigenvalue corresponds to the maximum possible overlap of ρ with a pure state. To reveal entanglement within a state ρ of the collective spin J, it is thus sufficient to show that the entropy of the reduced pair state ρ_{pair} is strictly higher than that of the original state ρ, i.e., if the conditional entropy satisfies [58]

$$S_\infty(14|2) \equiv S_\infty(\rho) - S_\infty(\rho_{\text{pair}}) < 0.$$

A. Entanglement of the W state

The evaluation of the pair state entropy $S_\infty(\rho_{\text{pair}})$ is based on the tomography of the pair density matrix [60]. Full information on the density matrix is contained in the Husimi function $Q_{\text{pair}}(\mathbf{n})$. We fit the measured Husimi function by a spherical harmonic expansion

$$Q_{\text{pair}}(\mathbf{n}) = \frac{1}{3} + \sqrt{\frac{4\pi}{3}} \sum_{\ell=1}^{2} \sum_{m=-\ell}^{\ell} \lambda_{\ell,m} Y_\ell^m(\mathbf{n}) \tag{6}$$

and infer the density matrix as

$$\rho_{\text{pair}} = \frac{1}{3}\mathbb{1} + \sum_{m=-1}^{1} \lambda_{1,m}\mathcal{L}_m + \sum_{m=-2}^{2} \lambda_{2,m}\mathcal{Q}_m, \tag{7}$$

where the $\mathcal{L}_m$ and $\mathcal{Q}_m$ matrices correspond to the $L = 1$ angular momentum components and quadrupole moments, respectively (see Appendix B).

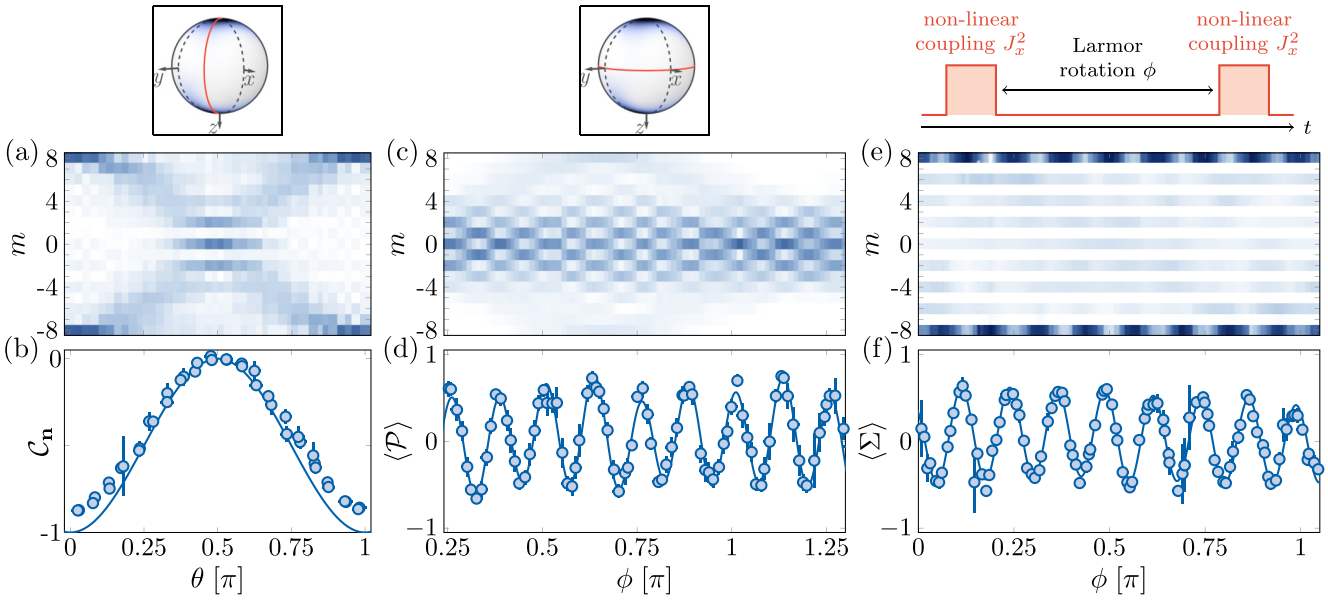

FIG. 5. Characterization of entanglement in a Schrödinger cat state. (a) Measured spin projection probabilities Π_m for a cat state, as a function of the polar angle θ. The azimuthal angle $\phi = 0.86(5)$ rad is chosen such that the two coherent-state Husimi functions destructively interfere for odd m values around $\theta = \pi/2$. (b) Distribution $\mathcal{C}_\mathbf{n}$ inferred from the probabilities shown in (a) (blue circles). The solid line is the expected variation for a perfect cat state. (c) Projection probabilities Π_m measured along equatorial directions ($\theta = \pi/2$) parametrized by the azimuthal angle ϕ. (d) Evolution of the mean parity $\langle\mathcal{P}\rangle$ deduced from (c). (e) Projection probabilities Π_m measured after a Larmor rotation of angle ϕ followed by a second nonlinear evolution. (f) Evolution of the mean sign of even projections $\langle\Sigma\rangle$ deduced from (e). The solid lines in (d) and (f) are fits with a Fourier series.

We apply this protocol to the W state, taking into account the slight variation of the Husimi function $Q_{\text{pair}}(\mathbf{n})$ with respect to the azimuthal angle ϕ in the prepared state [50]. We infer a density matrix

$$\rho_{\text{pair}} \simeq \begin{pmatrix} 0.88 & 0.01+0.05i & -0.01-0.01i \\ 0.01-0.05i & 0.12 & 0.01i \\ -0.01+0.01i & -0.01i & 0 \end{pmatrix},$$

with typically 1% statistical uncertainty. The reconstructed density matrix matches well the expected one

$$\rho_{\text{pair}} = \begin{pmatrix} 7/8 & 0 & 0 \\ 0 & 1/8 & 0 \\ 0 & 0 & 0 \end{pmatrix}.$$

Diagonalization of the reconstructed density matrix gives a maximum eigenvalue $\lambda_{\max}(\rho_{\text{pair}}) = 0.882(5)$.

We now consider the global spin-J state. The projection probability $\Pi_{-J+1} = 0.91(1)$ with the Dicke state $|m = -J+1\rangle$ provides a lower bound on the maximum overlap $\lambda_{\max}(\rho)$ with pure states.

Combining these results together, we obtain

$$S_\infty(14|2) < -0.03(1).$$

Its negative value shows that the prepared state is not separable with respect to a 14|2 partition, and is thus entangled.

B. Entanglement of a Schrödinger cat state

We now consider the case of a Schrödinger cat state, for which the effect of the 14|2 partition is more striking. Schrödinger cat states, which constitute archetypal states with highly nonclassical properties, have been realized in different types of experiments [30,56,61–77].

The cat state considered here is the coherent superposition of two quasiclassical spin states $|m = \pm J\rangle$ [78]. To produce it, we use the one-axis twisting dynamics discussed above, with a stronger nonlinear coupling $\chi = 2\pi \times 1.25$ MHz and a reduced magnetic field $B = 53.7(1)$ mG. After showing quadrature squeezing at short times ($t \sim 10$ ns), the spin quadratures collapse to a featureless spin distribution, before a revival at a time $t_{\text{cat}} = \pi/(2\chi) = 200$ ns, at which the system forms a coherent superposition of stretched states $|m = \pm J\rangle$ [56].

In Fig. 5(a), we show the measured probabilities $\Pi_m(\mathbf{n})$ for various polar angles θ with a fixed azimuthal angle ϕ. For $\theta = 0$, we confirm the dominant population of the two stretched states, with $\Pi_{-J} = 0.38(2)$ and $\Pi_J = 0.42(2)$. When varying θ, the distribution is a superposition of the contributions of each of the two coherent states forming the cat state. Interestingly, we observe an interference between the two distributions when they overlap, i.e., for $\theta \simeq \pi/2$. As shown in Fig. 5(c), the interference pattern depends on the azimuthal angle ϕ, with an alternation between even- and odd-m projections of period $2\pi/(2J)$ [79].

We first test whether a qubit pair extracted from this state features nonclassical behavior. We expect the distribution $\mathcal{C}_\mathbf{n}$ to be rotationally invariant around z and thus study its variation with the polar angle θ in Fig. 5(b) [80]. Our measurements are consistent with $\mathcal{C}_\mathbf{n} < 0$ for all angles θ, showing that the reduced two-qubit state is classical. This measurement highlights the well-known property of this state that any of its subsystems is classical.

We now extend the tomography protocol to the cat state and obtain the reduced two-body density matrix

$$\rho_{\rm pair} \simeq \begin{pmatrix} 0.46 & -0.01i & -0.03+0.05i \\ 0.01i & 0.05 & -0.01i \\ -0.03-0.05i & 0.01i & 0.49 \end{pmatrix},$$

which we compare with the expected matrix

$$\rho_{\rm pair} = \begin{pmatrix} 1/2 & 0 & 0 \\ 0 & 0 & 0 \\ 0 & 0 & 1/2 \end{pmatrix} \tag{8}$$

obtained for a perfect cat state. We compute the maximum eigenvalue $\lambda_{\rm max}(\rho_{\rm pair}) = 0.53(1)$ of the reconstructed matrix.

In order to reveal entanglement in the prepared state, we evaluate its overlap with perfect cat states $|{\rm cat}(\alpha)\rangle = (|m=-J\rangle + e^{i\alpha}|m=J\rangle)/\sqrt{2}$, which constitute a family of pure quantum states. The simple form of these states in the Dicke basis allows us to express the overlap with a state ρ as

$$\mathcal{O}_\alpha = \frac{\rho_{-J,-J} + \rho_{J,J} + 2\,{\rm Re}(\rho_{-J,J}\, e^{i\alpha})}{2},$$

where the diagonal elements $\rho_{m,m}$ correspond to the spin projection probabilities Π_m. The overlap $\mathcal{O}_\alpha$ takes its maximum value $\mathcal{O}$ for $\alpha = -\arg\rho_{-J,J}$, with

$$\mathcal{O} = \frac{\Pi_{-J} + \Pi_J + 2|\rho_{-J,J}|}{2}.$$

We present two protocols giving a lower bound on the extremal coherence $|\rho_{-J,J}|$, both based on the measurement of an observable A defined on the spin J. We consider its mean value in a state obtained after the cat state preparation, followed by a Larmor rotation around z of angle ϕ, as

$$\langle A\rangle(\phi) = \sum_{m,m'} a_{m,m'}\rho_{m',m} e^{i(m'-m)\phi}.$$

The extremal coherence can be singled out by measuring the Fourier coefficient $A_{2J} = |a_{J,-J}\rho_{-J,J}|$ at frequency $2J$ [77,79]. We will use observables that can take values in the interval $[-1, 1]$ only, such that $|a_{J,-J}| \leqslant 1$. The coefficient A_{2J} then provides a lower bound on the extremal coherence $|\rho_{-J,J}|$.

The first observable we consider is the parity $\mathcal{P}$ of the spin projection along an equatorial direction $\mathbf{n} \perp \mathbf{e}_z$—an observable commonly used to characterize cat states [64,65,69,70,75–77]. We fit its oscillation, shown in Fig. 5(d), with a Fourier series, from which we get the Fourier coefficient $\mathcal{P}_{2J} = 0.26(1)$. The second observable uses a nonlinear evolution, obtained by repeating the one-axis twisting evolution used to produce the cat state [56,81–84] [see the scheme in Fig. 5(e)]. In the absence of imperfections, the system is brought to a superposition $\sin(J\phi)|m=-J\rangle + \cos(J\phi)|m=J\rangle$, which allows us to extract the maximal coherence from the projection probabilities in stretched states only. The projection probabilities measured with this protocol are shown in Fig. 5(e). In practice, we observe residual probabilities in other projection values m, with m even only, as expected from parity symmetry. We thus use an observable Σ defined as the sign of the spin projection on even states, with

$$\langle\Sigma\rangle = \sum_{m\ {\rm even}} {\rm sgn}(m)\Pi_m.$$

Its oscillation, shown in Fig. 5(f), gives a Fourier coefficient $\Sigma_{2J} = 0.247(5)$. The advantage of the second method will become clear when we consider a more complex quantum state in the next section.

The two protocols lead to comparable estimates of the extremal coherence. Using the measured probabilities $\Pi_{\pm J}$ quoted above, we infer a lower bound on the overlap $\mathcal{O} \geqslant 0.66(2)$ and thus on the eigenvalue $\lambda_{\rm max}(\rho)$. Together, these measurements provide a conditional entropy

$$S_\infty(14|2) < -0.23(3),$$

which proves entanglement more evidently than for the W state. We note that the requirement $\mathcal{O} > \lambda_{\rm max}(\rho_{\rm pair}) = 0.53(1)$, which we used to demonstrate the nonseparability of the 14|2 partition, is consistent with the entanglement witness $\mathcal{O} > 0.5$ extensively used for cat states [25].

V. DECOHERENCE UPON QUBIT LOSS

We now consider the removal of a pair of qubits randomly drawn from the electronic spin, irrespective of its quantum state. For this purpose, we prepare a quantum state of interest ρ' in an excited level of angular momentum $J' = 9$, corresponding to a symmetric state of $2J' = 18$ qubits [see Fig. 1(b)]. The spontaneous emission of a photon drives the system to the ground state $J = 8$, which has two missing qubits. Since the emitted photon can carry an arbitrary polarization, the process allows for three independent quantum jumps associated with the polarizations $\mathbf{e}_-, \mathbf{e}_z, \mathbf{e}_+$, with $\mathbf{e}_\pm = (\mathbf{e}_x \pm i\mathbf{e}_y)/\sqrt{2}$. The ground-state density matrix then reads

$$\rho = \sum_{\mathbf{e}_u=\mathbf{e}_-,\mathbf{e}_z,\mathbf{e}_+} \langle\mathbf{e}_u|\rho'|\mathbf{e}_u\rangle,$$

which can be simply written as

$$\rho = {\rm Tr}_2\rho',$$

corresponding to the loss of an arbitrary qubit pair.

A. Robustness of pairwise quantum correlations

We first investigate the effect of particle loss on a W state prepared in an excited electronic level of angular momentum $J' = J + 1$, coupled to the ground state with an optical transition of wavelength 626 nm. To produce the state $|m' = -J' + 1\rangle$ in the excited level, we start in the coherent state $|m = -J\rangle$ of the lowest energy manifold and use π polarized resonant light to couple the system to the desired state [see Fig. 6(a)]. As shown in Fig. 6(b), we monitor the Rabi oscillation via the atom recoil upon light absorption. The comparison with a master equation model taking into account spontaneous emission during the Rabi flopping allows us to estimate a fidelity of 0.98 for a pulse duration $t_{\rm pulse} \simeq 62$ ns—the excited state lifetime being $\tau_{\rm exc} \simeq 1.2\ \mu$s [85].

Following the light pulse, we wait for spontaneous emission to occur before measuring the spin state in the ground level. We observe significant populations only in the states $|m = -J\rangle$ and $|m = -J + 1\rangle$, as expected from the selection rule $|m' - m| \leqslant 1$. The state $|m = -J + 1\rangle$ is dominantly populated, showing that, in most cases, the $|\uparrow\rangle$ excitation of the W state is not removed upon the loss of a qubit pair. The

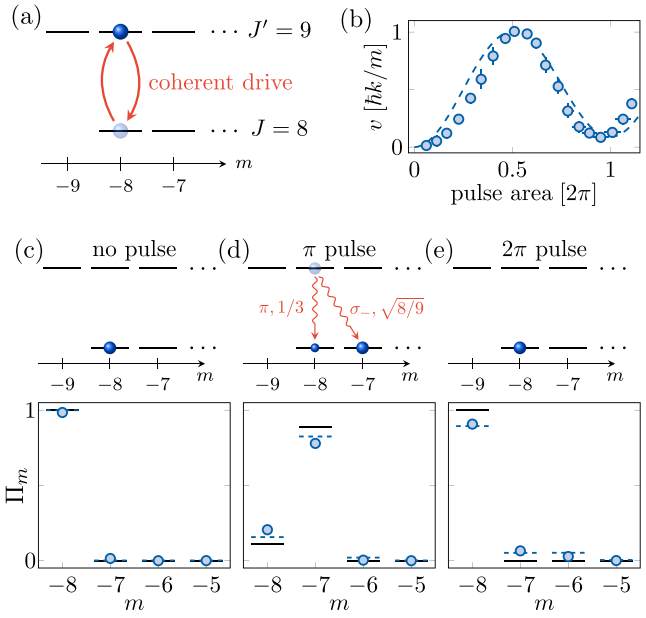

FIG. 6. Loss of a qubit pair in a W state. (a) Scheme for the preparation of the W state in the excited electronic level. (b) Evolution of the mean atom velocity acquired due to the photon absorption recoil, as a function of the light pulse duration. The dashed line is a model taking into account spontaneous emission during the pulse. (c)–(e) Top panels: expected states, with a scheme of spontaneous emission in (d) showing the Clebsch-Gordan coefficients for the two possible quantum jumps. Bottom panels: spin projection probabilities in the absence of the resonant light pulse (c), for a π pulse (d), and for a 2π pulse (e). The solid lines are the probabilities expected for a perfect W state, while the dashed lines use the same model as in (b).

projection probabilities, shown in Fig. 6(d), are close to the expected values $\Pi_{-J+1} = 1/(J+1)$ and $\Pi_{-J} = 1 - \Pi_{-J+1}$, with a residual difference mostly explained by the imperfect state preparation.

The nonclassicality of qubit pairs in the final state is probed via the distribution $\mathcal{C}_{\mathbf{n}}$ introduced in Sec. III A. We remind the reader that $\mathcal{C}_{\mathbf{n}}$ is obtained from the spin projection probabilities along $\mathbf{n}$. Since its maximum value is expected to be reached along z, we only consider projections along this direction, and obtain $\mathcal{C}_z = 0.104(3)$. This value provides a lower bound on the qubit pair concurrence, expected to be $\mathcal{C} = 1/(J+1) \simeq 0.111$ in the initial state. The proximity of the initial state concurrence and the measured one after decay illustrates that losing qubits does not alter nonclassicality of the remaining qubit pairs [24].

B. Fragility of macroscopic coherence

We contrast this behavior with the fragility of entanglement in coherent superpositions of states distant in phase space [86].

We consider two examples, namely, a cat state $|\psi_1\rangle = (|m' = -J'\rangle + |m' = J'\rangle)/\sqrt{2}$ and the superposition $|\psi_2\rangle = (|m' = -J'+1\rangle + |m' = J'-1\rangle)/\sqrt{2}$. Their preparation consists in producing a cat state in the ground manifold $(|m = -J\rangle + |m = J\rangle)/\sqrt{2}$ (see Sec. IV B) and then applying resonant light to couple it to the excited manifold. The state $|\psi_1\rangle$ is produced using an x-linear polarization $\mathbf{e}_x = (\mathbf{e}_+ + \mathbf{e}_-)/\sqrt{2}$, which dominantly couples the stretched states $|m = \pm J\rangle$ to states $|m' = \pm J'\rangle$ [see Fig. 7(a)]. Couplings to states $|m' = \pm(J'-2)\rangle$ also occur, albeit with very small Clebsch-Gordan coefficients, such that these processes can be neglected [87]. The state $|\psi_2\rangle$ is obtained using a z-linear polarization [see Fig. 7(d)]. In both cases, a coherent Rabi oscillation is observed when varying the pulse duration, and the fidelity of the preparation is limited by that of the cat state in the ground level. We show in Appendix C that the coherence of the superposition is maintained during Rabi flopping, by studying the states reached after 2π pulses.

We study the effect of qubit loss, triggered by spontaneous emission, on the superposition states $|\psi_1\rangle$ and $|\psi_2\rangle$. For the cat state $|\psi_1\rangle$, we only expect the population of the stretched states $|m = \pm J\rangle$ [see Fig. 7(b)]. To check the

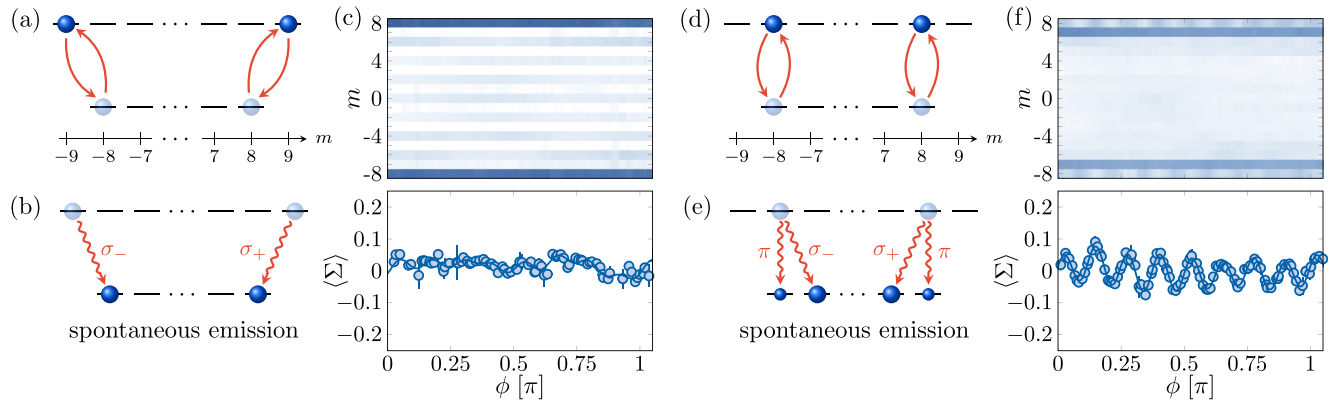

FIG. 7. Loss of a qubit pair from superposition states. (a) Preparation method for the Schrödinger cat state $|\psi_1\rangle$ in the excited electronic level. Given the small values of their Clebsch-Gordan coefficients, we neglect the couplings between $|m = \pm 8\rangle$ and $|m' = \pm 7\rangle$. (b) Scheme of the subsequent spontaneous emission. (c) Top panel: spin projection probabilities measured in the xy plane, as a function of the azimuthal angle ϕ. Bottom panel: The corresponding sign observable $\langle\Sigma\rangle$, together with a fit with a Fourier series. The y-axis range has been reduced compared with Fig. 5(f) to highlight the absence of oscillation. (d)–(f) show the same information for the superposition state $|\psi_2\rangle = (|m' = -8\rangle + |m' = 8\rangle)/\sqrt{2}$.

coherence between them, we measure the sign observable $\langle\Sigma\rangle$ as a function of the azimuthal angle ϕ, as in Sec. IV B. As shown in the bottom panel of Fig. 7(c), its oscillation is completely washed out, with a measured Fourier component $\Sigma_{2J} = 0.006(10)$, indicating an absence of coherence. For the superposition state $|\psi_2\rangle$, we observe dominant projection probabilities in the states $|m = \pm(J-1)\rangle$, corresponding to the spontaneous emission of a $\sigma_\mp$ polarized photon, respectively [see Fig. 7(e)]. We do not measure any significant variation of these probabilities with the azimuthal angle ϕ, excluding coherence between them. We also measure residual projection probabilities in the stretched states $|m = \pm J\rangle$, which occur via the spontaneous emission of a π polarized photon. The advantage of the sign observable Σ becomes clear here: It allows one to test the coherence between the states $|m = \pm J\rangle$, without being perturbed by the atoms populating odd-m states. The measured probabilities in stretched states coherently oscillate as a function of the angle ϕ [see Fig. 7(f)]. More quantitatively, the sign observable, which involves even m only, evolves with a Fourier component $\Sigma_{2J} = 0.024(1)$.

The complete loss of coherence when starting in the cat state $|\psi_1\rangle$ can be interpreted as follows. The spontaneous decay involves two orthogonal polarizations, with a σ_+ polarized photon emitted when starting in the component $|m' = -J'\rangle$, while a σ_- polarized photon is associated with the decay of the state $|m' = J'\rangle$ [see Fig. 7(b)]. The photon polarization thus holds complete *which path* information on the spin state polarization—a term referring to Einstein's version of the double-slit interference experiment [88,89]. In this case, the coherence between the different paths is erased after spontaneous emission.

For the state $|\psi_2\rangle$, the most probable quantum jumps correspond to the emission of σ_+ and σ_- polarized photons, which carry information about the state polarization [see Fig. 7(e)]. In contrast, the quantum jump associated with the emission of a π polarized photon does not give this information, which explains the residual coherence. The measured Fourier coefficient Σ_{2J} corresponds to 9.7(5)% of the value measured in the absence of the excitation. This reduction is consistent with the probability $1/(J+1) \simeq 11.1\%$ of scattering a π polarized photon for the considered state, showing that this channel fully preserves coherence.

VI. SUMMARY AND OUTLOOK

In this paper, we show that the $2J$-qubit ensemble associated with an atomic electronic spin J can be partitioned via the optical coupling to an excited level $J' = J - 1$. Among these qubits, $2J-2$ of them constitute the excited level, and the remaining two are annihilated by the absorbed photon, in a state defined by the light polarization. We investigate this process using atomic dysprosium and use it to probe entanglement in nonclassical states of spin $J = 8$. We fully characterize the nonclassical character of its reduced two-qubit state and study the increase of entropy upon partition as a smoking gun for entanglement.

In a second set of experiments, we consider the partition of an angular momentum $J' = J + 1$ of an excited electronic state. There, a random qubit pair is extracted by spontaneous emission towards the ground state J. We show that nonclassical pairwise correlations are robust to particle loss. In contrast, we observe that coherent superpositions of states distant in phase space are very fragile.

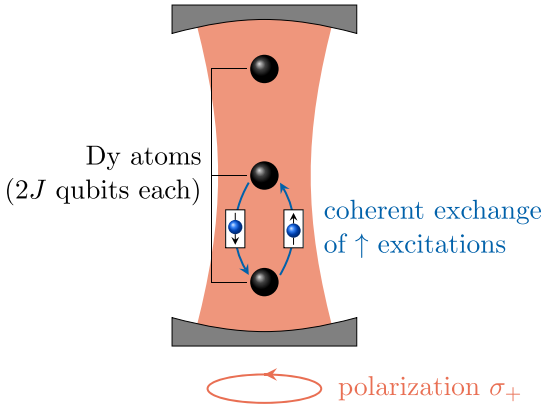

FIG. 8. Proposed scheme for entangling several Dy atoms in an optical resonator. An off-resonant optical cavity in the strong-coupling regime couples an ensemble of N atoms together. For σ_+ polarized cavity light, the total spin projection along z is conserved, and the cavity mediates the coherent exchange of $\uparrow$ qubit excitations between atoms. Such couplings can be used to stabilize a W state, with a single $\uparrow$ excitation symmetrically shared between the $N\times(2J)$ qubits.

In this paper, the study of light-spin interaction is limited to measurements of the electronic spin. A first extension would be to collect the spontaneously emitted photon, whose polarization is entangled with the electronic spin, as for experiments performed with trapped ions, atoms in optical cavities, or solid-state qubits [90–93]. One would thus explicitly access the *which path* information carried by the photon upon spontaneous emission of a Schrödinger cat state. More generally, the photon would allow one to couple qubit pairs from the electronic spin $J = 8$ to "flying qubits," which could then be manipulated to entangle distant atoms [94], and generalize quantum communication schemes to a mesoscopic degree of freedom [95].

Another interesting perspective would be to place the atomic gas in an optical cavity. The electronic spin J of a single atom would be coherently coupled to the cavity light mode, leading to a compound light-spin object [96]. For an atomic ensemble, the cavity light would also couple the electronic spins together, similarly to standard ensembles of spin-1/2 atoms coupled to optical cavities [4,97,98]. For a set of N dysprosium atoms—each hosting $2J$ qubits—the size of the Hilbert space would be $(2J+1)^N$, much smaller than the size 2^{2JN} for the same number of qubits realized with spin-1/2 atoms. This favorable scaling will mitigate decoherence effects associated with, for example, particle loss.

To be more concrete, we show in Fig. 8 an example of an application, with an ensemble of N atoms coupled to σ_+ polarized cavity light. The light mediates the coherent exchange of $|\uparrow\rangle$ excitations among the atoms, which could serve to stabilize a W state with one excitation symmetrically shared among $N \times (2J)$ qubits. Such many-body entangled states could feature a strong quantum enhancement of magnetic

sensitivity [99,100] or serve as a playground for studies of decoherence.

ACKNOWLEDGMENT

This work is supported by the European Union (Grant No. TOPODY 756722 from the European Research Council). We thank Jean Dalibard for stimulating discussions.

APPENDIX A: DEVIATION FROM z ROTATION SYMMETRY IN THE W AND CAT STATES

The W state $|m = -J + 1\rangle$ is invariant upon rotations around z, such that all observables should depend on the polar angle θ only. In practice, the state prepared close to the W state is not perfectly rotationally symmetric, because

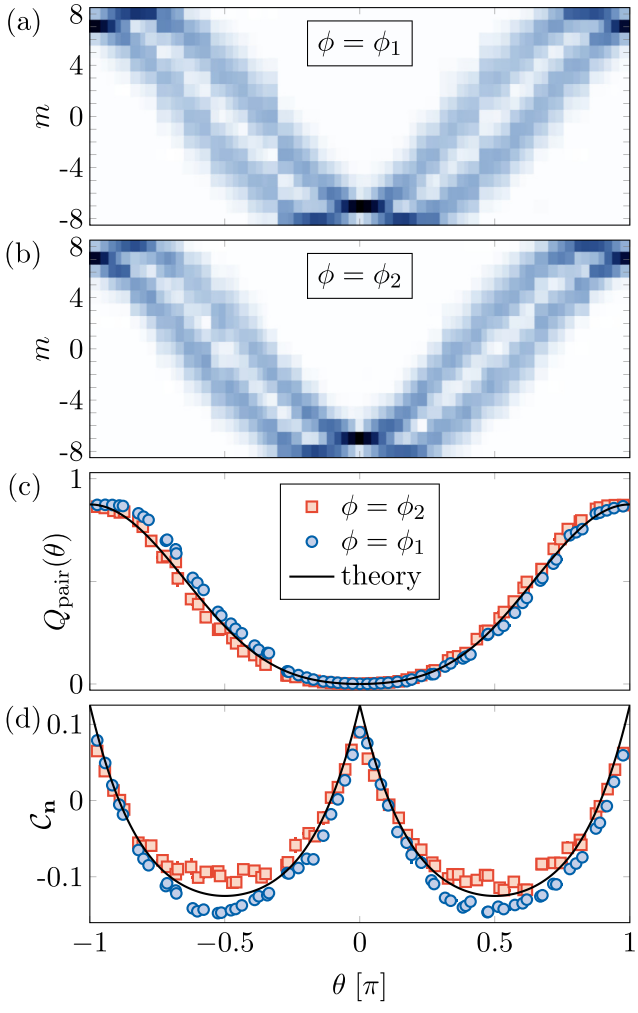

FIG. 9. Deviation from z rotation symmetry in the prepared W state. (a) and (b) Projection probabilities Π_m as a function of the polar angle θ, for $\phi_1 = 0.36(5)$ rad and $\phi_2 = \phi_1 - \pi/2$. (c) Pair Husimi functions Q_{pair} inferred from the (a) and (b) data (blue circles and red squares, respectively). The error bars represent the statistical uncertainty from a bootstrap random sampling analysis. The line corresponds to the expected variation for the W state. (d) Distribution $\mathcal{C}_{\mathbf{n}}$ as a function of θ. The two azimuthal angles ϕ_1 and ϕ_2 are chosen to minimize and maximize the measured $\mathcal{C}_{\mathbf{n}}$, respectively.

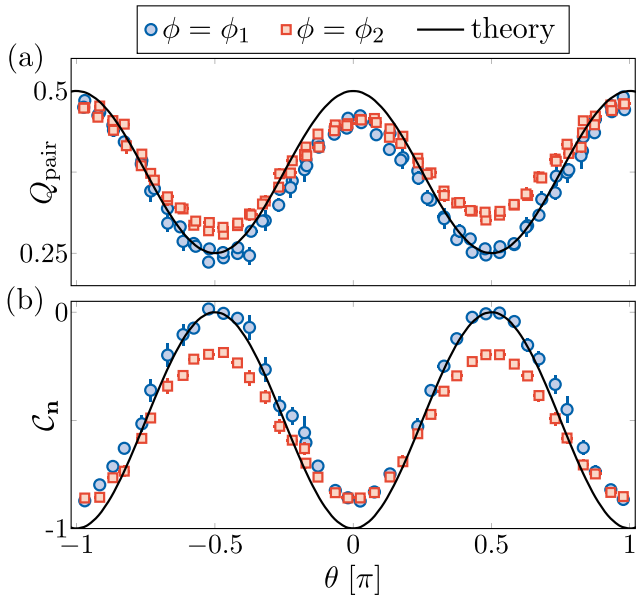

FIG. 10. Deviation from z rotation symmetry in the prepared Schrödinger cat state. (a) Pair Husimi functions Q_{pair} as a function of the polar angle θ, for $\phi_1 = 3.3(1)$ rad and $\phi_2 = \phi_1 - \pi/2$ (blue circles and red squares, respectively). The line corresponds to the expected variation for a perfect cat state. (b) Distribution $\mathcal{C}_{\mathbf{n}}$ as a function of θ deduced from the data in (a).

of a residual coherent admixture with other Dicke states. We measure a small ϕ variation of the measured probability distributions $\Pi_m(\mathbf{n})$, as well as the pair Husimi function Q_{pair} and distribution $\mathcal{C}_{\mathbf{n}}$ deduced from them. We show in Fig. 9 the

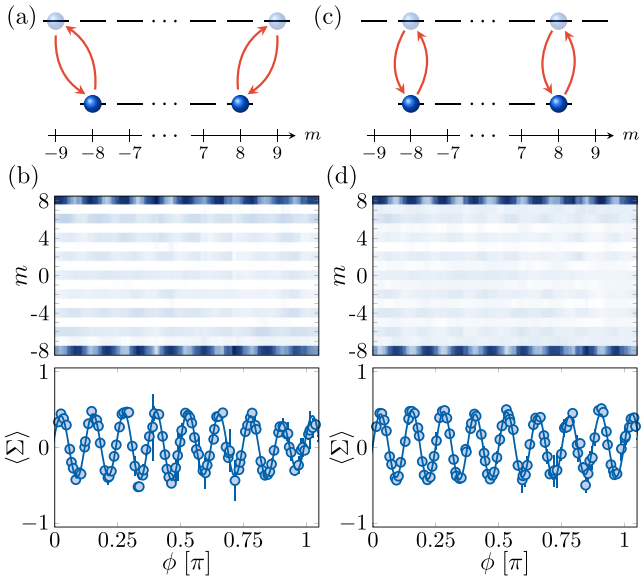

FIG. 11. (a) Scheme of the 2π Rabi oscillation starting in a Schrödinger cat state of the electronic ground level, for an x-polarized laser excitation. (b) Top panel: spin projection probabilities measured in the xy plane, as a function of the azimuthal angle ϕ. Bottom panel: the corresponding sign observable $\langle\Sigma\rangle$, together with a fit with a Fourier series. (c) and (d) show the same information for a z-polarized laser excitation.

measured data for two azimuthal angles $\phi_1 = 0.36(5)$ rad and $\phi_2 = \phi_1 - \pi/2$, for which $\mathcal{C}_\mathbf{n}$ is minimized and maximized, respectively. The data shown in Fig. 3 of the main text correspond to an average over ϕ, the error bars taking into account this dispersion.

The cat state $|m = -J\rangle + |m = J\rangle$ is not rotationally invariant. Yet, its reduced two-body density matrix, given by Eq. (8), is invariant such that the pair Husimi function Q_{pair} and distribution $\mathcal{C}_\mathbf{n}$ should depend on θ only. As for the W state, we measure a slight variation of these quantities with ϕ, as shown in Fig. 10. Since we focus on extracting the concurrence from the maximum of $\mathcal{C}_\mathbf{n}$, we show in the main text the data measured for an azimuthal angle $\phi_1 = 3.3(1)$ rad that maximizes $\mathcal{C}_\mathbf{n}$.

APPENDIX B: SPIN-1 TOMOGRAPHY USING THE PAIR HUSIMI FUNCTION

The Husimi function of a spin-1 quantum state ρ expands on the spherical harmonics Y_ℓ^m with $\ell = 1, 2$ and $|m| \leqslant \ell$, as written in Eq. (6). This linear decomposition allows us to retrieve the density matrix ρ, as given by Eq. (7), where we introduce the operators

$$\mathcal{L}_0 = L_z, \tag{B1}$$

$$\mathcal{L}_{\pm1} = \mp(L_x \pm iL_y)/\sqrt{2}, \tag{B2}$$

$$\mathcal{Q}_0 = \sqrt{\frac{5}{3}}\left(3L_z^2 - 2\right), \tag{B3}$$

$$\mathcal{Q}_{\pm1} = \mp\sqrt{\frac{5}{2}}[(L_x \pm iL_y)L_z + L_z(L_x \pm iL_y)], \tag{B4}$$

$$\mathcal{Q}_{\pm2} = \sqrt{\frac{5}{2}}(L_x \pm iL_y)^2. \tag{B5}$$

APPENDIX C: COHERENCE OF SUPERPOSITION STATES DURING RABI FLOPPING

The preparation of superposition states in the excited electronic state, as studied in Sec. V B, uses coherent Rabi oscillations, starting in a Schrödinger cat state of the ground electronic level $(|m = -J\rangle + |m = J\rangle)/\sqrt{2}$. To check that coherence is maintained during the Rabi oscillation, we study it after a 2π excitation, by measuring the oscillation of the sign observable $\langle\Sigma\rangle$.

As shown in Fig. 11, we find that the coherence $|\rho_{-J,J}|$, estimated by the Fourier component Σ_{2J}, is reduced to 0.202(2) [0.211(6)] for the x-polarized (z-polarized) excitation, i.e., above 80% of the value obtained with no Rabi pulse. These measurements confirm that coherence is preserved during the Rabi oscillation.

[1] S. J. Freedman and J. F. Clauser, Experimental Test of Local Hidden-Variable Theories, Phys. Rev. Lett. **28**, 938 (1972).

[2] A. Aspect, J. Dalibard, and G. Roger, Experimental Test of Bell's Inequalities Using Time-Varying Analyzers, Phys. Rev. Lett. **49**, 1804 (1982).

[3] L. Amico, R. Fazio, A. Osterloh, and V. Vedral, Entanglement in many-body systems, Rev. Mod. Phys. **80**, 517 (2008).

[4] L. Pezzè, A. Smerzi, M. K. Oberthaler, R. Schmied, and P. Treutlein, Quantum metrology with nonclassical states of atomic ensembles, Rev. Mod. Phys. **90**, 035005 (2018).

[5] A. Sørensen, L.-M. Duan, J. I. Cirac, and P. Zoller, Many-particle entanglement with Bose–Einstein condensates, Nature (London) **409**, 63 (2001).

[6] A. S. Sørensen and K. Mølmer, Entanglement and Extreme Spin Squeezing, Phys. Rev. Lett. **86**, 4431 (2001).

[7] J. Esteve, C. Gross, A. Weller, S. Giovanazzi, and M. Oberthaler, Squeezing and entanglement in a Bose–Einstein condensate, Nature (London) **455**, 1216 (2008).

[8] M. F. Riedel, P. Böhi, Y. Li, T. W. Hänsch, A. Sinatra, and P. Treutlein, Atom-chip-based generation of entanglement for quantum metrology, Nature (London) **464**, 1170 (2010).

[9] C. Gross, T. Zibold, E. Nicklas, J. Estève, and M. K. Oberthaler, Nonlinear atom interferometer surpasses classical precision limit, Nature (London) **464**, 1165 (2010).

[10] P. Hyllus, W. Laskowski, R. Krischek, C. Schwemmer, W. Wieczorek, H. Weinfurter, L. Pezzé, and A. Smerzi, Fisher information and multiparticle entanglement, Phys. Rev. A **85**, 022321 (2012).

[11] G. Tóth, Multipartite entanglement and high-precision metrology, Phys. Rev. A **85**, 022322 (2012).

[12] J.-W. Pan, Z.-B. Chen, C.-Y. Lu, H. Weinfurter, A. Zeilinger, and M. Żukowski, Multiphoton entanglement and interferometry, Rev. Mod. Phys. **84**, 777 (2012).

[13] G. Wendin, Quantum information processing with superconducting circuits: A review, Rep. Prog. Phys. **80**, 106001 (2017).

[14] R. Blatt and D. Wineland, Entangled states of trapped atomic ions, Nature (London) **453**, 1008 (2008).

[15] M. Saffman, T. G. Walker, and K. Mølmer, Quantum information with Rydberg atoms, Rev. Mod. Phys. **82**, 2313 (2010).

[16] R. Horodecki, P. Horodecki, M. Horodecki, and K. Horodecki, Quantum entanglement, Rev. Mod. Phys. **81**, 865 (2009).

[17] O. Gühne and G. Tóth, Entanglement detection, Phys. Rep. **474**, 1 (2009).

[18] S. Hill and W. K. Wootters, Entanglement of a Pair of Quantum Bits, Phys. Rev. Lett. **78**, 5022 (1997).

[19] W. K. Wootters, Entanglement of Formation of an Arbitrary State of Two Qubits, Phys. Rev. Lett. **80**, 2245 (1998).

[20] F. A. Bovino, G. Castagnoli, A. Ekert, P. Horodecki, C. M. Alves, and A. V. Sergienko, Direct Measurement of Nonlinear Properties of Bipartite Quantum States, Phys. Rev. Lett. **95**, 240407 (2005).

[21] S. P. Walborn, P. H. Souto Ribeiro, L. Davidovich, F. Mintert, and A. Buchleitner, Experimental determination of entanglement with a single measurement, Nature (London) **440**, 1022 (2006).

[22] C. Schmid, N. Kiesel, W. Wieczorek, H. Weinfurter, F. Mintert, and A. Buchleitner, Experimental Direct Observation of Mixed State Entanglement, Phys. Rev. Lett. **101**, 260505 (2008).

[23] R. Islam, R. Ma, P. M. Preiss, M. Eric Tai, A. Lukin, M. Rispoli, and M. Greiner, Measuring entanglement entropy in a quantum many-body system, Nature (London) **528**, 77 (2015).

[24] W. Dür, G. Vidal, and J. I. Cirac, Three qubits can be entangled in two inequivalent ways, Phys. Rev. A **62**, 062314 (2000).

[25] G. Tóth and O. Gühne, Detecting Genuine Multipartite Entanglement with Two Local Measurements, Phys. Rev. Lett. **94**, 060501 (2005).

[26] R. Lapkiewicz, P. Li, C. Schaeff, N. K. Langford, S. Ramelow, M. Wieśniak, and A. Zeilinger, Experimental non-classicality of an indivisible quantum system, Nature (London) **474**, 490 (2011).

[27] S. Chaudhury, S. Merkel, T. Herr, A. Silberfarb, I. H. Deutsch, and P. S. Jessen, Quantum Control of the Hyperfine Spin of a Cs Atom Ensemble, Phys. Rev. Lett. **99**, 163002 (2007).

[28] T. Fernholz, H. Krauter, K. Jensen, J. F. Sherson, A. S. Sørensen, and E. S. Polzik, Spin Squeezing of Atomic Ensembles via Nuclear-Electronic Spin Entanglement, Phys. Rev. Lett. **101**, 073601 (2008).

[29] D. Gatteschi and R. Sessoli, Quantum tunneling of magnetization and related phenomena in molecular materials, Angew. Chem. Int. Ed. **42**, 268 (2003).

[30] A. Facon, E.-K. Dietsche, D. Grosso, S. Haroche, J.-M. Raimond, M. Brune, and S. Gleyzes, A sensitive electrometer based on a Rydberg atom in a Schrödinger-cat state, Nature (London) **535**, 262 (2016).

[31] E. Majorana, Atomi orientati in campo magnetico variabile, Nuovo Cim. **9**, 43 (1932).

[32] In practice, since the light shift amplitudes strongly vary with m, we vary the pulse duration in the range 10–100 μs and the detuning in the range 50 MHz to 1 GHz, in order to keep similar displacements for all m states (except the dark states). For the smallest detunings, we take into account the corrections to the second-order light shifts. The uncertainties in the laser beam waist $w = 40(5)$ μm and in the excited state lifetime $\tau \simeq 11$ μs [101] lead to a systematic error. We correct an overall 20% error using the constraint $\sum_m Q_m = (2J+1)/3$, which states that in a completely undetermined state, a symmetric qubit pair has 1/3 chance to be in $|\uparrow\uparrow\rangle$.

[33] R. H. Dicke, Coherence in spontaneous radiation processes, Phys. Rev. **93**, 99 (1954).

[34] K. S. Choi, A. Goban, S. B. Papp, S. J. van Enk, and H. J. Kimble, Entanglement of spin waves among four quantum memories, Nature (London) **468**, 412 (2010).

[35] F. Haas, J. Volz, R. Gehr, J. Reichel, and J. Estève, Entangled states of more than 40 atoms in an optical fiber cavity, Science **344**, 180 (2014).

[36] R. McConnell, H. Zhang, J. Hu, S. Ćuk, and V. Vuletić, Entanglement with negative Wigner function of almost 3,000 atoms heralded by one photon, Nature (London) **519**, 439 (2015).

[37] M. Ebert, M. Kwon, T. G. Walker, and M. Saffman, Coherence and Rydberg Blockade of Atomic Ensemble Qubits, Phys. Rev. Lett. **115**, 093601 (2015).

[38] J. Zeiher, P. Schauß, S. Hild, T. Macrì, I. Bloch, and C. Gross, Microscopic Characterization of Scalable Coherent Rydberg Superatoms, Phys. Rev. X **5**, 031015 (2015).

[39] H. Häffner, W. Hänsel, C. F. Roos, J. Benhelm, D. Chek-al-kar, M. Chwalla, T. Körber, U. D. Rapol, M. Riebe, P. O. Schmidt, C. Becher, O. Gühne, W. Dür, and R. Blatt, Scalable multiparticle entanglement of trapped ions, Nature (London) **438**, 643 (2005).

[40] F. Fröwis, P. C. Strassmann, A. Tiranov, C. Gut, J. Lavoie, N. Brunner, F. Bussières, M. Afzelius, and N. Gisin, Experimental certification of millions of genuinely entangled atoms in a solid, Nat. Commun. **8**, 907 (2017).

[41] Y. Pu, Y. Wu, N. Jiang, W. Chang, C. Li, S. Zhang, and L. Duan, Experimental entanglement of 25 individually accessible atomic quantum interfaces, Sci. Adv. **4**, 3931 (2018).

[42] P. Facchi and S. Pascazio, Quantum Zeno Subspaces, Phys. Rev. Lett. **89**, 080401 (2002).

[43] F. Schäfer, I. Herrera, S. Cherukattil, C. Lovecchio, F. S. Cataliotti, F. Caruso, and A. Smerzi, Experimental realization of quantum Zeno dynamics, Nat. Commun. **5**, 3194 (2014).

[44] A. Signoles, A. Facon, D. Grosso, I. Dotsenko, S. Haroche, J.-M. Raimond, M. Brune, and S. Gleyzes, Confined quantum Zeno dynamics of a watched atomic arrow, Nat. Phys. **10**, 715 (2014).

[45] The W-state fidelity is mostly limited by inelastic collisions between atoms, which redistribute the spin among neighboring m states.

[46] E. C. G. Sudarshan, Equivalence of Semiclassical and Quantum Mechanical Descriptions of Statistical Light Beams, Phys. Rev. Lett. **10**, 277 (1963).

[47] R. J. Glauber, Coherent and Incoherent States of the Radiation Field, Phys. Rev. **131**, 2766 (1963).

[48] O. Giraud, P. Braun, and D. Braun, Classicality of spin states, Phys. Rev. A **78**, 042112 (2008).

[49] J. K. Korbicz, J. I. Cirac, and M. Lewenstein, Spin Squeezing Inequalities and Entanglement of N Qubit States, Phys. Rev. Lett. **95**, 120502 (2005).

[50] While the W state is rotationally symmetric around z, we observe in the prepared state a small but significant variation of the projection probabilities with the azimuthal angle ϕ. We show in Figs. 3(b)–3(d) the ϕ-averaged values of our measurements. The variation with ϕ of the measured quantities is taken into account in the error bars and is explicitly shown in Appendix A.

[51] M. Hillery, Nonclassical distance in quantum optics, Phys. Rev. A **35**, 725 (1987).

[52] T.-C. Wei and P. M. Goldbart, Geometric measure of entanglement and applications to bipartite and multipartite quantum states, Phys. Rev. A **68**, 042307 (2003).

[53] J. Vidal, Concurrence in collective models, Phys. Rev. A **73**, 062318 (2006).

[54] M. Koashi, V. Bužek, and N. Imoto, Entangled webs: Tight bound for symmetric sharing of entanglement, Phys. Rev. A **62**, 050302(R) (2000).

[55] M. Kitagawa and M. Ueda, Squeezed spin states, Phys. Rev. A **47**, 5138 (1993).

[56] T. Chalopin, C. Bouazza, A. Evrard, V. Makhalov, D. Dreon, J. Dalibard, L. A. Sidorenkov, and S. Nascimbene, Quantum-enhanced sensing using non-classical spin states of a highly magnetic atom, Nat. Commun. **9**, 4955 (2018).

[57] X. Wang and B. C. Sanders, Spin squeezing and pairwise entanglement for symmetric multiqubit states, Phys. Rev. A **68**, 012101 (2003).

[58] R. Horodecki and M. Horodecki, Information-theoretic aspects of inseparability of mixed states, Phys. Rev. A **54**, 1838 (1996).

[59] R. Konig, R. Renner, and C. Schaffner, The operational meaning of min- and max-entropy, IEEE Trans. Inf. Theory **55**, 4337 (2009).

[60] V. I. Man'ko and O. V. Man'ko, Spin state tomography, J. Exp. Theor. Phys. **85**, 430 (1997).

[61] C. Monroe, D. Meekhof, B. King, and D. J. Wineland, A "Schrödinger cat" superposition state of an atom, Science **272**, 1131 (1996).

[62] M. Brune, E. Hagley, J. Dreyer, X. Maître, A. Maali, C. Wunderlich, J. M. Raimond, and S. Haroche, Observing the Progressive Decoherence of the "Meter" in a Quantum Measurement, Phys. Rev. Lett. **77**, 4887 (1996).

[63] J. R. Friedman, V. Patel, W. Chen, S. Tolpygo, and J. E. Lukens, Quantum superposition of distinct macroscopic states, Nature (London) **406**, 43 (2000).

[64] C. A. Sackett, D. Kielpinski, B. E. King, C. Langer, V. Meyer, C. J. Myatt, M. Rowe, Q. A. Turchette, W. M. Itano, D. J. Wineland, and C. Monroe, Experimental entanglement of four particles, Nature (London) **404**, 256 (2000).

[65] D. Leibfried, E. Knill, S. Seidelin, J. Britton, R. B. Blakestad, J. Chiaverini, D. B. Hume, W. M. Itano, J. D. Jost, C. Langer, R. Ozeri, R. Reichle, and D. J. Wineland, Creation of a six-atom 'Schrödinger cat' state, Nature (London) **438**, 639 (2005).

[66] A. Ourjoumtsev, R. Tualle-Brouri, J. Laurat, and P. Grangier, Generating optical Schrödinger kittens for quantum information processing, Science **312**, 83 (2006).

[67] J. S. Neergaard-Nielsen, B. M. Nielsen, C. Hettich, K. Mølmer, and E. S. Polzik, Generation of a Superposition of Odd Photon Number States for Quantum Information Networks, Phys. Rev. Lett. **97**, 083604 (2006).

[68] S. Deleglise, I. Dotsenko, C. Sayrin, J. Bernu, M. Brune, J.-M. Raimond, and S. Haroche, Reconstruction of non-classical cavity field states with snapshots of their decoherence, Nature (London) **455**, 510 (2008).

[69] T. Monz, P. Schindler, J. T. Barreiro, M. Chwalla, D. Nigg, W. A. Coish, M. Harlander, W. Hänsel, M. Hennrich, and R. Blatt, 14-Qubit Entanglement: Creation and Coherence, Phys. Rev. Lett. **106**, 130506 (2011).

[70] X.-C. Yao, T.-X. Wang, P. Xu, H. Lu, G.-S. Pan, X.-H. Bao, C.-Z. Peng, C.-Y. Lu, Y.-A. Chen, and J.-W. Pan, Observation of eight-photon entanglement, Nat. Photon. **6**, 225 (2012).

[71] G. Kirchmair, B. Vlastakis, Z. Leghtas, S. E. Nigg, H. Paik, E. Ginossar, M. Mirrahimi, L. Frunzio, S. M. Girvin, and R. J. Schoelkopf, Observation of quantum state collapse and revival due to the single-photon Kerr effect, Nature (London) **495**, 205 (2013).

[72] C. L. Degen, F. Reinhard, and P. Cappellaro, Quantum sensing, Rev. Mod. Phys. **89**, 035002 (2017).

[73] X.-L. Wang, Y.-H. Luo, H.-L. Huang, M.-C. Chen, Z.-E. Su, C. Liu, C. Chen, W. Li, Y.-Q. Fang, X. Jiang, J. Zhang, L. Li, N.-L. Liu, C.-Y. Lu, and J.-W. Pan, 18-Qubit Entanglement with Six Photons' Three Degrees of Freedom, Phys. Rev. Lett. **120**, 260502 (2018).

[74] E. K. Dietsche, A. Larrouy, S. Haroche, J. M. Raimond, M. Brune, and S. Gleyzes, High-sensitivity magnetometry with a single atom in a superposition of two circular Rydberg states, Nat. Phys. **15**, 326 (2019).

[75] C. Song, K. Xu, H. Li, Y.-R. Zhang, X. Zhang, W. Liu, Q. Guo, Z. Wang, W. Ren, J. Hao, H. Feng, H. Fan, D. Zheng, D.-W. Wang, H. Wang, and S.-Y. Zhu, Generation of multicomponent atomic Schrödinger cat states of up to 20 qubits, Science **365**, 574 (2019).

[76] A. Omran, H. Levine, A. Keesling, G. Semeghini, T. T. Wang, S. Ebadi, H. Bernien, A. S. Zibrov, H. Pichler, S. Choi, J. Cui, M. Rossignolo, P. Rembold, S. Montangero, T. Calarco, M. Endres, M. Greiner, V. Vuletić, and M. D. Lukin, Generation and manipulation of Schrödinger cat states in Rydberg atom arrays, Science **365**, 570 (2019).

[77] K. X. Wei, I. Lauer, S. Srinivasan, N. Sundaresan, D. T. McClure, D. Toyli, D. C. McKay, J. M. Gambetta, and S. Sheldon, Verifying multipartite entangled Greenberger-Horne-Zeilinger states via multiple quantum coherences, Phys. Rev. A **101**, 032343 (2020).

[78] N. D. Mermin, Extreme Quantum Entanglement in a Superposition of Macroscopically Distinct States, Phys. Rev. Lett. **65**, 1838 (1990).

[79] J. J. Bollinger, W. M. Itano, D. J. Wineland, and D. J. Heinzen, Optimal frequency measurements with maximally correlated states, Phys. Rev. A **54**, R4649(R) (1996).

[80] In practice, we observe a small variation of the measured $\mathcal{C}_{\mathbf{n}}$ with the azimuthal angle ϕ, discussed in Appendix A. We show in Fig. 5(b) the variation of $\mathcal{C}_{\mathbf{n}}$ with the polar angle θ with a fixed angle $\phi = 3.3(1)$ rad, which maximizes the value of $\mathcal{C}_{\mathbf{n}}$.

[81] E. Davis, G. Bentsen, and M. Schleier-Smith, Approaching the Heisenberg Limit without Single-Particle Detection, Phys. Rev. Lett. **116**, 053601 (2016).

[82] D. Linnemann, H. Strobel, W. Muessel, J. Schulz, R. J. Lewis-Swan, K. V. Kheruntsyan, and M. K. Oberthaler, Quantum-Enhanced Sensing Based on Time Reversal of Nonlinear Dynamics, Phys. Rev. Lett. **117**, 013001 (2016).

[83] F. Fröwis, P. Sekatski, and W. Dür, Detecting Large Quantum Fisher Information with Finite Measurement Precision, Phys. Rev. Lett. **116**, 090801 (2016).

[84] T. Macrì, A. Smerzi, and L. Pezzè, Loschmidt echo for quantum metrology, Phys. Rev. A **94**, 010102(R) (2016).

[85] M. Gustavsson, H. Lundberg, L. Nilsson, and S. Svanberg, Lifetime measurements for excited states of rare-earth atoms using pulse modulation of a cw dye-laser beam, J. Opt. Soc. Am. **69**, 984 (1979).

[86] C.-W. Lee and H. Jeong, Quantification of Macroscopic Quantum Superpositions within Phase Space, Phys. Rev. Lett. **106**, 220401 (2011).

[87] The coupling amplitudes between $|m = \pm J\rangle$ and $|m' = \pm(J'-2)\rangle$ are $1/\sqrt{153}$ smaller than the couplings between $|m = \pm J\rangle$ and $|m' = \pm J'\rangle$. When the population of $|m' = \pm J'\rangle$ is maximized, we expect a residual population of the states $|m' = \pm(J'-2)\rangle$ of 3% due to these small couplings.

[88] W. K. Wootters and W. H. Zurek, Complementarity in the double-slit experiment: Quantum nonseparability and a quantitative statement of Bohr's principle, Phys. Rev. D **19**, 473 (1979).

[89] B.-G. Englert, Fringe Visibility and Which-Way Information: An Inequality, Phys. Rev. Lett. **77**, 2154 (1996).

[90] B. B. Blinov, D. L. Moehring, L.-M. Duan, and C. Monroe, Observation of entanglement between a single trapped atom and a single photon, Nature (London) **428**, 153 (2004).

[91] J. Volz, M. Weber, D. Schlenk, W. Rosenfeld, J. Vrana, K. Saucke, C. Kurtsiefer, and H. Weinfurter, Observation of Entanglement of a Single Photon with a Trapped Atom, Phys. Rev. Lett. **96**, 030404 (2006).

[92] T. Wilk, S. C. Webster, A. Kuhn, and G. Rempe, Single-atom single-photon quantum interface, Science **317**, 488 (2007).

[93] E. Togan, Y. Chu, A. S. Trifonov, L. Jiang, J. Maze, L. Childress, M. V. G. Dutt, A. S. Sørensen, P. R. Hemmer, A. S. Zibrov, and M. D. Lukin, Quantum entanglement between an optical photon and a solid-state spin qubit, Nature (London) **466**, 730 (2010).

[94] D. L. Moehring, P. Maunz, S. Olmschenk, K. C. Younge, D. N. Matsukevich, L.-M. Duan, and C. Monroe, Entanglement of single-atom quantum bits at a distance, Nature (London) **449**, 68 (2007).

[95] D. Cozzolino, B. D. Lio, D. Bacco, and L. K. Oxenløwe, High-dimensional quantum communication: Benefits, progress, and future challenges, Adv. Quantum Technol. **2**, 1900038 (2019).

[96] N. Brahms and D. M. Stamper-Kurn, Spin optodynamics analog of cavity optomechanics, Phys. Rev. A **82**, 041804(R) (2010).

[97] F. Brennecke, T. Donner, S. Ritter, T. Bourdel, M. Köhl, and T. Esslinger, Cavity QED with a Bose–Einstein condensate, Nature (London) **450**, 268 (2007).

[98] Y. Colombe, T. Steinmetz, G. Dubois, F. Linke, D. Hunger, and J. Reichel, Strong atom–field coupling for Bose–Einstein condensates in an optical cavity on a chip, Nature (London) **450**, 272 (2007).

[99] L. M. Norris, C. M. Trail, P. S. Jessen, and I. H. Deutsch, Enhanced Squeezing of a Collective Spin via Control of Its Qudit Subsystems, Phys. Rev. Lett. **109**, 173603 (2012).

[100] G. Vitagliano, I. Apellaniz, I. L. Egusquiza, and G. Tóth, Spin squeezing and entanglement for an arbitrary spin, Phys. Rev. A **89**, 032307 (2014).

[101] V. A. Dzuba, V. V. Flambaum, and B. L. Lev, Dynamic polarizabilities and magic wavelengths for dysprosium, Phys. Rev. A **83**, 032502 (2011).

Appendix B : Publication - Laughlin's topological charge pump in an atomic Hall cylinder

We provide the article relating our experimental implementation of Laughlin's topological charge pump [120], briefly mentioned in chapter III.

Laughlin's topological charge pump in an atomic Hall cylinder A. Fabre, J.-B. Bouhiron, T. Satoor, R. Lopes, S. Nascimbene Phys. Rev. Lett. 128, 173202 (2022)

Laughlin's topological charge pump in an atomic Hall cylinder

Aurélien Fabre, Jean-Baptiste Bouhiron, Tanish Satoor, Raphael Lopes, and Sylvain Nascimbene*
Laboratoire Kastler Brossel, Collège de France, CNRS, ENS-PSL University, Sorbonne Université, 11 Place Marcelin Berthelot, 75005 Paris, France
(Dated: March 8, 2022)

The quantum Hall effect occurring in two-dimensional electron gases was first explained by Laughlin, who developed a thought experiment that laid the groundwork for our understanding of topological quantum matter. His proposal is based on a quantum Hall cylinder periodically driven by an axial magnetic field, resulting in the quantized motion of electrons. We realize this milestone experiment with an ultracold gas of dysprosium atoms, the cyclic dimension being encoded in the electronic spin and the axial field controlled by the phases of laser-induced spin-orbit couplings. Our experiment provides a straightforward manifestation of the non-trivial topology of quantum Hall insulators, and could be generalized to strongly-correlated topological systems.

The quantization of Hall conductance observed in two-dimensional electronic systems subjected to a perpendicular magnetic field [1] is intimately linked to the non-trivial topology of Bloch bands [2] and the occurrence of chiral edge modes protected from backscattering [3]. The first step in its understanding was provided by Laughlin, who gave an elegant argument by considering a Hall system in a cylindrical geometry (Fig. 1) [4]. Besides the radial magnetic field $\mathbf{B}_\perp$ yielding the Hall effect, this geometry authorizes an axial field $\mathbf{B}_\parallel$, which does not pierce the surface but threads the cylinder with a flux $\Phi_\parallel$. Varying the flux $\Phi_\parallel$ controls a quantized electronic motion along the tube, which is directly linked to the underlying band topology. Such quantization of transport was later generalized by Thouless to any physical system subjected to a slow periodic deformation [5], as implemented in electronic quantum dots [6, 7], photonic waveguides [8] and ultracold atomic gases [9, 10].

So far, the topology of magnetic Bloch bands has been revealed in planar systems only, by measuring the quantization of transverse response [1, 11–13] or observing chiral ballistic edge modes [14–16]. The realization of Laughlin's pump experiment requires engineering periodic boundary conditions, which is challenging when using genuine spatial dimensions. The concept of a synthetic dimension encoded in an internal degree of freedom provides an alternative method for the generation of gauge fields [17]. Synthetic dimensions were first implemented with open boundary conditions, leading to the observation of chiral edge modes [18, 19]. More recently, synthetic Hall cylinders were engineered using several spin states coupled in a cyclic manner [20–22]. Nevertheless, the realization of Laughlin's topological charge pump was not realized yet, due to the absence of control over an axial magnetic field $\mathbf{B}_\parallel$.

In this work, we use an ultracold gas of ^{162}Dy atoms to engineer a Hall cylinder whose azimuthal coordinate is encoded in the electronic spin $J = 8$ [23]. We manipulate the spin using coherent optical transitions, such that a triplet of internal states coupled in a cyclic manner emerges at low energy, leading to an effective cylindrical geometry [24]. The exchange of momentum between light and atoms leads to a spin-orbit coupling that mimics a radial magnetic field $\mathbf{B}_\perp$ [25]. The phases of the laser electric fields also control an effective axial field $\mathbf{B}_\parallel$, which is the crucial ingredient to implement Laughlin's thought experiment and reveal the underlying topology. The topological character of the ground Bloch band manifests as well in a complementary pump experiment driven by Bloch oscillations.

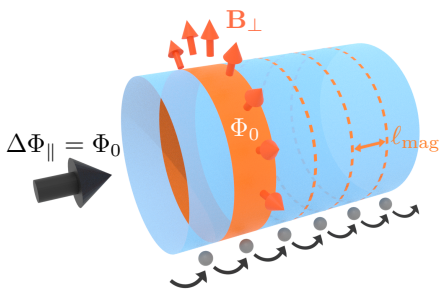

FIG. 1. **Laughlin's thought experiment.** Scheme of a two-dimensional electronic system in a cylindrical geometry, with a radial magnetic field $\mathbf{B}_\perp$ producing a quantum Hall effect. The orange area, pierced by one magnetic flux quantum Φ_0, defines the length ℓ_{mag} of the magnetic unit cell – each cell being filled with one electron in a quantum Hall insulator. Laughlin's thought experiment consists in performing an adiabatic cycle by threading one flux quantum $\Delta\Phi_\parallel = \Phi_0$ through the cylinder. The cycle shifts electron occupations by one unit cell, such that a single electron is pumped from one edge to the other, or equivalently the center-of-mass position is displaced by ℓ_{mag}.

In our experimental protocol, we apply a magnetic field in order to lift the degeneracy between the magnetic sub-levels m (with $-J \leq m \leq J$ and integer m). Spin transitions of first and second order, *i.e.* $\Delta m = \pm 1$ and ± 2, are induced by resonant two-photon optical transitions, using a pair of laser beams counter-propagating along x (Fig. 2a) [26]. The configuration of laser frequencies is chosen such that the atoms undergo

a momentum kick $-2\hbar k$ upon either resonant process $m \to m+1$ or $m \to m-2$ shown in Fig. 2b. Here, $k = 2\pi/\lambda$ is the photon momentum for the laser wavelength $\lambda = 626.1\,\mathrm{nm}$. The resulting spin-orbit coupling breaks continuous translation symmetry, but conserves the quasi-momentum $q = Mv_x/\hbar + 2km \pmod{6k}$, defined over the magnetic Brillouin zone $-3k \le q < 3k$, where M and v_x are the atomic mass and velocity. The atom dynamics is described by the Hamiltonian

$$H = \frac{1}{2}Mv_x^2 + V, \tag{1}$$

$$V = -\mathcal{T}_y\, \mathrm{e}^{-2\mathrm{i}kx} + \mathrm{hc}, \quad \mathcal{T}_y = t_a \mathrm{e}^{\mathrm{i}\varphi_a}\frac{J_+}{J} + t_b \mathrm{e}^{\mathrm{i}\varphi_b}\frac{J_-^2}{J^2}, \tag{2}$$

where J_+ and J_- are the spin ladder operators, and $t_a, t_b > 0$ are the strengths of the first and second-order transitions. The phase difference $\varphi_a - \varphi_b$ can be gauged away using a suitable spin rotation, such that we retain hereafter a single phase $\varphi \equiv \varphi_a = \varphi_b$.

The combination of the two types of transitions induces non-trivial 3-cycles $m \to m+1 \to m+2 \to m$ (Fig. 2b), with chiral dynamics in the cyclic variable $y = m \pmod 3$ – each step increasing y by one unit. As explained in a previous theoretical work [24] and in the Supplemental Material [26], this dynamics leads to the emergence at low energy of a closed subsystem of dimension 3, spanned by three spin states $|y\rangle$, with $y = 0, 1, 2$ and where $|y\rangle$ expands on projection states $|m\rangle$ with $m = y \pmod 3$ only. The $|y\rangle$ states are obtained by linear combinations of three coherent spin states oriented along equatorial directions of azimuthal angles $\phi = \varphi + \{0, 2\pi/3, 4\pi/3\}$. Hence, they only involve magnetic projections m around 0, with an r.m.s. width $\Delta m = \sqrt{J/2} = 2$. The $|y\rangle$ states will be interpreted in the following as position eigenstates along a cyclic synthetic dimension of length $Y = 3$. The operator $\mathcal{T}_y$ involved in the spin coupling (2) then acts as a translation $\mathcal{T}_y\,|y\rangle = t\,|y+1\rangle$, with a hopping amplitude $t = t_a + t_b$. The low-energy spin dynamics is described by the effective potential

$$V_{\mathrm{eff}} = -t\sum_{y=0}^{2}\left(\mathrm{e}^{\mathrm{i}(\varphi-2kx)}\,|y+1\rangle\langle y| + \mathrm{hc}\right). \tag{3}$$

Together with the kinetic energy $\frac{1}{2}Mv_x^2$, it describes the motion of a particle on a cylinder discretized along its circumference (see Fig. 2c). The complex phase $2kx$ mimics the Aharonov-Bohm phase associated with a radial magnetic field $B_\perp = 2\hbar k$ (assuming a particle charge $q = -1$). It defines a magnetic length $\ell_{\mathrm{mag}} = \lambda/6$, such that the magnetic flux $\Phi_\perp = \ell_{\mathrm{mag}} Y B_\perp$ through a portion of cylinder of length ℓ_{mag} equals the flux quantum $\Phi_0 = h/|q|$.

Experimentally, we use a gas of about 4×10^4 atoms, initially prepared at a temperature $T = 0.54(3)\,\mu\mathrm{K}$, such that the thermal momentum width $\sigma_q \simeq 1.3\,k$ is much smaller than the Brillouin zone extent $6k$, and

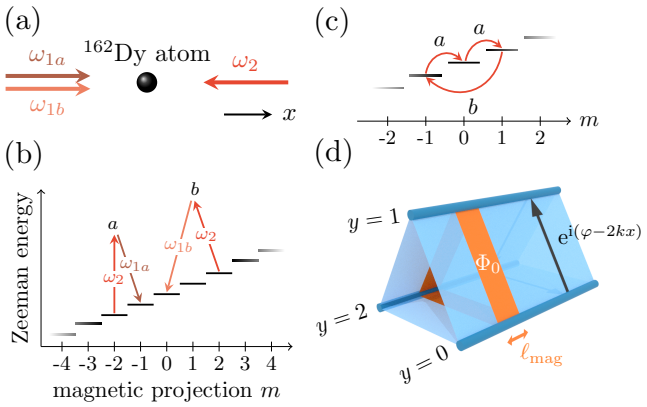

FIG. 2. **Emerging quantum Hall cylinder.** (a) Sketch of the laser configuration involving two beams counter-propagating along x and sent on a thermal sample of dysprosium atoms – one beam having two frequency components. (b) Scheme of the two-photon optical transitions resonantly driving first- and second-order spin transitions, labelled a and b, respectively. (c) Representation of a non-trivial 3-cycle between magnetic sub-levels induced by the light couplings. (d) Scheme of the Hall cylinder dynamics emerging at low energy, involving three spin states $|y\rangle$ (with $y = 0, 1, 2$). The hopping amplitudes have a complex phase $\varphi - 2kx$, where $2\hbar k$ plays the role of a radial magnetic field $B_\perp$ and φ is linked to an axial field $B_\parallel$. The orange area, of length $\ell_{\mathrm{mag}} = \lambda/6$ is threaded by one unit of magnetic flux quantum Φ_0.

interaction effects can be neglected on the timescale of our experiments. The atoms are adiabatically loaded in the ground Bloch band with $t_a = 11.5(3)E_{\mathrm{r}}$ and $t_b = 7.1(2)E_{\mathrm{r}}$, by ramping the light coupling parameters. Here, $E_{\mathrm{r}} = \hbar^2k^2/(2M)$ is the single-photon recoil energy. The mean quasi-momentum $\langle q\rangle$ is controlled by applying a weak force F_x after the loading (see the Supplementary Materials [26]). We simultaneously probe the distribution of velocity v_x and spin projection m. For this, we abruptly switch off the light couplings and ramp up a magnetic field gradient that spatially separates the different magnetic sub-levels along z. The velocity distribution is obtained from the density profile along x measured after a 2.3 ms expansion. A typical spin-resolved velocity distribution is shown in Fig. 3a.

The velocity distribution, plotted in Fig. 3b as a function of q, exhibits a period $2k$, similar to the case of a simple $\lambda/2$-lattice. The mean velocity $\langle v_x\rangle$, shown as a red line, remains close to zero. Since it is linked to the slope of the ground-band energy $\partial_q E_0(q) = \hbar\langle v_x\rangle$, this shows that the band is quasi-flat. In fact, the band's flatness in protected from pertubations, such as external magnetic field fluctuations, by the zero net magnetization of the $|y\rangle$ spin states – a similar effect has been used in another implementation of a Hall cylinder using dynamical decoupling techniques [22].

The probabilities Π_m of projection on each sub-level

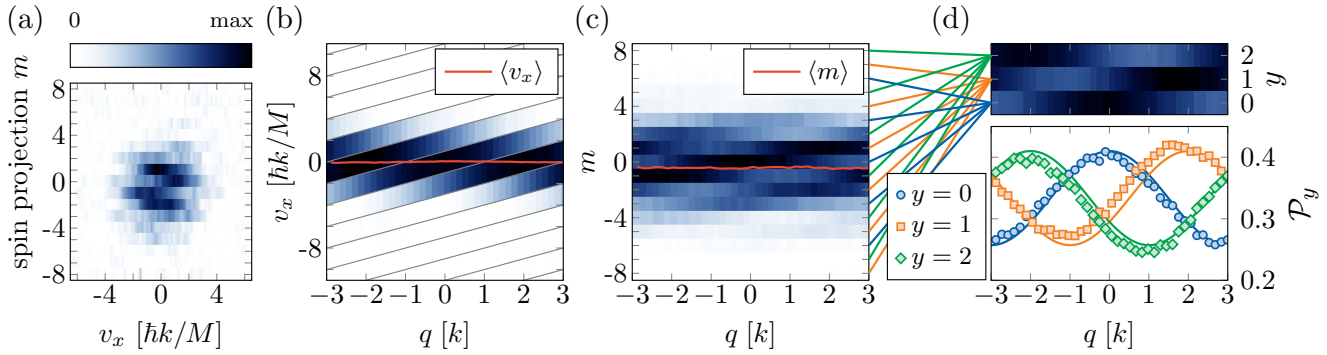

FIG. 3. **Ground band characterization.** (a) Spin-resolved velocity distribution measured for a gas of mean quasi-momentum $\langle q \rangle \simeq 2k$. (b) Distribution of discrete velocity components $v_x = \hbar(q + 2kp)/M$ (with integer p) for states of quasi-momentum q. The red line shows the mean velocity $\langle v_x \rangle$. (c) Spin projection probabilities Π_m measured as a function of q. The red line stands for the mean spin projection $\langle m \rangle$. (d) Probabilities $\mathcal{P}_y$ of projection on $y = m$ (mod 3). The blue circles, orange squares and green diamonds correspond to $y = 0$, 1 and 2, respectively. Statistical error bars, computed from a bootstrap random sampling analysis, are smaller than the symbols. The lines are calculated from the expected band structure.

m reveal a longer periodicity $6k$ (Fig. 3c), corresponding to the full extent of the magnetic Brillouin zone. It experimentally confirms the spatial separation of magnetic orbitals $\ell_{\rm mag} = 2\pi/(6k) = \lambda/6$ introduced above. The Π_m measurements also give access to the probabilities $\mathcal{P}_y$ of projection on the synthetic coordinate y, by summing the Π_m's with $m = y$ (mod 3) (Fig. 3d). The q-variation of these distributions reveals a chirality typical of the Hall effect: when increasing the momentum by $2k$, the $\mathcal{P}_y$ distributions cycle along the synthetic dimension in a directional manner, as $\mathcal{P}_y \to \mathcal{P}_{y+1}$ [27, 28]. We stress that such a drift does not occur on the mean spin projection $\langle m \rangle$, which remains close to zero (red line in Fig. 3c).

The adiabatic y-drift occurring during Bloch oscillations provides a first insight into the topological character of the lowest energy band – similar to the quantized flow of Wannier function charge centers in Chern insulators [29]. To quantify this drift, we cannot rely on the mean y position, which is ill-defined for a cyclic dimension [30]. Instead, it is reconstructed by integrating the anomalous velocity $\langle v_y \rangle \equiv \partial_\varphi H/\hbar$ induced by the force F_x driving the Bloch oscillation. For this purpose, we conduct a separate experiment, in which we suddenly switch off the force F_x, such that the center-of-mass undergoes a cyclotron oscillation, with the x- and y-velocities oscillating in quadrature. More precisely, the rate of change of the x-velocity gives access to the y-velocity, via the exact relation

$$\partial_t \langle v_x \rangle = \frac{\mathrm{i}}{\hbar}[H, v_x] = -\frac{2\hbar k}{M}\langle v_y \rangle.$$

Hence, the velocity $\langle v_y \rangle$ induced by the force F_x is given by the initial slope of $\langle v_x \rangle$ (Fig. 4b).

The center-of-mass drift $\langle \Delta y \rangle$, obtained upon integration of $\langle v_y \rangle$ is shown in Fig. 4a. We find that it varies linearly with the quasi-momentum variation Δq (Fig. 4a), such that the drift per Bloch oscillation cycle reads

$$\frac{\langle \Delta y \rangle}{Y} = 0.97(5), \tag{4}$$

consistent with a unit winding around the cylinder of circumference Y [26]. The rotation along y occurring over a Bloch oscillation cycle is thus quantized, providing a first manifestation of the non-trivial band topology.

We now characterize the global band topology by implementing Laughlin's charge pump experiment, and extend the protocol to reveal the local geometrical properties. To simulate the axial magnetic field used to drive the pump, we interpret the complex phase φ involved in the y-hoppings (see equation 3) as the Peierls phase associated with the field $\mathbf{B}_\parallel$ threading the cylinder with a flux

$$\Phi_\parallel = \frac{3\varphi}{2\pi}\Phi_0. \tag{5}$$

We vary $\Phi_\parallel$ by adjusting the phase difference φ between the laser electric fields involved in the spin transitions using acousto-optic modulators.

We drive the pump by slowly ramping the phase φ, and measure the induced shift of the center-of-mass along the real dimension x. The experiment is performed for various values of the quasi-momentum $\langle q \rangle$ uniformly spanning the magnetic Brillouin zone. The q-averaged drift, shown in Fig. 4c, is consistent with a linear variation

$$\frac{\langle \Delta x \rangle}{\ell_{\rm mag}} = \mathcal{C}\frac{\Phi_\parallel}{\Phi_0}, \quad \mathcal{C} = 1.00(4),$$

in agreement with the expected quantization of transport by the Chern number $\mathcal{C} = 1$. The pump adiabaticity is checked by repeating the experiment for various speeds

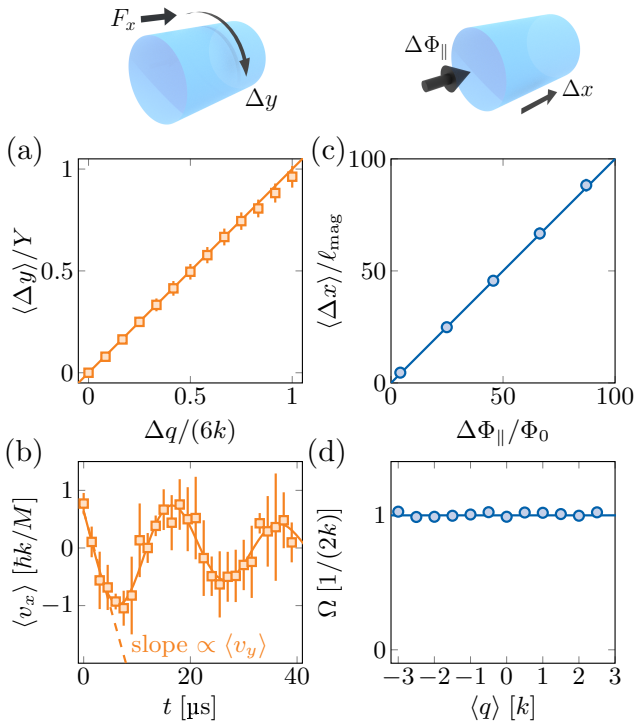

FIG. 4. **Topological charge pumps.** (a) Center-of-mass displacement $\langle\Delta y\rangle$ as a function of the quasi-momentum shift Δq induced by a force F_x (orange squares), together with a linear fit (orange line). (b) Evolution of the mean velocity $\langle v_x\rangle$ immediately after switching off the force F_x (orange squares), fitted with a damped sine (solid line). The velocity $\langle v_y\rangle$ is obtained from the initial slope of the fit (dashed line). (c) Displacement of the center of mass $\langle\Delta x\rangle$ induced by an axial magnetic flux $\Phi_\parallel$ and averaged over the magnetic Brillouin zone (blue cicles). The blue line is a linear fit. (d) Berry curvature Ω measured as a function of the mean quasi-momentum $\langle q\rangle$ (blue circles). The solid line is the expected Berry curvature, which is not distinguishable from the constant value $\Omega(q) = 1/(2k)$.

of the flux ramp, and measuring identical responses for slow enough ramps [26].

Our experiments also give access to the anomalous drift of individual momentum states $\Delta x = \Omega(q)\varphi$, proportional to the Berry curvature $\Omega(q)$ that quantifies the local geometrical properties of quantum states [31]. As shown in Fig. 4d, the measured Berry curvature is flat within error bars, consistent with theory, which predicts $\Omega(q) = 1/(2k)$ with negligible q variation. The flatness of the Berry curvature is a consequence of the continuous translation symmetry along x, making our system similar to continuous two-dimensional systems with flat Landau levels. In contrast, discrete lattice systems, such as Hofsdtater and Haldane models [32, 33], or previous implementations of synthetic Hall cylinders [20–22], exhibit dispersive bands with inhomogeneous Berry curvatures.

We have shown that implementing a quantum Hall cylinder gives direct access to the underlying topology of Bloch bands. Our realization of Laughlin's pump protocol could be generalized to interacting atomic systems, which are expected to form strongly correlated topological states of matter at low temperature. In particular, at fractional fillings, one expects the occurrence of charge density waves as one-dimensional precursors of two-dimensional fractional quantum Hall states [34]. The pumped charge would then be quantized to a rational value, revealing the charge fractionnalization of elementary excitations [35].

We thank Jean Dalibard for insightful discussions and careful reading of the manuscript, and Thomas Chalopin for discussions at an early stage of this work. This work is supported by European Union (grant TOPODY 756722 from the European Research Council).

* sylvain.nascimbene@lkb.ens.fr

[1] K. v. Klitzing, G. Dorda, and M. Pepper, New Method for High-Accuracy Determination of the Fine-Structure Constant Based on Quantized Hall Resistance, Phys. Rev. Lett. **45**, 494 (1980).
[2] D. J. Thouless, M. Kohmoto, M. P. Nightingale, and M. den Nijs, Quantized Hall Conductance in a Two-Dimensional Periodic Potential, Phys. Rev. Lett. **49**, 405 (1982).
[3] B. I. Halperin, Quantized Hall conductance, current-carrying edge states, and the existence of extended states in a two-dimensional disordered potential, Phys. Rev. B **25**, 2185 (1982).
[4] R. B. Laughlin, Quantized Hall conductivity in two dimensions, Phys. Rev. B **23**, 5632 (1981).
[5] D. J. Thouless, Quantization of particle transport, Phys. Rev. B **27**, 6083 (1983).
[6] M. Switkes, C. M. Marcus, K. Campman, and A. C. Gossard, An Adiabatic Quantum Electron Pump, Science **283**, 1905 (1999).
[7] S. K. Watson, R. M. Potok, C. M. Marcus, and V. Umansky, Experimental Realization of a Quantum Spin Pump, Phys. Rev. Lett. **91**, 258301 (2003).
[8] Y. E. Kraus, Y. Lahini, Z. Ringel, M. Verbin, and O. Zilberberg, Topological States and Adiabatic Pumping in Quasicrystals, Phys. Rev. Lett. **109**, 106402 (2012).
[9] M. Lohse, C. Schweizer, O. Zilberberg, M. Aidelsburger, and I. Bloch, A Thouless quantum pump with ultracold bosonic atoms in an optical superlattice, Nat. Phys. **12**, 350 (2016).
[10] S. Nakajima, T. Tomita, S. Taie, T. Ichinose, H. Ozawa, L. Wang, M. Troyer, and Y. Takahashi, Topological Thouless pumping of ultracold fermions, Nat. Phys. **12**, 296 (2016).
[11] C. R. Dean, L. Wang, P. Maher, C. Forsythe, F. Ghahari, Y. Gao, J. Katoch, M. Ishigami, P. Moon, M. Koshino, T. Taniguchi, K. Watanabe, K. L. Shepard, J. Hone, and P. Kim, Hofstadter's butterfly and the fractal quantum Hall effect in moiré superlattices, Nature **497**, 598 (2013).
[12] L. A. Ponomarenko, R. V. Gorbachev, G. L. Yu, D. C. Elias, R. Jalil, A. A. Patel, A. Mishchenko, A. S.

Mayorov, C. R. Woods, J. R. Wallbank, M. Mucha-Kruczynski, B. A. Piot, M. Potemski, I. V. Grigorieva, K. S. Novoselov, F. Guinea, V. I. Fal'ko, and A. K. Geim, Cloning of Dirac fermions in graphene superlattices, Nature **497**, 594 (2013).

[13] M. Aidelsburger, M. Lohse, C. Schweizer, M. Atala, J. T. Barreiro, S. Nascimbene, N. Cooper, I. Bloch, and N. Goldman, Measuring the Chern number of Hofstadter bands with ultracold bosonic atoms, Nat. Phys. **11**, 162 (2015).

[14] Z. Wang, Y. Chong, J. D. Joannopoulos, and M. Soljačić, Observation of unidirectional backscattering-immune topological electromagnetic states, Nature **461**, 772 (2009).

[15] M. Hafezi, S. Mittal, J. Fan, A. Migdall, and J. Taylor, Imaging topological edge states in silicon photonics, Nat. Photonics **7**, 1001 (2013).

[16] M. C. Rechtsman, J. M. Zeuner, Y. Plotnik, Y. Lumer, D. Podolsky, F. Dreisow, S. Nolte, M. Segev, and A. Szameit, Photonic Floquet topological insulators, Nature **496**, 196 (2013).

[17] A. Celi, P. Massignan, J. Ruseckas, N. Goldman, I. B. Spielman, G. Juzeliūnas, and M. Lewenstein, Synthetic Gauge Fields in Synthetic Dimensions, Phys. Rev. Lett. **112** (2014).

[18] M. Mancini, G. Pagano, G. Cappellini, L. Livi, M. Rider, J. Catani, C. Sias, P. Zoller, M. Inguscio, M. Dalmonte, and L. Fallani, Observation of chiral edge states with neutral fermions in synthetic Hall ribbons, Science **349**, 1510 (2015).

[19] B. K. Stuhl, H.-I. Lu, L. M. Aycock, D. Genkina, and I. B. Spielman, Visualizing edge states with an atomic Bose gas in the quantum Hall regime, Science **349**, 1514 (2015).

[20] J. H. Han, J. H. Kang, and Y. Shin, Band Gap Closing in a Synthetic Hall Tube of Neutral Fermions, Phys. Rev. Lett. **122**, 065303 (2019).

[21] C.-H. Li, Y. Yan, S. Choudhury, D. B. Blasing, Q. Zhou, and Y. P. Chen, A Bose-Einstein condensate on a synthetic Hall cylinder, arXiv:1809.02122 (2018).

[22] Q.-Y. Liang, D. Trypogeorgos, A. Valdés-Curiel, J. Tao, M. Zhao, and I. B. Spielman, Coherence and decoherence in the Harper-Hofstadter model, Phys. Rev. Research **3**, 023058 (2021).

[23] T. Chalopin, T. Satoor, A. Evrard, V. Makhalov, J. Dalibard, R. Lopes, and S. Nascimbene, Probing chiral edge dynamics and bulk topology of a synthetic Hall system, Nat. Phys. **16**, 1017 (2020).

[24] A. Fabre, J.-B. Bouhiron, T. Satoor, R. Lopes, and S. Nascimbene, Simulating two-dimensional dynamics within a large-size atomic spin, Phys. Rev. A **105**, 013301 (2022).

[25] J. Dalibard, F. Gerbier, G. Juzeliūnas, and P. Öhberg, *Colloquium* : Artificial gauge potentials for neutral atoms, Rev. Mod. Phys. **83**, 1523 (2011).

[26] See Supplemental Material for details on the experimental protocol, additional information on the derivation of the three-state model and on the link between adiabatic pumps and band topology, a study of the pump adiabaticity and measurements of low-energy excitations. It includes Refs. [36-38].

[27] Y. Yan, S.-L. Zhang, S. Choudhury, and Q. Zhou, Emergent periodic and quasiperiodic lattices on surfaces of synthetic Hall tori and synthetic Hall cylinders, arXiv:1810.12331 (2018).

[28] R. P. Anderson, D. Trypogeorgos, A. Valdés-Curiel, Q.-Y. Liang, J. Tao, M. Zhao, T. Andrijauskas, G. Juzeliūnas, and I. B. Spielman, Realization of a deeply subwavelength adiabatic optical lattice, Phys. Rev. Research **2**, 013149 (2020).

[29] M. Taherinejad, K. F. Garrity, and D. Vanderbilt, Wannier center sheets in topological insulators, Phys. Rev. B **89**, 115102 (2014).

[30] R. Lynch, The quantum phase problem: A critical review, Physics Reports **256**, 367 (1995).

[31] H.-I. Lu, M. Schemmer, L. M. Aycock, D. Genkina, S. Sugawa, and I. B. Spielman, Geometrical Pumping with a Bose-Einstein Condensate, Phys. Rev. Lett. **116**, 200402 (2016).

[32] D. R. Hofstadter, Energy levels and wave functions of Bloch electrons in rational and irrational magnetic fields, Phys. Rev. B **14**, 2239 (1976).

[33] F. D. M. Haldane, Model for a Quantum Hall Effect without Landau Levels: Condensed-Matter Realization of the "Parity Anomaly", Phys. Rev. Lett. **61**, 2015 (1988).

[34] R. Tao and D. J. Thouless, Fractional quantization of Hall conductance, Phys. Rev. B **28**, 1142 (1983).

[35] R. B. Laughlin, Nobel lecture: Fractional quantization, Rev. Mod. Phys. **71**, 863 (1999).

[36] C. Cohen-Tannoudji and J. Dupont-Roc, Experimental Study of Zeeman Light Shifts in Weak Magnetic Fields, Phys. Rev. A **5**, 968 (1972).

[37] F. T. Arecchi, E. Courtens, R. Gilmore, and H. Thomas, Atomic Coherent States in Quantum Optics, Phys. Rev. A **6**, 2211 (1972).

[38] X.-W. Luo, J. Zhang, and C. Zhang, Tunable flux through a synthetic Hall tube of neutral fermions, Phys. Rev. A **102**, 063327 (2020).

Appendix C : Berry curvature components in the ground band

We display in this appendix the Berry curvature components in the ground band, for the couplings $t_x = 5.69E_{\text{rec}}$, $t_z = 5.1E_{\text{rec}}$, $\beta = -2t_z$.

The Berry curvature components of the n^{th} band for the wavector $\boldsymbol{k}$ are computed via Kubo formula :

$$F_n^{\alpha\beta}(\boldsymbol{k}) = i\hbar^2 \sum_{m\neq n} \frac{\langle\psi_n(\boldsymbol{k})|\, v_\alpha\, |\psi_m(\boldsymbol{k})\rangle \langle\psi_m(\boldsymbol{k})|\, v_\beta\, |\psi_n(\boldsymbol{k})\rangle}{\left[E_m(\boldsymbol{k}) - E_n(\boldsymbol{k})\right]^2}, \tag{7.1}$$

where v_α is the velocity operator in the direction α, E_m refers to the energy of the m^{th} band and $\psi_m(\boldsymbol{k})$ is the wavefunction of the m^{th} band for a momentum $\boldsymbol{k}$.

This formula involves the velocity operators in the spatial and in the synthetic dimensions. The first are defined by :

$$v_\xi = \partial_p H \tag{7.2}$$
$$v_\nu = \partial_q H \tag{7.3}$$

To define the velocity in the synthetic dimensions, we follow the same prescription proposed in chapter III. We define the velocity operator along m by identifying the operator J_z as a position. We obtain :

$$v_m = \frac{i}{\hbar}\left[H, J_z\right] \tag{7.4}$$
$$= -t_x\left(i\mathrm{e}^{-2ikx}\frac{J_+}{J} + \text{h.c}\right) - t_z\left(-2i\mathrm{e}^{-2ikz}\frac{J_-^2}{J^2} + \text{h.c}\right) \tag{7.5}$$

The velocity operator along r, v_r, can be derived from the above expression, by replacing the -2 prefactor in front of J_-^2 by $+1$, since J_-^2 decreases m by two units but increases r by one unit.

Using these formula, we compute numerically the Berry curvature components in the ground band. We see on the figures below that they are constant in the bulk. Their decay for $|p| > 7p_{\text{rec}}$ is due to the edges at $m \pm J$. We do not show F^{mr} and $F^{\xi\nu}$ that are vanishing in the full Brillouin zone.

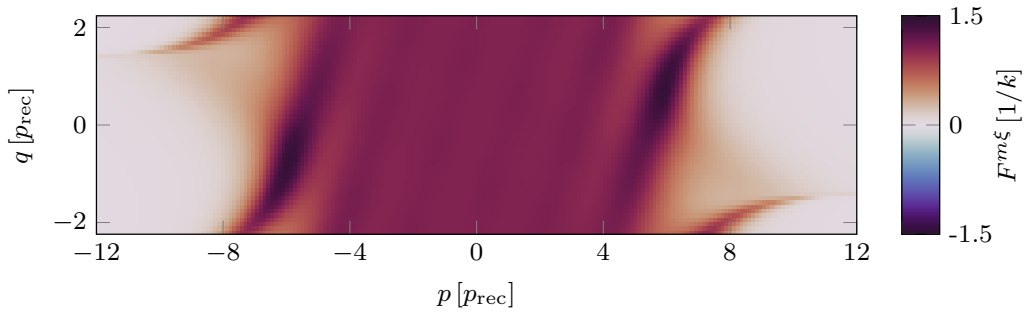

Figure 7.1: Ground band Berry curvature $F^{m\xi}$.

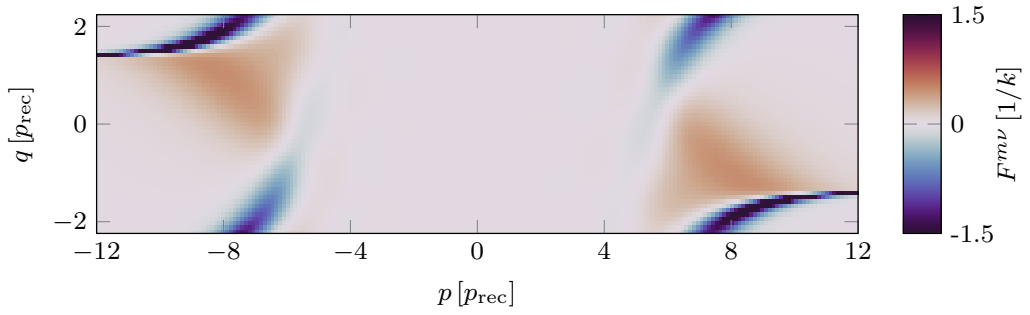

Figure 7.2: Ground band Berry curvature $F^{m\nu}$.

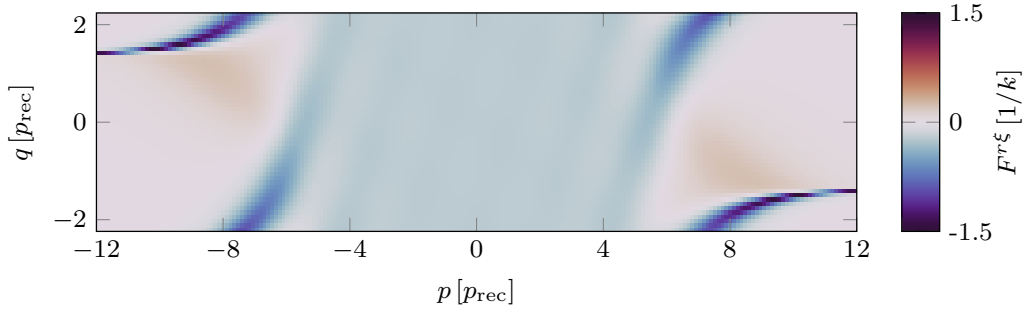

Figure 7.3: Ground band Berry curvature $F^{r\xi}$.

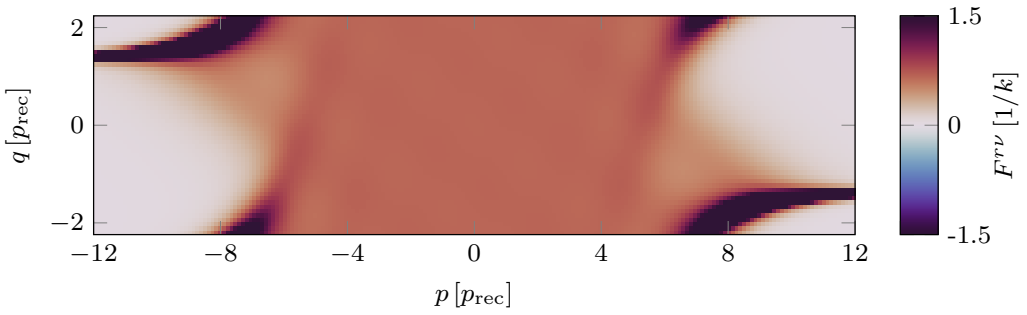

Figure 7.4: Ground band Berry curvature $F^{r\nu}$.

Résumé détaillé

En 1980, Klaus von Klitzing et al ont fait la découverte inattendue de l'effet Hall quantique [1]. En étudiant le mouvement d'un gaz quasi bidimensionnel d'électrons dans un transistor MOSFET à basse température, ils ont pu détecter la quantification de la conductance de Hall. Cette découverte a eu des applications à la fois pratiques et fondamentales. Par exemple, l'effet Hall quantique est utilisé comme étalon pour mesurer les résistances en définissant l'ohm sur la base de constantes fondamentales [2, 3]. D'un point de vue plus théorique, cette découverte a conduit à l'émergence de la théorie TKKN deux ans plus tard, introduite par Thouless, Kohmoto, Nightingale et den Nijs dans leur article fondateur [4]. Ils y proposent une interprétation de la quantification de la conductance de Hall basée sur la topologie.

Topologie dans les systèmes physiques

La topologie est une branche des mathématiques étudiant les propriétés des objets qui sont conservées sous des déformations continues. Son application à la physique quantique a débuté dans les années 1970, lorsque des arguments topologiques ont été utilisés dans les théories de jauge, par exemple pour comprendre l'effet Aharonov-Bohm ou pour étudier les monopôles magnétiques [5, 6]. Avec la découverte de l'effet Hall quantique, la topologie a joué un rôle de plus en plus important dans la physique de la matière condensée. En suivant les travaux de TKKN et de S.Pancharatnam [7], Michael Berry a popularisé les concepts de phase de Berry et de courbure de Berry [8, 9], qui sont désormais communément utilisés dans le domaine. En intégrant la courbure de Berry sur la zone de Brillouin d'un système, on peut calculer l'invariant topologique de ce système et ainsi caractériser ses propriétés topologiques. En bref, une propriété topologique est robuste à un désordre modéré ou à des déformations continues. La quantification de la conductance de Hall est un exemple de propriété topologique.

Initialement, on pensait que les propriétés topologiques n'apparaissaient que dans les systèmes électroniques bidimensionnels soumis à des champs magnétiques élevés. En 1988, Haldane a apporté le premier changement à ce paradigme [10], en montrant que l'ingrédient clé pour obtenir l'effet Hall quantique n'est pas la présence d'un champ magnétique, mais la rupture de la symétrie par renversement du temps. Plus récemment, Kane et Mele ont généralisé le concept de topologie au cas des systèmes invariants dans le temps [11, 12], grâce à la découverte théorique de l'effet Hall quantique de spin en deux dimensions, qui a été observé depuis lors [13–16]. Cela a aussi conduit à la notion d'isolant topologique [17, 18].

La création de la classification topologique à la fin des années 2000 [19–21] a généralisé l'étude des systèmes topologiques. Cette classification prédit, en fonction des symétries du système et de sa dimensionnalité, la présence d'une topologie non triviale. Cette classification ne considère pas seulement les systèmes de Hall quantique ou les isolants topologiques, mais elle inclut également les supraconducteurs topologiques [22]. En résumé, l'étude des propriétés topologiques est passée de l'effet Hall quantique en deux dimensiosn à une famille

beaucoup plus riche de systèmes physiques, de dimensions et de symétries diverses. Certains de ces systèmes topologiques devraient présenter des propriétés intéressantes, en particulier si l'on considère ceux de haute dimensionalité. Ainsi, la généralisation de l'effet Hall quantique en 4D [23] et en 6D [24, 25], ou la généralisation des semi-métaux de Weyl topologiques en 3D [26] à 5D [27] prédit des phénomènes physiques exotiques. Par exemple, l'effet Hall quantique 4D est quantifié par un nouvel invariant topologique, le second nombre de Chern, qui quantifie la réponse non linéaire du système à une perturbation électromagnétique.

L'extension de la classification aux systèmes en interaction conduit également à de nouveaux phénomènes physiques. Par exemple, les états de Hall quantiques fractionnaires en deux dimensions [28–30] pourraient accueillir des excitations anyoniques non-Abéliennes [31–33], dont la statistique n'est ni bosonique ni fermionique. Ces anyons pourraient avoir d'importantes applications en information quantique [34].

La plupart des systèmes topologiques restent à explorer, et d'autres domaines de la physique se sont joints à l'effort des systèmes de matière condensée pour étudier ces nouvelles phases exotiques de la matière. La photonique est l'un de ces domaines [35–37]. La photonique a permis l'observation de nombreuses nouvelles phases topologiques, avec par exemple l'observation d'isolants topologiques de Floquet [38–40] ou de la physique de Hall quantique en quatre dimensions [41]. Une branche plus récente, les circuits électroniques topologiques, a permis de mesurer le premier isolant topologique en classe AI et en quatre dimensions [42]. Les gaz atomiques ultrafroids représentent un autre domaine pouvant contribuer à l'exploration de la matière quantique topologique [43–46].

Expériences d'atomes froids

Les expériences sur les atomes froids étudient des gaz ultrafroids dilués d'atomes neutres, avec un haut degré de contrôle obtenu grâce à des champs électromagnétiques. Ce domaine de recherche a été très productif au cours des trente dernières années et a permis d'observer de nombreuses prédictions théoriques concernant de nouvelles phases de la matière. Ainsi, la condensation de Bose-Einstein a été observée en 1995 [47, 48] et la dégénérescence d'un gaz de Fermi a été mesurée en 1999 [49]. Plus récemment, des efforts dans ce domaine ont été déployés pour simuler des phases topologiques de la matière.

Les expériences d'atomes froids offrent diverses méthodes pour simuler des systèmes topologiques de matière condensée. La plus courante consiste à utiliser des réseaux optiques, qui imitent naturellement la physique des électrons dans un potentiel cristallin. Comme nous le verrons plus loin, les propriétés topologiques nécessitent généralement des champs de jauge externes et un couplage spin-orbite pour apparaître [43]. La communauté des atomes froids a donc développé plusieurs outils pour concevoir ces champs de jauge sur des atomes neutres, allant au-delà des réseaux optiques statiques standards.

Un avantage significatif des expériences d'atomes froids réside dans leur capacité à régler finement les interactions entre les atomes, par exemple par le biais des résonances de Feshbach. Il s'agit donc d'une plateforme intéressante pour réaliser des phases topologiques de la matière à plusieurs corps, telles que des états de Hall quantique fractionnaires. Un exemple récent de la réalisation de tels états a été obtenu en utilisant deux atomes sur un réseau 4×4 [30], et pourrait être utilisée pour sonder les excitations anyoniques non-abéliennes si la taille du système était augmentée. Un autre avantage clé de ces expériences est la possibilité de sonder la nature topologique du modèle simulé, ce qui est souvent une tâche difficile en raison de l'absence de paramètre d'ordre local pour l'identifier. Par exemple, les états de bord peuvent être observés grâce à la possibilité de charger des atomes directement dans

ces états et grâce à l'imagerie atomique in situ [50], révélant la topologie du système via la correspondance entre le centre du système et ses bords [51]. Aussi, l'invariant topologique du modèle simulé (par exemple, le nombre de Chern dans un système de Hall quantique) peut être obtenu en mesurant la réponse du centre de masse à une perturbation [52] permettant la caractérisation de la topologie.

Champs de jauge artificiels

De nombreux effets topologiques sont la conséquence d'un couplage spin-orbite et de champs de jauge extérieurs [43]. C'est le cas des bandes de Bloch topologiques qui apparaissent dans les systèmes à effet Hall quantique. Cependant, les expériences sur les atomes froids impliquent des atomes neutres, qui ne subissent pas la force de Lorentz, à l'origine de l'effet Hall quantique. Au lieu de cela, nous utilisons des champs de jauge artificiels qui imitent de manière analogue les effets des champs magnétiques sur les électrons. De cette manière, des Hamiltoniens de la forme

$$H = \frac{[\boldsymbol{p} - \boldsymbol{A}(\boldsymbol{r})]^2}{2M}, \tag{7.6}$$

peuvent être simulés sur des atomes neutres, où des champs de jauge artificiels $\boldsymbol{A}(\boldsymbol{r})$ peuvent être rendus Abéliens ou non-Abéliens [53, 54].

Ces champs de jauge artificiels peuvent être conçus de différentes manières dans le cadre d'expériences d'atomes froids. La première manière consiste à mettre un gaz d'atomes en rotation, où la force de Coriolis remplace la force de Lorentz [55]. Une deuxième possibilité fructueuse est l'utilisation de réseaux optiques comme mentionné précédemment. En induisant un effet tunnel entre les différents sites du réseau optique [56, 57], ou par les méthodes de Floquet [58], des champs de jauge artificiels peuvent être produits, conduisant à la simulation de plusieurs phases de la matière. Par exemple, [59] a reporté l'exploration de la physique de Hall en quatre dimensions par modulation temporelle d'un super réseau optique. Aussi, le modèle de Haldane [58], ou l'Hamiltonien de Hofstadter [52] ont été réalisés dans des réseaux optiques modulés. Une troisième approche, employée dans notre laboratoire, consiste à traiter le spin des atomes comme une dimension synthétique. En utilisant des procédés Raman, nous pouvons coupler le spin des atomes à leur quantité de mouvement, générant ainsi un couplage spin-orbite.

Dimensions synthétiques

L'utilisation de dimensions synthétiques présente plusieurs avantages. Tout d'abord, elles permettent de simuler des systèmes de dimensions supérieures [60]. Par exemple, un réseau unidimensionnel peut être transposé à un système bidimensionnel en tenant compte du degré de liberté interne des atomes. Deuxièmement, les dimensions synthétiques permettent de concevoir à la fois un centre et des bords nets, ce qui permet d'observer les états de bord qui émergent aux limites d'un système topologique. En outre, ils permettent la mise en œuvre de champs de jauge artificiels radiaux [61–63], ce qui est difficile à mettre en œuvre dans les systèmes de matière condensée. Il convient de noter que les dimensions synthétiques ne se limitent pas aux expériences d'atomes froids et qu'elles sont largement utilisées dans d'autres domaines, tels que la photonique [36, 64, 65].

Cette méthode d'ingénierie de champs de jauge artificiels présente un inconvénient : elle nécessite la mise en œuvre de décalages lumineux assez forts, qui se traduisent souvent par un échauffement important dû à la diffusion de photons hors résonance lorsqu'ils sont utilisés avec des atomes alcalins, les espèces les plus courantes dans les expériences d'atomes froids. Ce problème peut être résolu en manipulant des atomes de la famille des lanthanides, dont

les structures électroniques conduisent à une interaction plus favorable entre la lumière et la matière.

Les lanthanides

Les lanthanides sont une famille d'éléments chimiques dont les numéros atomiques sont compris entre 57 et 71. Bien qu'elle soit plus difficile à manipuler et à refroidir que la plupart des éléments alcalins, cette famille d'espèces atomiques suscite un intérêt croissant.

La structure électronique particulière des lanthanides (c'est-à-dire leur couche f ouverte) conduit à un riche paysage de transitions électroniques et, pour certains d'entre eux, à un spin important dans l'état fondamental. Par exemple, l'erbium et le dysprosium ont respectivement un spin $J = 6$ et $J = 8$ dans leur état fondamental, résultant en un important moment magnétique et donc à des interactions dipolaires importantes. Pour illustrer cela, l'interaction dipolaire entre deux atomes de dysprosium est en ordre de grandeur 100 fois supérieure que celle entre deux atomes de rubidium [66]. Ces interactions dipolaires sont la principale raison de la popularité croissante des expériences sur les lanthanides. En effet, ces interactions à longue portée peuvent donner naissance à de nouveaux états de la matière, tels que les gouttes quantiques qui ont été observées récemment [67, 68]. Un autre exemple frappant est le spectre roton-maxon et son caractère supersolide, qui ont été étudiés expérimentalement [69–72].

Un autre domaine de recherche utilisant les atomes de lanthanides (et plus particulièrement les atomes de dysprosium) consiste à considérer leur spin macroscopique J comme $2J$ qubits fictifs. Cette méthode peut être utilisée pour étudier des états non classiques constitués de ces qubits virtuels et a des applications potentielles dans le domaine de la métrologie [73–75].

Dans notre groupe, nous nous sommes récemment intéressés à la simulation quantique de systèmes topologiques en considérant le spin du dysprosium comme des dimensions synthétiques. Nous tirons parti du grand spin du dysprosium $J = 8$ pour avoir à la fois un cœur et des bords. De plus, nos protocoles nécessitent l'utilisation de décalages lumineux importants, qui entraîneraient un chauffage significatif s'ils étaient mis en œuvre avec des atomes alcalins, comme nous l'avons mentionné précédemment. Le dysprosium est bien adapté pour résoudre ce problème car l'arrangement de ses transitions, qui consiste en de nombreuses transitions étroites isolées, permet d'éviter la diffusion hors résonance. De plus, la forme des interactions lumière-matière pour le dysprosium (et plus généralement pour les lanthanides) bénéficie d'une polarisabilité tensorielle non-nulle, et nous pouvons créer des décalages de lumière de premier et de second ordre. Il est important de noter également que la combinaison de l'interaction lumière-matière avec des interactions dipolaires-dipolaires pourrait conduire à la réalisation de phases topologiques de la matière plus exotiques [66].

Dans cette thèse, nous nous concentrons sur la simulation de systèmes de Hall quantiques topologiques en utilisant un gaz ultra-froid d'atomes de dysprosium. Un champ de jauge artificiel est généré en utilisant le processus Raman et en considérant le spin du dysprosium comme des dimensions synthétiques. Ce manuscrit est organisé comme suit :

Le chapitre 1 est dédié à la présentation de notre dispositif expérimental et des propriétés du dysprosium. Nous commençons par donner la structure électronique de l'atome de dysprosium et voyons qu'elle a, notamment, trois conséquences avantageuses. Tout

d'abord, elle conduit à un grand spin dans l'état fondamental $J = 8$, ce qui nous permet d'avoir un grand nombre (17) de sous-états Zeeman, qui seront très intéressants une fois interprétés comme des positions selon une dimension synthétique. Ensuite, la structure électronique du dysprosium lui confère un paysage de transitions électroniques particuliers. Trois transitions larges (de plusieurs MHz) sont situées dans le domaine bleu-proche UV. De nombreuses transitions fines (de quelques kHz) et bien espacées, éloignées de ces transitions larges, permettent d'appliquer des décalages lumineux dépendants du spin sans trop souffrir du chauffage causé par ces transitions larges. Enfin, nous voyons que l'interaction lumière-dysprosium contient un terme tensoriel non négligeable, qui nous permet de simuler des Hamiltoniens quadratiques en spin J_x^2, J_y^2, J_z^2. Nous voyons que la polarisation de la lumière est l'élément principal pour contrôler la forme de l'interaction lumière-dysprosium. Nous proposons différents protocoles pour calibrer finement la polarisation de la lumière dans différent régimes, en utilisant les atomes comme une sonde. Ensuite, nous montrons comment nous pouvons mesurer la norme du champ magnétique avec des atomes de dysprosium, en mettant en place le protocole d'interférométrie de Ramsey. Enfin, nous proposons une amélioration possible de l'expérience, consistant en l'utilisation d'un faisceau haute puissance modulé pour l'étape de transport.

Le chapitre 2 introduit nos protocoles pour simuler des systèmes de Hall quantiques avec des atomes de dysprosium. Nous présentons tout d'abord un systèmes de fils quantiques en deux dimensions, et montrons qu'un champ magnétique artificiel, à l'origine d'un effet Hall quantique, émerge dans cette structure. Nous introduisons avec ce système des notions de topologies, comme le nombre de Chern. Nous faisons ensuite le lien entre ce modèle de fils quantiques et notre système, où nous traitons la projection du spin selon l'axe de quantification, m, comme une dimension synthétique. Nous voyons que notre système est proche du système de fils quantiques, et qu'en particulier, les propriétés topologiques sont conservées. Notre protocole consiste à utiliser des lasers en configuration Raman sur un atome de Dysprosium. Ce faisant, nous couplons le spin du dysprosium à son moment selon un axe x. En d'autres termes nous générons un couplage spin-orbite, à l'origine du champ magnétique artificiel, donc de l'effet Hall quantique dans notre système en deux dimensions. Une dimension réelle, notée x, est infinie, et l'autre dimension synthétique, m, est discrète et faite des 17 sous-états Zeeman du dysprosium.

Le chapitre 3 montre comment il est possible de considérer deux dimensions synthétique au sein du spin du dysprosium. L'idée consiste à combiner deux procédés Raman. L'un couplant m à $m + 1$, l'autre couplant m à $m - 2$. Ce faisant, nous générons au sein des 17 sous-états Zeeman, des cycles $m \to m + 1 \to m + 2 \to m$. Nous montrons théoriquement que cela conduit à l'émergence de deux dimensions synthétiques. La première, notée m, est la projection du spin selon l'axe de quantification. La seconde, notée r, est le reste de la division euclidienne de m par 3. Enfin, nous utilisons cette dimension cylique afin de réaliser expérimentalement un cylindre de Hall quantique. Nous implémentons dans ce cylindre, pour la première fois, la pompe topologique de Laughlin.

Le chapitre 4 propose une exploration théorique des systèmes de Hall quantique en quatre dimensions. Nous commençons par introduire la classification topologique. La plupart des classes topologiques n'ont pas encore été étudié expérimentalement, et c'est en partie le cas pour les systèmes de haute dimensionnalité. Cette introduction motive l'étude des systèmes topologiques en quatre dimensions. Nous abordons quelques

propriétés topologiques particulières de l'effet Hall quantique à quatre dimensions. En particulier, nous introduisons la réponse non-linéaire, quantifié par le second nombre de Chern. Enfin, nous abordons théoriquement un système de Hall synthétique en quatre dimensions, avec deux dimensions spatiales et deux dimensions synthétiques. Ce système résulte de la combinaison des systèmes de Hall présentés dans les deux chapitres précédents.

Le chapitre 5 présente le résultat principal de cette thèse : la réalisation expérimentale d'un système de Hall en quatre dimensions. Nous commençons par dériver l'Hamiltonien de notre système et nous détaillons notre protocole expérimental. Nous présentons ensuite des résultats expérimentaux. Nous commençons par révéler la topologie non-triviale de notre système en mesurant des états de bord anisotropes à la frontière de notre système. Ces états de bord anisotrope sont spécifiques à la haute dimensionnalité. Ensuite, nous caractérisons la topologie du bulk, en mesurant un second marqueur de Chern égale à 1. Ce second marqueur de Chern quantifie la réponse non-linéaire du système, un aspect aussi spécifique à la haute dimensionnalité. Enfin, nous mesurons des orbites cyclotrons en quatre dimensions, et voyons que leur trajectoire est fondamentalement différente de celle de leur équivalent en deux et trois dimensions.

Le chapitre 6 se concentre sur la notion de d'Hamiltonien d'intrication. Nous commençons le chapitre par motiver l'étude de l'Hamiltonien d'intrication. Ce dernier permet de déterminer l'ordre topologique d'un système de manière unique, et contient plus d'information que la quantité habituellement utilisée : l'entropie de Von Neumann. Cependant, cet Hamiltonien est très difficile à calculer pour des systèmes en interaction, et sa réalisation expérimentale est difficile. Nous suivons le théorème de Bisognano-Wichmann pour réaliser une approximations de l'Hamiltonien d'intrication d'un système de Hall quantique en deux dimensions sans interaction. Cet Hamiltonien est obtenu en réalisant une déformation de l'Hamiltonien original. Nous mesurons le spectre de cet Hamiltonien et obtenons une relation de dispersion chirale. Via la conjecture de Li-Haldane, cette relation de dispersion démontre l'existence d'un ordre topologique dans notre système. Finalement, nous proposons une extension de notre protocole pour des systèmes en interaction, où la notion d'Hamiltonien d'intrication prend tout son sens.

Durant ma thèse, j'ai participé à quatre projets différents, trois d'entre eux étant discutés dans ce mémoire, avec un fort accent sur la réalisation d'un système de Hall quantique en quatre dimensions. J'ai eu aussi l'opportunité de travailler sur la notion d'intrication de paire, que je n'ai pas détaillée dans le mémoire. En bref, nous avons considéré le spin J du dysprosium comme $2J$ qubits virtuels, et avons étudié les propriétés d'intrication entre ces qubits. Cette étude a conduit à une publication [76] que nous fournissons en appendice A. Elle est décrite de manière exhaustive dans les thèses suivantes [77, 78].

Bibliography

[1] K. v. Klitzing, G. Dorda, and M. Pepper, "New Method for High-Accuracy Determination of the Fine-Structure Constant Based on Quantized Hall Resistance", Physical Review Letters **45**, Publisher: American Physical Society, 494–497 (1980) (cited on pages 11, 51, 87, 185).

[2] A. Tzalenchuk, S. Lara-Avila, A. Kalaboukhov, S. Paolillo, M. Syväjärvi, R. Yakimova, O. Kazakova, T. J. B. M. Janssen, V. Fal'ko, and S. Kubatkin, "Towards a quantum resistance standard based on epitaxial graphene", en, Nature Nanotechnology **5**, Number: 3 Publisher: Nature Publishing Group, 186–189 (2010) (cited on pages 11, 185).

[3] H. He, K. Cedergren, N. Shetty, S. Lara-Avila, S. Kubatkin, T. Bergsten, and G. Eklund, "Accurate graphene quantum Hall arrays for the new International System of Units", en, Nature Communications **13**, Number: 1 Publisher: Nature Publishing Group, 6933 (2022) (cited on pages 11, 185).

[4] D. J. Thouless, M. Kohmoto, M. P. Nightingale, and M. den Nijs, "Quantized Hall Conductance in a Two-Dimensional Periodic Potential", Physical Review Letters **49**, Publisher: American Physical Society, 405–408 (1982) (cited on pages 11, 87, 88, 185).

[5] P. A. M. Dirac, "Quantised Singularities in the Electromagnetic Field", Proceedings of the Royal Society of London. Series A, Containing Papers of a Mathematical and Physical Character **133**, Publisher: The Royal Society, 60–72 (1931) (cited on pages 11, 185).

[6] M. Asorey, "Space, matter and topology", en, Nature Physics **12**, Number: 7 Publisher: Nature Publishing Group, 616–618 (2016) (cited on pages 11, 185).

[7] S. Pancharatnam, "Generalized theory of interference, and its applications", en, Proceedings of the Indian Academy of Sciences - Section A **44**, 247–262 (1956) (cited on pages 11, 185).

[8] M. V. Berry, "Quantal phase factors accompanying adiabatic changes", Royal Society **392**, `https://doi.org/10.1098/rspa.1984.0023` (1984) (cited on pages 11, 54, 185).

[9] M. Berry, "Pancharatnam, virtuoso of the Poincaré sphere: an appreciation", Current Science **67**, Publisher: Current Science Association, 220–223 (1994) (cited on pages 11, 185).

[10] F. D. M. Haldane, *Phys. Rev. Lett. 61, 2015 (1988) - Model for a Quantum Hall Effect without Landau Levels: Condensed-Matter Realization of the "Parity Anomaly"* (cited on pages 11, 82, 88, 185).

[11] C. L. Kane and E. J. Mele, "Quantum Spin Hall Effect in Graphene", Physical Review Letters **95**, Publisher: American Physical Society, 226801 (2005) (cited on pages 11, 88, 185).

[12] C. L. Kane and E. J. Mele, "Z2 Topological Order and the Quantum Spin Hall Effect", Physical Review Letters **95**, Publisher: American Physical Society, 146802 (2005) (cited on pages 11, 88, 185).

[13] B. A. Bernevig and S.-C. Zhang, "Quantum Spin Hall Effect", Physical Review Letters **96**, Publisher: American Physical Society, 106802 (2006) (cited on pages 11, 88, 185).

[14] M. König, S. Wiedmann, C. Brüne, A. Roth, H. Buhmann, L. W. Molenkamp, X.-L. Qi, and S.-C. Zhang, "Quantum Spin Hall Insulator State in HgTe Quantum Wells", Science **318**, Publisher: American Association for the Advancement of Science, 766–770 (2007) (cited on pages 11, 88, 185).

[15] I. Knez, R.-R. Du, and G. Sullivan, "Evidence for Helical Edge Modes in Inverted InAsGaSb Quantum Wells", Physical Review Letters **107**, Publisher: American Physical Society, 136603 (2011) (cited on pages 11, 185).

[16] S. Wu, V. Fatemi, Q. D. Gibson, K. Watanabe, T. Taniguchi, R. J. Cava, and P. Jarillo-Herrero, "Observation of the quantum spin Hall effect up to 100 kelvin in a monolayer crystal", Science **359**, Publisher: American Association for the Advancement of Science, 76–79 (2018) (cited on pages 11, 185).

[17] J. E. Moore and L. Balents, "Topological invariants of time-reversal-invariant band structures", Physical Review B **75**, Publisher: American Physical Society, 121306 (2007) (cited on pages 11, 87, 88, 185).

[18] Y. Ando, "Topological Insulator Materials", Journal of the Physical Society of Japan **82**, Publisher: The Physical Society of Japan, 102001 (2013) (cited on pages 11, 185).

[19] A. P. Schnyder, S. Ryu, A. Furusaki, and A. W. W. Ludwig, "Classification of topological insulators and superconductors in three spatial dimensions", en, Physical Review B **78**, 195125 (2008) (cited on pages 11, 88, 89, 185).

[20] S. Ryu, A. P. Schnyder, A. Furusaki, and A. W. W. Ludwig, "Topological insulators and superconductors: tenfold way and dimensional hierarchy", en, New Journal of Physics **12**, 065010 (2010) (cited on pages 11, 88–90, 185).

[21] M. Z. Hasan and C. L. Kane, "Colloquium: Topological insulators", Reviews of Modern Physics **82**, Publisher: American Physical Society, 3045–3067 (2010) (cited on pages 11, 88, 89, 96, 185).

[22] M. Sato and Y. Ando, "Topological superconductors: a review", en, Reports on Progress in Physics **80**, Publisher: IOP Publishing, 076501 (2017) (cited on pages 11, 185).

[23] S.-C. Zhang and J. Hu, "A Four-Dimensional Generalization of the Quantum Hall Effect", Science **294**, Publisher: American Association for the Advancement of Science, 823–828 (2001) (cited on pages 12, 65, 87, 88, 186).

[24] C. H. Lee, Y. Wang, Y. Chen, and X. Zhang, "Electromagnetic response of quantum Hall systems in dimensions five and six and beyond", Phys. Rev. B **98**, Publisher: American Physical Society, 094434 (2018) (cited on pages 12, 186).

[25] I. Petrides, H. M. Price, and O. Zilberberg, "Six-dimensional quantum Hall effect and three-dimensional topological pumps", Physical Review B **98**, Publisher: American Physical Society, 125431 (2018) (cited on pages 12, 65, 186).

[26] S.-Y. Xu et al., "Discovery of a Weyl fermion semimetal and topological Fermi arcs", Science **349**, _eprint: https://www.science.org/doi/pdf/10.1126/science.aaa9297, 613–617 (2015) (cited on pages 12, 186).

[27] B. Lian and S.-C. Zhang, "Five-dimensional generalization of the topological Weyl semimetal", Physical Review B **94**, Publisher: American Physical Society, 041105 (2016) (cited on pages 12, 65, 186).

[28] D. C. Tsui, H. L. Stormer, and A. C. Gossard, "Two-Dimensional Magnetotransport in the Extreme Quantum Limit", Physical Review Letters **48**, Publisher: American Physical Society, 1559–1562 (1982) (cited on pages 12, 186).

[29] R. B. Laughlin, "Anomalous Quantum Hall Effect: An Incompressible Quantum Fluid with Fractionally Charged Excitations", Physical Review Letters **50**, Publisher: American Physical Society, 1395–1398 (1983) (cited on pages 12, 186).

[30] J. Léonard, S. Kim, J. Kwan, P. Segura, F. Grusdt, C. Repellin, N. Goldman, and M. Greiner, "Realization of a fractional quantum Hall state with ultracold atoms", en, Nature **619**, Number: 7970 Publisher: Nature Publishing Group, 495–499 (2023) (cited on pages 12, 160, 186).

[31] J. Fröhlich, "Statistics of Fields, the Yang-Baxter Equation, and the Theory of Knots and Links", en, in *Nonperturbative Quantum Field Theory*, edited by G. 't Hooft, A. Jaffe, G. Mack, P. K. Mitter, and R. Stora, Nato Science Series B: (Springer US, New York, NY, 1988), pp. 71–100 (cited on pages 12, 186).

[32] G. Moore and N. Read, "Nonabelions in the fractional quantum hall effect", en, Nuclear Physics B **360**, 362–396 (1991) (cited on pages 12, 186).

[33] X. G. Wen, "Non-Abelian statistics in the fractional quantum Hall states", Physical Review Letters **66**, Publisher: American Physical Society, 802–805 (1991) (cited on pages 12, 186).

[34] C. Nayak, S. H. Simon, A. Stern, M. Freedman, and S. Das Sarma, "Non-Abelian anyons and topological quantum computation", Reviews of Modern Physics **80**, Publisher: American Physical Society, 1083–1159 (2008) (cited on pages 12, 186).

[35] T. Ozawa et al., "Topological photonics", Reviews of Modern Physics **91**, Publisher: American Physical Society, 015006 (2019) (cited on pages 12, 186).

[36] H. Price et al., "Roadmap on topological photonics", Journal of Physics: Photonics **4**, Publisher: IOP Science, 032501 (2022) (cited on pages 12, 13, 186, 187).

[37] L. Lu, J. D. Joannopoulos, and M. Soljačić, "Topological states in photonic systems", en, Nature Physics **12**, Number: 7 Publisher: Nature Publishing Group, 626–629 (2016) (cited on pages 12, 186).

[38] M. C. Rechtsman, J. M. Zeuner, Y. Plotnik, Y. Lumer, D. Podolsky, F. Dreisow, S. Nolte, M. Segev, and A. Szameit, "Photonic Floquet topological insulators", en, Nature **496**, Number: 7444 Publisher: Nature Publishing Group, 196–200 (2013) (cited on pages 12, 186).

[39] L. J. Maczewsky, J. M. Zeuner, S. Nolte, and A. Szameit, "Observation of photonic anomalous Floquet topological insulators", en, Nature Communications **8**, Number: 1 Publisher: Nature Publishing Group, 13756 (2017) (cited on pages 12, 186).

[40] S. Mukherjee, A. Spracklen, M. Valiente, E. Andersson, P. Öhberg, N. Goldman, and R. R. Thomson, "Experimental observation of anomalous topological edge modes in a slowly driven photonic lattice", en, Nature Communications **8**, Number: 1 Publisher: Nature Publishing Group, 13918 (2017) (cited on pages 12, 186).

[41] O. Zilberberg, S. Huang, J. Guglielmon, M. Wang, K. P. Chen, Y. E. Kraus, and M. C. Rechtsman, "Photonic topological boundary pumping as a probe of 4D quantum Hall physics", en, Nature **553**, Number: 7686 Publisher: Nature Publishing Group, 59–62 (2018) (cited on pages 12, 58, 88, 98, 99, 186).

[42] Y. Wang, H. M. Price, B. Zhang, and Y. D. Chong, "Circuit implementation of a four-dimensional topological insulator", en, Nature Communications **11**, Number: 1 Publisher: Nature Publishing Group, 2356 (2020) (cited on pages 12, 65, 88, 90, 97–99, 186).

[43] N. Goldman, G. Juzeliūnas, P. Öhberg, and I. B. Spielman, "Light-induced gauge fields for ultracold atoms", en, Reports on Progress in Physics **77**, Publisher: IOP Publishing, 126401 (2014) (cited on pages 12, 186, 187).

[44] N. Cooper, J. Dalibard, and I. Spielman, "Topological bands for ultracold atoms", Reviews of Modern Physics **91**, Publisher: American Physical Society, 015005 (2019) (cited on pages 12, 135, 160, 186).

[45] N. Goldman, J. C. Budich, and P. Zoller, "Topological quantum matter with ultracold gases in optical lattices", en, Nature Physics **12**, Number: 7 Publisher: Nature Publishing Group, 639–645 (2016) (cited on pages 12, 186).

[46] D.-W. Zhang, Y.-Q. Zhu, Y. X. Zhao, H. Yan, and S.-L. Zhu, "Topological quantum matter with cold atoms", Advances in Physics **67**, Publisher: Taylor & Francis _eprint: https://doi.org/10.1080/00018732.2019.1594094, 253–402 (2018) (cited on pages 12, 186).

[47] M. H. Anderson, J. R. Ensher, M. R. Matthews, C. E. Wieman, and E. A. Cornell, "Observation of Bose-Einstein Condensation in a Dilute Atomic Vapor", Science **269**, Publisher: American Association for the Advancement of Science, 198–201 (1995) (cited on pages 12, 186).

[48] K. B. Davis, M. .-. Mewes, M. R. Andrews, N. J. van Druten, D. S. Durfee, D. M. Kurn, and W. Ketterle, "Bose-Einstein Condensation in a Gas of Sodium Atoms", Phys. Rev. Lett. **75**, Publisher: American Physical Society, 3969–3973 (1995) (cited on pages 12, 186).

[49] B. DeMarco and D. S. Jin, "Onset of Fermi Degeneracy in a Trapped Atomic Gas", Science **285**, Publisher: American Association for the Advancement of Science, 1703–1706 (1999) (cited on pages 12, 186).

[50] M. Mancini et al., "Observation of chiral edge states with neutral fermions in synthetic Hall ribbons", Science **349**, Publisher: American Association for the Advancement of Science, 1510–1513 (2015) (cited on pages 12, 58, 187).

[51] H. Li and F. D. M. Haldane, "Entanglement Spectrum as a Generalization of Entanglement Entropy: Identification of Topological Order in Non-Abelian Fractional Quantum Hall Effect States", Physical Review Letters **101**, Publisher: American Physical Society, 010504 (2008) (cited on pages 12, 47, 56, 138, 149–151, 154, 187).

[52] M. Aidelsburger, M. Lohse, C. Schweizer, M. Atala, J. T. Barreiro, S. Nascimbène, N. R. Cooper, I. Bloch, and N. Goldman, "Measuring the Chern number of Hofstadter bands with ultracold bosonic atoms", en, Nature Physics **11**, Number: 2 Publisher: Nature Publishing Group, 162–166 (2015) (cited on pages 12, 13, 187).

[53] Z. Wu, L. Zhang, W. Sun, X.-T. Xu, B.-Z. Wang, S.-C. Ji, Y. Deng, S. Chen, X.-J. Liu, and J.-W. Pan, "Realization of two-dimensional spin-orbit coupling for Bose-Einstein condensates", Science **354**, Publisher: American Association for the Advancement of Science, 83–88 (2016) (cited on pages 13, 187).

[54] Z.-Y. Wang et al., "Realization of an ideal Weyl semimetal band in a quantum gas with 3D spin-orbit coupling", Science **372**, Publisher: American Association for the Advancement of Science, 271–276 (2021) (cited on pages 13, 187).

[55] N. Cooper, "Rapidly rotating atomic gases", Advances in Physics **57**, Publisher: Taylor & Francis _eprint: https://doi.org/10.1080/00018730802564122, 539–616 (2008) (cited on pages 13, 160, 187).

[56] D. Jaksch, C. Bruder, J. I. Cirac, C. W. Gardiner, and P. Zoller, "Cold Bosonic Atoms in Optical Lattices", Phys. Rev. Lett. **81**, Publisher: American Physical Society, 3108–3111 (1998) (cited on pages 13, 187).

[57] J. Ruostekoski, J. Javanainen, and G. V. Dunne, "Manipulating atoms in an optical lattice: Fractional fermion number and its optical quantum measurement", Phys. Rev. A **77**, Publisher: American Physical Society, 013603 (2008) (cited on pages 13, 187).

[58] G. Jotzu, M. Messer, R. Desbuquois, M. Lebrat, T. Uehlinger, D. Greif, and T. Esslinger, "Experimental realization of the topological Haldane model with ultracold fermions", en, Nature **515**, Number: 7526 Publisher: Nature Publishing Group, 237–240 (2014) (cited on pages 13, 187).

[59] M. Lohse, C. Schweizer, H. M. Price, O. Zilberberg, and I. Bloch, "Exploring 4D quantum Hall physics with a 2D topological charge pump", en, Nature **553**, Number: 7686 Publisher: Nature Publishing Group, 55–58 (2018) (cited on pages 13, 88, 98, 99, 187).

[60] H. Price, O. Zilberberg, T. Ozawa, I. Carusotto, and N. Goldman, "Four-Dimensional Quantum Hall Effect with Ultracold Atoms", en, Physical Review Letters **115**, 195303 (2015) (cited on pages 13, 58, 94, 95, 97, 140, 187).

[61] C.-H. Li, Y. Yan, S.-W. Feng, S. Choudhury, D. B. Blasing, Q. Zhou, and Y. P. Chen, "Bose-Einstein Condensate on a Synthetic Topological Hall Cylinder", PRX Quantum **3**, Publisher: American Physical Society, 010316 (2022) (cited on pages 13, 58, 83, 187).

[62] J. H. Han, J. H. Kang, and Y. Shin, "Band Gap Closing in a Synthetic Hall Tube of Neutral Fermions", Physical Review Letters **122**, Publisher: American Physical Society, 065303 (2019) (cited on pages 13, 58, 83, 187).

[63] Q.-Y. Liang, D. Trypogeorgos, A. Valdés-Curiel, J. Tao, M. Zhao, and I. B. Spielman, "Coherence and decoherence in the Harper-Hofstadter model", Physical Review Research **3**, Publisher: American Physical Society, 023058 (2021) (cited on pages 13, 58, 83, 187).

[64] E. Lustig, S. Weimann, Y. Plotnik, Y. Lumer, M. A. Bandres, A. Szameit, and M. Segev, "Photonic topological insulator in synthetic dimensions", en, Nature **567**, Number: 7748 Publisher: Nature Publishing Group, 356–360 (2019) (cited on pages 13, 58, 187).

[65] A. Dutt, Q. Lin, L. Yuan, M. Minkov, M. Xiao, and S. Fan, "A single photonic cavity with two independent physical synthetic dimensions", Science **367**, Publisher: American Association for the Advancement of Science, 59–64 (2020) (cited on pages 13, 187).

[66] L. Chomaz, I. Ferrier-Barbut, F. Ferlaino, B. Laburthe-Tolra, B. L. Lev, and T. Pfau, "Dipolar physics: a review of experiments with magnetic quantum gases", en, Reports on Progress in Physics **86**, Publisher: IOP Publishing, 026401 (2022) (cited on pages 13, 14, 20, 188).

[67] H. Kadau, M. Schmitt, M. Wenzel, C. Wink, T. Maier, I. Ferrier-Barbut, and T. Pfau, "Observing the Rosensweig instability of a quantum ferrofluid", en, Nature **530**, Number: 7589 Publisher: Nature Publishing Group, 194–197 (2016) (cited on pages 14, 188).

[68] I. Ferrier-Barbut, M. Wenzel, F. Böttcher, T. Langen, M. Isoard, S. Stringari, and T. Pfau, "Scissors Mode of Dipolar Quantum Droplets of Dysprosium Atoms", Physical Review Letters **120**, Publisher: American Physical Society, 160402 (2018) (cited on pages 14, 20, 188).

[69] L. Chomaz et al., "Long-Lived and Transient Supersolid Behaviors in Dipolar Quantum Gases", Physical Review X **9**, Publisher: American Physical Society, 021012 (2019) (cited on pages 14, 21, 188).

[70] L. Chomaz, R. M. W. van Bijnen, D. Petter, G. Faraoni, S. Baier, J. H. Becher, M. J. Mark, F. Wächtler, L. Santos, and F. Ferlaino, "Observation of roton mode population in a dipolar quantum gas", en, Nature Physics **14**, Number: 5 Publisher: Nature Publishing Group, 442–446 (2018) (cited on pages 14, 188).

[71] L. Tanzi, E. Lucioni, F. Famà, J. Catani, A. Fioretti, C. Gabbanini, R. Bisset, L. Santos, and G. Modugno, "Observation of a Dipolar Quantum Gas with Metastable Supersolid Properties", Physical Review Letters **122**, Publisher: American Physical Society, 130405 (2019) (cited on pages 14, 21, 188).

[72] F. Böttcher et al., "Dilute dipolar quantum droplets beyond the extended Gross-Pitaevskii equation", Physical Review Research **1**, Publisher: American Physical Society, 033088 (2019) (cited on pages 14, 20, 188).

[73] T. Chalopin, C. Bouazza, A. Evrard, V. Makhalov, D. Dreon, J. Dalibard, L. A. Sidorenkov, and S. Nascimbene, "Quantum-enhanced sensing using non-classical spin states of a highly magnetic atom", en, Nature Communications **9**, Number: 1 Publisher: Nature Publishing Group, 4955 (2018) (cited on pages 14, 188).

[74] A. Evrard, V. Makhalov, T. Chalopin, L. A. Sidorenkov, J. Dalibard, R. Lopes, and S. Nascimbene, "Enhanced Magnetic Sensitivity with Non-Gaussian Quantum Fluctuations", Physical Review Letters **122**, Publisher: American Physical Society, 173601 (2019) (cited on pages 14, 188).

[75] R. Kaubruegger, A. Shankar, D. V. Vasilyev, and P. Zoller, "Optimal and Variational Multiparameter Quantum Metrology and Vector-Field Sensing", PRX Quantum **4**, Publisher: American Physical Society, 020333 (2023) (cited on pages 14, 188).

[76] T. Satoor, A. Fabre, J.-B. Bouhiron, A. Evrard, R. Lopes, and S. Nascimbene, "Partitioning dysprosium's electronic spin to reveal entanglement in nonclassical states", en, Physical Review Research **3**, 043001 (2021) (cited on pages 15, 69, 161, 190).

[77] T. Satoor, "Manipulating ultracold dysprosium's atomic spin to encode quantum critical, entangled, and topological states of matter", en, PhD thesis (PSL Université, Oct. 2022) (cited on pages 15, 190).

[78] A. Fabre, "Realisation of Laughlin's topological charge pump in an atomic Hall cylinder", en, PhD thesis (Université Paris Sciences Lettres, Dec. 2022) (cited on pages 15, 28, 41, 66, 71, 73, 85, 127, 190).

[79] J. R. d. Laeter, J. K. Böhlke, P. D. Bièvre, H. Hidaka, H. S. Peiser, K. J. R. Rosman, and P. D. P. Taylor, "Atomic weights of the elements. Review 2000 (IUPAC Technical Report)", de, Pure and Applied Chemistry **75**, Publisher: De Gruyter, 683–800 (2003) (cited on page 18).

[80] M. Lu, S. H. Youn, and B. L. Lev, "Spectroscopy of a narrow-line laser-cooling transition in atomic dysprosium", Physical Review A **83**, Publisher: American Physical Society, 012510 (2011) (cited on page 19).

[81] T. Ohmi and K. Machida, "Bose-Einstein Condensation with Internal Degrees of Freedom in Alkali Atom Gases", Journal of the Physical Society of Japan **67**, Publisher: The Physical Society of Japan, 1822–1825 (1998) (cited on page 19).

[82] D. M. Stamper-Kurn and M. Ueda, "Spinor Bose gases: Symmetries, magnetism, and quantum dynamics", Reviews of Modern Physics **85**, Publisher: American Physical Society, 1191–1244 (2013) (cited on page 19).

[83] Y. Tang, A. Sykes, N. Q. Burdick, J. L. Bohn, and B. L. Lev, "s-wave scattering lengths of the strongly dipolar bosons ^{162}Dy and ^{164}Dy", Physical Review A **92**, Publisher: American Physical Society, 022703 (2015) (cited on page 19).

[84] S. Kotochigova and A. Petrov, "Anisotropy in the interaction of ultracold dysprosium", en, Physical Chemistry Chemical Physics **13**, Publisher: The Royal Society of Chemistry, 19165–19170 (2011) (cited on page 19).

[85] B. Pasquiou, "Effets de l'interaction dipôle-dipôle sur les propriétés magnétiques d'un condensat de chrome", fr, PhD thesis (Université Paris-Nord - Paris XIII, Nov. 2011) (cited on page 20).

[86] S. Hensler, J. Werner, A. Griesmaier, P. Schmidt, A. Görlitz, T. Pfau, S. Giovanazzi, and K. Rzażewski, "Dipolar relaxation in an ultra-cold gas of magnetically trapped chromium atoms", en, Applied Physics B **77**, 765–772 (2003) (cited on page 20).

[87] B. Laburthe-Tolra, "Supersolids go two-dimensional", en, Nature **596**, Bandiera_abtest: a Cg_type: News And Views Number: 7872 Publisher: Nature Publishing Group Subject_term: Atomic and molecular physics, Quantum physics, Condensed-matter physics, 348–349 (2021) (cited on page 21).

[88] M. A. Norcia, C. Politi, L. Klaus, E. Poli, M. Sohmen, M. J. Mark, R. N. Bisset, L. Santos, and F. Ferlaino, "Two-dimensional supersolidity in a dipolar quantum gas", en, Nature **596**, Number: 7872 Publisher: Nature Publishing Group, 357–361 (2021) (cited on page 21).

[89] P. A. Altin, G. McDonald, D. Döring, J. E. Debs, T. H. Barter, J. D. Close, N. P. Robins, S. A. Haine, T. M. Hanna, and R. P. Anderson, "Optically trapped atom interferometry using the clock transition of large 87Rb Bose–Einstein condensates", en, New Journal of Physics **13**, 065020 (2011) (cited on page 21).

[90] F. Le Kien, P. Schneeweiss, and A. Rauschenbeutel, "Dynamical polarizability of atoms in arbitrary light fields: general theory and application to cesium", en, The European Physical Journal D **67**, Company: Springer Distributor: Springer Institution: Springer Label: Springer Number: 5 Publisher: Springer-Verlag, 1–16 (2013) (cited on pages 22, 23).

[91] D. Dreon, "Designing and building an ultracold Dysprosium experiment : a new framework for light-spin interaction", en, PhD thesis (Université Paris sciences et lettres, July 2017) (cited on pages 23, 25, 28).

[92] A. Evrard, "Non-gaussian spin states of ultracold dysprosium atoms", These de doctorat (Université Paris sciences et lettres, Sept. 2020) (cited on pages 23, 25, 29, 41).

[93] C. Bouazza, "Ultracold dysprosium gas in optical dipole traps : control of interactions between highly magnetic atoms", en, PhD thesis (Université Paris sciences et lettres, May 2018) (cited on page 28).

[94] D. Dreon, L. A. Sidorenkov, C. Bouazza, W. Maineult, J. Dalibard, and S. Nascimbene, "Optical cooling and trapping of highly magnetic atoms: the benefits of a spontaneous spin polarization", en, Journal of Physics B: Atomic, Molecular and Optical Physics **50**, Publisher: IOP Publishing, 065005 (2017) (cited on page 28).

[95] T. Chalopin et al., "Anisotropic light shift and magic polarization of the intercombination line of dysprosium atoms in a far-detuned dipole trap", Physical Review A **98**, Publisher: American Physical Society, 040502 (2018) (cited on pages 28, 29).

[96] K. Aikawa, "Bose-Einstein Condensation of Erbium", Physical Review Letters **108**, 10.1103/PhysRevLett.108.210401 (2012) (cited on page 29).

[97] D. Aerts and M. Sassoli de Bianchi, "The extended Bloch representation of quantum mechanics and the hidden-measurement solution to the measurement problem", Annals of Physics **351**, 975–1025 (2014) (cited on page 30).

[98] T. Chalopin, "Quantum-enhanced sensing and synthetic Landau levels with ultracold dysprosium atoms", English, PhD thesis (Sorbonne Université, 2019) (cited on pages 39, 47, 48).

[99] J. Raimond and H. Perrin, *Atoms and photons*, Oct. 2020 (cited on page 39).

[100] N. F. Ramsey, "A Molecular Beam Resonance Method with Separated Oscillating Fields", Physical Review **78**, Publisher: American Physical Society, 695–699 (1950) (cited on page 40).

[101] T. Klostermann, C. R. Cabrera, H. von Raven, J. F. Wienand, C. Schweizer, I. Bloch, and M. Aidelsburger, "Fast long-distance transport of cold cesium atoms", Physical Review A **105**, Publisher: American Physical Society, 043319 (2022) (cited on page 41).

[102] C. L. Kane, R. Mukhopadhyay, and T. C. Lubensky, "Fractional Quantum Hall Effect in an Array of Quantum Wires", Physical Review Letters **88**, Publisher: American Physical Society, 036401 (2002) (cited on pages 47, 51).

[103] T. Chalopin, T. Satoor, A. Evrard, V. Makhalov, J. Dalibard, R. Lopes, and S. Nascimbene, "Probing chiral edge dynamics and bulk topology of a synthetic Hall system", en, Nature Physics **16**, Number: 10 Publisher: Nature Publishing Group, 1017–1021 (2020) (cited on pages 47, 48, 58, 59).

[104] J. Dalibard, *Champs magnétiques artificiels* (Collège de France, 2014) (cited on page 48).

[105] J. Dalibard, *La matière topologique et son exploration avec les gaz quantiques* (2018) (cited on page 48).

[106] S. L. Sondhi and K. Yang, "Sliding phases via magnetic fields", Physical Review B **63**, Publisher: American Physical Society, 054430 (2001) (cited on page 51).

[107] D. Xiao, M.-C. Chang, and Q. Niu, "Berry phase effects on electronic properties", Reviews of Modern Physics **82**, Publisher: American Physical Society, 1959–2007 (2010) (cited on pages 54, 94, 109).

[108] R. Bianco and R. Resta, "Mapping topological order in coordinate space", Physical Review B **84**, Publisher: American Physical Society, 241106 (2011) (cited on pages 57, 111, 139).

[109] A. Celi, P. Massignan, J. Ruseckas, N. Goldman, I. Spielman, G. Juzeliunas, and M. Lewenstein, "Synthetic Gaug Fields in Synthetic Dimensions", Physical Review Letters **112**, Publisher: American Physical Society, 043001 (2014) (cited on pages 58, 160).

[110] Y.-J. Lin, R. L. Compton, K. Jiménez-García, J. V. Porto, and I. B. Spielman, "Synthetic magnetic fields for ultracold neutral atoms", eng, Nature **462**, 628–632 (2009) (cited on page 58).

[111] B. K. Stuhl, H.-I. Lu, L. M. Aycock, D. Genkina, and I. B. Spielman, "Visualizing edge states with an atomic Bose gas in the quantum Hall regime", Science **349**, Publisher: American Association for the Advancement of Science, 1514–1518 (2015) (cited on page 58).

[112] D. Xie, T.-S. Deng, T. Xiao, W. Gou, T. Chen, W. Yi, and B. Yan, "Topological Quantum Walks in Momentum Space with a Bose-Einstein Condensate", Physical Review Letters **124**, Publisher: American Physical Society, 050502 (2020) (cited on page 58).

[113] F. A. An, E. J. Meier, J. Ang'ong'a, and B. Gadway, "Correlated Dynamics in a Synthetic Lattice of Momentum States", Physical Review Letters **120**, Publisher: American Physical Society, 040407 (2018) (cited on page 58).

[114] M. Yang, H.-Q. Zhang, Y.-W. Liao, Z.-H. Liu, Z.-W. Zhou, X.-X. Zhou, J.-S. Xu, Y.-J. Han, C.-F. Li, and G.-C. Guo, "Realization of exceptional points along a synthetic orbital angular momentum dimension", Science Advances **9**, Publisher: American Association for the Advancement of Science, eabp8943 (2023) (cited on page 58).

[115] L. Yuan, M. Xiao, Q. Lin, and S. Fan, "Synthetic space with arbitrary dimensions in a few rings undergoing dynamic modulation", Physical Review B **97**, Publisher: American Physical Society, 104105 (2018) (cited on pages 58, 65, 97).

[116] D. Jukić and H. Buljan, "Four-dimensional photonic lattices and discrete tesseract solitons", Physical Review A **87**, Publisher: American Physical Society, 013814 (2013) (cited on pages 58, 65, 97).

[117] M. Ezawa, "Electric circuits for non-Hermitian Chern insulators", Physical Review B **100**, Publisher: American Physical Society, 081401 (2019) (cited on page 65).

[118] L. Li, C. H. Lee, and J. Gong, "Emergence and full 3D-imaging of nodal boundary Seifert surfaces in 4D topological matter", en, Communications Physics **2**, Number: 1 Publisher: Nature Publishing Group, 1–11 (2019) (cited on page 65).

[119] R. B. Laughlin, "Quantized Hall conductivity in two dimensions", Physical Review B **23**, Publisher: American Physical Society, 5632–5633 (1981) (cited on pages 66, 82).

[120] A. Fabre, J.-B. Bouhiron, T. Satoor, R. Lopes, and S. Nascimbene, "Laughlin's Topological Charge Pump in an Atomic Hall Cylinder", en, Physical Review Letters **128**, 173202 (2022) (cited on pages 66, 82, 85, 176).

[121] A. Fabre, J.-B. Bouhiron, T. Satoor, R. Lopes, and S. Nascimbene, "Simulating two-dimensional dynamics within a large-size atomic spin", en, Physical Review A **105**, 013301 (2022) (cited on pages 66, 67, 74).

[122] F. T. Arecchi, E. Courtens, R. Gilmore, and H. Thomas, "Atomic Coherent States in Quantum Optics", Physical Review A **6**, Publisher: American Physical Society, 2211–2237 (1972) (cited on page 68).

[123] T. Holstein and H. Primakoff, "Field Dependence of the Intrinsic Domain Magnetization of a Ferromagnet", Physical Review **58**, Publisher: American Physical Society, 1098–1113 (1940) (cited on page 68).

[124] M. D. Frye, S. L. Cornish, and J. M. Hutson, "Prospects of Forming High-Spin Polar Molecules from Ultracold Atoms", Physical Review X **10**, Publisher: American Physical Society, 041005 (2020) (cited on page 70).

[125] N. Goldman and J. Dalibard, "Periodically Driven Quantum Systems: Effective Hamiltonians and Engineered Gauge Fields", Physical Review X **4**, Publisher: American Physical Society, 031027 (2014) (cited on page 73).

[126] S. M. Barnett and D. T. Pegg, "Quantum theory of rotation angles", Physical Review A **41**, Publisher: American Physical Society, 3427–3435 (1990) (cited on page 74).

[127] R. Lynch, "The quantum phase problem: a critical review", en, Physics Reports **256**, 367–436 (1995) (cited on page 74).

[128] H. Kim, W. Lee, S. Park, K. Kyhm, K. Je, R. A. Taylor, G. Nogues, L. S. Dang, and J. D. Song, "Quasi-one-dimensional density of states in a single quantum ring", en, Scientific Reports **7**, Number: 1 Publisher: Nature Publishing Group, 40026 (2017) (cited on page 82).

[129] E. Ribeiro, A. O. Govorov, W. Carvalho, and G. Medeiros-Ribeiro, "Aharonov-Bohm Signature for Neutral Polarized Excitons in Type-II Quantum Dot Ensembles", Physical Review Letters **92**, Publisher: American Physical Society, 126402 (2004) (cited on page 82).

[130] S. Rathinavel, K. Priyadharshini, and D. Panda, "A review on carbon nanotube: An overview of synthesis, properties, functionalization, characterization, and the application", Materials Science and Engineering: B **268**, 115095 (2021) (cited on page 82).

[131] S. Iijima and T. Ichihashi, "Single-shell carbon nanotubes of 1-nm diameter", en, Nature **363**, Number: 6430 Publisher: Nature Publishing Group, 603–605 (1993) (cited on page 82).

[132] S. Iijima, "Helical microtubules of graphitic carbon", en, Nature **354**, Number: 6348 Publisher: Nature Publishing Group, 56–58 (1991) (cited on page 82).

[133] Z. Zhang, P. Gao, W. Liu, Z. Yue, Y. Cheng, X. Liu, and J. Christensen, "Structured sonic tube with carbon nanotube-like topological edge states", en, Nature Communications **13**, Number: 1 Publisher: Nature Publishing Group, 5096 (2022) (cited on page 82).

[134] J. Preskill, "Magnetic Monopoles", Annual Review of Nuclear and Particle Science **34**, _eprint: https://doi.org/10.1146/annurev.ns.34.120184.002333, 461–530 (1984) (cited on page 82).

[135] D. J. Thouless, "Quantization of particle transport", Physical Review B **27**, Publisher: American Physical Society, 6083–6087 (1983) (cited on pages 83, 97).

[136] R. Citro and M. Aidelsburger, "Thouless pumping and topology", en, Nature Reviews Physics **5**, Number: 2 Publisher: Nature Publishing Group, 87–101 (2023) (cited on page 83).

[137] R. Laughlin, "Fractional Quantization - Nobel Lecture", in (Dec. 1998) (cited on page 83).

[138] L. Fu, C. L. Kane, and E. J. Mele, "Topological Insulators in Three Dimensions", Physical Review Letters **98**, Publisher: American Physical Society, 106803 (2007) (cited on pages 87, 88).

[139] R. Roy, "Topological phases and the quantum spin Hall effect in three dimensions", Physical Review B **79**, Publisher: American Physical Society, 195322 (2009) (cited on pages 87, 88).

[140] J. Fröhlich and B. Pedrini, "New applications of the chiral anomaly", in *Mathematical Physics 2000* (PUBLISHED BY IMPERIAL COLLEGE PRESS and DISTRIBUTED BY WORLD SCIENTIFIC PUBLISHING CO., May 2000), pp. 9–47 (cited on page 87).

[141] J.-B. Bouhiron, A. Fabre, Q. Liu, Q. Redon, N. Mittal, T. Satoor, R. Lopes, and S. Nascimbene, *Realization of an atomic quantum Hall system in four dimensions*, arXiv:2210.06322 [cond-mat, physics:quant-ph], Oct. 2022 (cited on pages 88, 111, 120, 134, 139).

[142] M. Kohmoto, B. I. Halperin, and Y. S. Wu, "Diophantine equation for the three-dimensional quantum Hall effect", eng, Physical Review. B, Condensed Matter **45**, 13488–13493 (1992) (cited on page 88).

[143] Halperin, "Possible states for a three-dimensional electron gas in a strong magnetic field.", en, Japanese Journal of Applied Physics. Supplement, 1913–1919 (1987) (cited on page 88).

[144] F. Tang et al., "Three-dimensional quantum Hall effect and metal–insulator transition in ZrTe5", en, Nature **569**, Number: 7757 Publisher: Nature Publishing Group, 537–541 (2019) (cited on page 88).

[145] M. R. Zirnbauer, "Riemannian symmetric superspaces and their origin in random-matrix theory", Journal of Mathematical Physics **37**, 4986–5018 (1996) (cited on page 89).

[146] A. Altland and M. R. Zirnbauer, "Nonstandard symmetry classes in mesoscopic normal-superconducting hybrid structures", Physical Review B **55**, Publisher: American Physical Society, 1142–1161 (1997) (cited on page 89).

[147] W. P. Su, J. R. Schrieffer, and A. J. Heeger, "Solitons in Polyacetylene", Physical Review Letters **42**, Publisher: American Physical Society, 1698–1701 (1979) (cited on page 89).

[148] W. S. Massey, "Cross Products of Vectors in Higher Dimensional Euclidean Spaces", The American Mathematical Monthly **90**, Publisher: Mathematical Association of America, 697–701 (1983) (cited on page 91).

[149] Y. Gao, S. A. Yang, and Q. Niu, "Field Induced Positional Shift of Bloch Electrons and Its Dynamical Implications", Physical Review Letters **112**, Publisher: American Physical Society, 166601 (2014) (cited on pages 94, 95, 140).

[150] G. Sundaram and Q. Niu, "Wave-packet dynamics in slowly perturbed crystals: Gradient corrections and Berry-phase effects", Physical Review B **59**, Publisher: American Physical Society, 14915–14925 (1999) (cited on page 94).

[151] B. Estienne, B. Oblak, and J.-M. Stéphan, "Ergodic Edge Modes in the 4D Quantum Hall Effect", en, (2021) (cited on pages 96, 133, 140).

[152] D. Karabali and V. P. Nair, "Quantum Hall Effect in Higher Dimensions", Nuclear Physics B **641**, arXiv:hep-th/0203264, 533–546 (2002) (cited on page 96).

[153] H. Elvang and J. Polchinski, *The Quantum Hall Effect on R^4*, arXiv:hep-th/0209104, Sept. 2002 (cited on page 96).

[154] H. M. Price, "Four-dimensional topological lattices through connectivity", Physical Review B **101**, arXiv:1806.05263 [cond-mat, physics:physics], 205141 (2020) (cited on pages 97, 98).

[155] T. Ozawa, H. M. Price, N. Goldman, O. Zilberberg, and I. Carusotto, "Synthetic dimensions in integrated photonics: From optical isolation to four-dimensional quantum Hall physics", Physical Review A **93**, Publisher: American Physical Society, 043827 (2016) (cited on page 97).

[156] Y. E. Kraus, Z. Ringel, and O. Zilberberg, "Four-Dimensional Quantum Hall Effect in a Two-Dimensional Quasicrystal", Physical Review Letters **111**, Publisher: American Physical Society, 226401 (2013) (cited on pages 97, 98).

[157] L. Wang, M. Troyer, and X. Dai, "Topological Charge Pumping in a One-Dimensional Optical Lattice", Physical Review Letters **111**, Publisher: American Physical Society, 026802 (2013) (cited on page 97).

[158] M. Lohse, C. Schweizer, O. Zilberberg, M. Aidelsburger, and I. Bloch, "A Thouless quantum pump with ultracold bosonic atoms in an optical superlattice", en, Nature Physics **12**, Number: 4 Publisher: Nature Publishing Group, 350–354 (2016) (cited on page 98).

[159] Y. E. Kraus, Y. Lahini, Z. Ringel, M. Verbin, and O. Zilberberg, "Topological States and Adiabatic Pumping in Quasicrystals", Physical Review Letters **109**, Publisher: American Physical Society, 106402 (2012) (cited on page 98).

[160] S. Nakajima, T. Tomita, S. Taie, T. Ichinose, H. Ozawa, L. Wang, M. Troyer, and Y. Takahashi, "Topological Thouless pumping of ultracold fermions", en, Nature Physics **12**, Number: 4 Publisher: Nature Publishing Group, 296–300 (2016) (cited on page 98).

[161] H.-I. Lu, M. Schemmer, L. Aycock, D. Genkina, S. Sugawa, and I. Spielman, "Geometrical Pumping with a Bose-Einstein Condensate", Physical Review Letters **116**, Publisher: American Physical Society, 200402 (2016) (cited on page 98).

[162] C. Schweizer, M. Lohse, R. Citro, and I. Bloch, "Spin Pumping and Measurement of Spin Currents in Optical Superlattices", Physical Review Letters **117**, Publisher: American Physical Society, 170405 (2016) (cited on page 98).

[163] X.-G. Wen, "Colloquium: Zoo of quantum-topological phases of matter", Reviews of Modern Physics **89**, Publisher: American Physical Society, 041004 (2017) (cited on page 149).

[164] X. Chen, Z.-C. Gu, and X.-G. Wen, "Local unitary transformation, long-range quantum entanglement, wave function renormalization, and topological order", Physical Review B **82**, Publisher: American Physical Society, 155138 (2010) (cited on page 149).

[165] A. Kitaev and J. Preskill, "Topological Entanglement Entropy", Physical Review Letters **96**, Publisher: American Physical Society, 110404 (2006) (cited on pages 149, 150).

[166] M. Levin and X.-G. Wen, "Detecting Topological Order in a Ground State Wave Function", Physical Review Letters **96**, Publisher: American Physical Society, 110405 (2006) (cited on pages 149, 150).

[167] N. Regnault, *Entanglement Spectroscopy and its Application to the Quantum Hall Effects*, arXiv:1510.07670 [cond-mat], Oct. 2015 (cited on page 149).

[168] Q. Redon, Q. Liu, J.-B. Bouhiron, N. Mittal, A. Fabre, R. Lopes, and S. Nascimbene, *Realizing the entanglement Hamiltonian of a topological quantum Hall system*, arXiv:2307.06251 [cond-mat, physics:quant-ph], July 2023 (cited on pages 150, 153, 155).

[169] M. Haque, O. Zozulya, and K. Schoutens, "Entanglement Entropy in Fermionic Laughlin States", Physical Review Letters **98**, Publisher: American Physical Society, 060401 (2007) (cited on page 150).

[170] A. M. Läuchli, E. J. Bergholtz, and M. Haque, "Entanglement scaling of fractional quantum Hall states through geometric deformations", en, New Journal of Physics **12**, 075004 (2010) (cited on page 150).

[171] R. Lundgren, J. Blair, M. Greiter, A. Läuchli, G. A. Fiete, and R. Thomale, "Momentum-Space Entanglement Spectrum of Bosons and Fermions with Interactions", Physical Review Letters **113**, Publisher: American Physical Society, 256404 (2014) (cited on page 151).

[172] R. Lundgren, "Momentum-space entanglement in Heisenberg spin-half ladders", Physical Review B **93**, Publisher: American Physical Society, 125107 (2016) (cited on page 151).

[173] K. Choo, C. W. von Keyserlingk, N. Regnault, and T. Neupert, "Measurement of the Entanglement Spectrum of a Symmetry-Protected Topological State Using the IBM Quantum Computer", Physical Review Letters **121**, Publisher: American Physical Society, 086808 (2018) (cited on page 151).

[174] H. Pichler, G. Zhu, A. Seif, P. Zoller, and M. Hafezi, "Measurement Protocol for the Entanglement Spectrum of Cold Atoms", Physical Review X **6**, Publisher: American Physical Society, 041033 (2016) (cited on page 151).

[175] T. V. Zache, C. Kokail, B. Sundar, and P. Zoller, "Entanglement Spectroscopy and probing the Li-Haldane Conjecture in Topological Quantum Matter", en-GB, Quantum **6**, Publisher: Verein zur Förderung des Open Access Publizierens in den Quantenwissenschaften, 702 (2022) (cited on page 152).

[176] M. Dalmonte, B. Vermersch, and P. Zoller, "Quantum simulation and spectroscopy of entanglement Hamiltonians", en, Nature Physics **14**, Number: 8 Publisher: Nature Publishing Group, 827–831 (2018) (cited on page 152).

[177] J. J. Bisognano and E. H. Wichmann, "On the Duality Condition for a Hermitian Scalar Field", J. Math. Phys. **16**, 985–1007 (1975) (cited on page 152).

[178] J. J. Bisognano and E. H. Wichmann, "On the duality condition for quantum fields", Journal of Mathematical Physics **17**, 10.1063/1.522898 (1976) (cited on pages 152, 159).

[179] G. Giudici, T. Mendes-Santos, P. Calabrese, and M. Dalmonte, "Entanglement Hamiltonians of lattice models via the Bisognano-Wichmann theorem", Physical Review B **98**, Publisher: American Physical Society, 134403 (2018) (cited on page 152).

[180] T. Mendes-Santos, G. Giudici, M. Dalmonte, and M. A. Rajabpour, "Entanglement Hamiltonian of quantum critical chains and conformal field theories", Physical Review B **100**, Publisher: American Physical Society, 155122 (2019) (cited on page 152).

[181] B. Oblak, N. Regnault, and B. Estienne, "Equipartition of entanglement in quantum Hall states", Physical Review B **105**, Publisher: American Physical Society, 115131 (2022) (cited on page 153).

[182] M. K. Joshi, C. Kokail, R. van Bijnen, F. Kranzl, T. V. Zache, R. Blatt, C. F. Roos, and P. Zoller, *Exploring Large-Scale Entanglement in Quantum Simulation*, arXiv:2306.00057 [quant-ph], May 2023 (cited on page 157).

[183] G. Bornet et al., "Scalable spin squeezing in a dipolar Rydberg atom array", en, Nature, Publisher: Nature Publishing Group, 1–6 (2023) (cited on page 157).

[184] M. Schlosser, D. O. d. Mello, D. Schäffner, T. Preuschoff, L. Kohfahl, and G. Birkl, "Assembled arrays of Rydberg-interacting atoms", en, Journal of Physics B: Atomic, Molecular and Optical Physics **53**, Publisher: IOP Publishing, 144001 (2020) (cited on page 157).

[185] N. Nishad, A. Keselman, T. Lahaye, A. Browaeys, and S. Tsesses, *Quantum simulation of generic spin exchange models in Floquet-engineered Rydberg atom arrays*, arXiv:2306.07041 [cond-mat, physics:physics, physics:quant-ph], June 2023 (cited on page 157).

[186] C. Chen et al., "Continuous symmetry breaking in a two-dimensional Rydberg array", en, Nature **616**, Number: 7958 Publisher: Nature Publishing Group, 691–695 (2023) (cited on page 157).

[187] T. Bilitewski and N. R. Cooper, "Synthetic dimensions in the strong-coupling limit: Supersolids and pair superfluids", Physical Review A **94**, Publisher: American Physical Society, 023630 (2016) (cited on page 159).

[188] S. Barbarino, L. Taddia, D. Rossini, L. Mazza, and R. Fazio, "Magnetic crystals and helical liquids in alkaline-earth fermionic gases", en, Nature Communications **6**, Number: 1 Publisher: Nature Publishing Group, 8134 (2015) (cited on page 159).

[189] M. O. Goerbig, "From fractional Chern insulators to a fractional quantum spin hall effect", en, The European Physical Journal B **85**, 15 (2012) (cited on page 159).

[190] Y. Li, G. I. Martone, L. P. Pitaevskii, and S. Stringari, "Superstripes and the Excitation Spectrum of a Spin-Orbit-Coupled Bose-Einstein Condensate", Physical Review Letters **110**, Publisher: American Physical Society, 235302 (2013) (cited on page 159).

[191] C. Hickey, P. Rath, and A. Paramekanti, "Competing chiral orders in the topological Haldane-Hubbard model of spin-1/2 fermions and bosons", Physical Review B **91**, Publisher: American Physical Society, 134414 (2015) (cited on page 159).

[192] B. I. Halperin, "Statistics of Quasiparticles and the Hierarchy of Fractional Quantized Hall States", Physical Review Letters **52**, Publisher: American Physical Society, 1583–1586 (1984) (cited on page 160).

[193] T. Chalopin, "Quantum-enhanced sensing and synthetic Landau levels with ultracold dysprosium atoms", en, PhD thesis (Sorbonne Université, Dec. 2019) (cited on page 160).

[194] L. Barbiero, L. Chomaz, S. Nascimbene, and N. Goldman, "Bose-Hubbard physics in synthetic dimensions from interaction Trotterization", Physical Review Research **2**, Publisher: American Physical Society, 043340 (2020) (cited on page 160).

[195] B. McCanna and H. M. Price, "Superfluid vortices in four spatial dimensions", Physical Review Research **3**, Publisher: American Physical Society, 023105 (2021) (cited on page 160).

[196] B. McCanna and H. M. Price, *Curved vortex surfaces in four-dimensional superfluids: I. Unequal-frequency double rotations*, arXiv:2309.08015 [cond-mat], Sept. 2023 (cited on page 160).

[197] B. McCanna and H. M. Price, *Curved vortex surfaces in four-dimensional superfluids: II. Equal-frequency double rotations*, arXiv:2309.08016 [cond-mat], Sept. 2023 (cited on page 160).

[198] J. Koplik and H. Levine, "Vortex reconnection in superfluid helium", Physical Review Letters **71**, Publisher: American Physical Society, 1375–1378 (1993) (cited on page 160).

[199] S. Nazarenko and R. West, "Analytical Solution for Nonlinear Schrödinger Vortex Reconnection", en, Journal of Low Temperature Physics **132**, 1–10 (2003) (cited on page 160).

[200] S. Zuccher, M. Caliari, A. W. Baggaley, and C. F. Barenghi, "Quantum vortex reconnections", Physics of Fluids **24**, 125108 (2012) (cited on page 160).

[201] A. L. Fetter, "Rotating trapped Bose-Einstein condensates", Reviews of Modern Physics **81**, Publisher: American Physical Society, 647–691 (2009) (cited on page 160).

RÉSUMÉ

Cette thèse présente des réalisations expérimentales de systèmes topologiques, obtenues avec des atomes de dysprosium. Nos protocoles consistent à encoder deux dimensions synthétiques dans le grand spin du dysprosium, $J = 8$, et à les coupler à la quantité de mouvement des atomes via des transitions Raman.
Tout d'abord, nous simulons des systèmes de Hall quantiques en deux dimensions, sur une géométrie plane et sur une géométrie cylindrique. Dans cette dernière, nous avons pu mettre en œuvre pour la première fois la pompe topologique de Laughlin, qui est intimement liée à la quantification de la conductance de Hall. Nous présentons ensuite le résultat principal de cette thèse : la réalisation d'un système de Hall quantique en 4D, en combinant deux dimensions spatiales et deux dimensions synthétiques. Nous comparons nos résultats avec les prédictions d'un modèle effectif, décrivant notre système comme une somme directe d'une paire de niveaux de Landau en 2D. Nous révélons des caractéristiques typiques de l'effet de Hall quantique en 4D, notamment les états de bord anisotropes, la réponse électromagnétique non linéaire et la quantification du second nombre de Chern.
Enfin, nous revenons à une géométrie bidimensionnelle et étudions l'hamiltonien d'intrication d'un système de Hall quantique à une particule. Une approximation de l'hamiltonien d'intrication est réalisée expérimentalement en s'appuyant sur le théorème de Bisognano-Wichmann. Nous présentons une feuille de route pour étendre ce protocole à des systèmes topologiques avec interactions.

MOTS CLÉS

Simulation quantique, gaz quantiques, effet Hall quantique, matière topologique

ABSTRACT

This thesis presents experimental realisations of topological systems obtained with dysprosium atoms. Our protocols consist in encoding synthetic dimensions in dysprosium's large spin, $J = 8$, and in coupling these synthetic dimensions to momentum via Raman transitions.
We first emulate quantum Hall systems in two dimensions (one synthetic and one spatial), on a planar geometry and on a cylindrical geometry. In the latter, we were able to implement for the first time Laughlin's topological charge pump, which is intimately linked to the Hall conductance quantization. Afterwards, we present the main result of this thesis : the realisation a 4D quantum Hall system, by combining two spatial dimensions and two synthetic ones. We compare our findings with the predictions of an effective model, which describes our system as a direct sum of a pair of 2D Landau levels. We unveil typical features of the 4D quantum Hall effect, including the anisotropic edge modes, the non-linear electromagnetic response and the quantization of the second Chern number.
Finally, we return to the 2D geometry, and investigate the entanglement Hamiltonian of a single-particle quantum Hall system. An approximation of the entanglement Hamiltonian is experimentally realised by following the Bisognano-Wichmann theorem. We present a roadmap for extending this protocol to interacting topological systems.

KEYWORDS

Quantum simulation, Quantum gases, Quantum Hall effect, Topological matter